Modelling the Disintegration of Pharmaceutical Tablets: Integrating a Single Particle Swelling Model with the Discrete Element Method

PhD Thesis

Mithushan Soundaranathan

Under the supervision of

Dr Daniel Markl

Professor Blair Johnston

Strathclyde Institute of Pharmacy and Biomedical Sciences
CMAC
University of Strathclyde, Glasgow

March 4, 2024

This thesis is the result of the author's original research. It has been composed by the author and has not been previously submitted for examination which has led to the award of a degree.

Signed:

Nithushan. S

Date: March 4, 2024

Abstract

The main aim of this research was to develop a model of the disintegration processes by considering each mechanism which includes liquid imbibition, swelling and the break-up of the interparticulate bonds. Tablet disintegration is a critical process for dissolving and enabling the absorption of the drug substance into the bloodstream.

The tablet disintegration process consists of multiple connected and interdependent mechanisms: liquid penetration, swelling, dissolution and break-up. One of the most critical processes is the liquid penetration through the porous tablet structure, which initiates the swelling of particles in the tablet. This swelling builds up internal stress that causes the break up of the tablet into smaller agglomerates and the primary particles. For the tablet to disintegrate, the internal swelling stress must exceed the strength of the bonds that are formed during compaction. It is important to note that there is a strong interdependence between these different disintegration mechanisms, e.g. particle swelling will cause a change in the pore structure which will directly affect the liquid penetration process. The performance of a tablet can thus only be understood and optimised by considering the interconnection of every step involved in the disintegration and dissolution processes. Modelling and simulating are great tools to better understand the fundamental disintegration process and its interdependence.

The tablet disintegration model developed in this study consists of three main parts: 1) tablet compaction model in Discrete element method (DEM), 2) tablet swelling model in DEM with a single particle swelling model and 3) liquid penetration data, which was determined by two different methods: 1) liquid penetration model and 2) experimental liquid penetration data. Both the compaction and disintegration model were implemented in the open-source DEM software Yade-DEM.

The tablet disintegration model developed by combining DEM with a single particle swelling model and experimental liquid penetration data, captures the difference in swelling behaviour of tablets with different porosities and formulations well. For all tablets, the pore size increases over time, and the pores open up shortly before the break-up of the tablet. The closure of pores hinders the liquid from accessing other particles and slows down the overall swelling process. The results also showed the closure of pores in both wetted volume and dry volume. The closure of pores hinders the liquid from accessing other particles and slows down the overall swelling process.

The tablet swelling model was further developed by including a dimensional liquid penetration model instead of experimental data. Using the liquid penetration model and calibration of modelling parameters for the liquid model, the liquid penetration in various formulations could be simulated. The model was able to simulate the disintegration of different formulations, by varying the porosity and the disintegrant concentrations. The liquid penetration model showed that adding disintegrant to the formulation increases the permeability thereby increasing the capability of the tablet to transmit fluid. The results showed that across all formulations the maximum swelling time increases with decreasing the porosity. The results also showed that increasing the disintegrant concentration above, $5\% w/w$ would have a negative effect on the disintegration time.

Contents

List of Figures

List of Tables

Acknowledgement

First and foremost, I would like to thank my supervisor Dr Daniel Markl for his support and encouragement during my PhD journey. I truly enjoy our working relationship, which is very dependable, interesting, honest and innovative. Thank you for shaping me to be a better researcher and person, which will truly help my future both professionally and personally. Also, thanks for putting up with me!

I would like also to thank Dr Kendal Pitt for all his help and for his insightful ideas to solve various issues and feedback for my work, and for all of the time he invested in this project. To my secondary supervisor and former MSc supervisor Professor Blair Johnston thank you for getting me interested in pursuing a PhD, as well for the expertise and support you offered for this project.

Next, I would like to thank members of the Markl research group and my colleagues in CMAC, you truly made my PhD journey a lot more enjoyable and thanks for the fun time at the social events, and also for reminding me of the bagpipe incident every single time we meet.

Huge thanks to Dr Thomas Sweijen for helping me with setting up my simulation and patiently answering the thousands of emails I sent him. I want to thank Dr Mohammed Al-Sharabi and Dr Prince Bawuah for conducting experimental work and preparing the experimental data to validate my models. To Peyman Mostafaei, thank you for our friendly meeting once a month to discuss disintegration modelling, for helping me see my project from another perspective and for sharing a lot of interesting papers. Special thanks to Anas Almudahka for letting me borrow the workstation to re-run my simulation.

I would also like to thank amma (mom) and appa (dad), and my brother for their continuous support. You have always encouraged me to follow my dreams and told me that anything is possible. Special thanks for the endless encouraging phone call during difficult periods in my PhD time. To my friend Hassan Nisar thank you for sending wonderful messages and sending funny memes almost daily, it really made day after tough working day. Finally, I would like to thank my uncle Alexis Rajkumar who has been by my side since the day I was born.

Abbreviations

API = Active pharmaceutical ingredient

BPM = Bonded particle model

CCS = Croscarmellose sodium

CFD = Computational fluid dynamics

DCPa = Dibasic calcium phosphate anhydrous

DEM = Discrete element method

DoE = Design of Experiments

vDoE = Virtual Design of Experiments

ESEM = Environmental scanning electron microscope

FEM = Finite element method

I.D = Inner diameter

L-HPC = Low-substituted hydroxypropyl cellulose

MCC = Microcrystalline cellulose

MCC500 = MCC Cellets®500

MCC700 = MCC Cellets®700

MCC1000 = MCC Cellets®1000

MRI = Magnetic resonance imaging

O.D = Outer diameter

PBE = Population balance equations

PH101 = MCC avicel PH101

PH102 = MCC avicel PH102

PFV = Pore finite volume

PLGA = Poly latic-co-glycolic acid

PS = Pore size
PSD = Pore size distribution
PUA = Pore unit assembly
RMSE = Root mean square error
SAP = Superabsorbent particles
SDI = Surface dissolution imaging
SSG = Sodium starch glycolate
THz = Terahertz
TPI = Terahertz pulsed imaging
XPVP = Crospovidone
XμCT = X-ray micro computed tomography

Symbols

Symbol	[Units]	Definition
A	m^2	Area
A_{actual}	m^2	Actual available surface area
A_{cap}	m^2	Surface area of overlapping cap
A_{ham}	J	Hamaker constant
A^f	m^2	Free area
A_{IJ}	m^2	Cross-area area of pore throat
A_{cap}	m^2	Particle surface area
a	-	Fitting parameter
a_c	-	Constant expressing the pore radius constriction
B^0	m/s	Rate term
b	-	Fitting parameter
b_d	s^{-1}	Damping force parameter
C	$\mathrm{kg/m}^3$	Concentration of particles
C_a	$\mathrm{kg/m}^3$	Solution concentration of drug substance
C_e	$\mathrm{kg/m}^3$	Concentration after complete dissolution
C_s	$\mathrm{kg/m}^3$	Concentration of solid on surface
C_{Loss}	J/m	Energy loss coefficient
$C^s_{\mathrm{SAP,0}}$	$\mathrm{kg/m}^3$	Initial solid bulk concentration of SAP
C_{sat}	$\mathrm{kg/m}^3$	Saturation concentration
D	$\mu m^2/s$	Diffusion coefficient
D_r	$\mu m^2/s$	Diffusion coefficient of non-Fickian contribution

d	m	Diameter
E	Pa	Young's modulus
$\mathbf{e}$	-	Gravity unit vector
$\mathbf{F}$	N	Force
$\mathbf{F}_d$	N	Drag force
$\mathbf{F}_{\mathrm{damp}}$	N	Damping force
$\mathbf{F}_{\mathrm{grav}}$	N	Global attractive force
$\mathbf{F}^n$	N	Force in normal direction
$\mathbf{F}_{\mathrm{rep}}$	N	Repulsion force
$\mathbf{F}^t$	N	Force in tangential direction
$\mathbf{F}_{pl}$	N	Coupling term between particle and liquid phase
$\mathbf{F}^{\mathrm{vdw}}$	N	Van der Waals force
F^b	N	Bonding force
f	-	Particle growth factor
f_w	-	Fraction of available surface area
G	Pa	Shear modulus
G_m	g/m	Unit column mass
g	9.81 m^2/s	Gravity of earth
g_{IJ}	m/s	Hydraulic conductivity
H_0	m	Initial tablet thickness
h	m	Height
I	kgm^2	Polar moment of inertia
J	kgm^2	Moment of inertia
J^s	-	Volume dilation function
k_1	N/m	Loading stiffness
k_2	N/m	Plastic unloading stiffness
k_c	N/m	Adhesion stiffness
k_p	N/m	Limit plastic unloading stiffness
$k_{\mathrm{t,stiff}}$	N/rad	Stiffness coefficient
$\mathbf{k}$	m/s	Conductivity

$\mathbf{K}^l$	m/s	Hydraulic conductivity tensor
$\mathscr{K}$	m^2	Intrinsic permeability
$\mathscr{K}_r^l$	m^2	Relative permeability for the liquid phase
k_b	-	kinetic parameter
k_{diss}	s^{-1}	Dissolution rate constant
k_{rep}	-	Repulsion force constant
k_{swe}	-	kinetic parameter
k_ω	s^{-1}	Kinetic constant
L	m	Liquid penetration depth
L_f	m	Actual length penetration length
l	m	Distance
M	N·m	Moment
m	kg	mass
m^s	kg	Particle mass
m^w	kg	Mass of absorbed water
n^{size}	-	Number size distribution
ΔP	Pa	Pressure difference
p_{air}	Pa	Air pressure
P_c	Pa	Capillary pressure
P_{fluid}	Pa	Fluid pressure
P_{liq}	Pa	Liquid pressure
p_y	Pa	Yield pressure for particle deforms plastically
q	$m^3/s{\cdot}m^2$	Volumetric flux
q_{IJ}	m^3/s	Volumetric flow rate
q_I^{abs}	-	Absorption rate in pore unit
Q_i^{abs}	g/g	Liquid absorption ratio
Q^{max}	g/g	Maximum liquid absorption ratio
Q_2^s	-	SAP Liquid uptake
$R*$	m	Equivalent radius
RD	m^5/s	Dissolution rate terms

r	m	Radius
r_b	m	Bonding radius
r_c	m	Pore radius
r_{col}	m	Inner column radius
r_h	m	Hydraulic radius
r_p	m	Particle radius
S	m	Interparticle separation
s	-	Saturation
s^l	-	Liquid saturation
$T*$	s	Normalised time
t	s	time
$\mathbf{u}_l$	m/s	Liquid velocity
$\mathbf{u}_p$	m/s	Particle velocity
u^s	m	Solid displacement
V	m^3	Volume
V_t	m^3	Tablet Volume
V_{IJ}	m^3	Void volume of pore throat
V_L	%	Volumetric liquid content
w	-	Mass fraction
z	-	Correction factor for intrinsic permeability calculation
α_a	kg/s^2	Attractive force strength coefficient
α_{shape}	-	Shape factor
β_l	$\text{kg/m}^3\text{s}$	Inter-phase momentum transfer coefficient
Δt	s/steps	Time steps
$\Delta\tau_{\text{vir}}$	s/steps	Virtual time steps
δ	m	Particles overlap
δ_0	m	Plastic contact deformation overlap
δ_{dd}	-	Dirac delta function
δ_{lim}	m	Plastic limit overlap
δ_{max}	m	Maximum compression overlap

δ_n	m	Normal overlap
γ	N/m	Surface tension
ϵ	-	Porosity
ζ	m	Swelling rate
ζ_v	%	Volumetric swelling
η	mPas	Liquid viscosity
η_{dyn}	mPas	Dynamic viscosity
η_{damp}	Ns/m	Damping coefficient
θ	rad	Contact angle
θ_e	rad	Euler angle
ι_t	m	displacement in tangential direction
κ	-	Geometrical constants
μ_s	-	Sliding friction coefficient
ν	-	Poisson ratio
$\xi_{a,3}$	kg·m/s	Third moment
ξ_s	m	Total tangential displacement of particles contact
$\xi_{s,max}$	m	Threshold value determining the onset of gross sliding
ϱ	g/cm^3	Density
ϱ_l	g/cm^3	Liquid density
ϱ_t	g/cm^3	True density
ϱ_w	g/cm^3	Water density
σ	m/s	Linear erosion rate
τ	-	Tortuosity
τ_l	N/m^2	Viscous stress tensor
υ	rad/s	Angular velocity
Φ	-	Friction coefficient
ϕ_{f}	-	Dimensionless plasticity depth
ψ^l	m	Pressure head of liquid phase
χ	-	Geometrical constants
ω_f	-	Local volume fraction

ω_l	-	Liquid volume fraction

Research Outputs

Publications

- Alshafiee, M., AlAlaween, W.H., Markl, D., **Soundaranathan, M.**, Almajaan, A., Walton, K., Blunt, L., Asare-Addo, K., 2019. A predictive integrated framework based on the radial basis function for the modelling of the flow of pharmaceutical powders. International Journal of Pharmaceutics, 568, 1185.
- **Soundaranathan, M.**, M., Vivattanaseth, P., Walsh, E., Pitt, K., Johnston, B., Markl, D., 2020. Quantification of Swelling Characteristics of Pharmaceutical Particles. International Journal of Pharmaceutics, 590, 119903.
- Maclean, N., Walsh, E., **Soundaranathan, M.**, Khadra, I., Mann, J., Williams, H., Markl, D., 2020. Exploring the Performance-Controlling Tablet Disintegration Mechanisms for Direct Compression Formulations. International Journal of Pharmaceutics, 599, 120221.
- **Soundaranathan, M.**, Al-Sharabi, M., Sweijen, T., Bawuah, P., Zeitler, J.A., Hassanizadeh, S.M., Pitt, K., Johnston, B.F., Markl, D., 2023. Modelling the Evolution of Pore Structure during the Disintegration of Pharmaceutical Tablets. Pharmaceutics, 15, 489.

Conference Contributions

- **Soundaranathan, M.**, Johnston, B. and Markl, D. Linking digital manufacturing to a digital tablet: Simulating tablet disintegration using discrete element and pore-scale modelling. EPSRC CMAC Summer School, 2019. Glasgow, UK. **Oral Presentation**.

- **Soundaranathan, M.**, Walsh, E., Johnston, B. and Markl, D. Quantifying the Swelling of Single Particles using a Custom Built Flow Cell. EPSRC CMAC Summer School, 2019. Glasgow, UK. **Poster Presentation**.
- **Soundaranathan, M.**, Walsh E., Johnston, B. and Markl, D. Quantifying the Swelling of Single Particles using a Custom-Built Flow Cell. 13th Pharmaceutical Solid State Research Cluster Annual Meeting, 2019. Düsseldorf, Germany. **Oral Presentation**.
- **Soundaranathan, M.**, Pitt, K. and Markl, D. Linking digital manufacturing to a digital tablet: Simulating tablet disintegration using discrete element and pore-scale modelling. SRPe Annual Conference, 2019. Glasgow, UK. **Poster Presentation**.
- **Soundaranathan, M.**, Vivattanaseth, P., Walsh, E., Pitt, K. and Markl, D. Quantifying the Swelling of Single Particles using a Custom-Built Flow Cell. EPSRC CMAC Internal Research Day, 2020. Glasgow, UK. **Poster Presentation**.
- **Soundaranathan, M.**, Vivattanaseth, P., Walsh, E., Pitt, K. and Markl, D. Quantification of Swelling Characteristics of Pharmaceutical Particles. EPSRC CMAC Open Day, 2020. Online. **Oral Presentation**.
- **Soundaranathan, M.**, Vivattanaseth, P., Walsh, E., Pitt, K. and Markl, D. Quantification of Swelling Characteristics of Pharmaceutical Particles. EPSRC CMAC Open Day, 2020. Online. **Poster Presentation**.
- **Soundaranathan, M.**, Vivattanaseth, P., Walsh, E., Pitt, K. and Markl, D. Quantification of Single Particle Swelling. 14th Pharmaceutical Solid State Research Cluster Annual Meeting, 2020. Online. **Oral Presentation**.
- **Soundaranathan, M.**, Pitt, K. and Markl, D. Linking digital manufacturing to

a digital tablet: Simulating tablet disintegration using discrete element and pore-scale modelling. SRPe Annual Conference, 2020. Online. **Poster Presentation**.

- **Soundaranathan, M.**, Sweijen, T., Hassanizadeh, S. M., Pitt, K., Blair Johnston, B. and Markl D. Discrete element modelling of tablet compaction and disintegration. CMAC Mini Symposia, 2021. Online. **Oral Presentation**.
- **Soundaranathan, M.**, Sweijen, T., Hassanizadeh, S. M., Pitt, K., Blair Johnston, B. and Markl D. Tablet compaction of deformable particles by discrete element modelling. CMAC Mini Symposia, 2021. Online. **Poster Presentation**.
- **Soundaranathan, M.**, Al-Sharabi, M., Sweijen, T., Pitt, K., Zeitler, J. A., Hassanizadeh, S. M., Blair Johnston, B. and Markl D. Modelling pharmaceutical tablet swelling using discrete element method and a single particle swelling model. 14^{th} Intepore Annual Meeting, 2022. Abu Dhabi, United Arab Emirates (online). **Oral Presentation**.
- **Soundaranathan, M.**, Al-Sharabi, M., Sweijen, T., Pitt, K., Zeitler, J. A., Hassanizadeh, S. M., Blair Johnston, B. and Markl D. Modelling the swelling of pharmaceutical tablets from single particle understanding using DEM. EPSRC CMAC Open Day, 2022. Glasgow, UK. **Poster Presentation**.
- **Soundaranathan, M.**, Al-Sharabi, M., Sweijen, T., Pitt, K., Zeitler, J. A., Hassanizadeh, S. M., Blair Johnston, B. and Markl D. Modelling the swelling of pharmaceutical tablets from single particle understanding using DEM. EPSRC CMAC Summer School, 2022. Crieff, UK. **Poster Presentation**.

Supervisory Roles

- Pattavet Vivattanaseth, Linking swelling of single superdisintegrant particles to their physical and chemical characteristics. Submitted in partial fulfilment for the degree of Master of Science in Advanced Pharmaceutical Manufacturing, 2019. University of Strathclyde, UK. **Secondary Supervisor** (Main advisor: Dr Daniel Markl).

- Safina Ludovick Kabelinde, Simulating the disintegration process using a discrete element model. Submitted in partial fulfilment for the degree of Master of Science in Advanced Pharmaceutical Manufacturing, 2021. University of Strathclyde, UK. **Secondary Supervisor** (Main advisor: Dr Daniel Markl).

Chapter 1

Introduction

1.1 Pharmaceutical industry

The pharmaceutical industry is one of world's largest industrial sectors, with an annual revenue exceeding one trillion dollars [Brown et al., 2018]. Recent reports are suggesting a further increase in revenue with approximately 13.7% within the next 6-7 years [Mikulic, 2020]. The cost associated with developing a new drug from a laboratory idea to a successful commercialised product is approximately two billion dollars. The manufacturing cost is about 27-30% of sales and the whole development of a new drug take more than ten years. Pharmaceutical companies invest heavily in research and development, a recent problem in the industry has been the decline in productivity (number of drugs released) [Basu et al., 2006, Federsel, 2009]. The patent protection of a drug molecule is approximately twenty years in the UK and lower in some other countries. A pharmaceutical company has about eight to twelve years, to recover their cost and gain profit. Since once the patent protection expire the generic companies can copy their formulation, and the patent protection is given to the drug molecule itself and not on the formulation.

1.2 Tablet compaction

The most preferred drug delivery method are oral solid dosage forms, which includes tablets and capsules. The market share of oral solid dosage forms is about 80% [Eggenreich et al., 2016]. About 90% of orally consumed pharmaceutical products [Indurkhya et al., 2018] are administered in the form of a tablet to deliver the active pharmaceutical ingredient (API) [Sugimori, 2015]. The most common tablets are manufactured by compacting a formulated powder blend that is composed of one drug substance and a number of different excipients [Kadiri et al., 2005]. The compaction process consist of four main steps:

- Filling of the die.
- Loading: punch moves towards the powder. During the loading stages the powder are repacking and reach their maximum compression pressure.
- Unloading: the punch moves away from the tablet.
- Ejection of the final tablet [Sanchez-Castillo and Anwar, 2003].

The physical and mechanical properties of the tablets, such as porosity and mechanical strength, are significantly affected by the selected formulation and the process conditions used to make the tablet compact [Cunningham et al., 2004]. The compaction of the powder blend is of critical importance since the particles experience intensive deformation and start to bond through van der Waals forces, mechanical interlocking and formation of solid bridges [Wu et al., 2008].

During the development of a drug product, formulation and process conditions must be selected to deliver a tablet with desired properties in terms of its strength, content and disintegration/dissolution performance. This typically requires a large number of experiments for every new product to explore the relationship between material attributes, process conditions and performance behaviour in order to identify suitable and robust conditions for the final product.

The physical properties and mechanical strength of the tablet control its disintegration behaviour, which is critical for dissolving and enabling the absorption of the drug substance into the blood stream.

1.3 Tablet disintegration

Disintegration is the process where a tablet is disaggregated into multiple smaller particles and agglomerates. The disintegration process will increase the surface area available for dissolution and thereby impacts the dissolution rate which is accelerated by smaller particles/agglomerates [Quodbach and Kleinebudde, 2015]. A faster and better controlled disintegration process results in a more predictive on-set of the desired therapeutic effect. The tablet disintegration process consists of multiple connected and interdependent mechanisms: liquid penetration, swelling, dissolution (excipients and drug) and break-up, an overview of the mechanism involved in the disintegration process is given in Figure 1.1. The importance of each process depends on the formulation and process conditions used. One of the most critical processes is the liquid penetration through the porous tablet structure, which initiates the swelling of particles in the tablet. This swelling builds up internal stress that causes the break up of the tablet into smaller agglomerates and the primary particles [Markl and Zeitler, 2017, York, 2022]. The size of the disintegrated particles/agglomerates then drives the dissolution rate of the drug. For the tablet to disintegrate, the internal swelling stress must exceed the strength of the bonds that are formed during compaction [Markl and Zeitler, 2017]. The liquid penetration rate is strongly influenced by the tablet porosity, i.e. it generally increases with increasing porosity [Al-Sharabi et al., 2020]. In many cases, liquid penetration is the controlling mechanism for the tablet disintegration, i.e. the time it takes to disintegrate a tablet highly depends on the liquid uptake. It is important to note that there is a strong interdependence between these different disintegration mechanisms, e.g. particle swelling will cause a change of the pore structure which will directly affect the liquid penetration process [Markl and Zeitler, 2017].

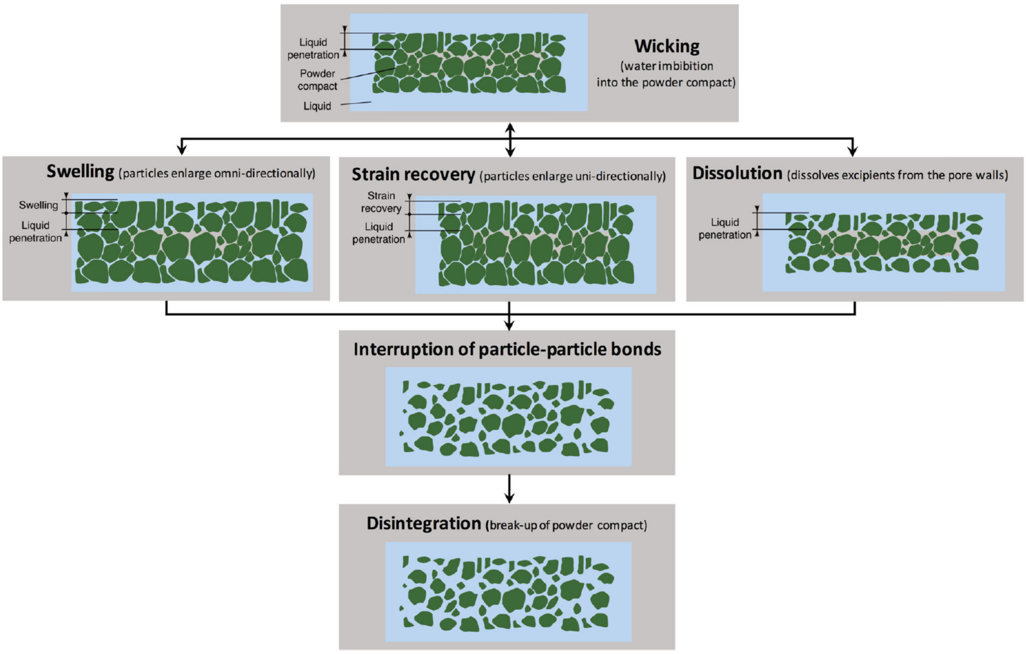

Figure 1.1: Overview of the mechanism involved in the disintegration process, taken from [Markl and Zeitler, 2017]

1.3.1 Liquid penetration

Wicking is the process of liquid imbibition in a tablet, the process is controlled by the capillary forces [Schoenmaker et al., 2011], and is considered as the first step in the tablet disintegration process. As observed by Shotton and Leonard [1972], the water does not only penetrate the tablet through pores but also through the hydrophilic network created by the disintegrant particles [Quodbach and Kleinebudde, 2015].

The rate of penetration is determined by the balance between capillary and opposite viscous forces (the force between a body and a fluid) and can be described by the Washburn equation (Equation 1.1) [Desai et al., 2015, Markl et al., 2017b]. In Washburn equation the pore structure is considered as a bundle of capillary tubes of varying diameter [Washburn, 1921].

$$L = \sqrt{\frac{\gamma \cos\theta r_{c,0}}{2\eta} t}, \tag{1.1}$$

where L is the liquid penetration length into the capillary, γ is the surface tension, θ is the solid-liquid contact angle, $r_{c,0}$ is the pore size, t is time and η is the liquid viscosity.

Both the capillary and viscous forces are affected by the physical properties of the fluid and pores structure, in the tablet formulation only the pores structure can be controlled as physical properties (after the excipients are selected) and the physical properties of disintegration media can not either be controlled or selected, as it depends on the site of action [Markl and Zeitler, 2017].

Mostly in the pharmaceutical industry, the tablet pore structure is only described by total porosity. The total porosity is defined as the fraction of the volume of voids over the total volume, which is in reality a measurement on the void space in the tablet. Previous research has shown the disintegration performance of a tablet is highly influenced by the tablet porosity [Bi et al., 1999]. As explained by Tye et al. [2005], the porosity of a tablet is directly affected by the compaction force and speed. However, porosity alone is not sufficient enough to describe and characterise a complex pore structure. The pore structure can be better described by a combination of a parameter such as characteristic length (effective pore radius in the porous medium), a constriction factor (fluctuation in local hydrodynamic radii), a tortuosity (effective length of the streamlines) and effective porosity (the ratio of the volume of the conducting pores to the total volume) [Berg, 2014, Koponen et al., 1997, Markl and Zeitler, 2017].

To gain a better understanding of liquid penetration, the permeability, $\mathscr{K}$ (as defined by Darcy's law [Darcy, 1856]), need to be taken into account. The permeability is a measure on the capability of a porous medium to transmit fluid [Markl and Zeitler, 2017]. Most of the previous research only measured the permeability of air in a tablet [Alderborn et al., 1985, Lowenthal and Burruss, 1971]. The method utilised in these studies can not be applied in measuring liquid penetration into the powder compact due to the complex interplay between liquid penetration kinetics, swelling and dissolution as well as time- and spatial dependence of the permeability [Markl and Zeitler, 2017]. Ganderton and Fraser [1970] analysed the relationship between the permeability of a tablet and its pore structure for various formulations including aspirin, lactose, magnesium carbonate, calcium phosphate, phenindione and sucrose tablets. They investigated how factors such as tablet compaction pressure, particle size, and granulation, influenced the porosity and permeability. Their results revealed that the fine particle of aspirin and pheninodione were impermeable and had a low penetration rate. While formulation containing lactose had high permeability and penetration rate.

The disintegration of powder compact is highly influenced by the chemical properties of the disintegration fluid [Zhao and Augsburger, 2005]. The main liquid attributes affecting the disintegration are: viscosity, contact angle, and surface tension. The study from Anwar et al. [2005] has shown that these parameters will have an impact on the liquid penetration rate, and thereby the disintegration time. Cooper and Brecht [1957] reported that the disintegration is more rapid in a liquid with low surface tension. The study conducted by Abbott et al. [1959] concluded that disintegration in liquid with a high viscosity will lead to a longer disintegration time. The reason is that high viscosity will potentially result in stronger adhesive forces between large particles, which work against the swelling mechanism of disintegration [Markl and Zeitler, 2017].

1.3.2 Swelling

The swelling of a tablets is caused by the swelling of individual particles inside the tablet. The swelling is initiated by particle absorbing the liquid penetrating through tablet pores. [Markl and Zeitler, 2017]. Particle swelling is the volumetric expansion of the particle during liquid contact [Faroongsarng and Peck, 1994]. The particle can enlarge in either omnidirectionally (all directions) or unidirectionally (single direction). The swelling ability of the particle depends on the particle size, chemical structure and degree of cross-linking of polymeric systems [Bell and Peppas, 1996, Desai et al., 2015]. To prevent polymers from dissolving into water during swelling, other polymers are used to bind them, which are referred to as cross-linkers [Sweijen et al., 2017a]. It has been observed that polymers with cross-linking produce a high swelling force but have a limited volume expansions, however, the disintegration time is quicker compared to other strongly swelling particles [Quodbach and Kleinebudde, 2015]. Typically, disintegrants are added to a formulation as a swelling agent, and therefore enhance the disintegration process.

During the swelling process of tablets, the particle enlarges omnidirectionally, which creates a pressure inside the tablet and thereby push apart adjoining components. This will eventually cause the tablet to break-up into smaller particles and agglomerates [Quodbach et al., 2014b]. The omnidirectional enlargement of a tablet is referred to swelling, whereas the uni-directional enlargement is called strain recovery. Swelling is the most accepted method in tablet disintegration [Patel and Hopponent, 1966]. A high swelling volume is not essential for disintegration since most of the binding forces within the tablet work only over very short distance [Quodbach and Kleinebudde, 2015].

The swelling ability is different for each material, therefore by changing the material in a formulation has an impact on how quickly a tablet breaks up (i.e. disintegration time) as seen in Figure 1.2(b). If the used material has a slow swelling ability, it would result in a longer disintegration time. If the swelling ability of the used particles is fast, the particle may close the pore space and hinder the liquid from accessing other particles and the swelling of these particle would be slowed down. This would slow down the break-up process. Other factors affecting the disintegration time is the pore size, as seen in Figure 1.2(a). The pore space within the tablet strongly influences the overall swelling of a tablet. For example, if the porous tablet has very large pores, then the fully swollen particles will not push the adjoining components which are needed to interrupt interparticle bonds. If the pores are too small it will hinder the liquid entering the the tablet, thereby the swelling will not occur or be minimised. The swelling of a single particle inside a table reduces the pore size. A smaller pore size will reduce the liquid penetration rate as there is smaller space for the liquid to enter, and less liquid is accessible for swelling, which eventually causes a slower swelling rate of a single particle.

Strain recovery is the reversible viscoelastic process of deformation. During tablet compression, the tablet is subject to high compaction pressure in the MPa range. The particle is deformed and interparticular bonds are forged during compression. For strain recovery, the particles recover to their original shape by the mechanical activation of disintegrants when the tablet encounters the liquid medium and assist the polymer chain to adopt the most energy-favourable position. The pressure created during this kinetic process activates the disintegration. Strain recovery is also called shape recovery [Desai et al., 2015]. The swelling and strain recovery of the particles causes the tablet to

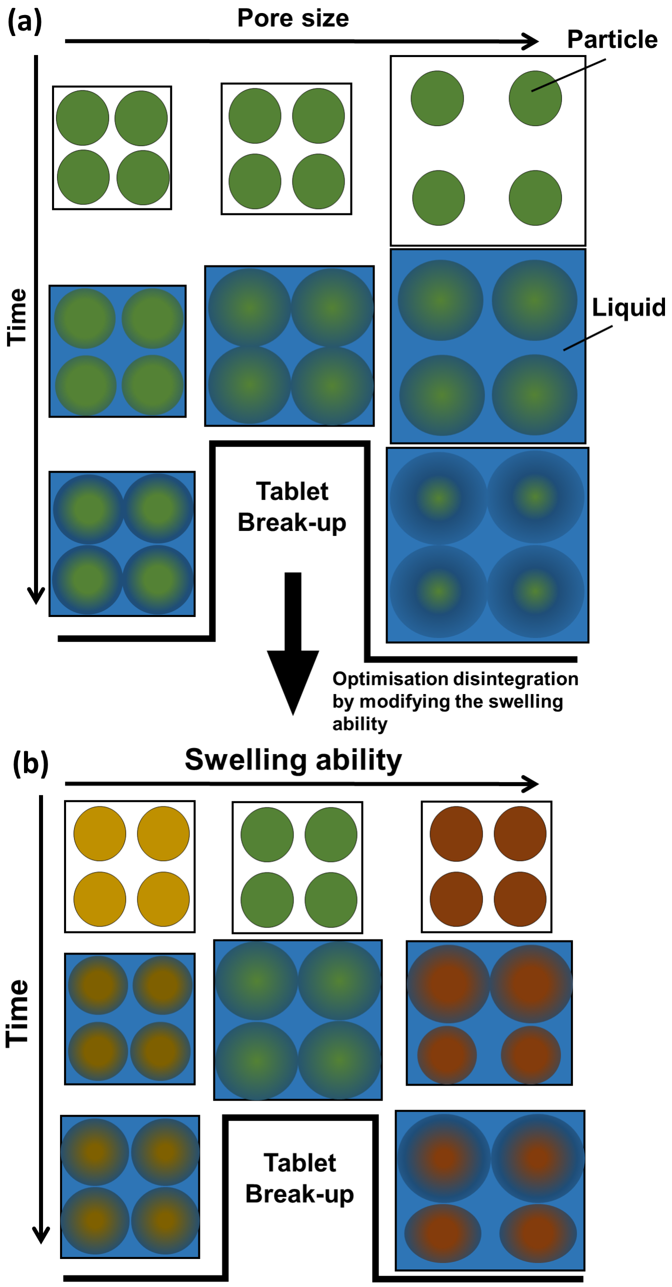

Figure 1.2: Schematic illustrating the interconnection of pore size, swelling ability of single particles and the break-up of the tablet.

eventually break-up into smaller agglomerates and particles.

1.3.3 Break-up of interparticular bonds

The tablets matrix break-up is mostly caused by the interruption of particle-particle bonds [Desai et al., 2015]. Previous research suggested that there are three different bonding mechanisms inside a tablet: solid bridges, mechanical interlocking and intermolecular forces [Karehill and Nyström, 1990]. The interruption of the interpartuclate bonds is a crucial step in the disintegration of a tablet. The swelling of the individual particle inside the tablet causes the tablet to swell, and eventually causes the tablet into breaking up into smaller agglomerates and particles. The interpartuclate bonds could potentially be interrupted by energy generated by wetting of tablet. However research, has shown that the energy generate is not sufficient for disintegration [Desai et al., 2015, Lowenthal, 1972] and therefore it is not considered in this project. The size of the broken up disintegrated particles/agglomerates then drives the dissolution rate of the drug.

1.3.4 Dissolution

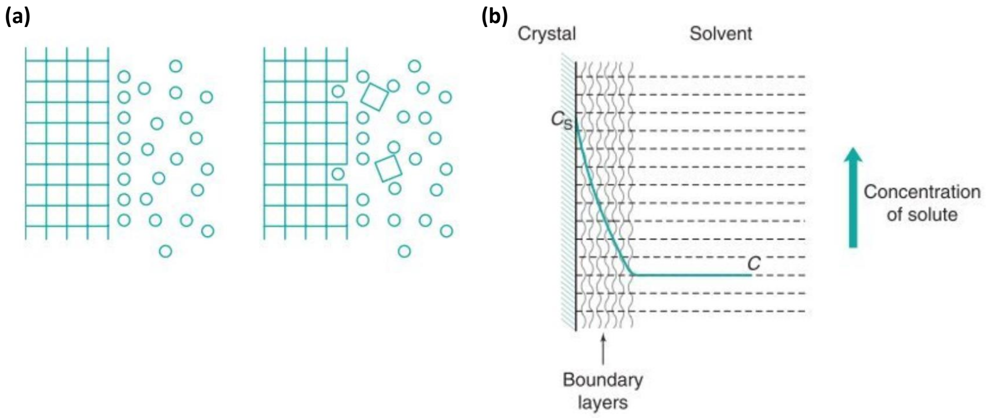

Figure 1.3: Illustration of the dissolution process. (a) Replacement of solid molecule with solvent molecules during dissolution, where cubes and circles indicate solute and solvents, respectively. (b) Boundary layer and concentration change surrounding a dissolving particle, taken from [Aulton, 2018].

Dissolution is defined as the process where particles are transferred into solution. The dissolution process consists of two stages: The first stage is the interfacial reaction where solid molecules are liberated from the solid phase, which includes the replacement of solid molecules by solvent molecules. The second stage is diffusion through the boundary layer of the solid [Aulton, 2018]. An illustration of the stages is given in Figure 1.3. The interfacial reaction stage consists of two parts: leaving the surface and moving into liquid. Leaving the surface is the process of removing solid molecules from the solid phase and replace it with solvent molecules. This process is determined by the relative affinity of the involved molecules and the cohesive forces that need to be overcome. The next part is moving into the liquid, where the solvent is known to contain a small amount of free volume. This free volume is considered as holes that are at a certain point not occupied by solvent molecules and the solute molecules will occupy these holes. The next stage in the dissolution process is diffusion through the boundary layer, which is about transporting the solid molecules through the solid-liquid interface into the liquid bulk phase under the influence of diffusion. The boundary layer is defined as a slow-moving liquid layer surrounding the solid surface in the liquid phase. The mass transfer through these layers is relatively slow. As shown in Figure 1.3 concentration of the boundary layer changes from saturated (C_s) at the solid surface to the same concentration (C) as the bulk solution at the outermost limit [Aulton, 2018].

The rate limiting steps in the dissolution process are the diffusion through the boundary layer since the mass transfers through the layer are slow, whereas the interfacial reaction step is almost instantaneous. The molecule movement through the diffusion layer can be described by Fick's first law of diffusion leading to [Aulton, 2018]:

$$\frac{dC}{dt} = k_{\text{diss}}(C_s - C), \tag{1.2}$$

where C is the concentration of solute in the solution at any position and at time t, and the constant k_{diss} is the dissolution rate constant (s^{-1}). The driving force for the dissolution is the energy difference between the two concentration states. C_s is the concentration of the solution at the solid surface C [Aulton, 2018]. The dissolution of a single spherical particle can be described by the Noyes-Whitney equation (Equation 1.3).

The equation describes the solute mass transfer through the diffusion layer, dm/dt, as a function of the area available for molecular migration, A_{sol}, the thickness of the boundary layer, H_b, and ΔC [Aulton, 2018].

$$\frac{dm}{dt} = \frac{DA_{\text{sol}}(C_s - C)}{H_b}, \tag{1.3}$$

where D (m^2/s) is the diffusion coefficient. Equation 1.3 indicates that a larger surface area of undissolved solid (A_{sol}) results in a higher the dissolution rate. This directly links the dissolution performance to the disintegration behaviour as the size of the disintegrated particles impacts the dissolution rate. Particles may have pores that allow the dissolution medium to enter and the dissolution will thus happen within the pore. The concentration difference between the solution at the solid surface and the bulk of the solution is influenced by the pH, temperature and molecular structure of the solute as well as by the presence of other compounds and the volume of the dissolution medium. The diffusion coefficient, D, is affected by the viscosity of the dissolution medium, and the molecular characteristics and size of diffusion molecules [Aulton, 2018].

1.4 Modelling of tablet disintegration

As mentioned in Section 1.1 the development time for a pharmaceutical is around 10 years, and patent protection is in most countries around 20 years, the company only have 10 years to recover their cost and make profit. To accelerate the development of new drugs modelling and simulations are one of the concepts to reduce drug product development times. Additionally, the material waste (sustainable manufacturing) be reduced by replacing physical experiments with digital experiments using the models from this activity. This also includes the reduction of solvents needed for dissolution testing. According to the American Chemical Society Green Chemistry Institute Pharmaceutical Roundtable, over 70% of waste in the pharmaceutical industry is related to solvent waste [Diorazio et al., 2016]. Another advantages of using mathematical modelling is that multiple solutions can be calculated in a very short amount of time, whereas finding these solutions experimentally will be extremely time consuming.

Other industries have developed advanced models and simulation technology, such as aeronautical industry with flight simulators, automotive industry for developing cars and technology company such as Microsoft, Google with their advanced technology in artificial intelligence. The pharmaceutical industry is still lagging behind some other industries [Gernaey et al., 2012]. However, in the last decade digital design approaches have been developed and deployed to reduce experimental effort and assist in the decision-making throughout the development cycle of new medicines [Kalaria et al., 2020].

Various modelling and simulation techniques have been utilised in the pharmaceutical industry, such as the:

- Discrete element method (DEM) to simulate tablet compaction and disintegration [Kalný et al., 2021, Persson and Frenning, 2015]. DEM is a particle-scale numerical method for modelling the bulk behaviour of granular materials and many geomaterials such as coal, ores, soil, rocks, aggregates, pellets, tablets and powders can be described by the method. DEM enables the investigation of the interaction of individual particles and the interparticle effects (stresses, deformation, thermal conductivity, creep). The most essential element of a DEM model is the underlying particle contact model. The particle contact model is used to calculate the forces acting on particle-particle and particle-wall contacts. Both contact modes can be modelled by the same model, however the material properties (e.g. coefficient of restitution, friction coefficient, etc.) for each contact type can differ in order to model dissimilar materials. The particle motion is calculated from the force a particle experiences based on these contact models [Ketterhagen et al., 2009].

- Population balance equations (PBE) to model tablet break-up [Wilson et al., 2011]. PBE is typically used to describe the change of particle property distributions. Population balances describe the dynamic evolution of the distribution of one or more properties [Solsvik and Jakobsen, 2015].

- Computational fluid dynamics (CFD) combined with DEM to model coating [Böhling et al., 2019]. Computational fluid dynamics (CFD) is an essential predictive tool, which can effectively forecast very detailed flow patterns [Santagata et al., 2020]. CFD is a simulation tool, which uses powerful computer and applied mathematics to model fluid flow situations for the prediction of heat, mass and momentum transfer and optimal design in industrial processes [Xia and Sun, 2002].

- Empirical model of the drug release [Schreiner et al., 2005]. Empirical models are models based on correlations obtained from analysis of experimental data. Empirical models offer simplistic solutions for quantitative comparisons between different operating conditions.
- Mechanistic model to describe the liquid flow in a swelling tablet [Markl et al., 2017b] or a drying process [Mortier et al., 2012]. Mechanistic model is a mathematical description of the elements forming a system, their mutual interactions and the interaction with the environment. Such models are used in technical systems to enable the extrapolation of systems behaviour relying on the mathematically described features of elements and mechanisms of their interaction [Stalidzans et al., 2020].
- Machine learning to predict powder flow [Alshafiee et al., 2019]. Machine learning is a subset of the discipline of artificial intelligence. The purpose of ML is to make a prediction or recognise patterns in a large dataset with many variables [Cleophas and Zwinderman, 2013].

As explained in Section 1.3, disintegration mechanisms are strongly interconnected as the swelling of particles dynamically changes the internal pore structure which influences the liquid imbibition process. The performance of a tablet can thus only be understood and optimised by considering the interconnection of every step involved in the disintegration and dissolution processes. Modelling and simulating are great tool to better understand the fundamental disintegration process and its interdependence. Even though there has been progress in the last decade on the modelling of the drug release from a tablet, the fundamental disintegration process and its interdependence is still not well understood. To realise the digital design of future oral medicines, it is essential to monitor and model the disintegration tablet.

A range of models have been developed to describe the disintegration and dissolution of a tablet. In general, an ideal model needs to capture all the mechanism and physics of the process accurately to be able to predict the performance of a tablet. The model needs to describe liquid penetration, swelling, strain recovery, disruption of particle-particle bonds, and dissolution of excipient and API particles. This includes taking into account the change of pore structure during swelling and how it affects the liquid penetration. There have been conducted several studies on modelling this process, to the groups best knowledge, there is no single model which combines all the phenomena and accounts for the pore structure change. The models of liquid penetration are given in Section 1.4.1, swelling models are given in Section 1.4.2, tablet break-up model are given in Section 1.4.3, drug release models are given in Section 1.4.4, the coupled models are given Section 1.4.5.

1.4.1 Liquid penetration model

Traditionally liquid penetration depth (L) as a function of time in porous media is described by the Washburn equation (Equation 1.1). The model presented in Cai and Yu [2011], Markl et al. [2017b], Masoodi and Pillai [2010], Masoodi et al. [2007], Schuchard and Berg [1991], Shi and Gardner [2000] modified the Washburn equation by including factors such as swelling of particle (change in pore radius), energy loss during liquid penetration and tortuosity.

Markl et al. [2017b] developed a model describing the liquid ingress in a swelling tablet. The model for liquid penetration is based on Darcy's law. In this model, the pore structure is considered as a bundle of capillary tubes of varying diameter. The volumetric flux, q, of a Newtonian liquid in an isotropic porous medium can then be described by Darcy's law:

$$q = -\frac{\mathscr{K}}{\eta}\frac{\Delta P}{L}. \tag{1.4}$$

ΔP is the pressure difference (can be described by Young-Laplace equation, Equation 1.5), $\mathscr{K}$ is the intrinsic permeability and η is the viscosity of the liquid.

$$\Delta P = \frac{\gamma \cos\theta}{r_{c,0}}. \tag{1.5}$$

$r_{c,0}$ is the initial capillary radius, γ is the surface tension and θ is the solid-liquid contact angle. Equation 1.5 is simplified by neglecting the atmospheric pressure and hydrostatic pressure. They assumed that the net mass flow in and out of the porous system is zero in a rigid porous system, then the continuity equation for incompressible fluids can be given as $\nabla q = 0$. L can be calculated from Equation 1.4 by considering that only a fraction of the volume is available for the liquid flow. By dividing q by the initial porosity, ε_0, gives an equation for the liquid front depending on time. The derivation of the equation is given in Masoodi et al. [2007].

$$L = \sqrt{\mathscr{K} \frac{4\gamma \cos\theta}{\varepsilon_0 \eta r_{c,0}} t}, \tag{1.6}$$

Shi and Gardner [2000] developed a model describing the liquid penetration depth in porous media, by considering the particle swelling in the tablet and the energy loss during the liquid rise process. They modified the Poiseuille's law to account for pore radius change during swelling and assumed that a small particle reaches its maximum swelling instantly after it interacts with the polar liquid. They described L by Equation 1.7.

$$L^2 = \frac{r_c \gamma \cos\theta}{2\eta r_{c,0}} - \frac{C_{\text{loss}} \zeta_v}{4\eta\pi} \left(\frac{r_c}{r_{c,0}} \right)^2 t, \tag{1.7}$$

where r_c (Equation 1.8) is the pore radius after (during in other cases) swelling, C_{loss} is the energy loss coefficient and ζ_v is the volumetric swelling.

$$r_c = \sqrt{\frac{\pi r_{\text{col}} \rho_t - (1+\zeta_v) G_m}{\pi \rho_t r_{\text{col}-G_m}} r_{c,0}}, \tag{1.8}$$

where r_{col} is inner column radius, ρ_t is the density of the material and G_m is the unit column mass. See Shi and Gardner [2000] for derivation of Equation 1.7 and 1.8.

Schuchard and Berg [1991] developed a model that describes the liquid penetration depth in a swelling porous media. They assumed a linear decrease with time of the pore radius in the wetted area of the porous medium. The described the hydraulic radius (r_h), which is the ratio of cross-sectional area for flow to the wetted pore perimeter. In their study it is defined as the effective hydrodynamic radius in the wetted region behind the advancing liquid front, i.e. $r_h = r_{c,0} - a_c t$. a_c is a constant and expresses the rate of pore radius constriction. Based on these assumptions, they modified the Washburn equation to:

$$L^2 = \left(\frac{r_{c,0}\gamma\cos\theta}{2\eta}\right)\left(t - \frac{a_c}{r_{c,0}}t^2 + \frac{a_c^2}{3r_{c,0}^2}t^3\right). \tag{1.9}$$

Cai and Yu [2011] developed a model which included tortuosity ($\tau = L_f/L$ where L_f is the actual length that liquid travels) by modify the Hagen–Poiseuille law, given in Equation 1.10

$$L = \frac{1}{2\tau}\sqrt{\frac{r_{c,0}\gamma\cos\theta}{2\eta}} \tag{1.10}$$

Computational fluid dynamics (CFD) is an essential predictive tool, which can effectively forecast very detailed flow patterns [Santagata et al., 2020]. Wang et al. [2018] developed a model describing one-phase liquid flow in porous rocks media using CFD coupled with discrete element method (DEM, read more about DEM in Section 3.1), and the pore structure is simulated by laying out some fixed big particles. The flow of liquid was described by Eulerian-Lagrangian method and the Navier-Stokes equation. The equations of conservation of mass and momentum for liquid phase, are given in Equation 1.11 and 1.12.

$$\frac{\partial \rho_l \epsilon_l}{\partial t} + \bigtriangledown \cdot (\rho_l \omega_l \mathbf{u}_l) = 0, \tag{1.11}$$

$$\frac{\partial \rho_l \omega_l \mathbf{u}_l}{\partial t} + \bigtriangledown \cdot (\rho_l \omega_l \mathbf{u}_l \mathbf{u}_l) = -\omega_l \bigtriangledown P_{\text{liq}} + \omega_l \bigtriangledown \cdot \tau_l + \omega_l \rho_l \mathbf{g} + \mathbf{F}_{pl}. \tag{1.12}$$

Where $\mathbf{g}$ is the acceleration due to gravity, P_{liq} is the liquid pressure, ω_l is the liquid volume fraction, τ_l is the viscous stress tensor, $\mathbf{u}_l$ is the liquid velocity, and ρ_l is the density of liquid. The coupling term $\mathbf{F}_{pl}$ between the particle and liquid phases is approximated as the sum of the drag on each particle within the corresponding fluid control volume.

In their model, the liquid-solid interaction force (drag force ($\mathbf{f}_d$)), was determined for each particle. The drag force is affected by the relative velocity between the solid particle and fluid and the presence of neighboring particles, i.e., local volume fraction of the solids phase, are given by Equation 1.13.

$$\mathbf{f}_d = \frac{\beta_l V_p}{1-\omega_l}(\mathbf{u}_l - \mathbf{u}_p), \tag{1.13}$$

Where β_l is an inter-phase momentum transfer coefficient and is predicted by the Huilin-Gidaspow model [Huilin et al., 2004]. V_p is the volume of particle and $\mathbf{u}_p$ is velocity of the particle.

Santagata et al. [2020] simulated the liquid flow in a swelling and absorbing Super Absorbent Polymer (SAP) porous media using Diersch et al. [2010] model which are based on Richards' equation. The model is based on mass and momentum balance equations defined for the liquid and the solid phases. They modified Darcy's law to model the liquid balance (Equation 1.14), which is a expressed in terms of pressure head (ψ^l) and involves a diffusive term, driven by gradients of pressure, and a sink term, which represents the absorption by solid. To be able to solve the equation, additional models are needed that describe porosity and saturated permeability dependences with swelling ratio, saturation dependences with pressure and swelling ratio and relative permeability dependences with saturation. The equations developed in Santagata et al. [2020] is,

$$\begin{gathered}\epsilon\frac{\partial s^l \psi^l}{\partial t} - \nabla\cdot[\mathscr{K}_r^l \mathbf{K}^l \cdot (\nabla\psi^l - \mathbf{e})] \\ = -\left[\frac{C^s_{\text{SAP},0}}{\rho_l J^s} + \epsilon\frac{\partial s^l}{\partial Q_2^s} + s^l\left(\frac{\partial\epsilon}{\partial Q_2^s} + \frac{\epsilon}{J^s}\frac{\partial J^s}{\partial Q_2^s}\right)\right]\frac{\partial Q_2^s}{\partial t}\end{gathered} \tag{1.14}$$

The primary variables in which the system is solved are the pressure head (ψ^l), SAP liquid uptake (Q_2^s) and the solid displacement (u^s). ϵ and s^l are porosity and liquid saturation, respectively, $\mathscr{K}_r^l$ is the relative permeability for the liquid phase, $\mathbf{K}^l$ is the hydraulic conductivity tensor, $\mathbf{e}$ is the gravity unit vector, $C^s_{\text{SAP},0}$ is the initial solid bulk concentration of SAP, ρ_l is the density of the liquid phase and J^s is the volume dilation of the domain.

Chareyre et al. [2012] developed the pore finite volume (PFV) method, a liquid model for modelling fluid movement through packed particles (porous media). First step is applying a triangulation to the particle packing using the solid particle centres as vertices for the tetrahedra. The tetrahedron spans across four neighbouring particles which defines the pore space and is referred to as a pore unit. Each pore unit is connected to four adjacent pore units. Consider two adjacent pore units I and J. A flat surface, or facet, separates them. This facet is the narrowest opening between the two pore units, which is refereed to as throat IJ. The throat IJ is resistance to the flow of the liqudi. The resistance is calculated via a hydraulic radius r^h_{IJ},

$$r^h_{IJ} = \frac{V_{IJ}}{A^V_{IJ}}. \tag{1.15}$$

Where V_{IJ} is the void volume that is associated with pore throat IJ; it is the void volume between three particle centres and two adjacent pore unit centres, and A^V_{IJ} is the solid surface area that is present in V_{IJ}. The hydraulic conductivity of pore throat IJ, g_{IJ}, is defined as:

$$g_{IJ} = \alpha_{\text{shape}} \frac{A_{IJ} {r^h_{IJ}}^2}{2\eta_{\text{dyn}}}, \tag{1.16}$$

where A_{IJ} is the cross-sectional area of throat IJ, η_{dyn} is the dynamic viscosity, and α_{shape} is a conductivity factor that is equal to 1 for spherical particles and smaller for other shapes. Each pore unit has a fluid pressure, p_{fluid} and each pore throat has a volumetric flow rate, q_{IJ}, which is proportional to the pressure difference given in Equation 1.17.

$$q_{IJ} = g_{IJ} \frac{p_{\text{I,fluid}} - p_{\text{J,fluid}}}{l_{IJ}}, \tag{1.17}$$

where l_{IJ} is the distance in between the two pore unit centres.

Sweijen et al. [2017a] modified this equation to account for the change of volume of a pore unit during swelling, by Equation 1.18.

$$\left.\frac{dV_i}{dt}\right|_{\text{abs}} + \left.\frac{dV_i}{dt}\right|_{\text{mov}} = \sum_{J=1}^{4} q_{IJ} - q_I^{\text{abs}}, \tag{1.18}$$

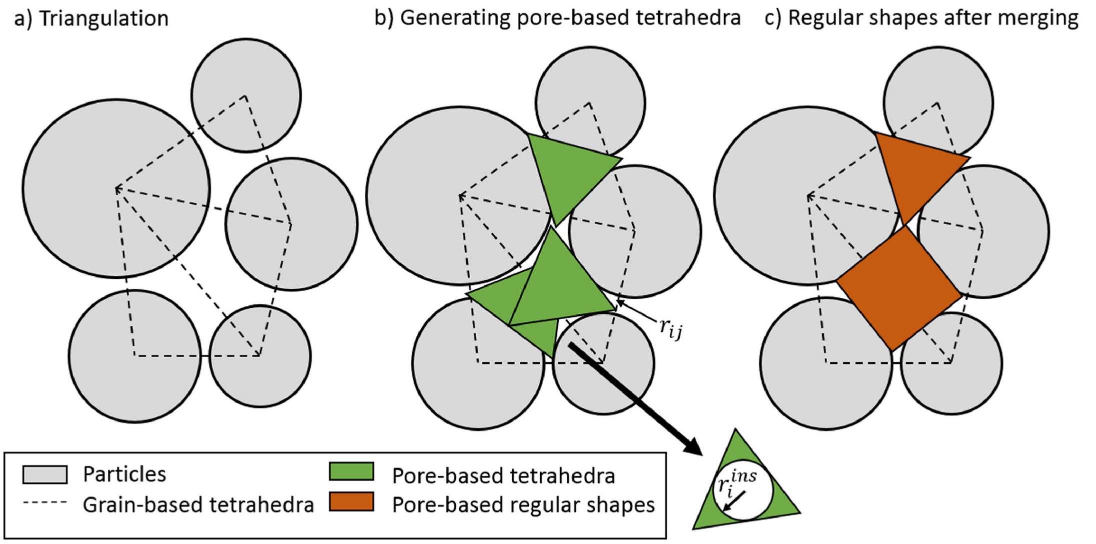

Figure 1.4: Schematic overview of the meshing algorithm to describe the pore-space inside a particle packing, taken from [Sweijen et al., 2018].

where $\left.\frac{dV_i}{dt}\right|_{\text{mov}}$ is the change in pore volume of pore unit I due to relative movement of its surrounding particles (or deformation), q_I^{abs} is the absorption rate that acts in pore unit i, and $\left.\frac{dV_i}{dt}\right|_{\text{abs}}$ is the volume change of pore unit I due to swelling of the four surrounding particles.

Sweijen et al. [2020] developed the PFV model further for swelling porous media by describing the pore unit not only by the tetrahedra, but with also regular shapes (tetrahedra, cubes, octahedra) for sake of simplifying the pore geometry during swelling. This model is refereed as pore-unit assembly (PUA) method. PUA based out of the particle configuration to describe the liquid penetration in a swelling porous media by introducing a meshing algorithm. The first step is in this method is similar to PFV, where each pore space is divided into tetrahedron using triangulation. Each tetrahedron encloses a pore-space that is than replaced by regular shape for sake of simplifying the pore geometry. When multiple tetrahedra enclose a single pore-space, the tetrahedra are merged and replaced by a different regular shape, as seen in Figure 1.4.

Each regular shape is assumed to have its corners wedged into the pore throats of the particle packing. The geometry of the regular shapes are known, and is used to describe the relation between capillary pressure (P_c) and saturation (s_i) within each pore-unit.

P_c is given by Equation 1.19, the derivation is given in Sweijen et al. [2018].

$$P_c = \frac{2\gamma}{\chi \sqrt[3]{V_i}(1 - e^{-\kappa s_i})}, \tag{1.19}$$

where γ is the surface tension, χ and κ are the geometrical constants, and V_i is the volume of a pore-unit.

Additional to the capillary pressure, there is an entry pressure of a pore throat IJ for air to invade a saturated pore unit J from a neighbouring pore unit I which needs to be overcome. The entry criteria are implemented in Sweijen et al. [2020] and entails $p_{\text{air}} - p_{\text{liq,J}} > \frac{2\gamma}{r_{c,IJ}}$, with $r_{c,IJ}$ being the effective radius of pore throat IJ.

In a swelling and moving porous media the pore unit volume will change (V_i). The change can be described by Equation 1.20,

$$\frac{dV_i}{dt} = \left.\frac{dV_i}{dt}\right|_{\text{abs}} + \left.\frac{dV_i}{dt}\right|_{\text{mov}}. \tag{1.20}$$

$\left.\frac{dV_i}{dt}\right|_{\text{abs}}$ is the volume change due to swelling of the surrounding particles and $\left.\frac{dV_i}{dt}\right|_{\text{mov}}$ is the volume change due to the relative movement of particles. In Sweijen et al. [2020], $\left.\frac{dV_i}{dt}\right|_{\text{abs}}$ is considered to be equal to the volume of absorbed water, since the mass density of the swollen particles is almost the same as the water density. The change caused by particle swelling does not affect flow of the liquid, since water is simply changed from being in a liquid state to a solid state. However, the movement of the particle will affect the pore unit volume, and cause the movement of the liquid. Therefore, $\left.\frac{dV_i}{dt}\right|_{\text{mov}}$ is considered in solving the pressure equation, while $\left.\frac{dV_i}{dt}\right|_{\text{abs}}$ is considered only for updating water saturation.

The liquid flow (Equation 1.21) in a pore unit I is given as a function of the water pressure (p_i), a water saturation (s_I) and it is connected to the neighbouring pore unit J via pore throat IJ that has a conductivity $\mathbf{k}_{IJ}$.

$$\sum_{J=1}^{N_I} \mathbf{k}_{ij}(p_I - p_J) = -\left.\frac{dV_I}{dt}\right|_{\text{mov}}. \tag{1.21}$$

The saturation s_i is updated while accounting for the water absorption by the swelling particles, as given in Equation 1.22.

$$s_I^{t+\Delta t} = s_I \frac{ds_I}{dp}\left[(p_{\text{liq,I}})^{t+\Delta t} - (p_{\text{liq,I}})^{t}\right] + \frac{\Delta t}{V_I^{t+\Delta t}} \frac{dV_I}{dt}\bigg|_{\text{abs}}. \tag{1.22}$$

Sweijen et al. [2017b] developed a model describing the water uptake on the particle surface. The water uptake on the particle surface is considered as a kinetic process. The local volume fraction of water is denoted by ω_f. The maximum and initial value of ω_f is denoted as, $\omega_{f,\max}$ and $\omega_{f,0}$, respectively, and are constant over time and space. The ω_f as boundary point is denoted as $\omega_{f,b}$. At a very fast uptake, $\omega_{f,b}$ can be given by a constant value of $\omega_{f,\max}$. They assume that it can be described by a first-order kinetic model:

$$\omega_{f,b} = \omega_{f,\max} - (\omega_{f,\max} - \omega_{f,0})e^{-k_\omega t}. \tag{1.23}$$

$k_\omega[T^-]$ is a kinetic constant, based on the kinetic law for water uptake at particle surface. Equation 1.23 is valid if the initial and boundary conditions are compatible such that $\omega_{f,b} = \omega_{f,0}$ at $\partial\Omega$ at $t = 0$. $\partial\Omega$ is the moving boundary.

1.4.2 Swelling model

Sweijen et al. [2017a] developed a discrete element modelling (DEM) model for swelling of single super absorbent polymer (SAP) particles. DEM is a particle model that is capable of simulating the deformation of granular materials by considering particle-scale interactions, read more about DEM in Section 3.1. DEM is capable of simulating the motion of each individual particles inside particle packing during deformation. Each particle, i, is characterised by the particle radius (r_p), Young's modulus (E_i), density (ρ_i), Poisson ratio (v_i). shear modulus (G_i) and friction coefficient (ϕ_i), with the equation of each property is given in Sweijen et al. [2017a]. The absorption ratio (Q_i^{abs}) of each individual particle i is described by the mass of absorbed water (m_i^w) and the dry mass of the particle (m_i^s):

$$Q_i^{\text{abs}} = \frac{m_i^w + m_i^s}{m_i^s} = \frac{(r_p)^3 \rho_w}{(r_{p,0})^3 \rho_s} - \frac{\rho_w}{\rho_t} + 1. \tag{1.24}$$

$r_{p,0}$ is initial particle radius, r_p is the particle radius at time t, ρ_t is the true density of the material and ρ_w is the density of water.

The swelling of a particle is driven by the difference in chemical potential between the particle and water (liquid medium) [Huyghe and Janssen, 1997]. Therefore, it is assumed that the swelling is attributed to the diffusion of the liquid into the particle. The absorption rate can thus be described by Equation 1.26, the derivation of the equation is explained in Sweijen et al. [2017a],

$$\frac{dQ_i^{\text{abs}}}{dt} = K_i\left(\frac{Q^{\max} - Q_i^{\text{abs}}}{Q_i^{\text{abs}}}\right), \tag{1.25}$$

$$K_i = \frac{3Dr_p}{(r_{p,0})^3}. \tag{1.26}$$

D is the diffusion coefficient for water molecules in SAP [L^2/T], and it is assumed to be constant and $Q^{\max}$ is the maximum value of Q_i^{abs}.

For spherical particles and an incompressible liquid, Equation 1.25 can be rewritten in term of $\frac{dr_p}{dt}$ as function of r_p:

$$\frac{dr_p}{dt} = \frac{D\varrho_s}{r_p\varrho_w}\left(\frac{Q^{\max} - Q_i^{\text{abs}}}{Q_i^{\text{abs}}}\right). \tag{1.27}$$

Markl et al. [2017b] developed a model for swelling based on the model presented in Schott [1992a,b]. The tablet was modelled as a cylinder with an initial thickness H_0 and diameter d_0. The authors simplified the swelling to a tablet enlargement only in axial direction to mimic their experimental setup, which allowed the tablet to swell only in axial direction. They showed that the capillary radius, r_c, decreases with increasing swelling. They assume that fractional increase in volume of the wetted powder compact is equal to the fractional increase in the volume of a single wetted particle. They also assumed that the capillary radius, r_c, is a function of the initial particle radius $r_{p,0}$ and particle radius during hydration, r_p yielding $r_c = r_{c,0} - (r_{p,0} - r_p)$. The derivation of the equation is given in Markl et al. [2017b].

$$r_c = r_{c,0} - \frac{r_{p,0}}{2}\left[\left(\frac{H_0 + \zeta \cdot t}{\delta_0}\right)^{1/3} - 1\right], \tag{1.28}$$

ζ is the swelling rate and is determine by the swelling model given in Markl et al. [2017b].

Sweijen et al. [2017b] developed a physically-based model, where the linear diffusion of water in the particles is accounted for. It assumed that the water uptake on the particle surface is a kinetic process, which along with water diffusion controls the swelling rate of the particle. They also assumed that the polymer and water are both incompressible. The swelling model of an irregular particle considers a particle with an arbitrary initial shape filling a domain indicated by $\Omega(0)$ and is given as $\Omega(t)$ when $t > 0$. Equations 1.29-1.31 express the diffusion into a particle.

$$\left.\begin{array}{l} \frac{\partial \omega_f}{\partial t} + \operatorname{div} \bar{q} = 0 \\ \bar{q} = -D \nabla \omega_f \end{array}\right\} \quad \text{for } \bar{x} \in \Omega \text{ and } t > 0, \tag{1.29}$$

$$\omega_f|_{\partial\Omega(t)} = \omega_{f,b} \qquad \text{for } t > 0, \tag{1.30}$$

$$\omega_f|_{t=0} = \omega_{f,0}. \tag{1.31}$$

$\bar{q}$ is the water flux and D is the diffusion coefficient, which is assumed to be constant for each material and is a function of time and location. D was simplified by assuming it is mathematically constant, whereas the diffusion of water into a dry particle can be a non-linear diffusion and in that case D is a function of ω_f.

During swelling water will enter the growing particle through its boundary, this needs to be considered in a model describing the movements of the boundary, $\partial\Omega(t)$. By considering a small surface element of $\partial\Omega(t)$, which has an area of A. The element moves in space from time t to time $t + \Delta t$. The particle will grow into the water, within which $\omega_f = 0$. This will give an excess volume of water, V_{excess}, inside the particle, which needs to diffuse into the particle. See Sweijen et al. [2017b] for the equations for V_{excess}

and volume of diffused water into the particle. The water uptake on the particle surface is considered a kinetic process by its own, and is explained in Section 1.4.1 (Equation 1.23).

The swelling of particle can be described by combining the model for swelling of an irregular particle with an equation of the diffusion coefficient, D, (see Equation 1.32). The initial radius is denoted as, $R_0 > 0$. The radius at time $t > 0$ is denoted as $R = R(t)$, they also assume radial symmetry and Equation 1.29 can be expressed in terms of radial coordinates,

$$D\frac{\partial \omega_f}{\partial r}|_R = (1-\omega_{f,b})\frac{dr}{dt} \tag{1.32}$$

$$\frac{\partial \omega_f(r,t)}{\partial t} = \frac{D}{r^2}\frac{\partial}{\partial r}\left(r^2\frac{\partial \omega_f(r,t)}{\partial r}\right) \quad \text{for } 0 < r < R(t)\text{and}t > 0. \tag{1.33}$$

Using diffusive reference time, $t_r = \frac{R_0^2}{D}$, then Equations 1.33 becomes dimensionless with the parameters T, r^* and $R^*(T)$. The equation of these parameter are given in Sweijen et al. [2017b]. To solve these equations they made some simplification, they transformed the equations into an equivalent problem on a fixed domain and defined a new spatial variable, X. They further transformed it by applying the chain rule of differentiation and introducing new variables. The transformed equations was solved using Euler schemes, and using the same method as a one-dimensional Stefan's type problems as explained in Kutluay et al. [1997] and the work on swelling particles by Bouklas and Huang [2012].

Sweijen et al. [2017b] compared their model to the models developed in Omidian et al. [1998] (see Equation 1.34) and in Sweijen et al. [2017a] to simulate the results from Esteves [2011] on swelling single SAP particles. The results showed that all the models performed similarly when the diffusion coefficient was reduced by multiplying with a factor D_{scale}. The D_{scale} is different for each model, and D_{scale} of each model is given in Sweijen et al. [2017b].

$$\frac{r_p}{r_{p,0}} = \left(\frac{r_m}{r_{p,0}} - 1\right)\left(1 - e^{-\frac{D}{r_{p,0}^2}}\right) + 1 \tag{1.34}$$

Kalný et al. [2021] developed a DEM model for simulating the disintegration process of directly compressed immediate-release tablets. The model was based on the disintegration process of tablet consisting of ibuprofen as API and CCS as a disintegrant, in their model only the swelling of the disintegrant particle are considered. They developed a model describing several forces affecting and involved in the disintegration process. By combing the models of the different forces and a simple single particle swelling model, they determine the positions, velocity and orientation of each particle during disintegration. In their simulation, they consider three forces: (i) contact force, which represents a repulsive force at the contact between two loose particles; (ii) attractive force, which represents the cohesion between two neighbouring particles prior to disintegration; and (iii) damping force, which represents the fluid resistance to particle movement. The position and velocity of each particle were calculated based Newton's law. The swelling of single particle was calculated using:

$$\frac{dr_p}{dt} = \begin{cases} r_{p,0}\zeta, & r_p < \zeta_{\max} r_{p,0} \\ 0, & r_p \geq q r_{p,0} \end{cases} \tag{1.35}$$

Where ζ is the rate of swelling of the disintegrant particles and is constant. $\zeta_{\max}$ is the maximum increase in radius of the particle.

Braile et al. [2022] studied the swelling of MCC PH102, SAP and rice kernel beds using DEM. They used a first order kinetic model to describe the swelling of single particle as given Equation 1.36,

$$V' = 1 - e^{-k_{\mathrm{swe}} t}. \tag{1.36}$$

Where V' is a dimensionless swelling volume parameter, based on particle initial volume and volume during swelling. k_{swe} is a kinetic parameter. Based on their swelling simulation, they developed an equation to describe the height change of the bed during swelling, given as:

$$H' = 1 - e^{-k_b t}, \tag{1.37}$$

Where H' is a dimensionless swelling height parameter, based on initial height of the bed and height during swelling. k_b is a kinetic parameter.

Kimber et al. [2012], Lamberti et al. [2011] developed models describing liquid penetration and swelling by a coupled model, and these models are summarised in Section 1.4.5.

1.4.3 Tablet break-up

Wilson et al. [2011] developed a model to describe the rate of break-up of a tablet into particles. As explained earlier due to swelling, the particles inside a tablet are released into the bulk dissolution media. Their model is based on a cylindrical shaped tablet and a linear erosion rate, σ, and the volume of the tablet, V_t is given as a function of time, t. The change of volume can be expressed as

$$V_t(t) = \frac{\pi}{4}(d_0 - 2\sigma t)^2(\delta_0 - 2\sigma t) \tag{1.38}$$

with d_0 as the tablet diameter and H_0 is the tablet thickness. The rate of volume of material released from the tablet due to erosion can be determined by:

$$V_t^{'}(t) = \frac{\pi}{4}(2\sigma(d_0 - 2\sigma t)^2 + \sigma(d_0 - 2\sigma t)(H_0 - 2\sigma t)) \tag{1.39}$$

They used a population balance model to express the change in the particle size distribution during dissolution. Population balance model is a rate-based equation used to describe the temporal rate of change of particles as a function of size and/or other properties. They used the following population balance to model the rate of release and dissolution of each component in the tablet, with drug substance, soluble excipient and insoluble excipient are denoted in the subscript as a, es and ei, respectively. The model describes the number size distribution, n^{size}, of each component,

$$\frac{\partial n_a^{\text{size}}}{\partial t} = B_a^0 \delta_{dd}(d - d_{0,a}) + RD_a \frac{\partial n_a^{\text{size}}}{\partial d}, \tag{1.40}$$

$$\frac{\partial n_{es}^{\text{size}}}{\partial t} = B_{es}^0 \delta_{dd}(d - d_{0,es}) + RD_{es} \frac{\partial n_{es}^{\text{size}}}{\partial d}, \tag{1.41}$$

$$\frac{\partial n_{ei}^{\text{size}}}{\partial t} = B_{ei}^0 \delta_{dd}(d - d_{0,ei}). \tag{1.42}$$

δ_{dd} is the Dirac delta function and the rate of release of particles from an eroding tablet into the dissolution media is captured by the rate terms B_a^0, B_{es}^0 and B_{ei}^0. The model is simplified by assuming that the size of the released particles was monodisperse at the sizes given by $d_{0,a}$, $d_{0,es}$ and $d_{0,ei}$. The terms RD_a and RD_{es} are the dissolution rate of the drug substances and soluble excipient particles, respectively. The equations for RD_a and $RD_{e,s}$ are given in Wilson et al. [2011]. The authors assumed that all materials have approximately the same density and released particle have the same average size and shape, which is reflected in the variables B_a^0, B_{es}^0 and B_{ei}^0. The equation for these variables are given in Wilson et al. [2011]. The population was solved by a discrete method.

1.4.4 Drug release

Most commonly used models for the dissolution process is the Noyes-Whitney equation (see Equation 1.3) and Fick's first law of diffusion (see Equation 1.2). Schreiner et al. [2005] modified the Noyes-Whitney equation to consider the effective surface area. As in the starting phase of the drug liberation from a solid dosage form, the solvent is not evenly distributed to the geometrical surface of the drug particles. The wettability of the drug substance is reduced, thereby the dissolution rate is reduced. They accounted for the effective surface area by including a modified distribution function, $y(t)$):

$$y(t) = a_0 + \frac{a_1}{t} exp\Big(-a_2(ln(t) - a_3)^2\Big). \tag{1.43}$$

Where a_0 - a_3 are fitting parameters. By including the modified distribution function, the dissolution rate is descibed as,

$$\frac{dm}{dt} = y(t)\left(1 - \frac{C(t)}{C_e}\right) \cdot C_{\text{sat}}, \tag{1.44}$$

Where C is concentration, C_{sat} is the saturation concentration and C_e is the concentration that is obtained after complete dissolution.

Wilson et al. [2011] developed a continuity equation to quantify the solution concentration of the drug substances, C_a, and soluble excipients. The concentration of drug substances are expressed in term of mass drug substance released from the tablet and the total mass of undissolved drug substance particles:

$$C_a(t) = w_a \rho \frac{V_t(0) - V_t(t)}{V_r} - \rho \alpha_{\text{shape}} \xi_{a,3}(t)(t), \tag{1.45}$$

where α_{shape} is the particle shape factor, V_r is the volume of dissolution media and $\xi_{a,3}(t)$ is the third moment of the drug substances size distribution at time t (see in Wilson et al. [2011] for the equations), w_a is mass fraction of the drug and ρ is the density of the drug substance. A similar equation was developed for the soluble excipient.

1.4.5 Coupled models

The model in Kimber et al. [2012] describes the polymer swelling and dissolution of cylindrical tablets. Their work presents a novel method combining DEM with Fickian mass transfer to model tablet swelling and dissolution. The main advantage of this is that only the physical properties of the material - which are not always easy to measure - need to be known and their initial heterogeneous spatial distribution (initial distribution of particle inside a tablet).

The model is based on a cylindrical polymer tablet with radius r_t discretised in 2D with a fixed height (dz) using discrete volume elements in the form of cylindrical DEM particles where each particle contains a set mass of one or more components. They assumed that the particles are packed in a hexagon. Each DEM particle is part of an overall continuum. The continuum is characterised by polymer mass, m^p and water mass, m^w. The volume V_i, swelling ratio ζ_i and radius $r_{p,i}$ of particle i are defined as:

$$V_i = \frac{m_i^s}{\rho_t} + \frac{m_i^w}{\rho_w}, \tag{1.46}$$

$$\zeta_i = \frac{m_i^w}{m_i^w + m_i^s}, \tag{1.47}$$

$$r_p = \sqrt{\frac{V_i}{2\sqrt{3}dz}}. \tag{1.48}$$

ρ_p and ρ_w are the density values of the polymer and the water, respectively. m_i^s and m_i^w are the mass of polymer and water, respectively, in DEM particle i.

The mass balance of water in each particle (1.49) is defined by the diffusion of water between particle i and its neighbours j (first term), the water uptake at the edges (second term) and released water due to polymer dissolution (third term).

$$\frac{dm_i^w}{dt} = \underbrace{\sum_{j\neq 0} A_{i,j} D_{i,j}^w \frac{c_j^w - c_i^w}{r_{p,i} + r_{p,j}}}_{\text{Diffusion of water}} + \underbrace{A_j^f \frac{D_i^w}{2r_p}(\rho_w - c_i^w)}_{\text{Uptake on the edges}} + \underbrace{\frac{m_i^w}{m_i^s}\frac{dm_i^s}{dt}}_{\text{Polymer dissolution}} . \tag{1.49}$$

c_i^w is the mass concentration of water in the DEM particle i and $A_{i,j}$ is the inter-particle contact area. See Kimber et al. [2012] for the definition of c_i^w and $A_{i,j}$.
In 1.49, $D_{i,j}^w$ is the diffusion coefficient of water between particle i and j, which is defined as a Fujita-type exponential expression. The Fujita-type expression is applicable only when the concentration of the solvent is sufficiently smaller than the concentration of the polymer [Fujita, 1961].

The second term in Equation 1.49 describes mass transition on the edges of the particles. The mass transport on the edges is not only due to exchanges between the particles but also with the surrounding layer of free water. This mass transfer area is defined by the free area, A_i^f. It is defined as the difference between the maximum area, $A_i^{\max}$, and is available for the free water and the inter-particle contact angle.

The third term in Equation 1.49 described the release of water due to polymer dissolution, this term is a function of the mass balance of the polymer. The dissolution of the polymer is expressed by a first-order dissolution expression when water mass fraction in the polymer reaches the disentanglement threshold of ζ^d. Between each mass transfer time step, Δt, the equilibrium position x_i of N particles are obtained so that they are in close contact. This can be obtained by using Newton's Laws of motion on each DEM particle.

Masoodi and Pillai [2010] developed a model based Darcy's law describing the wicking and swelling of paper by considering a dynamic change of porosity. They developed an expression for liquid penetration in a swelling porous medium:

$$L = \sqrt{\frac{2P_c}{\varepsilon_0 \eta} \int_0^t \mathscr{K}(t')dt'}. \tag{1.50}$$

Where P_c is capillary pressure, and is calculated by Young-Laplace equations (see Equation 1.5). The derivation of Equation 1.50 can be found in [Masoodi and Pillai, 2010]. Markl et al. [2017b] calculated $\mathscr{K}$ (intrinsic permeability) by using a modified Carman-Kozeny equation,

$$\mathscr{K} = (2r_{p,0})^2 \frac{z}{180} \frac{\varepsilon^3}{(1-\varepsilon)^2}, \tag{1.51}$$

$r_{p,0}$ is the mean radius of the powder particles, and a constant z is added to the equation to compensate the overestimation made by Carman-Kozeny.

1.5 Monitoring and quantifying disintegration mechanisms

To validate the models and gaining fundamental understanding of the disintegration process and mechanisms involved it is important to quantify and analyse the disintegration process through experimental work. The traditional method for quantifying the tablet disintegration process is very basic and is defined in the European Pharmacopoeia (Ph. Eur). This method measures the time a tablets takes to disintegrate, i.e. the disintegration time. In this method, a tablet placed in open ended transparent tube with a 2 mm mesh on the bottom. The tube is then moved up and down with a given am-

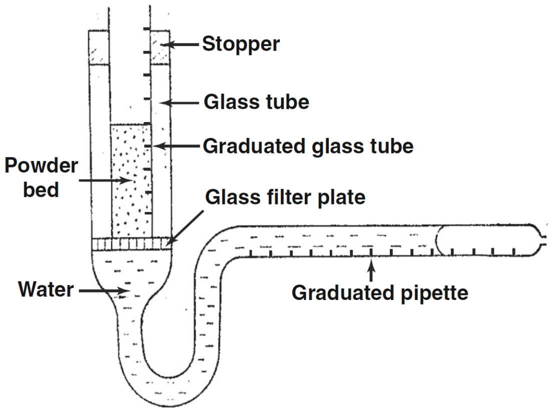

Figure 1.5: Apparatus to measure water uptake and swelling of a powder bed (modified from Nogami et al. [1969]).

plitude and frequency. If the tablet disintegrates within 15 min, the tablet passes the test and have met the requirement from the Ph. Eur. This method is a compliance test and does not provide information about the tablet quality nor reveals insights about the fundamental processes driving tablet disintegration.

Several studies demonstrate the measurement of the water uptake of tablets and powder beds. Nogami et al. [1969] developed an apparatus to measure the water uptake (Figure 1.5). The apparatus consists of a graduated pipette to measure the swelling and water uptake by weight change in the graduated glass tube. The same apparatus was used by Gissinger and Stamm [1980] to investigate the water uptake of different disintegrants. Their results show that the disintegration process is faster for compounds with a small contact angle. They concluded that to be able to understand and measure the disintegration process the following parameters need to be considered: wettability (contact angle), water absorption and swelling capability of the powder compact. As mentioned before, the disintegration mechanisms wicking, swelling and dissolution affect each other. Therefore it is important to measure and quantifying each mechanism individually, to understand their complex interconnection [Markl and Zeitler, 2017]. Dees [1980] developed an apparatus to measure and characterise the water penetration, water uptake and swelling simultaneously. In their apparatus, a tablet is placed on a thin metal foil on a glass filter, and the tablet is wetted by removing the thin metal foil. A microbalance was used to measure the amount of absorbed water by the tablet. The swelling of the tablet was monitored using an inductive displacement transducer. To be able to measure and calculate the penetration depth, the apparatus is equipped with a humidity sensor to measure when the water reached the top of the tablet.

Caramella et al. [1990] developed a apparatus to compare the disintegration force and water uptake of different disintegrants. They combined these two measurements into one parameter, namely the force-equivalent parameter. The parameter is a measurement on the capacity of a disintegrant to transform water into force and will indicate the swelling efficiency. Bell and Peppas [1996] developed an apparatus to measure swelling behaviour of cross-linked hydrophilic polymers under an applied load as a function of time and absorbed the weight. They concluded that the swelling capacity highly depends on the degree of cross-link between polymeric systems. One of the advantages of swelling force and water uptake measurements is that it enables the analysis of the driving disintegration mechanism of the materials. Quodbach and Kleinebudde [2014] conducted swelling force and water uptake measurements of the disintegrants sodium starch glycolate (SSG), croscarmellose sodium (CCS) and crospovidone (XPVP) using the apparatus designed by Caramella et al. [1990] and the authors concluded that the mechanisms of SSG and CCS are swelling and XPVP is primarily driven by strain recovery. The same results were also found by Desai et al. [2012] using a high-speed video imaging to visualise the disintegration of compacts and effect of wetting on free disintegrant particles.

Tablet swelling capacity is strongly influenced by single particle swelling. Previous research has shown that the swelling of a single particle can be analysed using an optical microscope [Esteves, 2011, Gasmi et al., 2015, Rudnic et al., 1982, Sweijen et al., 2017a]. Gasmi et al. [2015] monitored the dynamic change in diameter during swelling of single Poly (lactic-co-glycolic acid) (PLGA) microparticles at different sizes using an optical microscope. Their results revealed that the swelling did not depend on the particle size. All particles increased in size by approximately 140%. They observed changes in the morphology during swelling of the particles: initially, surfaces were smooth and became rougher during swelling. The environmental scanning electron microscope (ESEM) has also been applied to analyse the swelling of particles [Jenkins and Donald, 1997]. The swelling of disintegrants in a suspension was quantified by Zhao and Augsburger [2005] using laser diffraction. They measured the volume mean diameter change during swelling and revealed that SSG had better swelling capacity (maximum swelling of particle) than CCS. Rudnic et al. [1982] analysed the wetting and swelling of individual SSG and sodium carboxymethyl starch particles using an optical microscope. Their results showed that the rate and extent of swelling for the measured particle varied with particle size, i.e. larger particles showed substantially greater rates and extent of swelling compared to smaller particles. Rojas et al. [2012] quantified the swelling value – the ratio between powder expanded volume upon water absorption and the initial sample weight – and water uptake ability of SSG, CCS and MCC powder in simulated gastric and intestinal fluid. SSG had the largest water uptake ability and swelling value followed by CCS and MCC. Desai et al. [2012] analysed and quantified the swelling of compacted disintegrant particle that contained 70% disintegrant and 30% glass beads using an optical microscope and a high speed camera. Their results revealed the trend in cross-sectional area increase during swelling for various compacts was as follows: SSG, CCS, MCC and L-HPC. Berardi et al. [2018] analysed the disintegration mechanism and quantified the swelling of pure CCS, SSG and XPVP tablets using a digital camera. SSG tablets swelled faster and more extensively compared to CCS tablets. The authors described the swelling mechanism of XPVP as strain recovery (swelling in axial direction).

In order to simultaneously study the penetration of liquid, microstructural changes and swelling, one needs to adequately visualise the process of disintegration from within a tablet in a non-destructive and contactless manner. Magnetic resonance imaging (MRI) was applied for simultaneously measuring the liquid penetration, microstructural changes and swelling. MRI facilitated the acquisition of cross-section images of modified-release tablets during the exposure to liquid [Chen et al., 2014, 2010, Nott, 2010, Tajarobi et al., 2009]. MRI has primarily been used to monitor slow mass transport and swelling processes over a time scale of hours. Recent technological advancements in MRI enabled the observation of tablet disintegration with relatively good temporal resolution [Uecker et al., 2010a,b]. A method utilised by [Quodbach et al., 2014b] to quantify the MRI data was based on grey value distribution of each image yielding information about the distribution and relative amount of water within a tablet during disintegration. Quodbach et al. [2014a] presented another method to quantify the MRI data based on fractal dimensions of tablet boundaries. The fractal dimension is related to the surface area of the tablet by that it will provide information on the effectiveness of the disintegration. An area which needs to be improved on MRI is sufficiently differentiating between tablets of varying relative densities and be more sufficient in measuring not only the initial stages of the disintegration process but the complete process.

A method which has been used recently to quantify tablet disintegration is terahertz pulsed imaging (TPI) [Beard et al., 2002, Markl and Zeitler, 2017]. Terahertz radiation (60 GHz–4 THz = 2–130 cm−1) is referred to radiation in the far-infrared region of the electromagnetic spectrum [Zeitler et al., 2007]. Since the most common pharmaceutical excipients are transparent or semi-transparent to terahertz radiation, it can penetrate through the surface and into the tablet matrix [Zeitler et al., 2007]. The penetration depth of TPI is typically between 1 and 3 mm [Zeitler et al., 2006]. Al-Sharabi et al. [2020, 2021], Markl et al. [2018b, 2017b], Obradovic et al. [2007], Yassin et al. [2015a,b] demonstrated that TPI can be used to monitor the liquid penetration into and swelling of powder compacts. Al-Sharabi et al. [2020] measured the liquid penetration and swelling of tablets by combining TPI with a custom built flow cell. Their results showed that the liquid penetration rate is strongly influenced by the tablet porosity, i.e. it generally increases with increasing porosity.

Surface dissolution imaging (SDI) was employed to analyse water penetration and swelling [Pajander et al., 2012, Ward et al., 2019]. SDI is a method based on UV imaging, where the contrast in the images is related to the absorbance of UV light by the sample. The intensity of light at a given wavelength passing through a known volume in a quartz cell is measured as a function of position and time [Østergaard et al., 2010]. Ward et al. [2019] analysed the swelling of tablets consisting of hypromellose as a hydrophilic matrix former. They used two different grades of hyporomellose and each grade had a different morphology. Their results showed SDI could be used to analyse the swelling, and swelling of each grade was approximately similar even though the morphology was different. Pajander et al. [2012] analysed the behaviour of the hydroxypropyl methylcellulose in a buffer solution. The results showed that the SDI could detect the three phases of the process. The first phase being gel formation due to liquid penetration, swelling of the gel and finally steady state condition. They observed that HPMC with higher viscosity swells faster and leads to a thicker gel layer.

1.6 Challenges

As seen from the model described in Section 1.4 a range of models have been developed to describe the different mechanims of the disintegration process. However, there is no single model which combines all the phenomena and also accounts for the pore structure change. In general, an ideal model needs to capture all the mechanism and physics of the process accurately to be able to predict the performance of a tablet. The model needs to describe liquid penetration, swelling and disruption of particle-particle bonds. This includes taking into account the change of pore structure during swelling and how it affects the liquid penetration. I.e in the study presented in Kalný et al. [2021] simulated the disintegration and dissolution of a two component tablet with ibuprofen as the API and croscarmellose sodium (CCS) as a disintegrant. They assumed that only the CCS particles contribute to the total swelling and the swelling was only occurring in two spatial directions. They simplified the swelling by assuming that all particle swell simultaneously and at a constant rate, i.e. the liquid penetration behaviour was not considered. Kimber et al. [2012] developed a model for simulating the swelling and dissolution process of a polymer tablet by combining DEM particles with Fickian mass transfer. The particle was assumed to be cylindrical with swelling only occurring in the radial direction. This study aims to develop a model of the tablet disintegration process by considering all the mechanism and physics and interconnection between the mechanisms, and also accounting for the pore structure change.

Chapter 2

Aims and objective

Once a tablet is administered orally, it comes in contact with a physiological fluid. The liquid will penetrate the porous tablet and in the majority of cases initiate the swelling of the tablet. This swelling builds up an internal stress that causes the break up of the tablet into smaller agglomerates and the primary particles. These steps are referred to as the tablet disintegration processes, which are critical steps to dissolve and enable the absorption of the drug substance [Markl and Zeitler, 2017, York, 2022]. The disintegration process is highly influenced by the interparticulate bonds and pores formed during the compaction process. The pores in a tablet directly affect the rate at which the physiological fluids enters the tablet, leading to the swelling of particles and eventually causing the break-up of the compact into smaller agglomerates. The size of the disintegrated particles/agglomerates then drives the dissolution rate of the drug. These mechanisms are strongly interconnected as the swelling of particles dynamically changes the internal pore structure which influences the liquid imbibition process. The performance of a tablet can thus only be understood and optimised by considering the interconnection of every step involved in the disintegration processes.

This project aims to advance the understanding and modelling of tablet disintegration. The project is divided into three main objectives:

1. To monitor and quantify the anisotropic swelling of single pharmaceutical particle by combining in-situ measurements with a swelling model. The particle swelling is monitored in real-time by a bespoke flow cell coupled to an optical microscope.

The collected swelling data is used to quantify the swelling characteristics of pharmaceutical particles.

2. To assess the changes in pore structure during tablet disintegration by coupling DEM with a single particle swelling model, and experimental liquid penetration data. A 3D discrete element model of the tablet is developed which is then used to simulate the tablet swelling utilising a single particle swelling model [Soundaranathan et al., 2020].

3. To explore the effect of porosity and disintegrant concentration on the disintegration performance using a virtual Design of Experiments approach. This study will focus on modelling the disintegration process by including a liquid penetration model enabling the prediction of the disintegration time of different formulations. This will enable the modelling of the tablet swelling and disintegration without the need of experimental data.

   The deliverables of this thesis will advance predictive and digital formulation design with the goal of accelerating the development of new medicines. This will reduce drug product development times by utilising a digital design approach and reduced material waste (sustainable manufacturing) by replacing physical experiments with digital experiments using the models from this activity. This also includes the reduction of solvents needed for dissolution testing. The model can be used to optimise the performance of tablets by having a scientific sound understanding of the link between the single particles and tablets.

Chapter 3

Methods

3.1 Discrete element method

The discrete element method (DEM) is a particle-scale numerical method for modelling the bulk behaviour of granular materials and many geomaterials such as coal, ores, soil, rocks, aggregates, pellets, tablets and powders. The purpose of implementing DEM is to study the interaction of individual particles and the interparticle effects (stresses, deformation, thermal conductivity, creep). There are four main classes of discrete element models: cellular automata, Monte Carlo methods, hard-particle methods, and soft-particle methods [Ketterhagen et al., 2009].

Cellular automata is a simple method used in the studies of flow in silos [Kozicki and Tejchman, 2005], the flow of granular materials [Baxter and Behringer, 1991] and rotating drums [Yanagita, 1999]. In this method, the particles are constrained to a lattice and the movements of the particle are modelled by simple rules determined by experimental observations. The main advantage of this method is that the simulation is relatively fast, but it only provides qualitative predictions [Ketterhagen et al., 2009]. Monte Carlo simulations are used to calculate the probability of a random arrangement of particles based on the energy associated with that arrangement [Ketterhagen et al., 2009]. Monte Carlo method has been applied to study the effect of non-spherical particle shapes on hopper flow [Abreu et al., 2003] and the distribution of coating in film coaters [KuShaari et al., 2006]. Both hard-particle methods, and soft-particle methods are more often used compared to Monte Carlo and cellular automata methods [Ketterhagen et al., 2009]. The primary difference between hard- and soft-particle methods, is that the particle deform during interaction in case of the soft particle method [Tripath and Khakhar, 2010].

For the hard particle method is it assumed that the particles are rigid so that collisions are instantaneous. Due to this assumption, the hard particle method is often used to simulate the dilute collisional flows. Hard-particle models often are embedded in event-driven collision detection schemes that increment the simulation time from one collision to the next [Ketterhagen et al., 2009]. Hopkins and Louge [1991] developed a hybrid version of the hard particle method, by including particle overlapping in their model. They coupled the hard particle collision model with particle equations of motion between collisions at a specified time step. Thus, this is referred to as a time-driven approach. In a dense system with many particles, the contact between particles happens often and endures. In these dense systems, i.e pharmaceutical tablets, a hard particle method is not applicable, and the soft particle model must be used [Ketterhagen et al., 2009]. The soft particle model was developed by Cundall and Strack [1979]. This model is suitable for investigating long-lasting and multiple particle contacts since it is not limited by the instantaneous contact time assumption as in hard particle model. This model considers the particle deformation by modelling the overlap between particles [Ketterhagen et al., 2009]. To avoid introducing excessive errors in the mean overlap value maintained to levels on the order of 0.1 - 1.0% of the particle size [Cleary and Sawley, 2002]. The overlap value is controlled by the selection of the spring stiffness. A small stiffness value results in large particle overlap value, which will cause an error in the determination of contact forces and thus post-contact quantities such as accelerations and velocities. The soft-particle model relies on a force-displacement (and/or force-displacement rate) relation to determine the interaction forces for each particle-particle and particle-wall contact. This approach proceeds via small time steps. To get an accurate simulation, ideally small time steps are used, but this results in high computational cost [Ketterhagen et al., 2009].

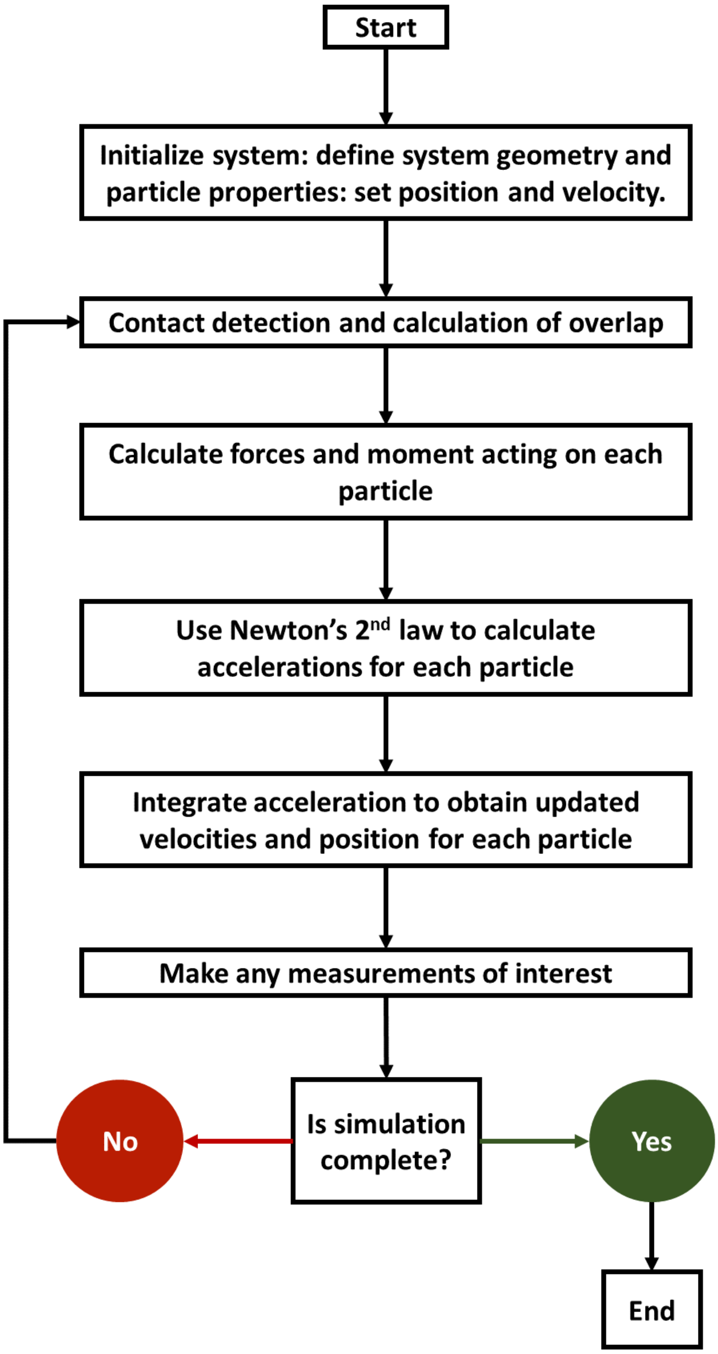

Figure 3.1: A flowchart of a general soft-particle DEM algorithm, modified from [Ketterhagen et al., 2009].

As seen in Figure 3.1 the algorithm of soft particle model is relatively straightforward. In a simulation, parameters such as particle size distribution (PSD), density, mass, and moment of inertia are defined and used as an input. The particle is inserted into the computation with a defined initial velocity and position, and are placed in either a fixed lattice or randomly distributed. After the particles have been placed, all particle-particle and particle-wall contacts are detected. For each contact, the soft-particle deformation, which is modelled as an overlap, is calculated. The forces affecting each particle are calculated from the overlap value and force-displacement relations. Then the sum of all forces and moments acting on each particle are calculated. The translational and rotational accelerations of each particle is calculate based on overall force acting on the particle and Newton's second law. From the calculated accelerations, are the position and velocity of the particle updated. Then any quantities of interest, such as velocity profiles, solid-phase stresses, or local concentrations are measured at the given time point, and then the simulation repeats the contact detection for the updated particle positions and the loop is repeated [Ketterhagen et al., 2009].

The most essential part of the DEM model is the particle interaction model. This particle interaction model is used to calculate the forces acting in either particle-particle or particle-wall contacts. Both contacts can be modelled by the same model, however, the material properties (e.g. coefficient of restitution, friction coefficient, etc.) for each contact type can differ so that dissimilar materials can be described. Based the calculated force, the acceleration is calculated and integrated over time to determine particle positions and velocity. The soft particle model forces are divided into two types: normal and tangential components. Walton and Braun [1986] developed a contact model by including materials plastically deforming during contact. They also developed a partially-latching, hysteretic spring model, that uses one linear spring to model the repulsive force during loading, and another stiffer linear spring to model the force during the unloading portion of the contact. Cundall and Strack [1979] developed a tangential force model, where the tangential forces are described by a linear spring and the associated displacement is integrated from the relative velocity at the contact point. This model is often used as it is relatively simple to implement and reproduces experimental observations fairly well. Table 1 in Zhu et al. [2007] have summarised the most important equations describing the normal and tangential forces.

Addition to contact forces, there are also non-contact forces interacting between the particles. Which includes i.e capillary cohesion, electrostatics, or van der Waals interaction (vdW). The importance and effect of these forces have been discussed in detail by Seville et al. [2000]. For example, to be able to simulate the disintegration process in DEM, it is important to develop models describing these non-contact forces [Markl and Zeitler, 2017].

- Van der Waals force is an attractive force acting between two atoms or molecules [Dzyaloshinskii et al., 1961]. The force between two particles is proportional to l^{-6}, where l is the distance between the two particles [Zhu et al., 2007]. It is common practice in DEM that the vdW force ($\mathbf{F}^{\text{vdw}}$) is modelled using Equation 3.1 [Hamaker, 1937]. It based on considering the interactions between individual atoms (or molecules) and postulates their additive so that the van der Waals attraction between macroscopic bodies can be calculated by integrating over all pairs of atoms.

  $$\mathbf{F}^{\text{vdw}} = -\frac{A_{\text{ham}} r_p}{12h^2}, \tag{3.1}$$

  where A_{ham} is the Hamaker constant, see Hamaker [1937] for further description of the Hamaker constant. This constant is affected by physical and chemical properties of the particle such as surface roughness or asperity, and medium chemistry [Zhu et al., 2007]. For plastic deformation, the van der Waals force must include a term for the extended contact area [Forsyth et al., 2002].

- The electrostatic force is the force of attraction or repulsion between two charged particles. For example, the force between the protons and electrons in an atom is electrostatic and is responsible for the atom's stability. In chemistry, the electrostatic bonding force is important and binds an ionic molecule.

- In addition to the force between particles, there are also forces working between the liquid and the particles due to particle fluid interactions. The particle fluid interaction force includes mainly the drag force which is the driving force for fluidisation, pressure gradient force, and other unsteady forces such as virtual mass force, Basset force, and lift forces [Zhu et al., 2007]. The equations describing all this different forces, are given in Table 3 in Zhu et al. [2007]. The drag force can be determine based on numerical simulations at a microscale, where the techniques used include the direct numerical simulation [Choi and Joseph, 2001] and the Lattice boltzmann method [Zhang et al., 1999].

- Another force to consider is the capillary force which is mainly due to the surface tension at solid/liquid/gas interfaces [Fisher, 1926]. To implement the capillary force in DEM simulation, liquid distribution among particles has to be determined [Zhu et al., 2007]. The studies presented in Muguruma et al. [2000] assume that liquid can be transported among particles and is distributed evenly among all gaps smaller than the rupture distance.

Most of the studies conducted in DEM have approximated particle shape to be either spherical (3D) or circular. The advantages of using spherical particles is that the contact detection and contact resolution are easier to determine. However, in most real problems the particles are not spherical, rendering the results with a spherical approximation is not always accurate [Ketterhagen et al., 2009]. In many cases spherical particles behave differently in terms of its flowability (e.g. angle of repose [Gallas and Sokolowski, 1993]) and strength [Ting et al., 1995] compared to non-spherical particles. The reason is that the rotation of spherical particles is caused by frictional contacts with neighbouring particles, whereas for non-spherical particles it is also caused by mechanical interlocking [Ketterhagen et al., 2009, Oda et al., 1982]. One of the simplest methods used for including non-spherical particles in DEM was by clustering two or more spheres together in either a rigid or flexible manner. This method uses the same simple contact detection and contact calculation as the spherical particles. It has been applied in studies of clustering of circular particles [Jensen et al., 2001, Thomas and Bray, 1999] and spherical particles [Abou-Chakra et al., 2004, Favier et al., 2001]. A particular challenge with this method is to describe particles with sharp edges and model the roughness of the particles which directly affects the dynamic behaviour [Ketterhagen et al., 2009]. Another method used to create non-spherical particles is based on mathematical dilation [Serra, 1986]. In this method spherical particles with same radius are placed at every point on some basic geometric shape. One of the shapes produced through dilation is spherocylinder, this shape is made by dilating a line segment with a sphere. With this method the particle surface will get smooth, however the contact detection of these shapes is difficult [Ketterhagen et al., 2009]. The studies presented in Lin and Ng [1997], Mustoe and Miyata [2001] characterised the particle as ellipsoid, which is described by Equation 3.2.

$$\frac{x^2}{l_x^2} + \frac{y^2}{l_y^2} + \frac{z^2}{l_z^2} = 1, \tag{3.2}$$

where l_x, l_y,and l_z is defined as the lengths of the three principle axes which are aligned with the local x, y, and z coordinates, respectively. Ellipsoids belong to the shape classes superquadric, which are used to represent non-spherical shapes (examples are given in Figure 4 in Ketterhagen et al. [2009]). These superquadric shapes can be modelled using Equation 3.3,

$$\left|\frac{x^2}{a^2}\right|^{\alpha} + \left|\frac{y^2}{b^2}\right|^{\alpha} + \left|\frac{z^2}{c^2}\right|^{\alpha} = 1, \tag{3.3}$$

where the exponent $\alpha > 0$ characterises the blockiness of the particle. The edges of the shape will get sharper and then shaper by increasing α. This model can be used to explore many different shapes. The problem with implementing this model in DEM, is the difficulty of calculating the contact detection between two non-linear functions. Williams and O'Connor [1995] developed a method for modelling non-spherical particles by discretising the surface of an arbitrarily shaped particle based on a single parameter. Song et al. [2006] developed a model of a round, bi-convex, tablet shape. This shape is based on three spheres, one small sphere that defines the tablet band and two larger spheres that define each of the convex caps. There are many different methods to include non-spherical particle in DEM simulations, by using these methods the computational time for the simulation will increases significantly.

3.1.1 Challenges of DEM simulations

There are many advantageous of using DEM, such as the behaviour of millions of particles can be simulated to better understand the physics behind the overall process. This enables the investigation on how different parameters such as particle properties, process parameters, and equipment design are affecting the process and particle behaviour.

The main limitation of DEM is the significant demand of high computational power. Since DEM tracks the behaviour of every single particle in a system, increasing the number of particle also increases the computational time. An increase of N particles, approximately increases the computational time by $N\log(N)$. The number of particle, N, in the system can be described by a function of the total volume, V, and the density, ρ_t, of the system as given in Equation 3.4.

$$N = \frac{6V\rho_t}{2\pi r_p}, \tag{3.4}$$

By either increasing the volume or decreasing the particle radius, the number of particle increases significantly. One method which have been used to decrease computational time is to use the symmetry in the process/system. By considering the symmetry, periodic boundary conditions can be implemented [Ketterhagen et al., 2008]. The periodic boundary conditions reduce the size of the computational domain. Another approach taken to reduce the number of particle is to increase the particle size. For example, particles with a size of 20 μm are approximated by 20 mm particles, a similar approach was taken by Gao et al. [2021].

The problem with this approach is the particle interaction and phenomena are affected by particle size. In addition to particle size, there are also other technical complexities affecting the computational time, such as non-spherical particle shape, moving boundaries and contact force models [Ketterhagen et al., 2009].

3.1.2 DEM applications in compaction and disintegration modelling

The studies presented in [Kalný et al., 2021, Kimber et al., 2012] used DEM to model the tablet disintegration. Kalný et al. [2021] simulated the disintegration and dissolution of a two component tablet with ibuprofen as the API and croscarmellose sodium (CCS) as a disintegrant. They assumed that only the CCS particles contribute to the total swelling and the swelling was only occurring in two spatial directions. They simplified the swelling by assuming that all particle swell simultaneously and at a constant rate, i.e. the liquid penetration behaviour was not considered. Kimber et al. [2012] developed a model for simulating the swelling and dissolution process of a polymer tablet by combining DEM particles with Fickian mass transfer. The particle was assumed to be cylindrical with swelling only occurring in the radial direction. Schütt et al. [2021] developed a model to simulate tablet disintegration in the human ascending colon using a discrete multiphysics approach coupled with a smoothed particle hydrodynamics and lattice spring model. Studies from other fields, such as hydrogeology [Sweijen et al., 2017a, 2020], have used DEM to simulate similar processes. Sweijen et al. [2017a] and Sweijen et al. [2020] applied DEM to simulate the swelling of superabsorbent particles (SAP) with an integrated liquid penetration model. Sweijen et al. [2017a] simulated the swelling of a bed of SAP particles using a single particle swelling model combined with the pore finite volume method to model the liquid flow in the compacts. The group developed this model further [Sweijen et al., 2020], where the unsaturated flow was computed using a scheme of implicit pressure solver and explicit saturation update. Braile et al. [2022] developed a DEM model for swelling of granular materials (MCC PH101, rice and superabsorbent particles), where they simulated the swelling of the material using the first order kinetic equation. Several studies have also demonstrated the use of DEM to simulate the tablet compaction process and extract information on the inter-particle forces and porosity and other properties affecting the tablet performance [Gao et al., 2021, Garner et al., 2018, Haustein et al., 2017, Nordström et al., 2018, Persson and Frenning, 2012, 2015, Thakur et al., 2014a].

As mentioned previously, the particle motion is calculated from the force a particle experiences using a contact model [Ketterhagen et al., 2009]. Common contact models applied for compaction process simulation includes the Luding elasto-plastic model [Luding, 2008], Storåkers model [Storåkers et al., 1997] and Hertz-Mindlin theorem [Johnson and Johnson, 1987]. Recent studies from Gao et al. [2021] and Toson et al. [2021] showed that the Luding model is suitable for pharmaceutical materials. [Kalný et al., 2021, Kimber et al., 2012, Sweijen et al., 2017a] model the swelling process in DEM, the contact model presented in these studies are given in Sections 3.1.2 and 3.1.2.

Compaction

He et al. [2015] studied link the die compaction with the strength and failure pattern of the compact under the uniaxial unconfined compression using DEM. They used the elastic-perfectly plastic contact model proposed by Thornton and Ning [1998] to describe the normal (denoted by n), contact force between particle i and j, $\mathbf{F}^{\mathrm{n}}$, given by Equation 3.5-3.9,

$$\mathbf{F}^{\mathrm{n}}_{ij} = \begin{cases} \frac{4}{3} E^*_n R^{*1/2} \delta_{\mathrm{n}}^{3/2} \hat{\mathbf{n}}_{ij} & \text{if } \delta_{\mathrm{n}} < \delta_0 \\ \Big[F_y + \pi p_y R^* (\delta_{\mathrm{n}} - \delta_0) \Big] \hat{\mathbf{n}}_{ij} & \text{if } \delta_{\mathrm{n}} \geq \delta_0, \end{cases} \tag{3.5}$$

$$R^* = \frac{r_{p,i} r_{p,j}}{r_{p,i} + r_{p,j}}, \tag{3.6}$$

$$\hat{\mathbf{n}}_{ij} = \frac{\mathbf{R_i} - \mathbf{R_j}}{\left| \mathbf{R_i} - \mathbf{R_j} \right|}, \tag{3.7}$$

$$E^*_n = \frac{E^*_i E^*_j}{E^*_i + E^*_j}, \tag{3.8}$$

$$E^*_i = \frac{E_i}{1 - \nu_i^2}. \tag{3.9}$$

Where δ_{n} is the normal overlap, p_y is the yield pressure beyond which the particle deforms plastically. δ_0 and F_y are the corresponding overlap and force at the onset of the plastic deformation. E_i is the Young's modulus and ν_i Poisson ratio. They assume that the unloading and reloading processes to be elastic.

The force in tangential (denoted by t) direction, $\mathbf{F}^{\mathrm{t}}$ was described using the modelled described in Mindlin and Deresiewicz [1953], and given by,

$$\mathbf{F}^{\mathrm{t}}_{ij} = -sgn(\xi_s) \mu_s \left| \mathbf{F}^{\mathrm{n}}_{ij} \right| \left[1 - (1 - min(\xi_s, \xi_{s,max}) / \xi_{s,max})^{3/2} \right]. \tag{3.10}$$

Where μ_s is the sliding friction coefficient, ξ_s the total tangential displacement of particles during contact. $\xi_{s,max}$ is the threshold value determining the onset of gross sliding. They modelled the capillary force, $\mathbf{F}^{\mathrm{cap}}$ using Equation 3.11.

$$\mathbf{F}_{ij}^{\text{cap}} = \begin{cases} \frac{2\pi R^* \gamma cos(\theta)}{1+\frac{1}{\sqrt{1+2V_L/(\pi R^* S^2)}-S}} \hat{\mathbf{n}}_{ik} & \text{if } P-P \\ \frac{4\pi R^* \gamma cos(\theta)}{1+\frac{S}{\sqrt{\pi r_p/V_L}}} \hat{\mathbf{n}}_{ik} & \text{if } P-W, \end{cases} \tag{3.11}$$

where P-P is particle-particle interaction and P-W particle-wall interacion, and γ is surface tension, θ is contact angle, V_L is the volumetric liquid content and S is the interparticle separation. To model the bonding force they used a bonded particle model (BPM) in which the bond can transmit both force and moment. They used the BPM developed by Potyondy and Cundall [2004] to describe the interparticle bonding forces and moments. The model has a simple, linear form (similar to the linear spring model for the contact forces). The bonds can be broken either by tension or by shear and the criteria for bond failure are given by Equation 3.12.

$$\min\left(\frac{-F_{ij}^{bn}}{A_{\text{cap}}} + \frac{\left| M_{ij}^{bt} \right| r_b}{J}, \frac{-F_{ij}^{bt}}{A_{\text{cap}}} + \frac{\left| M_{ij}^{bn} \right| r_b}{I} \right) \geq \sigma_b, \tag{3.12}$$

where F^b is bonding force, A_{cap} is the bonding area, M is the moment, r_b is bonding radius, J is the moment of inertia, I is the polar moment of inertia and σ_b is the strength of the bonds. Once broken, they assume these bonds can not longer be restored.

Several studies demonstrated the use of the Luding elasto-plastic contact model [Luding, 2008] for particle-particle and particle-wall interactions during tablet compaction. Both Gao et al. [2021] and Toson et al. [2021] used the Luding model for pharmaceutical materials. The Luding elasto-plastic contact model is given in Eqs, 3.13-3.15. The force in normal direction, $\mathbf{F}^{\text{n}}$, is given as

$$\mathbf{F}^{\text{n}} = \begin{cases} k_1 \delta_{\text{n}} & \text{if } k_2(\delta_{\text{n}} - \delta_0) \geq k_1 \delta_{\text{n}} \\ k_2(\delta_{\text{n}} - \delta_0) & \text{if } k_1 \delta_{\text{n}} \geq k_2(\delta_{\text{n}} - \delta_0) \geq -k_{\text{c}} \delta_{\text{n}} \\ -k_{\text{c}} \delta_{\text{n}} & \text{if } -k_{\text{c}} \delta_{\text{n}} \geq k_2(\delta_{\text{n}} - \delta_0). \end{cases} \tag{3.13}$$

with k_1 as the loading stiffness, k_2 as the plastic unloading stiffness, k_{c} as the adhesion stiffness. δ_{n} as the normal overlap and δ_0 as the plastic contact deformation overlap. k_2

is defined as

$$k_2 = \begin{cases} k_\mathrm{p} & \text{if } \delta_\mathrm{max}/\delta_\mathrm{lim} \geq 1 \\ k_1 + \frac{(k_\mathrm{p}-k_1)\delta_\mathrm{max}}{\delta_\mathrm{lim}} & \text{if } \delta_\mathrm{max}/\delta_\mathrm{lim} < 1. \end{cases} \tag{3.14}$$

k_p is the limit plastic unloading stiffness. δ_max and δ_lim (see Equation 3.15) are the maximum compression overlap and the plastic limit, respectively.

$$\delta_\mathrm{lim} = \frac{k_\mathrm{p}}{k_\mathrm{p} - k_1} \phi_\mathrm{f} R^*, \tag{3.15}$$

where ϕ_f is dimensionless plasticity depth and R^* is an equivalent radius. Gao et al. [2021] showed that the parameters k_1 (loading stiffness), k_p (limit plastic unloading stiffness) of Luding elasto-plastic model and the particle density impacted the compression profile mostly and adjustment on these three parameters could cover most of the variations of the compression profile.

Disintegration and swelling

Kimber et al. [2012] developed a model for simulating the swelling and dissolution process of a polymer tablet by combining DEM particles with Fickian mass transfer to model diffusion of water, see Equations 1.46-1.49. Between each mass transfer time step, Δt, the equilibrium position x_i of N particle are obtained. This was obtained using Newton's Laws of motion on each DEM particle. The overlapping particles interact by a linear spring method with damping, and these forces are resolved over virtual time steps $\Delta\tau_\mathrm{vir}$. The $\Delta\tau_\mathrm{vir}$ are independent from Δt, until the average force for all particles fall below a set threshold. The forces applied on each particle are inter-particle repulsion forces $\mathbf{F}_{i,j}^\mathrm{rep}$, a small global attractive force $\mathbf{F}^\mathrm{grav}$ is applied on all the particles to have closed packed structure, by pulling the particle towards the centre of the domain $\mathbf{x}_c$. $\mathbf{F}^\mathrm{grav}$ is strong enough to hold the shrinking particle in contact with the main body, but it is also small enough to prevent overlapping of particles. Also a damping force, $\mathbf{F}_i^\mathrm{damp}$ is applied, which is expressed in terms of the particle velocities, $\mathbf{u}_i$. The equation of the forces are given in Equations 3.17-3.19. The total force, $\mathbf{F}_i$, applied on each particle, is given by:

$$\mathbf{F}_i = \sum_{j\neq 0}^{N} \mathbf{F}_{i,j}^{\mathrm{rep}} + \mathbf{F}_i^{\mathrm{grav}} + \mathbf{F}_i^{\mathrm{damp}}. \tag{3.16}$$

The inter-particle repulsion force, $\mathbf{F}_{i,j}^{rep}$, is defined as,

$$\mathbf{F}_{i,j}^{\mathrm{rep}} = \begin{cases} 0 & \text{if } l_{i,j} > (r_{p,i} + r_{p,j}) \\ -k_{rep} \frac{r_{p,i}+r_{p,j}-d_{i,j}}{r_{p,i}+r_{p,j}} \frac{\mathbf{x}_i - \mathbf{x}_j}{\|\mathbf{x}_i - \mathbf{x}_j\|} & \text{if } l_{i,j} < (r_{p,i} + r_{p,j}). \end{cases} \tag{3.17}$$

The small global attractive force F^{grav}, is given as:

$$\mathbf{F}_i^{grav} = \frac{\mathbf{x}_i - \mathbf{x}_j}{\| \mathbf{x}_i - \mathbf{x}_j \|} F^{grav} \tag{3.18}$$

The damping force is defined as:

$$\mathbf{F}_i^{damp} = -\eta_{\mathrm{damp}} \mathbf{u}_i. \tag{3.19}$$

Kalný et al. [2021] developed a DEM model for simulating the disintegration process of directly compressed immediate-release tablets. The model was based on the disintegration process of tablet consisting of ibuprofen as API and CCS as disintegrants, in their model only the swelling of the disintegrant particle are considered, the swelling for this study is given in Equation 1.35. The described each the particle initially by its mass m, radius r_p, position and velocity vectors $\mathbf{r}$ and $\mathbf{v}$, orientation specified by Euler angle θ_e and angular velocity v. At each time step they calculated the contact forces of each particles, and updated particle position and velocity using Equation 3.20 and 3.21.

$$\frac{d^2\mathbf{r}}{dt^2} = \frac{d\mathbf{v}}{dt} = \frac{\sum_i F_i}{m} \tag{3.20}$$

$$\frac{d^2\theta_e}{dt^2} = \frac{dv}{dt} = \frac{\sum_i M_i}{J} \tag{3.21}$$

In their model the contact force, was considered as a repulsive force between the pair of overlapping particles. They used the soft-sphere model developed by Cundall and Strack [1979] to describe the viscoelastic deformation of the particles. They determine if two particle was overlapping using Equation 3.22.

$$\delta_{ij} = r_{p,i} + r_{p,j} - \left|\mathbf{r}_i - \mathbf{r}_j\right|, \tag{3.22}$$

$\delta_{i,j}$ is the overlap between i-th and j-th particle. Then the contact force is calculated as:

$$\mathbf{F}_{ij} = \begin{cases} \mathbf{F}^n_{i,j} + \mathbf{F}^t_{i,j} & \delta_{i,j} > 0 \\ 0 & \delta_{i,j} \leq 0 \end{cases} \tag{3.23}$$

Where superscripts n and t denote the normal and the tangential component of the force. The normal force consists of a dissipative (viscous) and a conservative (elastic) part. In this study the Kelvin-Voigt model was used to describe the normal force, which is represented as a combination of elastic spring and viscous damper connected in parallel. The normal force was defined as given in Equation 3.24.

$$\mathbf{F}^n_{ij} = (-k_{\text{n,stiff}}\delta^{\frac{3}{2}}_{ij} - \eta_{\text{n,damp}}\delta^{\frac{1}{2}}_{ij})\mathbf{n}_{ij}, \tag{3.24}$$

$k_{\text{n,stiff}}$ is the normal stiffness coefficient, which is a function of material parameters E (Young modulus) and ν (Poisson ratio) and are given by the Hertzian theory. $\eta_{\text{n,damp}}$ is the damping coefficient and $\mathbf{n}_{ij}$ is the unit vector pointing from i-th to j-th particle centres. The equations for calculating the different parameter are given in Kalný et al. [2021]. The authors also used the Kelvin-Voigt model to describe the normal force and the tangential part of the contact force. This is represented as a combination of elastic spring and viscous damper in parallel. This force is oriented perpendicular to the surface of the particles in contact, the tangential force was defined as given in Equation 3.25.

$$\mathbf{F}^t_{ij} = -k_{\text{t,stiff}}\iota_t - \eta_{\text{t,damp}}\mathbf{v}_{\text{rel}}, \tag{3.25}$$

where ι_t is the displacement in tangential direction, $k_{\text{t,stiff}}$ is the tangential stiffness, $\eta_{\text{t,damp}}$ is the tangential damping coefficient and $\mathbf{v}_{\text{rel}}$ is the relative velocity of spheres at their point of contact. The equations for calculating the different parameter are given in Kalný et al. [2021].

The attractive force ($\mathbf{F}^{\text{grav}}$), the force which represents the cohesion between two neighbouring particles prior to disintegration. Ideally the interarticular cohesion should be described by intermolecular bonds, solid bridges and mechanical interlocking. However, in their the simplified it, and combined all the forces and modelled as a single attractive force that acts between the points on the surface of two neighbouring particles. The equation attractive force is given in Equation 3.26,

$$\mathbf{F}^{\text{grav}} = \alpha_a \delta^a_{ij} \mathbf{n}^a_{ij}. \tag{3.26}$$

Where α_a is the attractive force strength coefficient, since this parameter physical meaning does need to be fitted with experimental data. $\mathbf{n_{ij}}^a$ is the unit vector between two points on the surfaces of the i-th and j-th particle and δ^a_{ij} is the current distance between these two points. The assume that the attractive force is the bonds formed between individual API or disintegrant particles during compressed and that new bonds are not created during the disintegration process.

They added a damping force, $\mathbf{F}_i^{\text{damp}}$, to their simulation, to minimise the fast movements of the fragments by damping the particle movements and also keep the simulation numerically stable. The damping force is given as a function of the particle mass and velocity, see Equation 3.27, where b_d is the damping force parameter.

$$\mathbf{F}_i^{\text{damp}} = -b_d \mathbf{v}_i m_i. \tag{3.27}$$

Sweijen et al. [2017a] developed a DEM model for swelling of bed of SAP particles. Each particle, i, is characterised by the particle radius (r_p, see Equation 1.27), Young's modulus (E_i), density (ρ_i), Poisson ratio (v_i), shear modulus (G_i) and friction coefficient (Φ_i). They assumed at a contact between two particles the following processes can occur: normal deformation, shear, and sliding. They defined the particle overlap as

$$\delta_{ij} = \begin{cases} 0 & \text{if } (r_{p,i} + r_{p,j}) \leq l_{i,j} \\ r_{p,i} + r_{p,j} - l_{i,j} & \text{if } (r_{p,i} + r_{p,j}) > l_{i,j}. \end{cases} \tag{3.28}$$

Where $l_{i,j}$ is the distance between the centres of particles i and j. An elastic force arises at the contact area of particles i and j, which acts towards reversing the overlap of particles. They used the Hertz-Mindlin theorem to calculate the elastic force. The theorem assumes that a small deformations occurs at the contact points between two particles. Based on the Hertz-Mindlin contact mechanics, they define these following effective parameters for two particles i and j that are in contact with each other:

$$E_{ij} = \left(\frac{1 - \nu_i}{E_i} + \frac{1 - \nu_j}{E_j} \right)^{-1} \tag{3.29}$$

$$G_{ij} = \frac{G_i + G_j}{2} \tag{3.30}$$

$$\nu_{ij} = \frac{\nu_i + \nu_j}{2} \tag{3.31}$$

The harmonic mean of particle radii, r_{ij} is defined as,

$$r_{ij} = \frac{r_{p,i} r_{p,j}}{r_{p,i} + r_{p,j}} \tag{3.32}$$

The force caused by normal displacement, $\mathbf{F}^n_{ij}$ is given as:

$$\mathbf{F}^n_{ij} = k^n_{ij} (\delta^n_{ij})^{3/2}. \tag{3.33}$$

Where k^n_{ij} is the contact stiffness in the normal direction and is given by:

$$k^n_{ij} = \frac{4}{3} E_{ij} \sqrt{r_{ij}}. \tag{3.34}$$

The elastic force in the tangential direction at a given time step, $\mathbf{F}^{n\ t+\Delta t}_{ij}$, is history dependent and thus depends on its old value, such that:

$$\mathbf{F}^{n\ t+\Delta t}_{ij} = \mathbf{F}^{n\ t}_{ij} + k^t_{ij} l^{\dot{t}}_{ij} \tag{3.35}$$

Where $l^{\dot{t}}_{ij}$ is the relative tangential velocity, as it is function of the relative velocity of the two particles and their spinning, see Sweijen et al. [2017a] for definition. Where k^t_{ij} is the contact stiffness in tangential direction and is given by:

$$k^t_{ij} = \frac{4\sqrt{r_{ij}}G_{ij}}{2-\nu_{ij}}(\delta^n_{ij})^{1/2}. \tag{3.36}$$

Since the recent studies from Gao et al. [2021] and Toson et al. [2021] showed that the Luding model is suitable for pharmaceutical materials, we used Luding [2008] contact model. As explained in Thakur et al. [2014b] switching contact model between process would have negative effect on the computional time and power, therefore we choose use a contact model primarily designed for compaction process and used it also for disintegration modelling.

3.1.3 DEM software package

The open source DEM software Yade-DEM [V. Smilauer et al., 2021] was used for the studies presented in Chapters 5 and 6. Yade-DEM is a 3-dimensional discrete element software The computation parts of Yade-DEM are written in C++ using a flexible object model and allowing independent implementation of new algorithms and interfaces. While, python is used for rapid and concise scene construction, set-up simulation, simulation control, post processing and debugging. The software has various different contact model implemented, such as the Luding elasto-plastic contact model [Haustein et al., 2017], Hertz-Mindlin contact [Sweijen et al., 2017a], Cundall Strack contact model [Haustein et al., 2017] etc. The advantages of using Yade-DEM is that the software provides the opportunity to change the contact models to be suitable for a specific application, and to add models not present in their library. The software also have in-built liquid transport models which are compatible with DEM such as the pore finite method [Chareyre et al., 2012], pore unit assembly method [Sweijen et al., 2018] and lattice Boltzmann method [Sibille et al., 2014].

3.2 Tablet compaction

The most common tablets are manufactured by compacting a formulated powder blend that is composed of one drug substance and a number of different excipients [Kadiri et al., 2005], i.e disintegrants are added to a formulation as a swelling agent, and therefore enhance the disintegration process. The compaction process consist of four steps: 1) filling of the die. 2) Loading, where the punch are mowing towards the powder. During the loading stages, the powder rearranges and deforms until it compaction processes reaches their maximum compression pressure. 3) Unloading, where the punch moves away from the tablet and 4) Ejection of the final tablet [Sanchez-Castillo and Anwar, 2003]. The physical and mechanical properties of the tablets, such as porosity and mechanical strength, are significantly affected by the selected formulation and the process conditions used to make the tablet compact [Cunningham et al., 2004]. The compaction of the powder blend is of critical importance when the particles experience intensive deformation and start to bond together through van der Waals forces, mechanical interlocking and formation of solid bridges [Wu et al., 2008]. The tablet used in Chapters 5 and 6, were prepared via direct compression using a compaction simulator (HB50, Huxley-Bertram Engineering, Cambridge, UK). The samples have a diameter and thickness of 10 and around 2 mm, respectively. The diameter and thickness were kept constant while the filling weight of the powder material was adjusted to vary the tablet porosity. The powder was filled manually into the die of the compaction simulator to achieve precise powder filling. The compaction process was performed using a sinusoidal compaction profile, with an average speed of 0.026 m/s.

3.3 Terahertz pulsed imaging

The model presented in Chapters 5 and 6 were validated using terahertz pulsed imaging (TPI) [Al-Sharabi et al., 2020, Markl and Zeitler, 2017]. Terahertz radiation is referred to radiation in the far-infrared region of the electromagnetic spectrum [Zeitler et al., 2007]. Since the most common pharmaceutical excipients are transparent or semi-transparent to terahertz radiation, the radiation can penetrate through a tablet matrix [Zeitler et al., 2007]. The methods are safe, non-destructive and fast, whilst exhibit excellent potential for exploring the inter-molecular structure and dynamics of organic molecular solids as well as being able to probe the microstructure of solid dosage forms [Zeitler, 2016]. Since it is possible to explore inter-molecular structures, it can be used to explore hydrogen bonds and thereby track water movements through porous media. TPI has typically excellent contrast. The good contrast in images are caused by the coherent detection scheme together with the resulting time-domain signal of the terahertz pulse lead to the high sensitivity [Zeitler and Shen, 2013]. The main advantage of using TPI in this work is that it can be used to monitor the liquid penetration into and swelling of powder compacts simultaneously [Al-Sharabi et al., 2020].

The liquid penetration and tablet swelling in this study was measured using a commercial terahertz pulsed imaging system (TPI, TeraPulse 4000, Teraview Ltd., Cambridge, UK) in combination with a bespoke flow cell [Al-Sharabi et al., 2021]. The TPI was set up with a fibre-based reflection probe equipped with an 18 mm focal length silicon lens. The probe head was on a linear scale for ease of spatial adjustment. The beam resulting of the THz optics had a beam waist of around 1 mm at the focus with an incident angle of 13°. The TPI setup with the flow cell (Figure 3.2) measures the change of the back face of the tablet which reflects both the swelling on the back face and on the front face where it takes up the liquid. Since the flow cell was not included in the DEM simulation setup for this study, only the front face swelling was recorded in the simulation. More details about the flow cell and its design can be found in [Al-Sharabi et al., 2021].

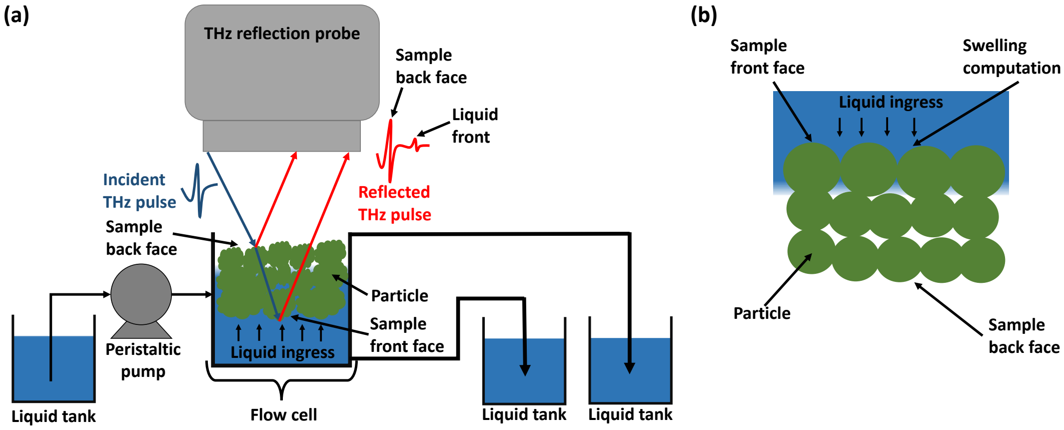

Figure 3.2: A schematic of the (a) experimental and (b) DEM setup.

Chapter 4

Quantification of swelling characteristics of pharmaceutical particles

Chapter Summary

This chapter determining swelling descriptors of single pharmaceutical particles by combining in-situ measurements with a swelling model. A bespoke flow cell coupled to an optical microscope was developed to monitor single particle swelling in real-time. The contents of this chapter have been published in the International Journal of Pharmaceutics, see [Soundaranathan et al., 2020].

4.1 Introduction

Once a tablet administered orally comes in contact with a physiological fluid, the liquid will penetrate the porous tablet and in the majority of cases initiate its swelling. This swelling builds up an internal stress that causes the break up of the tablet into smaller agglomerates and the primary particles. These steps are referred to as the tablet disintegration processes, which are critical steps to dissolve and enable the absorption of the drug substance [Markl and Zeitler, 2017, York, 2022]. A controlled disintegration process is essential to ensure the desired on-set of the therapeutic effect.

Tablet swelling is the most accepted mechanism for tablet disintegration [Patel and Hopponent, 1966] and it primarily depends on the swelling of the individual particles. To be able to disintegrate, the interparticulate bonds inside a tablet need to be disrupted by the swelling of excipient particles [Quodbach and Kleinebudde, 2015]. Particle swelling is the volumetric and omnidirectional expansion of the particle during liquid contact [Faroongsarng and Peck, 1994]. The swelling ability of the particle depends on the particle size, chemical structure and degree of cross-linking of polymeric systems [Bell and Peppas, 1996, Desai et al., 2015]. To prevent polymers from dissolving in the aqueous media during swelling, other polymers are used to bind them, which are referred to as cross-linkers [Sweijen et al., 2017a]. It has been observed that polymers with cross-linking produce a high swelling force but have a limited volume expansion, however, the disintegration time is quicker compared to other strongly swelling particles [Quodbach and Kleinebudde, 2015]. Typically, disintegrants are added to a formulation as a swelling agent, and therefore enhance the disintegration process.

Common disintegrants include starch- and cellulose-based excipients such as corn starch, partially pregelatinized starch and lowsubstituted hydroxypropyl cellulose (L-HPC) [Desai et al., 2015, Patel and Hopponent, 1966, Quodbach and Kleinebudde, 2015]. To accelerate the disintegration process further, synthetic polymers such as sodium starch glycolate (SSG), croscarmellose sodium (CCS) and crospovidone (XPVP) were developed, which are referred to as superdisintegrants. Besides the swelling of disintegrants, other excipients such as microcrystalline cellulose (MCC)- typically used as a diluent, filler or binder - may also exhibit swelling and contribute to the overall swelling of a tablet [Desai et al., 2015, Reier and Shangraw, 1966].

Generally, materials have been classified in either omni-directional or uni-directional (against the direction of compaction) swelling. The uni-directional swelling is commonly referred to as strain recovery, which is the reversible viscoelastic process of deformation. The particles recover to their original shape by the mechanical activation of the disintegrant polymer when the particle comes in contact with liquid. The polymer chain then adopts to the most energy-favourable position and causes a uni-direction expansion of the particle [Desai et al., 2015]. Crospovidone is considered as a material that undergoes strain recovery [Berardi et al., 2018, Desai et al., 2012, Quodbach and Kleinebudde, 2014]. The accepted mechanism of MCC, L-HPC, CCS and SSG is omni-directional swelling, which is driven by the swelling ability of the particles. For omni-directional swelling materials the swelling ability is a material property, whereas for strain recovery materials it is dominated by the manufacturing settings (e.g. compression force in tableting).

A range of studies have been performed to quantify the swelling of particles and also to model the swelling. The swelling of disintegrants in a suspension was quantified by Zhao and Augsburger [2005] using laser diffraction. They measured the volume mean diameter change during swelling and revealed that SSG had better swelling capacity (maximum swelling of particle) than CCS. Rudnic et al. [1982] analysed the wetting and swelling of individual SSG and sodium carboxymethyl stach particles using an optical microscope. Their results showed that the rate and extent of swelling for the measured particle varied with particle size, i.e. larger particles showed substantially greater rates and extent of swelling compared to smaller particles.

Rojas et al. [2012] quantified the swelling value – the ratio between powder expanded volume upon water absorption and the initial sample weight – and water uptake ability of SSG, CCS and MCC powder in simulated gastric and intestinal fluid. SSG had the largest water uptake ability and swelling value followed by CCS and MCC. Desai et al. [2012] analysed and quantified the swelling of compacted disintegrant particle that contained 70% disintegrant and 30% glass beads using an optical microscope and a high speed camera. Their results revealed the trend in cross-sectional area increase during swelling for various compacts was as follows: SSG, CCS, MCC and L-HPC.

Berardi et al. [2018] analysed the disintegration mechanism and quantified the swelling of pure CCS, SSG and XPVP tablets. SSG tablets swelled faster and more extensively compared to CCS tablets. The authors described the swelling mechanism of XPVP as strain recovery (swelling in axial direction). Botzolakisi and Augsburger [1988] quantified the swelling and liquid uptake rate of pure disintegrant tablets revealing that CCS tablets exhibited the greatest swelling and highest liquid uptake rate followed by SSG. Several studies quantified the disintegrant swelling of powder compacts Berardi et al. [2018], Botzolakisi and Augsburger [1988], Desai et al. [2012], Rojas et al. [2012] and suspensions [Zhao and Augsburger, 2005]. The swelling behaviour of a group of particles (e.g. powder bulk or compacts) is not only influenced by the single particle swelling, but also by the microstructure of the entire sample. The microstructure of a bulk of particles – loose particles or as a compact – strongly influences the wetting process of the particles [Markl et al., 2018c]. In such a case, the particles are wetted by a liquid front that moves from the surface through the sample. The total swelling of the bulk of particles is thus a superposition of asynchronous swelling of individual particles. The swelling of a bulk of particles is directly controlled by the wetting process and hence strongly depends on additional factors such as the used preparation method as well as particle properties (e.g. size, shape, surface energy) [Al-Sharabi et al., 2020]. Although the swelling behaviours of a bulk of particles can be compared between different materials by ensuring that microstructural factors are negligible, the extracted swelling characteristics cannot be generalised. Characteristic swelling properties should be independent of the bulk behaviour in order to make it generally applicable and for it to be useful for a rational design of a formulation and the manufacturing conditions. This study aims to determine such characteristic swelling properties for common pharmaceutical excipients. The analysis of single non-pharmaceutical particle swelling is commonly performed using an optical microscope [Esteves, 2011, Gasmi et al., 2015, Sweijen et al., 2017a]. An environmental scanning electron microscope (ESEM) has also been applied to analyse the swelling of single particles [Jenkins and Donald, 1997].

To better understand the swelling behaviour, several groups have developed models to describe the swelling of individual particles as a function of time. These models range from (semi-)empirical [Esteves, 2011, Omidian et al., 1998] to physical based models [Sweijen et al., 2017a,b]. Sweijen et al. [2017a] developed a swelling rate equation considering the diffusion of water into a single spherical super absorbent polymer (SAP) particle. The same group improved their model for SAP particles to account for an irregular particle shape, water uptake on the surface, diffusion into the particle and subsequence particle swelling Sweijen et al. [2017b]. Markl et al. [2017b] modified a mathematical model based on an empirical equations from Schott [1992a] for MCC particles to describe the tablet swelling and also the liquid penetration kinetics. Kimber et al. [2012] developed a model for swelling of polymer particles considering Fickian mass transfer, which was incorporated in a discrete element model to simulate tablet swelling and dissolution.

This study presents a method for determining anisotropic swelling descriptors of single pharmaceutical particles by combining in-situ measurements with a swelling model. A bespoke flow cell coupled to an optical microscope was developed to monitor single particle swelling in real-time. The particle swelling was measured from the microscope images using a bespoke algorithm. From the collected swelling data, the diffusion coefficient, maximum absorption and swelling capacity of the materials were determined. This study was conducted for the most common superdisintegrants (CCS, L-HPC and SSG) that are classified as omni-directional swelling materials and also for five different grades of MCC.

4.2 Material and Methods

4.2.1 Materials

This study was conducted for five different grades of MCC and three different superdisintegrants: Cellets®500 (MCC500, Harke Pharma, Dresden, Germany), Cellets®700 (MCC700, Harke Pharma, Dresden, Germany) and Cellets®1000 (MCC1000, Harke Pharma, Dresden, Germany) and MCC PH101 (Avicel PH101, Roquette, Lestrem, France), MCC PH102 (Avicel PH102, FMC International, Philadelphia, USA) as well as sodium starch glycolate (Primojel®, SSG, DFE Pharma, Goch, Germany), croscarmellose sodium (Ac-Di-Sol, CCS, SDW-802, FMC International, Philadelphia, USA) and low-substituted hydroxypropyl cellulose (L-HPC, Shin Etsu, Tokyo, Japan).

The MCC grades differ in terms of particle size, microstrucutre and moisture content. MCC is produced through an acid hydrolysis process by spray drying, which breaks down only the amorphous region of the cellulose. Cellulose consists of several β1-4-linked glucose subunits and is more crystalline than starches. Cellulose consist of both a compact microcrystalline region and less dense amorphous region [Desai et al., 2015, Thoorens et al., 2014]. PH101 and PH102 are produced by varying and controlling the spray drying conditions, and thereby control the agglomeration (particle size distribution) and moisture content (loss on drying) [Thoorens et al., 2014]. The larger MCC grades (MCC500–1000) are made from MCC powder [Russell et al., 2018] through direct wet pelletisation or extrusion-spheronisation [Kleinebudde and Knop, 2007] in order to manufacture highly spherical particles.

4.2.2 Particle characterisations

Particle size

The dynamic imaging instrument QICPIC (Sympatec GmbH, Clausthal-Zellerfeld, Germany) was used to characterise the particles in terms of size and shape. Before the measurement approximately 2 g of the material was dispersed into the measurement area with a speed of up to 100 m/s using the RODOS powder disperser. The M7 lens (size range 4.2 - 8665 μm) was selected for this study, and three replicates were performed for each material to determine the median particle diameter (D_{50}, particle size) and circularity (S_{50}). The particle size represents the equivalent circle diameter. The circularity is the ratio between the perimeter of a circle with the same area as the particle and the real perimeter. S_{50} is in the range of 0 and 1. The smaller the value, the more irregular the shape of the particle is.

Particle density measurements

The true density of the materials were measured by helium pycnometer (MicroUltrapyc 1200, Quantachrome instrument, Graz, Austria). The test was carried out using a multi-run system (three runs) with a sample size of 1 g, 0.5 g and 0.1 g for MCC500–1000, PH101/PH102 and the disintegrants, respectively.

Maximum absorption ratio measurement

The maximum absorption ratio of single particles ($Q^{\max}$) was estimating by placing 0.5 ± 0.1 g for MCC500-1000 and 0.7 ± 0.1 g PH101/PH102, of dry material in a beaker and subsequently hydrating it. After 40 min the water was filtrated by vacuum filtration, and the mass of the swollen particles were measured. $Q^{\max}$ is the ratio between the mass of the hydrated particles and the mass of the dry particle.

4.2.3 *In-situ* Measurement of swelling of single particles

Custom-built flow cell for swelling measurements

A flow cell was developed to *in-situ* monitor the swelling of single particles. The main requirements for the flow cell were:

1. have an enclosed space for the particle, where it can be monitored with a microscope.
2. prevent particles from moving.
3. wet the entire particle instantaneously.
4. have a continuous flow to control the environment (liquid properties).

If the particle is not wetted entirely and instantaneously, then we would need to account for the contact angle and the wetted surface in the swelling models. The contact angle, however, cannot be determined accurately for a single (and probably porous) particle.

The design of the flow cell is given in Figure 4.1. The flow cell was printed using a Formlabs Stereolithography (SLA) 3D printer with a clear V4 resin. After printing

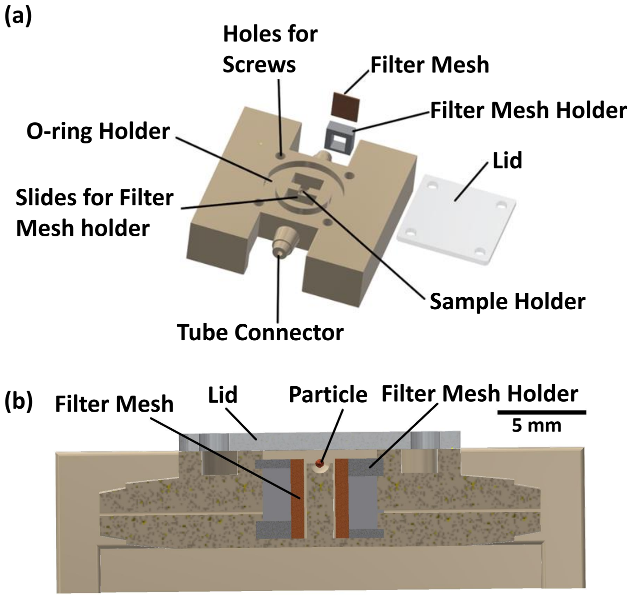

Figure 4.1: Schematic representation of the flow cell. (a) An explosion view of the 3D design of the flow cell. (b) Cross-section view of the flow cell indicating the particle position.

the lid, the lid was sanded to increase the optical transparency. Which allowed seeing through the lid. To close the lid, a 17 mm long screw and nuts with 2 mm outer diameter (O.D). were used.

The particle is placed in a spherical-shaped sample holder with a diameter of 3 mm and a total volume of 0.03 mL. Tube connectors for inlet and outlet are designed into the flow cell. A filter mesh was placed after the inlet and before the outlet to prevent the particle moving into the tubes and leaving the area of view of the microscope. A twill woven wire mesh with a 0.026 mm aperture and 0.025 mm wire diameter from The Mesh Company (Warrington) Ltd was used for this purpose.

The flow cell was sealed by using an RS PRO nitrile rubber O-ring. The O-ring has an inner diameter (I.D). of 18.66 mm, O.D. of 25.72 mm with a thickness of 3.18 mm. The total height of the setup is 18 mm including the 2 mm thick lid.

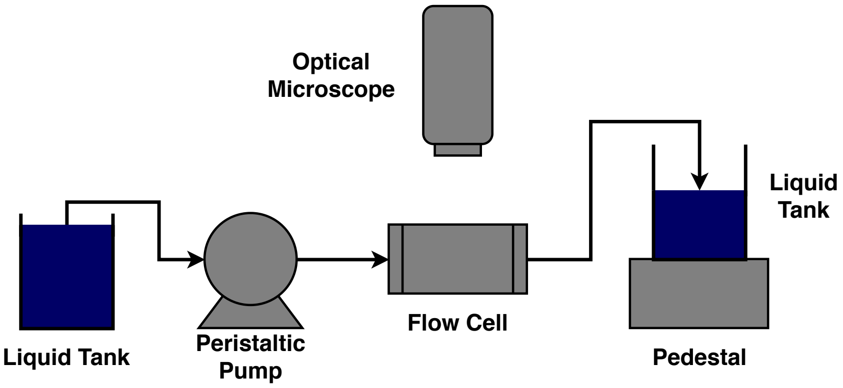

Figure 4.2: Schematic representation of the experimental setup of the flow cell coupled with an optical microscope.

Experimental setup

Figure 4.2 illustrates a schematic representation of the experimental setup of the flow cell coupled with an optical microscope to measure the swelling of a single particle.

Deionised water at 20°C was pumped from a 500 mL glass bottle into the custom-built flow cell by a peristaltic pump (520s, Watson Marlow Ltd) with a flow rate of 1.83 mL/min through tubes with an O.D. of 6 mm and an I.D. of 2 mm. The swelling process was monitored by an optical microscope (Leica DM6000, Leica Microsystems CMS GmbH, Germany) with a magnification of 10x for PH101 and PH102, 5x for MCC500-1000, 5x/10x for CCS, 10x for SSG and 10x/20x for L-HPC. The frame rate of the videos capturing of the swelling process was 10 fps. The outlet glass container is placed on a pedestal to generate a pressure difference between the flow cell and the outlet container to avoid the formation of bubbles inside the flow cell during the measurement as they may affect the swelling measurement. Six individual particles were measured per material.

4.2.4 Data analysis to quantify single particle swelling

Individual frames from the optical microscope were processed to quantify the swelling of the particles. In this study, the processing techniques applied on the microscopic images are grayscale conversion, denoising and binarisation by thresholding. The entire workflow to analyse and quantify the swelling of a single particle is presented in Figure

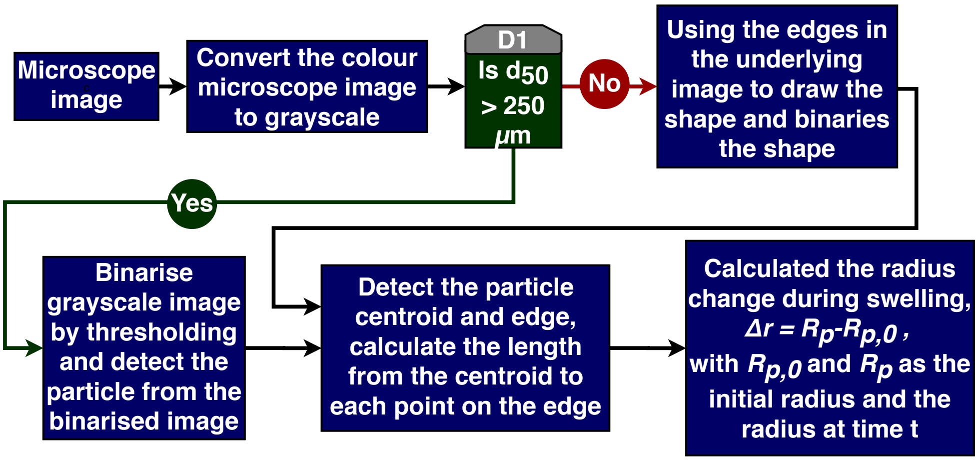

Figure 4.3: The workflow of the data processing to analyse and quantify the swelling of single particles.

4.3.

Image denoising is used to remove random fluctuations in pixels values which arise from the characteristics of the image acquisition [Russ and Neal, 2016]. There are many sources of noise in images and one of the major reasons for noise in the microscope images of this study is the variation of the brightness. The image sensors count photons, the counting process is randomly quantified, and therefore the microscope images also often have photon counting noise [Boncelet, 2009]. In this study, an edge preserving filter, i.e. an anisotropic diffusion filter [Manjón et al., 2008, Perona and Malik, 1990], was applied for denoising the individual images. The edges are preserved by averaging pixels in the orthogonal direction of the local gradient [Manjón et al., 2008]. The binarisation of the denoised microscope images was performed by two different methods depending on the particle size. If the particle diameter was larger than 250 μm, the image was binarised by thresholding. If particle diameter was smaller 250 μm, the particle shape was first detected using the underlying edge and then the enclosed object was binarised.

The edge and centroid of the particle was detected, and the distance from centroid to each point on the edge was determined. The particle radius (r_P) was calculated from an average distance from the centroid to the edge points of the particle. The object properties (area, perimeter, minor axis and major axis of a fitted ellipsoid) were calculated. The analysis was implemented in Matlab (2019b, Mathworks, Massachusetts, USA), and the codes for the image analysis are given in Appendix A.1.

4.2.5 Swelling model

The swelling model in this study to extract characteristic swelling properties is based on the model from Sweijen et al. [2017a], which was originally developed for describing the swelling process of SAP particles. The absorption ratio (Q_i^{abs}) of each individual particle i is described by the mass of absorbed water (m_i^w) and the dry mass of the particle (m_i^s):

$$Q_i^{\mathrm{abs}} = \frac{m_i^w + m_i^s}{m_i^s} = \frac{r_p^3 \varrho_w}{r_{p,0}^3 \varrho_t} - \frac{\varrho_w}{\varrho_t} + 1. \tag{4.1}$$

$r_{p,0}$ is the initial particle radius, r_p is the particle radius at time t, ϱ_t is the density of a dry particle (true density) and ϱ_w is the density of the liquid (deionised water in this study).

The swelling of a particle is driven by the difference in chemical potential between the particle and water (liquid medium) Huyghe and Janssen [1997]. Therefore, it is assumed that the swelling is attributed to the diffusion of the liquid into the particle. The absorption rate can thus be described by [Sweijen et al., 2017a]

$$\frac{dQ_i^{\mathrm{abs}}}{dt} = K_i \left(\frac{Q^{\max} - Q_i^{\mathrm{abs}}}{Q_i^{\mathrm{abs}}} \right), \tag{4.2}$$

$$K_i = \frac{3 D r_p}{r_{p,0}^3}. \tag{4.3}$$

D (μm^2/s) is the diffusion coefficient for water molecules in the particle, which is assumed to be constant. $Q^{\max}$ is the maximum absorption ratio. For spherical particles and an incompressible liquid, Equation 4.2 can be rewritten in term of $\frac{dr_p}{dt}$ as function of r_p:

$$\frac{dr_p}{dt} = \frac{D \varrho_t}{r_p \varrho_w} \left(\frac{Q^{\max} - Q_i^{\mathrm{abs}}}{Q_i^{\mathrm{abs}}} \right). \tag{4.4}$$

4.3 Results and discussion

4.3.1 Particle characterisation

Material	D_{50} (μm)	S_{50}	ϱ_s (g/cm^3)	$Q^{\max}$ (g/g)
PH101	78 ± 1	0.73 ± 0.00	1.561 ± 0.003	1.45 ± 0.31
PH102	111 ± 1	0.75 ± 0.01	1.564 ± 0.008	1.38 ± 0.15
MCC500	662 ± 2	0.94 ± 0.00	1.441 ± 0.002	1.19 ± 0.06
MCC700	924 ± 6	0.94 ± 0.00	1.446 ± 0.002	1.20 ± 0.03
MCC1000	1215 ± 20	0.94 ± 0.00	1.437 ± 0.004	1.18 ± 0.02
CCS	54 ± 1	0.66 ± 0.01	1.403 ± 0.017	-
SSG	54 ± 1	0.87 ± 0.02	1.414 ± 0.001	-
L-HPC	79 ± 0	0.63 ± 0.00	1.136 ± 0.095	-

Table 4.1: Size, shape, density and maximum absorption ratio of the particles.

Table 4.1 shows the results from the particle characterisation including the particle size, sphericity, true density and maximum absorption ratio of the different materials. Unsurprisingly, MCC1000 has the largest particle size, while SSG and CCS have the smallest. The large MCC grades (MCC500–1000) are almost spherical ($S_{50} > 0.9$) and SSG particles are the most spherical of the disintegrants. CCS and L-HPC have a needle-like shape, which is in agreement with the literature [Desai et al., 2015]. MCC PH101 and PH102 have a similar cylindrical shape [Desai et al., 2015].

$Q^{\max}$ could only be measured for the different MCC grades as SSG formed a gel and CCS/L-HPC dissolved during the measurement. MCC500–1000 have very similar $Q^{\max}$ values and the relative difference between PH101 and PH102 is only 5%. Since the larger MCC grades (MCC500–1000) are made from MCC powder [Russell et al., 2018] through direct wet pelletisation or extrusion-spheronisation [Kleinebudde and Knop, 2007], a lack of difference in terms of $Q^{\max}$ between the smaller and larger MCC grades is not surprising. The results also indicate that the $Q^{\max}$ of the particle is primarily material dependent and is not affected by particle size.

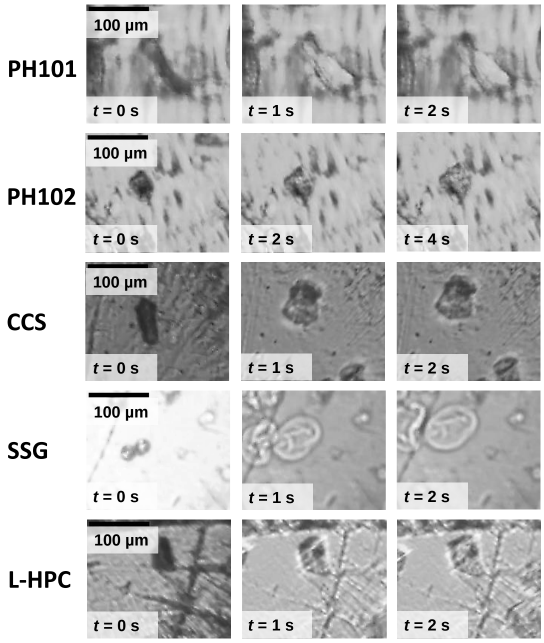

Figure 4.4: Microscope images of the disintegrant and PH101/PH102 particles from different time points during swelling. The time points were 0, 1 and 2 s for all materials except for PH102 where images were taken at 0, 2 and 4 s due to its slower swelling behaviour.

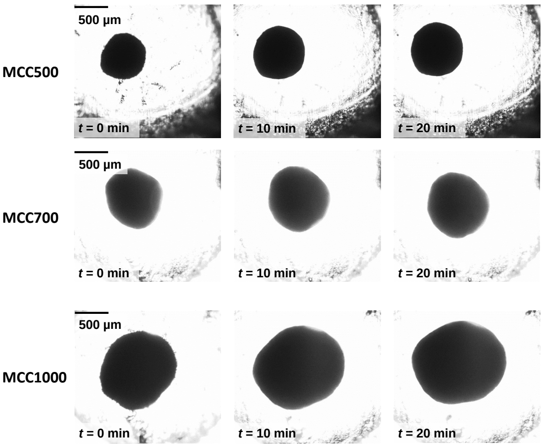

Figure 4.5: Microscope images of the MCC500-1000 particles from different time points during swelling. The time points were 0, 10 and 20 min for all materials.

4.3.2 Swelling of single particle

Swelling data

Figures 4.4 and 4.5 depict the images of a particle at different time points during the swelling process for the different materials. These images were processed (see Figure 4.3) to extract the change of radius as a function of time. The measured particle radius change, Δr, during swelling of different materials are given in Figure 4.6, which clearly indicate a varying swelling rate and also swelling capacity ($\Delta r^{\max}$), i.e. the maximum swelling of a particle.

The swelling capacity of the MCC particle indicates to be size dependent, since the larger MCC1000 particle showed the greatest swelling capacity followed by MCC700, MCC500, PH101 and PH102. D_{50} values (Table 4.1) shows that PH102 is larger than PH101 leading to different swelling profiles where PH101 swells 5 μm within 3 s and PH102 swells 4 μm within 6 s (Figure 4.6a).

Both L-HPC and CCS are modified cellulose with a significantly larger swelling capacity than MCC (Figure 4.6). L-HPC is a modified hydrophilic, water-insoluble cellulose (a low substituted form of cellulose ether), whereas CCS is a crosslinked carboxymethyl cellulose sodium [Desai et al., 2015]. The results indicate that SSG has the highest swelling capacity followed by CCS and L-HPC. This is in agreement with the results from Desai et al. [2012], Zhao and Augsburger [2005]. The results from Zhao and Augsburger [2005] showed that volume mean diameter change during swelling of SSG was greater than CCS. This is also in agreement with Desai et al. [2012] who demonstrated that the swelling of SSG compacts is greater than that of CCS compacts followed by L-HPC compacts. SSG is the sodium salt of cross-linked carboxymethylated starch, modified by two chemical processes: substitution to increase hydrophilicity and cross-linking to reduce solubility [Desai et al., 2015, Shah and Augsburger, 2002]. The high swelling capacity of SSG is due to the high spacing between cross-linking of the phosphate groups. The high spacing allows water penetration and swelling and facilitates gel formation [Rojas et al., 2012]. In contrast, the CCS cross-linking through esterification does not allow high spacing between polymer chain [Zarmpi et al., 2017] and thus has a

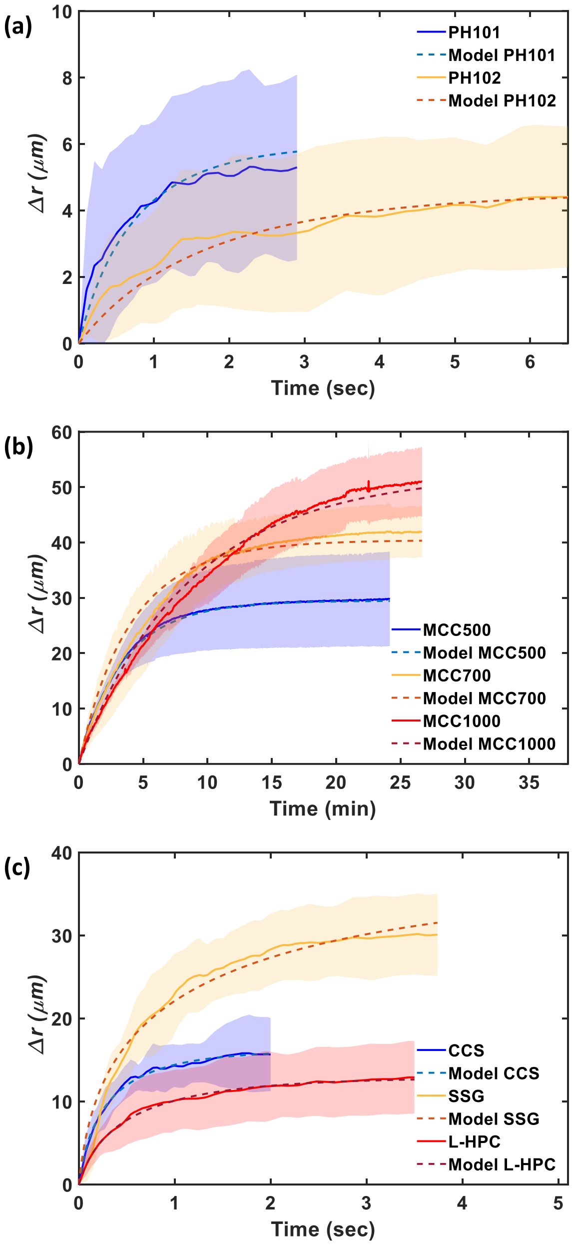

Figure 4.6: The measured change in radius, $\Delta r = r_p - r_{p,0}$, during particle swelling compared to the swelling model (Equation 4.4). (a) PH101 and PH102. (b) MCC 500, MCC700 and MCC1000. (c) L-HPC, CCS and SSG. The solid line and shaded area correspond to the average and standard deviation, respectively, of six particles.

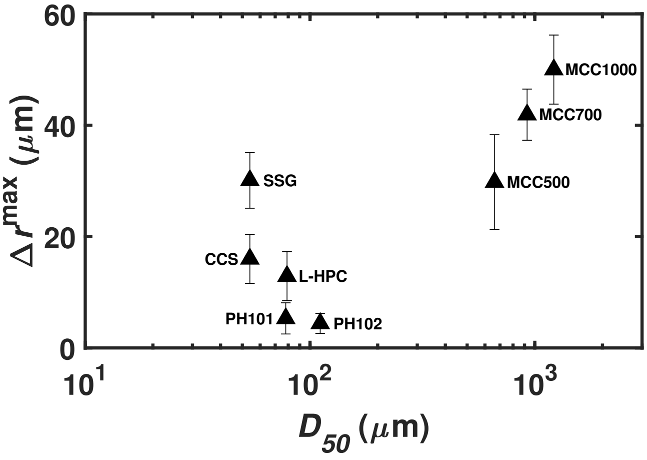

Figure 4.7: Swelling capacity, $\Delta r^{\max}$, as a function of the particle size, D_{50}.

lower swelling capacity as seen in Figure 4.6c.

The particle swelling process consist of two mechanisms: water uptake at the particle surface and the swelling ability of the particle. Since SSG has a relatively slow initially swelling, the surface water uptake of SSG is low. The hydration of SSG is driven by the interaction between the anionic carboxyl group and water [Zhao and Augsburger, 2005]. CCS, however, shows a fast swelling: it swells 14 μm in the first 0.8 s and swells further 2 μm within the next 1.6 s. The swelling of CCS is driven by the hydration of the carboxymethyl group [Zarmpi et al., 2017].

Quantification of swelling characteristics

Characteristic swelling properties were determined for each material to analyse the swelling-controlling mechanisms, i.e. diffusion- or absorption capacity-limited swelling. The swelling model (Equation 4.4) was used to extract the diffusion coefficient for all materials and determine the maximum absorption ratio for the disintegrants from the experimental data (Figure 4.6). For a particle with a small diffusion coefficient, the swelling process was limited by the diffusion of water into a spherical particle. For a particle with a small maximum absorption ratio, the swelling process is limited by the particles liquid absorption capacity.

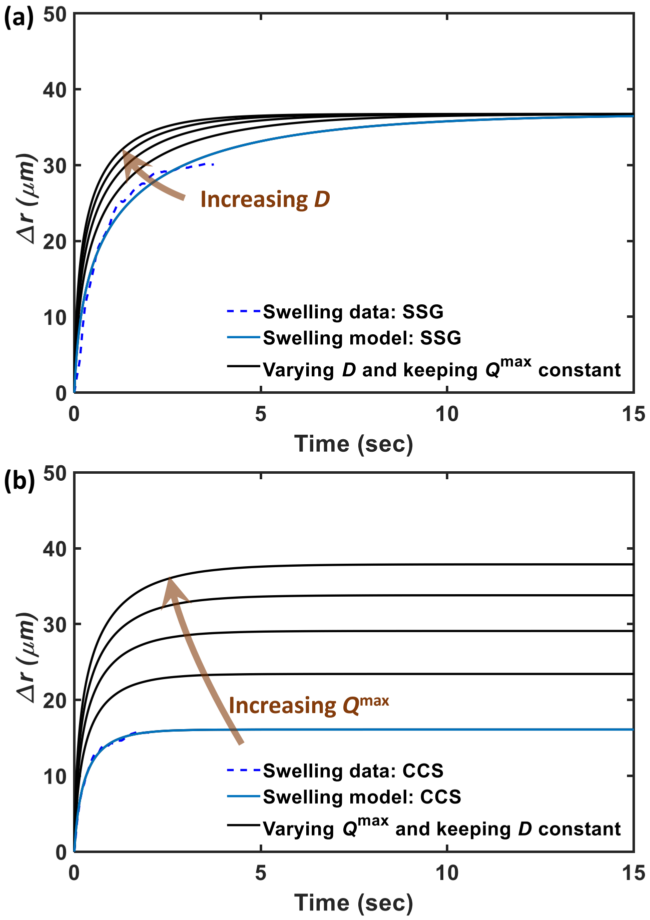

Figure 4.8: Simulations of swelling profiles using Equation 4.4 and experimental data (average profiles) of SSG and CCS particles. a) D is varied from 231.14 μm^2/s to 739.75 μm^2/s with uniform increments of 127.15 μm^2/s. $Q^{\max}$ is kept constant at 10.04 g/g. b) $Q^{\max}$ is varied from 3.16 g/g to 10.94 g/g with uniform increments of 1.72 g/g. D is kept constant at 739.75 μm^2/s.

Material	$Q^{\max}$ (g/g)	D (μm^2/s)	$\Delta r^{\max}$ (μm)	RMSE(μm)
PH101	-	396.39	5.3	0.35
PH102	-	134.68	4.4	0.38
MCC500	-	194.95	29.8	0.26
MCC700	-	279.28	41.9	1.81
MCC1000	-	273.70	50.0	1.30
CCS	3.16	739.75	16.0	0.25
SSG	10.04	231.14	30.1	1.28
L-HPC	3.19	392.61	12.9	0.18

Table 4.2: Characteristic swelling properties (maximum absorption ratio, $Q^{\max}$; diffusion coefficient, D; swelling capacity, $\Delta r^{\max}$) extracted from the experimental data (Figure 4.6) and the swelling model (Equation 4.4). Root mean squared error (RMSE) was calculated to assess the accuracy of the fit between the swelling model and experimental data.

Considering that only D was fitted, and the other parameters were measured experimentally, the swelling model captures the behaviour of the different MCC grades very well (see RMSE in Table 4.2). The RMSE is also small for the different disintegrant materials, where both D and $Q^{\max}$ were fitting parameters. The largest RMSE for the disintegrants was observed for the SSG.

$Q^{\max}$ and D of the different materials are given in Table 4.2. $Q^{\max}$ for the MCC grades is provided in Table 4.1 as these values were measured following the procedure described in section 4.2.2. The high $Q^{\max}$ value of SSG is attributed to the high spacing, which can be occupied by the water [Rojas et al., 2012, Zarmpi et al., 2017]. The $Q^{\max}$ value of CCS and L-HPC are similar as they are both modified cellulose materials. The $Q^{\max}$ values of the different MCC grades are relatively close to each other. The results overall indicate that $Q^{\max}$ primarily depends on the material characteristics and is not influenced by the particle size/shape. The diffusion coefficient, D is higher for CCS due to its fast hydration characteristics [Zarmpi et al., 2017]. There is a significant difference between D of PH101 and PH102, where both the size and the moisture content can affect the diffusivity of water in the particle.

The diffusion coefficient of SSG is significantly smaller than that of the other disintegrants, while it has the highest absorption capacity. This means that the swelling process of SSG is limited by the diffusion of liquid into the particle. CCS has a relatively high diffusion coefficient, which results in a faster initial swelling. Since the absorption capacity of CCS is relatively small compared to SSG, the swelling process of CCS is limited by its liquid absorption capacity. The absorption capacity of L-HPC is similar to the one of CCS, but its diffusion coefficient is between the values of SSG and CCS. L-HPC is thus categorised as diffusion and absorption capacity-limited swelling.

Simulations using Equation 4.4 (Figure 4.8) were conducted to gain a better understanding of the effect of D and $Q^{\max}$ on the swelling profile. An increase in D, while keeping $Q^{\max}$ constant, accelerates the particle swelling process (Figure 4.8a). The diffusion coefficient thus primarily affects the swelling rate and not the swelling capacity ($\Delta r^{\max}$). On the contrary, increasing $Q^{\max}$ leads to an increase in the swelling capacity and does not affect the initial swelling rate (see Figure 4.8b).

The swelling capacity increases with increasing particle size for the MCC500–1000 particles (Figure 4.7). This is attributed to the fact that these MCC grades are agglomerates of smaller MCC particles and the MCC content therefore increases with size. This also results in a much larger swelling capacity for the MCC500–1000 compared to the PH101 and PH102 grades.

Not only the swelling capacity affects the disintegration of a tablet, but also the initial swelling rate which is driven by the water uptake rate. Considering that the majority of pores in a tablet are $< 10\mu$m [Markl et al., 2018a, 2017a, Ridgway et al., 2017], the particles will induce stress on the interparticle bonds at an early stage in the swelling process. The initial swelling rate driven by the uptake of liquid on the particle surface might thus be the rate-determining process for tablet disintegration. The particle swelling needed to break up the tablet depends on both the pore size and the strength of the interparticle bonds.

The results indicate that SSG has the largest $Q^{\max}$ but smallest D of the three disintegrants studied. When comparing the results of single particles to the swelling behaviour of a powder compact, the exact formulation and microstructure of a tablet needs to be considered. Quodbach et al. [2014a] measured how the disintegration time of dibasic calcium phosphate tablet is affected by the used disintegrant and Botzolakisi and Augsburger [1988] measured the swelling and liquid uptake rate of pure disintegrant compacts. Both indicated that the use of CCS results in faster tablet disintegration compared to a SSG tablet. Considering that the average pore size of tablets are $< 10\mu$m [Markl et al., 2018a, 2017a, Ridgway et al., 2017], most interparticle bonds will be interrupted before the particles reach their maximum swelling capacity. The initial particle swelling, and not the swelling capacity of the particles, thus may drive the disintegration process. CCS particles have a higher initial swelling rate compared to SSG tablets even though the SSG swelling capacity is larger. This higher initial swelling rate can thus result in a faster disintegration of a tablet. However, the prediction of the swelling and disintegration behaviour of a powder compact from single particle information requires a better understanding of the interplay between the particle properties, tablet microstructure, the liquid uptake dynamics and the interparticle bonding.

4.3.3 Anisotropic swelling

The microscope images in Figure 4.4 indicate that the swelling process is not isotropic for all particles. This is particularly obvious for PH101, where the particle shape changes from a needle- to bottle-like shape during swelling. Such an anisotropic swelling is also reflected in facet-dependent characteristic particle swelling properties. D, $Q^{\max}$ and $\Delta r^{\max}$ were thus estimated along the minor ($r_{p,\text{minor}}$) and major ($r_{p,\text{major}}$) axes for the non-spherical ($S_{50} < 0.9$) particles (Figure 4.9).

In the majority of cases, D, $Q^{\max}$ and $\Delta r^{\max}$ values of r_p lay between that of $r_{p,\text{minor}}$ and $r_{p,\text{major}}$. The diffusion of the water into the particles is generally faster along its larger axis. In contrast, the maximum absorption ratio is larger for the smaller particle axis for the disintegrants, while it does not change for PH101 and PH102 particles. In terms of swelling capacity, there is not a noticeable trend across the materials studied. The swelling capacity of SSG is clearly larger along the major axis, while it decreases for CCS from the minor to the major axis. The difference in terms of swelling capacity between the minor and major axes is not significant for PH101, PH102 and L-HPC.

The anisotropic swelling behaviour of PH101, PH102, CCS, SSG and L-HPC is attributed to its fibrous structure [Desai et al., 2015, Krishnamoorthy et al., 2013, Sunada and Bi, 2002, Thoorens et al., 2014]. Fibrous materials mainly swell anistropical [Pre-

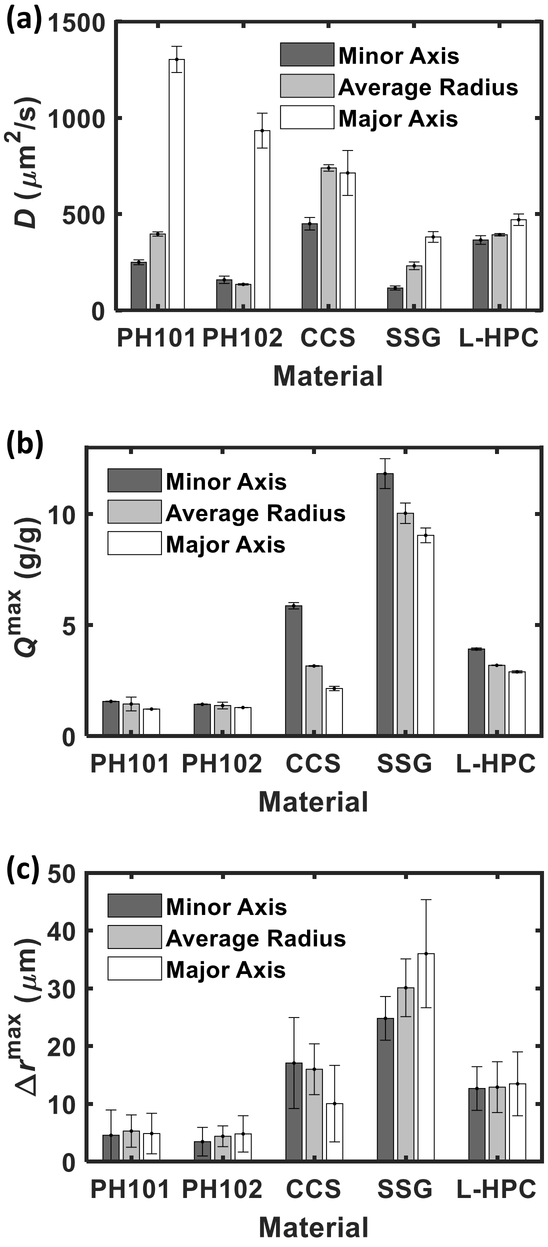

Figure 4.9: Anisotropic swelling analysis for PH101/PH102 and the three disintegrants. The a) diffusion coefficient, D, b) maximum absorption ratio, $Q^{\max}$, and c) swelling capacity, $\Delta r^{\max}$, were extracted for the swelling using the average particle radius, r_p, the semi-minor axis, $r_{p,\text{minor}}$, and the semi-major axis, $r_{p,\text{major}}$, for each material. A 95% confidence interval for the fitted parameters, D and $Q^{\max}$, is also shown.

ston and Nimkar, 1949] as they prefer to orientate their linear macromolecules parallel to the fibre axis. The more aligned the macromolecules are, the more these materials swell anistropically.

4.4 Conclusion

The in-situ monitoring of the expansion of single particles paired with a model facilitated the quantification of the swelling of eight pharmaceutical materials. The results clearly highlighted the different swelling behaviour for the various materials, where the swelling capacity (maximum swelling of particle) of the disintegrants follows SSG > CCS > L-HPC and MCC1000 > MCC700 > MCC500 > PH101 > PH102 for the MCC grades. CCS has the highest diffusion coefficient with D = 739.70 µm^2/s due to high initial hydration and SSG has the highest maximum absorption ratio with $Q^{\max}$ = 10.04 g/g due to high spacing between the cross-linking. In summary for the disintegrants, the swelling performance of SSG is liquid uptake ability limited, whereas it is absorption capacity limited for CCS and L-HPC. The anisotropic swelling is significant for PH101 and PH102 in terms of its diffusion of liquid ability with a relative change of 423% and 457% for D from the minor to major particle axes for PH101 and PH102, respectively. The absorption capacity considerably depends on the particle facet for CCS, where the relative change of $Q^{\max}$ is -45% from the minor to major particle axes. The swelling of single XPVP particles were also studied. However, the results did not reveal any swelling exceeding the resolution limit of the used experimental setup. XPVP in a tablet is described as a strain recovery process [Desai et al., 2012, Quodbach and Kleinebudde, 2014], which is primarily controlled by the compaction process.

Considering the large concentration of MCC in a typical formulation, MCC contributes significantly to tablet swelling and the disintegration process. It is therefore crucial to understand the swelling characteristics of all excipients to predict the swelling of a tablet and hence be able to rank different formulations in terms of disintegration performance.

Quantifying the swelling characteristics of single particles will contribute to a better rational design of a formulation for oral solid dosage forms. It is particularly critical for modelling the tablet disintegration process, where particle swelling is a key performance-controlling mechanism.

In terms of future work, the method presented in this study can be used to measure the swelling of a single particle at different temperatures and dissolution media (e.g. biorelevant media) to better understand the impact of the liquid on the swelling process. Data of single particle swelling at various relevant fluids and temperatures can improve the understanding of variations in the disintegration time in response to liquid temperature changes [Basaleh et al., 2020] and other fluid characteristics.

Furthermore, coupling a swelling model of the materials used in a formulation with liquid transport models [Markl et al., 2017b] will enable the development of a disintegration model. Such a product model can be used to inform formulators to make rational decisions about the formulation and the manufacturing settings.

In this study, a new method was developed to quantify the swelling of single pharmaceutical particles, by using an optical microscope coupled with a bespoke flow cell. A single particle swelling model was utilised to characterise diffusion coefficient, maximum liquid absorption ratio and swelling capacity. Compared to previous studies, most of them focused on the swelling of powder compacts of the materials discussed in this work. For example Berardi et al. [2018], Botzolakisi and Augsburger [1988], Desai et al. [2012], Rojas et al. [2012], Zhao and Augsburger [2005] quantified the swelling of disintegrants in powder compacts or suspensions. In powder compacts other factors can affect the swelling capacity and the process, such as liquid penetration rate, diffusion of liquid between particles, pore size, inter-particle bonds and deformation of particles. There are few studies conducted on quantifying swelling of single particles [Gasmi et al., 2015, Rudnic et al., 1982].

Chapter 5

Modelling the evolution of pore structure during the disintegration of pharmaceutical tablets

Chapter Summary

This chapter assessed the changes in the pore structure during disintegration by coupling discrete element method (DEM) with a single-particle swelling model and experimental liquid penetration data. First, the compaction of the powders were simulated using DEM. This delivers a 3D discrete element model of the tablet, which is then used to simulate the tablet swelling utilising a single-particle swelling model. The contents of this chapter have been published in Pharmaceutics, see [Soundaranathan et al., 2023].

5.1 Introduction

About 90% of orally consumed pharmaceutical products [Indurkhya et al., 2018] are administered in the form of a tablet to deliver the active pharmaceutical ingredient (API) [Sugimori, 2015]. The most-common tablets are manufactured by compacting a formulated powder blend that is composed of one drug substance and a number of different excipients [Kadiri et al., 2005]. The physical and mechanical properties of tablets, such as porosity and mechanical strength, are significantly affected by the selected formulation and the process conditions used to make the tablet compact [Cunningham et al., 2004]. The compaction of the powder blend is of critical importance for the particle–particle interaction, as the particles experience intensive deformation during compaction and start to bond together through van der Waals forces, mechanical interlocking, and the formation of solid bridges [Wu et al., 2008].

The physical properties and mechanical strength of the tablet control its disintegration behaviour, which is critical for dissolving and enabling the absorption of the drug substance into the blood stream. The tablet disintegration process consists of multiple connected and interdependent mechanisms: liquid penetration, swelling, dissolution of excipients and drug, and break-up. The importance of each process depends on the formulation and process conditions used. One of the most-critical processes is the liquid penetration through the porous tablet structure, which initiates the swelling of the particles in the tablet. This swelling builds up an internal stress, which causes the break up of the tablet into smaller agglomerates and primary particles [Markl and Zeitler, 2017, York, 2022]. For the tablet to disintegrate, the internal swelling stress must exceed the strength of the bonds that are formed during compaction [Markl and Zeitler, 2017]. The liquid penetration rate is strongly influenced by the tablet porosity, i.e., it generally increases with increasing porosity [Al-Sharabi et al., 2020]. In many cases, liquid penetration is the controlling mechanism for tablet disintegration, i.e., the time it takes for the tablet to disintegrate highly depends on the liquid uptake. It is important to note that there is a strong interdependence between these different disintegration mechanisms, e.g., particle swelling will cause a change of the pore structure, which will directly affect the liquid penetration process [Markl and Zeitler, 2017].

During the development of a drug product, the formulation and process conditions must be selected to deliver a tablet with the desired properties in terms of its strength, content, and disintegration/dissolution performance. This typically requires a large number of experiments for every new product to explore the relationship between material attributes, process conditions, and performance behaviour in order to identify suitable and robust conditions for the final product. In the last decade, digital design approaches have been developed and deployed to reduce experimental effort and assist in the decision-making throughout the development cycle of new medicines [Kalaria et al., 2020].

Wilson et al. [2011] developed a population model to describe the rate of break-up of a tablet into particles and their size distribution coupled with the Noyes–Whitney equation to predict the dissolution of particles. Masoodi and Pillai [2010] developed a mathematical model based on Darcy's law describing the wicking and swelling of paper by considering a dynamic change of porosity. Markl et al. [2017b] modified this model based on an empirical equation from Schott [1992a] for microcrystalline cellulose (MCC) particles to describe the tablet swelling and also the liquid penetration kinetics. Markl et al. [2017b] simplified the swelling of a tablet enlargement in the axial direction only to match their experimental setup. They showed that the capillary radius, R_c, decreases with increasing swelling. They assumed that the fractional increase in the volume of the wetted compacted powder was equal to the fractional increase in the volume of a single wetted particle.

Several studies demonstrated the use of discrete element modelling (DEM) to simulate the tablet compaction process and extract information on the interparticle forces and porosity and other properties affecting the tablet performance [Gao et al., 2021, Garner et al., 2018, Haustein et al., 2017, Nordström et al., 2018, Persson and Frenning, 2012, 2015, Thakur et al., 2014a]. DEM is a particle-scale numerical method for modelling the bulk behaviour of granular materials. Many geomaterials such as coal, ores, soil, rocks, aggregates, pellets, tablets, and powders can be described by this method. DEM enables the investigation of the interaction of individual particles and the interparticle effects (stresses, deformation, thermal conductivity, creep). The most-essential element of a DEM model is the underlying particle contact model. The particle contact model is used to calculate the forces acting on particle–particle and particle–wall contacts. Both contact modes can be modelled by the same model. However, the material properties (e.g., coefficient of restitution, friction coefficient, etc.) for each contact type can differ in order to model dissimilar materials. The particle motion is calculated from the force a particle experiences based on these contact models [Ketterhagen et al., 2009]. Common contact models applied for tablet compaction simulation include the Luding elasto-plastic model [Luding, 2008], Storåkers model [Storåkers et al., 1997], and Hertz–Mindlin theorem [Johnson and Johnson, 1987]. Recent studies from Gao et al. [2021] and Toson et al. [2021] showed that the Luding model is suitable for pharmaceutical materials.

DEM has also been used to model the disintegration process of tablets with the ultimate goal of predicting the drug release [Kalný et al., 2021, Kimber et al., 2012]. Kalný et al. [2021] simulated the disintegration and dissolution of a two-component tablet with ibuprofen as the API and croscarmellose sodium (CCS) as a disintegrant. They assumed that only the CCS particles contribute to the total swelling and the swelling was only occurring in the axial direction. They simplified the swelling by assuming that all particles swell simultaneously and at a constant rate, i.e., the liquid penetration behaviour was not considered. Kimber et al. [2012] developed a model for simulating the swelling and dissolution process of a polymer tablet by incorporating the Fickian diffusion of water into a particle in their DEM model. The particle was assumed to be cylindrical with swelling only occurring in the radial direction. Schütt et al. [2021] developed a model to simulate tablet disintegration in the human ascending colon using a discrete multiphysics approach coupled with a smoothed particle hydrodynamics and lattice spring model.

Studies from other fields, such as hydrogeology [Sweijen et al., 2017a, 2020], have used DEM to simulate similar processes. Sweijen et al. [2017a] and Sweijen et al. [2020] applied DEM to simulate the swelling of superabsorbent polymer particles (SAPs) with an integrated liquid penetration model. Sweijen et al. [2017a] simulated the swelling of a bed of SAPs using a single-particle swelling model combined with the pore finite volume method to model the liquid flow in the compacts. They developed this model further [Sweijen et al., 2020], where the unsaturated flow was computed using a scheme of an implicit pressure solver and an explicit saturation update.Braile et al. [2022] developed a DEM model for the swelling of granular materials (MCC PH101, rice, and superabsorbent particles), and they simulated the swelling of the material using the first-order kinetics equation to model the swelling of single particles and the materials soaking in water.

In existing studies on tablet disintegration, the pore structure change during the disintegration process and the effect of the dynamically changing pore structure on the disintegration time are not fully understood. This study assessed the changes in the pore structure during disintegration by coupling DEM with a single-particle swelling model and experimental liquid penetration data. First, the compaction of the powders were simulated using DEM with the Luding contact model [Luding, 2008]. This delivers a 3D discrete element model of the tablet, which is then used to simulate the tablet swelling utilising a single-particle swelling model [Soundaranathan et al., 2020]. The use of the coupled model is demonstrated for pure MCC tablets with three porosities and MCC with three different concentrations of CCS. The model was validated against the experimental results.

5.2 Materials and Methods

5.2.1 Materials

The materials analysed in this study included MCC PH101 (Avicel PH101, Roquette, Lestrem, France) and the disintegrant croscarmellose sodium (Ac-Di-Sol, CCS, SDW-802, FMC International, Philadelphia, USA). MCC, in particular grade PH101, was selected as a model compound as it is one of the most commonly used excipients in the pharmaceutical industry. The values of particles' properties are given in Tables 5.1 and 5.2. The particle size and sphericity were measured by QICPIC (Sympatec GmbH, Clausthal-Zellerfeld, Germany). The true density of the material was measured by a

Material	D_{50} (μm)	ϱ_s (kg/m^3)	S_{50}	$Q^{\max}$ (g/g)	D (μm^2/s)
PH101	78 ± 1	1561 ± 3	0.73 ± 0.00	1.45 ± 0.31	396.39
CCS	54 ± 1	1403 ± 17	0.66 ± 0.01	3.16	739.75

Table 5.1: Values of the particle properties: size (D_{50}), true density (ϱ_s), shape (S_{50}), liquid absorption ($Q^{\max}$), and diffusion coefficient (D) of the two materials (obtained from Soundaranathan et al. [2020]).)

Material	D_{10} (μm)	D_{50} (μm)	D_{90} (μm)
PH101	45 ± 1	78 ± 1	135 ± 1
CCS	33 ± 1	54 ± 1	90 ± 1

Table 5.2: Particle size distribution of the two materials (obtained from Soundaranathan et al. [2020])

helium pycnometer (MicroUltrapyc 1200, Quantachrome instrument, Graz, Austria).

5.2.2 Experimental

Tablet Compaction

These tablet were prepared via direct compression using a compaction simulator (HB50, Huxley-Bertram Engineering, Cambridge, U.K.). The samples had a diameter of 10 mm and a thickness around 2 mm. The diameter and thickness were kept constant, while the filling weight of the powder material was adjusted to vary the tablet porosity. The powder was filled manually into the die of the compaction simulator to achieve precise powder filling. The compaction process was performed using a sinusoidal compaction profile, with an average speed of 0.026 m/s. The formulations of the tablets, the compression pressure, and the porosity values are given in Table 5.3.

Material	c_{PH101} ($\%w/w$)	Material	c_{CCS} ($\%w/w$)	σ (MPa)	ϵ (%)
PH101	100	-	-	387	10
PH101	100	-	-	170	15
PH101	100	-	-	105	22
PH101	98	CCS	2	162	15
PH101	95	CCS	5	162	15
PH101	92	CCS	8	158	16

Table 5.3: Tablet formulations (PH101 concentration, c_{PH101}; CCS concentration, c_{CCS}), compaction pressure (σ) and porosity (ϵ) investigated.

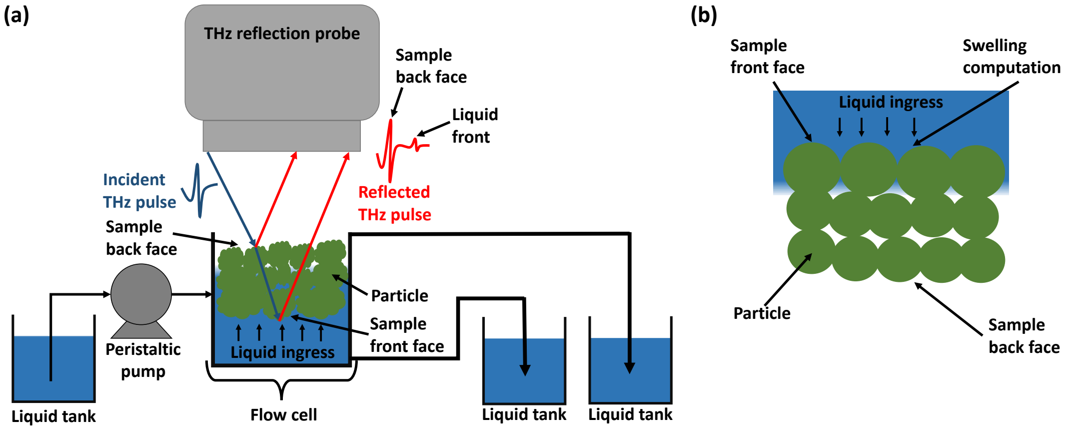

Figure 5.1: A schematic of the (a) experimental and (b) DEM modelling domain.

Liquid Penetration & Tablet Swelling

The liquid penetration and tablet swelling were measured using a commercial terahertz pulsed imaging system (TPI, TeraPulse 4000, Teraview Ltd., Cambridge, UK) in combination with a bespoke flow cell [Al-Sharabi et al., 2021]. The TPI was set up with a fibre-based reflection probe equipped with an 18 mm focal length silicon lens. The probe head was on a linear scale for ease of spatial adjustment. The beam resulting of the THz optics had a beam waist of around 1 mm at the focus with an incident angle of 13°. The TPI setup with the flow cell (Figure 5.1 (a)) measures the change of the back face of the tablet which reflects the swelling of both the back face and the front face where the liquid uptake occurs. Since the flow cell was not included in the DEM simulation (Figure 5.1 (b)), only the front face swelling was recorded in the simulation. More details about the flow cell and its design can be found in [Al-Sharabi et al., 2021]. The experimental procedure and THz in general are described in Section 3.3.

5.2.3 Modelling

Figure 5.2 depicts a diagram summarising the integration of the models and experimental data to simulate tablet swelling and break-up. The tablet swelling and break-up model consists of three main parts: (1) tablet compaction model in DEM, (2) disintegration model in DEM with a single-particle swelling model [Soundaranathan et al., 2020],

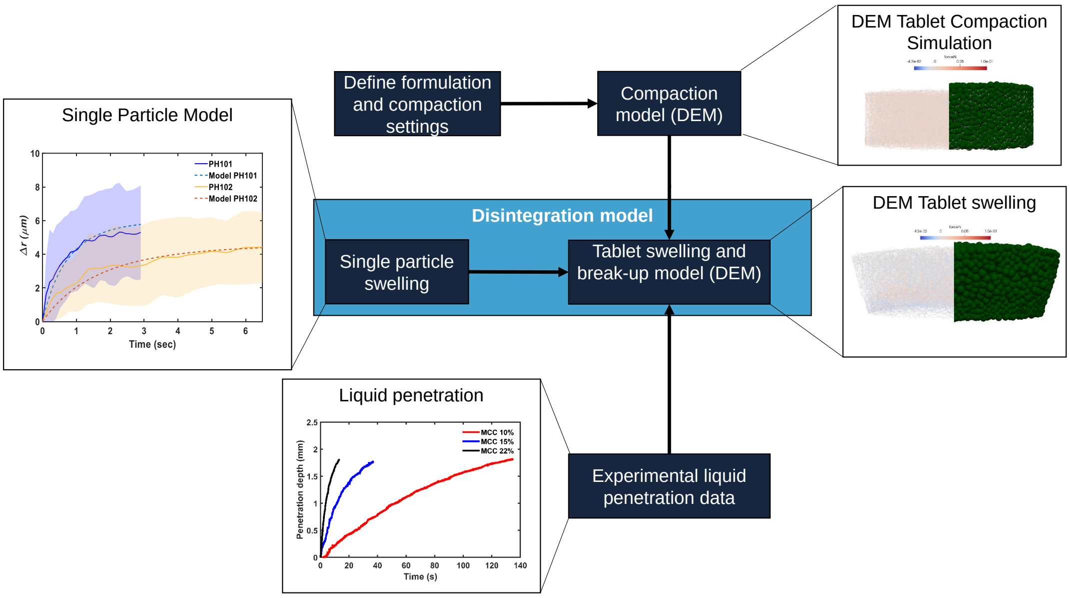

Figure 5.2: Work flow of the tablet swelling and break-up model. A single-particle model, DEM tablet compaction model, and experimental liquid penetration data are combined to model the swelling and break-up process.

and (3) experimental liquid penetration data. Both compaction and disintegration models were implemented in the open-source DEM software Yade-DEM [V. Smilauer et al., 2021].

Tablet compaction

The compaction process was simulated by compressing the particles, which were assumed to be spherical under gravity, to a loose, random packing in a cylindrical compression die with a height of 3 mm and a radius of 1 mm. To decrease the computational cost, the simulated tablet was scaled down to a diameter of 2 mm and a thickness of 0.8–1 mm while using the experimental particle size distribution (Table 5.2) in the DEM. The concentration of each material, the compression force, and the punch speed were set according to the experimental setup described in Section 5.2.2 and Table 5.3. The number of particles simulated for each formulation is given in Table 5.4. The compression force and porosity were recorded during the simulation.

The Luding elasto-plastic contact model [Luding, 2008] was applied for particle–

Formulation	Number of particles PH101	Number of particles CCS
PH101, ϵ_0 = 10 %	11,117	-
PH101, ϵ_0 = 15 %	10,426	-
PH101, ϵ_0 = 22 %	9,720	-
PH101/CCS, c_{CCS} = 2	10,134	720
PH101/CCS, c_{CCS} = 5	9,699	1778
PH101/CCS, c_{CCS} = 8	9,335	2828

Table 5.4: The number of particles simulated for each formulation.

particle and particle–wall interactions; the model is given in Equations (5.1)–(5.3). The force in the normal direction, $\mathbf{F}_\mathrm{n}$, is given as

$$\mathbf{F}_\mathrm{n} = \begin{cases} k_1\delta_\mathrm{n} & \text{if } k_2(\delta_\mathrm{n}-\delta_0) \geq k_1\delta_\mathrm{n} \\ k_2(\delta_\mathrm{n}-\delta_0) & \text{if } k_1\delta_\mathrm{n} \geq k_2(\delta_\mathrm{n}-\delta_0) \geq -k_\mathrm{c}\delta_\mathrm{n} \\ -k_\mathrm{c}\delta_\mathrm{n} & \text{if } -k_\mathrm{c}\delta_\mathrm{n} \geq k_2(\delta_\mathrm{n}-\delta_0). \end{cases} \tag{5.1}$$

with k_1 as the loading stiffness, k_2 as the plastic unloading stiffness, k_c as the adhesion stiffness, δ_n as the normal overlap and δ_0 as the plastic contact deformation overlap. k_2 is defined as

$$k_2 = \begin{cases} k_\mathrm{p} & \text{if } \delta_\mathrm{max}/\delta_\mathrm{lim} \geq 1 \\ k_1 + \frac{(k_\mathrm{p}-k_1)\delta_\mathrm{max}}{\delta_\mathrm{lim}} & \text{if } \delta_\mathrm{max}/\delta_\mathrm{lim} < 1. \end{cases} \tag{5.2}$$

Where k_p is the limit plastic unloading stiffness. δ_max and δ_lim (see Equation 5.3) are the maximum compression overlap and the plastic limit, respectively.

$$\delta_\mathrm{lim} = \frac{k_\mathrm{p}}{k_\mathrm{p}-k_1}\phi_\mathrm{f}R^*, \tag{5.3}$$

where ϕ_f is dimensionless plasticity depth and R^* is an equivalent radius. The values of parameters used in this study are given in Table 5.5.

Gao et al. [2021] showed that the parameters k_1 (loading stiffness) and k_p (limit plastic unloading stiffness) of the Luding elasto-plastic model and the particle density impacted the compression profile mostly and the adjustment of these three parameters could cover most of the variations of the compression profile. As Gao et al. [2021] in-

Properties	Value
k_1	10,000 N/m
k_p/k_1	14
k_c/k_1	0.1[1]
ϕ_f	0.999[1]
Simulation time step (Δt)	$1 \cdot 10^{-8}$ s
Angle of repose, PH101	0.41 rad[2]
Angle of repose, CCS	0.69 rad[3]

Table 5.5: Summary of the DEM parameters used for all simulations. k_1 and k_p were identified through an optimisation procedure. [1] [Gao et al., 2021], [2] [Suryadi et al., 2018], [3] measured experimentally.

creased the particle size in the model compared to the experiments, they accounted for this in the model by calibrating the particle density. In this work, the particle size in the model was the same as in the experiments, and hence, the measured particle (true) density was used for the simulations.

The two unknown parameters in the model, k_1 and k_p, were determined through an optimisation procedure that minimises the error between the porosity values calculated from the DEM model and the experimental data. For the pure MCC tablets, this was performed for the medium compression pressure (15% porosity tablets) and was validated using the data from the experiments with low- and high-compression pressure. The calibration method was based on the work of [Gao et al., 2021]. As k_1 only affects the loading stage of the compaction process, the process was simulated for various different values of k_1, ranging from 500 to 20,000 N/m, simultaneously using the batch simulation mode in Yade. The root-mean-squared error (RMSE) between the experimental tablet porosity and simulated tablet porosity during loading for various k_1 values was minimised to identify the optimal value. Thakur et al. [2014a] highlighted that the difference between initial experimental porosity and that of a simulated DEM tablet is primarily caused by the deviation of the real particle shape from the assumed spherical shape in the DEM. Other factors affecting the initial packing of the powder such as intra-particle porosity and surface asperities were also not considered in the DEM. This difference in initial porosity caused an error in the estimation of k_1. To minimise the effect of this initial difference in the packing of the powder, the porosity in the loading process was scaled to a value between 0 (minimum observed porosity) and 1 (maximum observed porosity) and the calculated RMSE values were used to determine the optimal k_1 value. This scaling significantly improves the estimation of k_1 as this parameter primarily controls the curvature of the loading profile. k_p was calibrated using the optimised k_1 value, and we simulated the process again at different k_p to reach the final desired tablet porosity.

Disintegration model

The simulations of the swelling of the tablets modelled in Section 5.2.3 was set up to closely mimic the experimental work described. The time step (Δt) was set at 10^{-6} s/step, it was selected based on critical time step, Δt,crit, calculation. Which is given as Δt,crit = $2\sqrt{m_p/k_c} = 2{\cdot}10^{-6}$ s/step [Otsubo et al., 2017], where m_p is the particle mass. The time step was selected to be close possible to Δt,crit and also ensuring simulation stability. The radius, mass, and inertia of individual particles were updated according to a single-particle swelling model (Equations (5.4)–(5.12)). Sweijen et al. [2017a] originally derived this model to describe the swelling process of SAPs. The model assumes that the swelling of a particle is driven by the difference in the chemical potential between the particle and water (liquid medium) [Huyghe and Janssen, 1997]. The single-particle swelling model is given as follows:

$$\frac{dr_\mathrm{p}}{dt} = f_\mathrm{w}\frac{D\varrho_\mathrm{s}}{r_\mathrm{p}\varrho_\mathrm{w}}\left(\frac{Q^\mathrm{max} - Q_\mathrm{i}^\mathrm{abs}}{Q_\mathrm{i}^\mathrm{abs}}\right), \tag{5.4}$$

$$Q_\mathrm{i}^\mathrm{abs} = \frac{m_\mathrm{i}^\mathrm{w} + m_\mathrm{i}^\mathrm{s}}{m_\mathrm{i}^\mathrm{s}} = \frac{r_\mathrm{p}^3\varrho_\mathrm{w}}{r_\mathrm{p,0}^3\varrho_\mathrm{s}} - \frac{\varrho_\mathrm{w}}{\varrho_\mathrm{s}} + 1. \tag{5.5}$$

where $r_\mathrm{p,0}$ is the initial particle radius, r_p is the particle radius at time t, ϱ_s is the density of a dry particle, and ϱ_w is the density of the liquid (deionised water in this study). D (μm^2/s) is the diffusion coefficient for water molecules in the particle, which was assumed to be constant. Q^max is the maximum absorption ratio. The values of D (μm^2/s) and Q^max for the various materials used in this study were taken from Soundaranathan et al. [2020] and are given in Table 5.1.

This model assumes that the entire particle is exposed to the liquid, which is not valid when the particle is part of a compact tablet. In a compact tablet, particles form bonds with neighbouring particles across a contact area. This reduces the effective (available) surface area of the particle that is exposed to the absorbing liquid. This is accounted for by introducing the factor f_w in Equation 5.4 that describes the fraction of the available surface (A_actual) to the total particle surface area ($A_p = 4\pi r_p$).

$$f_\mathrm{w} = \frac{A_\mathrm{actual}}{A_\mathrm{p}}. \tag{5.6}$$

A_actual is defined as the particle surface area subtracted by the sum of the overlapping area with neighbouring particles:

$$A_\mathrm{actual} = A_\mathrm{p} - \sum_i^n A_\mathrm{cap}, \tag{5.7}$$

A_cap is the surface area of the normal displaced volume between two neighbouring particles, particle i and j, and is given as a function of the particle, i centroid, x_i, y_i, z_i and coordinate of the contact point between i and j (x_j, y_j, z_j). n is the number of neighbouring particles. A_cap is can be given as

$$A_\mathrm{cap} = 2\pi r_\mathrm{p} h, \tag{5.8}$$

with h as the height of the overlapping cap defined as

$$h = r_\mathrm{p} - \sqrt{(x_\mathrm{j} - x_\mathrm{i})^2 + (y_\mathrm{j} - y_\mathrm{i})^2 + (z_\mathrm{j} - z_\mathrm{i})^2}. \tag{5.9}$$

Figure **??** analysed the effect the time step for updating the liquid position has on the swelling time and profile. The liquid position was updated at every 10,000th, 50,000th and 100,000th time step, the results showed that the time step does not have a signficant impact on the results. Since higher time steps reduced the computational time, was the position of the liquid updated every 100,000th time step using the experimental data. As the time instances of the experimental liquid penetration data did not match the simulation time points, a power law ($y = a \cdot t^b$) was fit to the experimental results from Section 5.2.2, enabling the calculation of the liquid front position in the tablet at

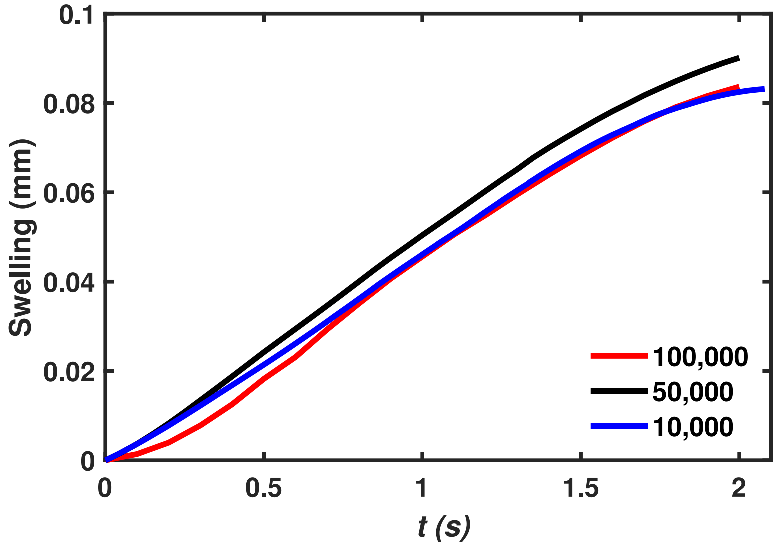

Figure 5.3: Analysis of DEM simulation of PH101 ϵ_0 = 22 tablet swelling where liquid position is updated at different rate: 10,000th, 50,000th and 100,000th time step.

the simulation time points. The fitting parameters for all formulations are shown in Table 5.6. The simulation of a single-particle swelling assumes that a particle starts to swell once the liquid reaches the particle centre; the model than considers the available wetted surface area to be A_{actual}. The particle size change was implemented in the DEM by defining a growth factor (f):

$$f = \frac{r_{\text{p}}(t+M\Delta t)}{r_{\text{p}}(t)} = 1 + \frac{M\Delta t}{r_{\text{p}}(t)}\frac{dr_{\text{p}}}{dt}. \tag{5.10}$$

To accelerate the simulation, the particle radius, mass and inertia was updated only every 100,000th time step ($M = 100,000$). $r_p(t+M\Delta t)$ is the radius at time $t+M\Delta t$. Due to the absorption of the liquid by the particle, the mass (m) and inertia (J) of a particle is also updated:

$$m(t+M\Delta t) = m(t)\cdot f^3, \tag{5.11}$$

$$J(t+M\Delta t) = J(t)\cdot f^5. \tag{5.12}$$

The entire workflow to simulate the tablet swelling and break-up is presented in

Formulation	a	b
PH101, ϵ_0 = 10 %	0.0535	0.7313
PH101, ϵ_0 = 15 %	0.2395	0.5470
PH101, ϵ_0 = 22 %	0.4646	0.5519
PH101/CCS, c_{CCS} = 2	0.1871	0.7339
PH101/CCS, c_{CCS} = 5	0.1359	0.8279
PH101/CCS, c_{CCS} = 8	0.0968	0.8739

Table 5.6: Parameters of the power law ($y = a \cdot t^b$) describing the experimental liquid penetration depth data.

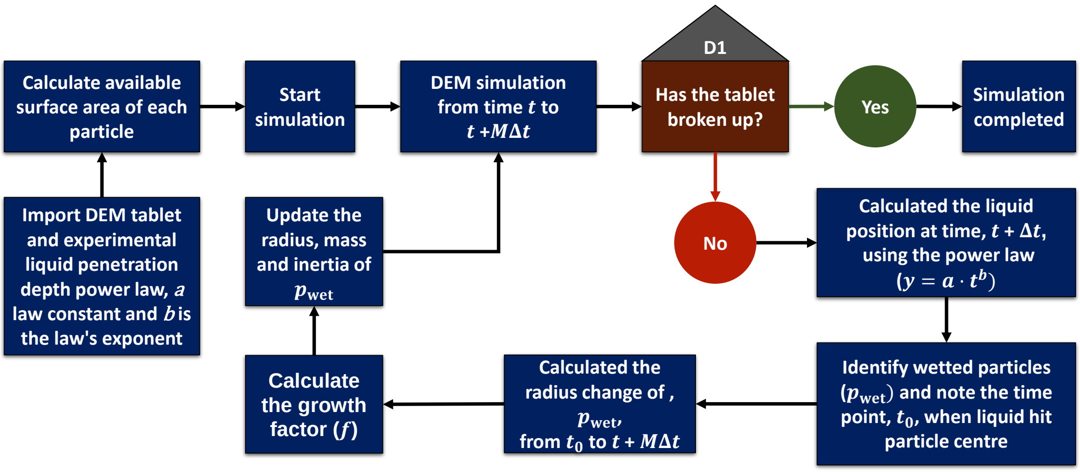

Figure 5.4: Flow chart for simulating tablet swelling using DEM incorporating a single-particle swelling model and experimental liquid penetration data.

Figure 5.4.

Pore structure analysis of DEM results

The porosity was measured using the voxel porosity method [V. Smilauer et al., 2021]. This approach divides the whole volume into a dense grid of voxels at a given resolution (resolution = 200 μm) and counts the voxels that fall inside any of the particles. The porosity, ϵ, is calculated as

$$\epsilon = \frac{V - V_{\text{v}}}{V}. \tag{5.13}$$

where V is volume of the tablet and V_{v} is volume of voxels that fall inside any particles.

The pore sizes were determined using the triangulation and pore finite volume method described in Chareyre et al. [2012] and subsequently Sweijen et al. [2017a]. First, a triangulation procedure was applied to the pore space of the tablet using solid particle centres as vertices for the tetrahedra. The tetrahedron spans across four neighbouring particles and defines the pore space. This is referred to as a pore unit. The size of each pore unit in the tablet was then calculated as the radius of inscribed circle of the tetrahedron.

Cumulative porosity maps were generated to analyse the pore space spatially. This method is described in detail in Markl et al. [2018a]. In brief, PoreSpy [Gostick et al., 2019] was used to generate a 3D voxel image of the tablet based on particles' position and radius. A cuboid subsection ($1400 \times 1400 \times 800\ \mu\text{m}^3$) of the voxel image at the centre of the tablet was selected for this analysis. The maps were obtained by dividing the sum of the number of voxels classified as voids along each dimension (x, y, and z) by the total number of voxels per dimension. The generated maps depict the void fraction at each position.

5.3 Results and Discussion

5.3.1 Tablet compaction and parameter calibration

The pure MCC PH101 tablet at the three different porosities and the tablet with MCC and CCS followed a very similar trend in the loading and unloading stage of the compression (Figure 5.5). The parameters k_1 and k_p were thus calibrated for the MCC PH101 tablet with $\epsilon_0 = 15\%$ and validated using the profiles of other conditions. Figure 5.6a shows the comparison between the experimental and simulated compression profiles for an MCC PH101 tablet with $\epsilon_0 = 15\%$. As discussed in Section 5.2.3, the deviation from the measured value ($\varepsilon = 0.56$ at $t = 0$) and of the DEM initial porosity ($\varepsilon = 0.44$ at $t = 0$) influenced the parameter estimation. A scaling procedure was applied to minimise the error caused by this discrepancy. The scaled loading profiles (Figure 5.6b) followed similar trends, which enabled an accurate determination of k_1.

The optimisation procedure with the scaled porosity profiles of a PH101 tablet with

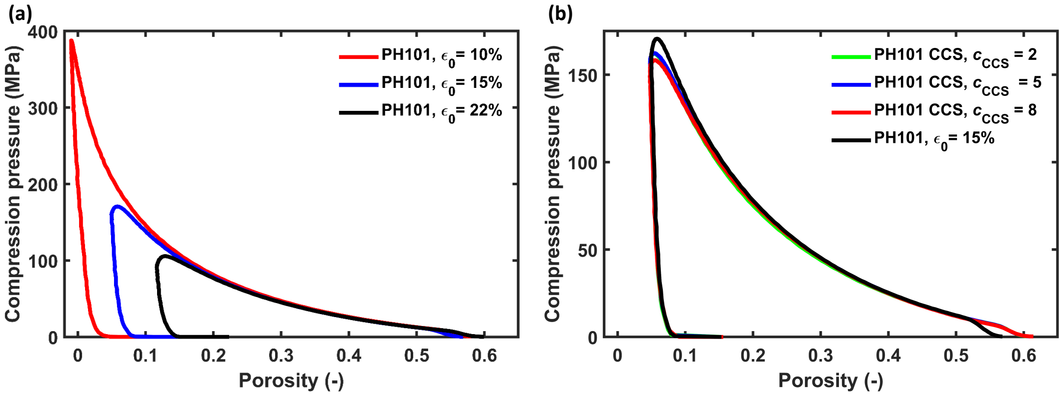

Figure 5.5: Experimental compression profile of (a) MCC PH101 tablet with porosities of 10%, 15% and 22%, (b) MCC PH101 and CCS tablet of c_{CCS} = 2, 5 and 8 compared with MCC PH101 tablet with porosity of 15%.

ϵ_0 = 15% yielded k_1 = 10,000 N/m, which in turn resulted in a k_p = 140,000 N/m to reach the final target porosity (Table 5.7). The parameters were validated for MCC PH101 ϵ_0 = 10 and 22% and MCC PH101, as well as MCC/CCS tablets with c_{CCS} = 2, 5, and 8% (Figure 5.6c–d)), validation data for the other formulation are given in Figure B.1). The DEM loading profiles followed the validation experiments closely, and the final porosity values obtained from the DEM simulation were in excellent agreement with the experimental values (Table 5.8).

Properties	Value
k_1	10,000 N/m
k_p	140,000 N/m

Table 5.7: Calibrated values of loading stiffness k_1 and plastic unloading stiffness limit k_p.

5.3.2 Experimental tablet swelling and liquid penetration data analysis

The uni-directional liquid penetration profile was determined experimentally. As the experimental time instances did not match the simulation time instances, a power law ($y = a \cdot t^b$) was fit to each experimental dataset. The power law was then evaluated at the simulation time points to retrieve the liquid position. The fit power law parameters

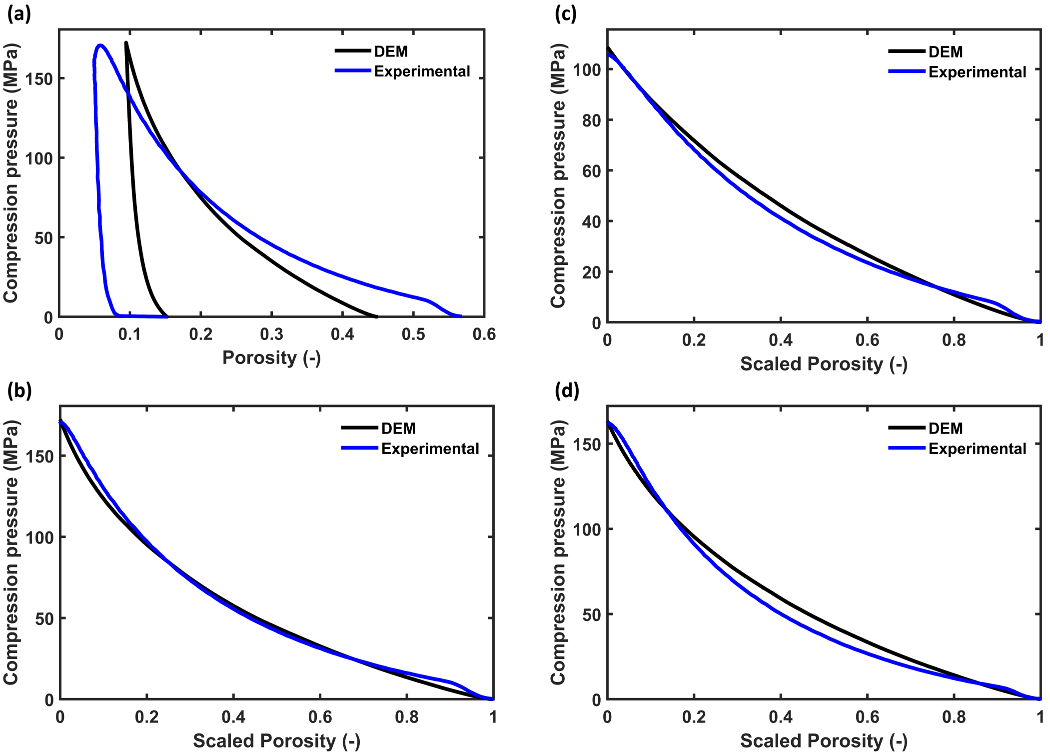

Figure 5.6: Comparison of experimental and DEM compression profiles. (**a**) Full compression profile of MCC PH101 tablet with a porosity of 15%. (**b**) Loading profile of MCC PH101 tablet with a porosity of 15% with scaled (to correct for the initial difference in porosity between experiment and DEM) porosity used for DEM parameter estimation. The validation data are shown in (**c**) for MCC PH101 $\epsilon_0 = 22\%$ and (**d**) for PH101/CCS with $c_{\text{CCS}} = 2\%$.

Formulation	Experimental porosity (%)	DEM porosity (%)
PH101	9.5 ± 0.2	8.2
PH101	14.6 ± 0.2	15.3
PH101	22.0 ± 0.3	22.2
PH101/CCS, c_{CCS} = 2%	15.1 ± 0.2	16.7
PH101/CCS, c_{CCS} = 5%	15.5 ± 0.3	16.9
PH101/CCS, c_{CCS} = 8%	15.5 ± 0.5	17.4

Table 5.8: Measured and simulated values of the tablet porosity for all conditions investigated.

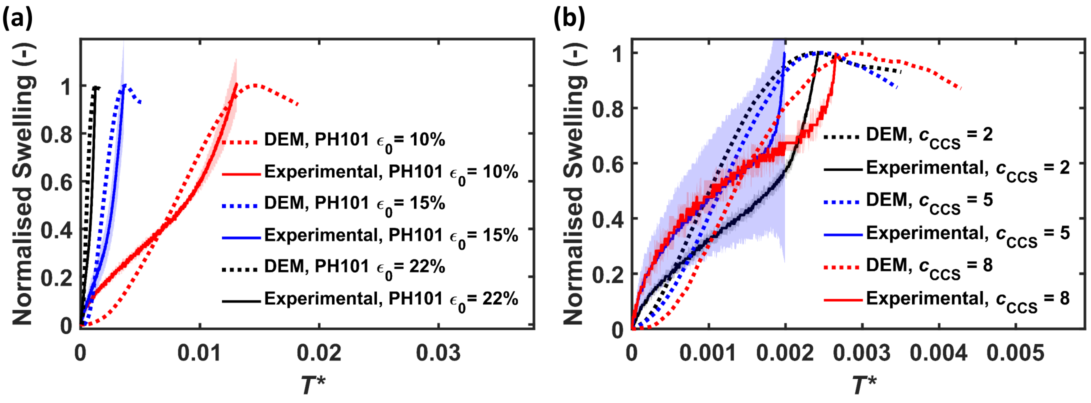

Figure 5.7: Analysis of the DEM simulation of PH101 tablets and comparison to experimental results, normalised swelling by height, as a function of normalised time, T^*. (**a**) PH101 tablets; (**b**) PH101/CCS tablets. The solid line and shaded area correspond to the average and standard deviation, respectively, of three samples (two for PH101/CCS, c_{CCS} = 5%).

for all formulations studied are given in Table 5.6.

The swelling profiles for six different conditions were simulated using the DEM with a single-particle swelling model and experimental liquid penetration depth data (Figure 5.7). To account for the effect of differences in thickness, H_0, between the DEM and the experimental tablet, the swelling profiles and the time were normalised. Each swelling profile was divided by its maximum. The time was normalised, T^*, using Equation (5.14) [Sweijen et al., 2017a].

$$T^* = \frac{t \cdot D}{H_0^2}. \tag{5.14}$$

As seen from Figure 5.7, PH101 with ϵ_0 = 22% swelled the fastest both in the DEM and experimentally, followed by ϵ_0 = 15% and ϵ_0 = 10%. The experimental and DEM swelling data were generally in very good agreement (Figure 5.7a). Both measured and DEM swelling profiles reached their maximum capacity at approximately the same time, indicating that the model captured the difference in swelling time for various tablets very well. Similar to the PH101 results, the simulated and experimental swelling profile of PH101/CCS (Figure 5.7b) reached the maximum swelling capacity at approximately the same time for c_{CCS} = 2% and PH101/CCS, c_{CCS} = 8%, while for c_{CCS} = 5%, the experimental swelling was faster.

The swelling profiles of the experiments and DEM followed different trends though. This was mainly attributed to: (1) limited consideration of the bonding types and compaction mechanisms in DEM, (2) the assumption of a spherical particle shape in the DEM, and (3) differences between the experimental flow cell and simulation setup.

Firstly, the bonds present in an MCC tablet are due to intermolecular forces such as Van der Waals force and hydrogen bonds, solid bridges, and mechanical interlocking [Nystrröm et al., 1993]. In particular, the mechanical interlocking was not captured in the DEM simulation. Compaction phenomena such as deformation and fragmentation during compaction were also not considered in the DEM model. Haustein et al. [2017] developed a method to account for the deformation during compaction. However, this was not considered at this stage as this would yield non-spherical particles in the final DEM tablet. Secondly, the single-particle swelling model was designed for spheres for simplicity and computational efficiency reasons. This is an approximation for the raw materials, as it is known that PH101 and CCS are typically non-spherical particles with a sphericity in the range of 0.66 to 0.73. The effect of the non-spherical shape on the anisotropic swelling process was discussed in Soundaranathan et al. [2020]. Thirdly, the TPI setup with the flow cell measured the change of the back face of the tablet, which reflects the swelling on both the back face and on the front face, where it takes up the liquid [Al-Sharabi et al., 2020]. The front face swelling lifts the tablet off the sample holder, causing the observed change of the back face tablet, as captured in the experimental data. As the sample holder was not included in the DEM setup, only the front face swelling was recorded in the simulation.

5.3.3 Analysis of time-dependent pore space

The swelling behaviour is primarily driven by the liquid penetration rate. The liquid penetration is strongly impacted by the change of the pore space caused by the swelling of particles. Both the pore space behind and ahead of the liquid front can change during the liquid uptake process. The data from the DEM simulations enabled the analysis of this in detail.

Pore space of entire tablet

Figures 5.8a and c show the porosity change during the swelling of the tablets for both the overall tablet and only the wetted volume. The initial delay in the porosity measurement for the wetted volume was due to the analysed volume being too small to be accurately measured and representative. The porosity decreased initially during the swelling of the wetted volume (Figure 5.8a). This was observed for PH101 tablets with $\epsilon_0 = 15\%$ and $\epsilon_0 = 22\%$, indicating that the pores were closing in the initial stages of the swelling process. After the initial decrease, the porosity increased for both the wetted volume and the whole tablet. This increase was primarily attributed to the fact that the tablets were eroding, i.e., individual particles were breaking away from the tablet. For PH101/CCS (Figure 5.8c), the porosity of the wetted volume increased rapidly in the first three seconds. This was attributed to the fast swelling of CCS particles, resulting in a rapid increase in porosity close to the surface of the tablets. The changes in porosity were caused by particles' movement. The changed in porosity along with the swelling of individual particles caused an increase in the tablet volume.

Unsurprisingly, the interparticle forces calculated in the DEM were strongly affected by the swelling process (Figure 5.8b,d). The swelling exerted stress on the particles, which caused an increase in the interparticle forces. The stress will reach a maximum, which then would lead to the disintegration of the tablet. The interparticle forces rose faster with increasing porosity (Figure 5.8b). For PH101/CCS (Figure 5.8d), the tablets with the two lower CCS concentrations had the same force profile, while the tablet with $c_{\mathrm{CCS}} = 8\%$ experienced a slower increase of the interparticle force.

Figure 5.9 shows the pore size (pore body) distributions (PSDs) of the tablets at dif-

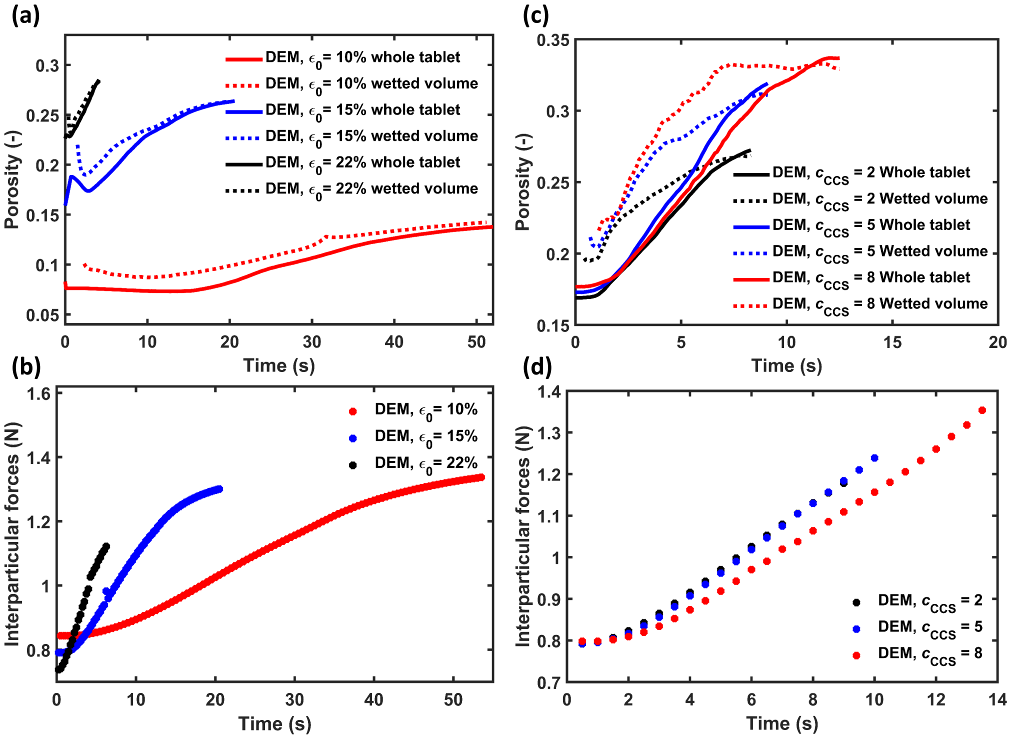

Figure 5.8: DEM simulation results. (**a**) PH101 tablets' porosity for the whole tablet and for the wetted volume only. (**b**) Interparticle forces for PH101 tablets. (**c**) PH101/CCS tablets' porosity analysed for the whole tablet and for the wetted volume only. (**d**) Interparticle forces for PH101/CCS tablets.

ferent time points during the swelling process. As expected, the initial average pore size was larger for tablets with a higher initial porosity, ϵ_0, i.e., a lower compaction pressure resulted in bigger pores. The initial pore size of the PH101/CCS tablets was in the same range as the PH101 tablets. PH101/CCS with $c_{\mathrm{CCS}} = 2\%$ tablets had similar PSDs as tablets with $\epsilon_0 = 15\%$, as both had approximately the same initial porosity, and the initial PSD was primarily driven by the PH101 as the major component in the tablet. As expected for the tablet with a higher CCS content, $c_{\mathrm{CCS}} = 5\%$ and 8%, the number of smaller pores (~10 μm) was higher than for $c_{\mathrm{CCS}} = 2\%$. For all tablets, the pore size increased over time, and the pores opened up shortly before the break-up of the tablet. At the maximum swelling capacity, there were pores >70 μm, which were not present at the two previous time points.

Cumulative porosity maps were generated to analyse the pore space spatially. This method is described in detail in Markl et al. [2018a]. In brief, PoreSpy [Gostick et al., 2019] was used to generate a 3D voxel image of the tablet based on particles' position and radius. A cuboid subsection ($1400 \times 1400 \times 800$ μm^3) of the voxel image at the centre of the tablet was selected for this analysis. The maps were obtained by dividing the sum of the number of voxels classified as voids along each dimension (x, y, and z) by the total number of voxels per dimension. The generated maps depict the void fraction at each position. These maps were obtained for different time instances during the swelling process (Figures 5.10 and 5.11).

As the liquid moves in one direction from the top to the bottom, resulting in the swelling of the particles from top to bottom, it is expected that the porosity will also mostly be affected along the z direction. However, it can be observed that the porosity changed across the entire tablet, though it had not been fully wetted.

The cumulative porosity analysis highlighted that the porosity was higher on the edges during the swelling process, which indicates that the tablet began to break up from the edges. For the PH101 tablets with $\epsilon_0 = 10\%$ and $\epsilon_0 = 15\%$, the trend in the porosity distribution was similar across the entire tablet, while for PH101, $\epsilon_0 = 22\%$, the porosity was significantly higher on the edges compared to the tablet centre.

The cumulative porosity maps for the PH101/CCS tablets were similar at the initial

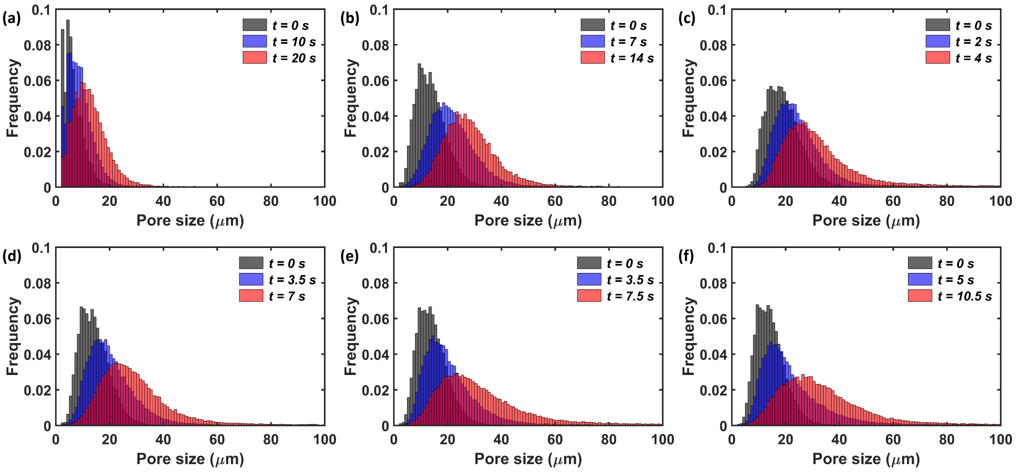

Figure 5.9: Pore size distribution at different time points during swelling of the tablet. (**a**) PH101, $\epsilon_0 = 10\%$. (**b**) PH101, $\epsilon_0 = 15\%$. (**c**) PH101, $\epsilon_0 = 22\%$. (**d**) PH101/CCS, $c_{\text{CCS}} = 2\%$. (**e**) PH101/CCS, $c_{\text{CCS}} = 5\%$. (**f**) PH101/CCS, $c_{\text{CCS}} = 8\%$. The time points analysed: starting point (0 s), halfway point of reaching maximum swelling capacity and at the time point of maximum swelling capacity.

and the halfway times. The porosity was slightly higher at the edges for PH101/CCS, $c_{\text{CCS}} = 8\%$, at the halfway point. At the final time, where the tablets reached their maximum swelling capacity, the porosity at areas close to the surface increased with increasing CCS content. This was in contrast to the overall swelling and disintegration of these tablets, where $c_{\text{CCS}} = 8\%$ was the tablet with the slowest swelling, i.e., the time to reach the maximum normalised swelling capacity. The disintegration of the $c_{\text{CCS}} = 8\%$ tablet was, therefore, not controlled by the swelling of the tablet, but the liquid uptake process, which is further discussed below. This slower liquid uptake means that a smaller number of particles were swelling for the $c_{\text{CCS}} = 8\%$ tablet, which in turn resulted in a slower change of the interparticle forces for this case compared to the lower CCS concentrations.

Pore space behind the liquid front

Both experiments and simulations showed a slower swelling rate for the tablet with the highest CCS content ($c_{\text{CCS}} = 8\%$) (see Figure 5.7). These tablets also had the slowest liquid penetration rate. A similar trend was observed by Berardi et al. [2018], Maclean et al. [2021], who showed that the disintegration time is prolonged with higher CCS

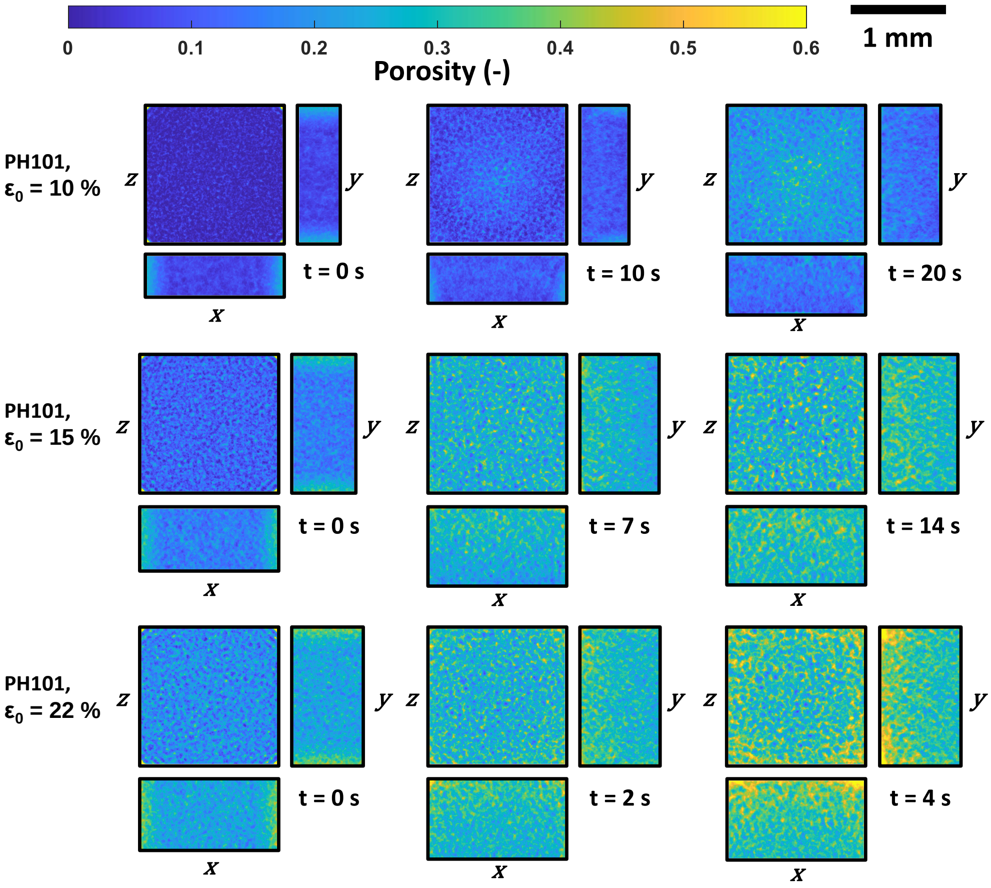

Figure 5.10: Cumulative porosity maps of the tablet at three different time points during the swelling process of PH101 tablets: Initially, halfway of reaching maximum swelling capacity and maximum swelling capacity. The cuboid subsection has a size of 1400 × 1400 × 800 pixels and was selected at the centre of the tablet for this analysis.

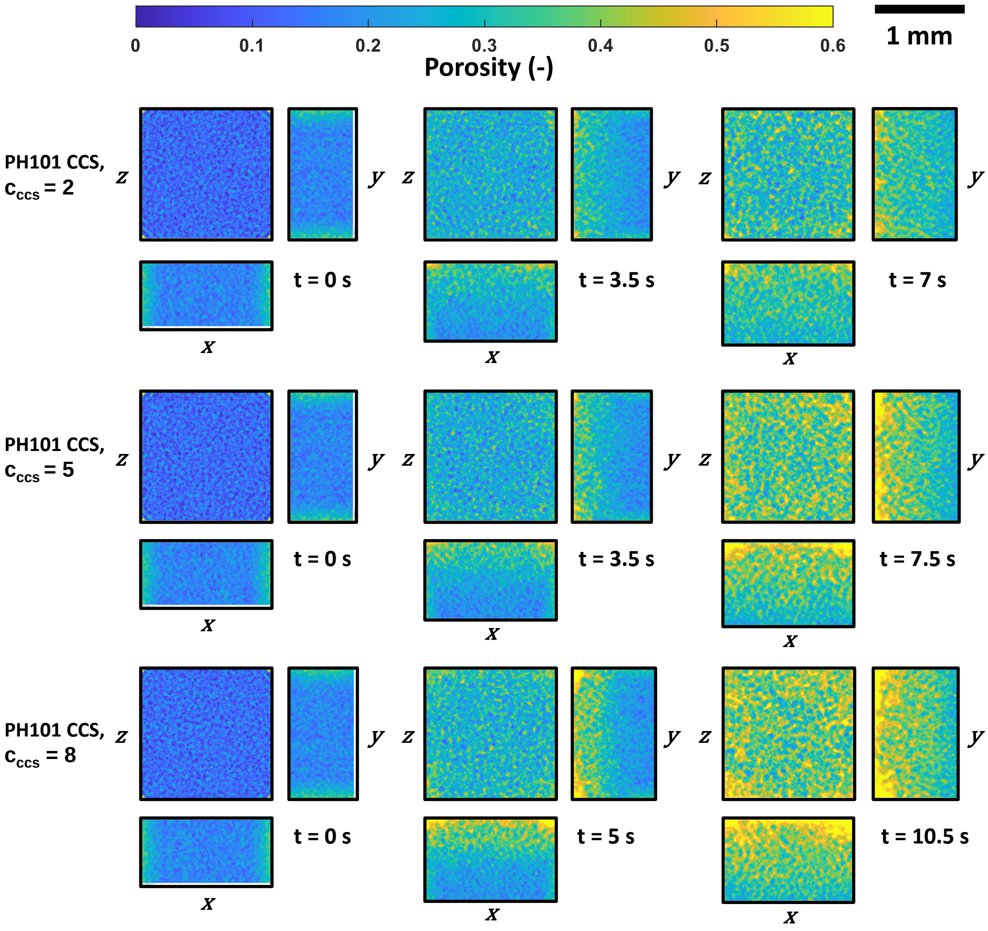

Figure 5.11: Cumulative porosity maps of the tablet at three different time points during the swelling process of PH101/CCS tablets. The cuboid subsection has a size of 1400 × 1400 × 800 pixels and was selected at the centre of the tablet for this analysis.

content. As the liquid penetration rate is directly linked to the pore size, it is crucial to understand how the pore size changes in the wetted domain, as well as in the dry domain of the tablet.

The average pore size of the wetted domain of PH101/CCS, c_{CCS} = 8%, decreased during the initial stages of the swelling (Figure 5.12a). The pore size of PH101/CCS, c_{CCS} = 5%, slightly decreased initially, whereas PH101/CCS c_{CCS} = 2% was constantly increasing. Sweijen et al. [2020] explained that the reason for the decrease in the pore size (porosity) was due to the swelling of particles being much faster than that particle contacts could dissipate their potential energy. Therefore, the particle movement would be limited and the particle packing would clog (i.e., the porosity would tend to decrease). The decrease in average pore size is an indication that the pores were closing, which reduces the liquid flow. The decrease in the pore size behind the liquid front could be observed across all formulations, but it was most significant (>30% reduction in pore size) for the tablets with c_{CCS} = 8%. Interestingly, the pore size reduction had a nonlinear dependence on the liquid penetration depth. CCS swelled significantly faster compared to PH101, causing the closing of the pore space, which reduced the liquid flow into the tablet.

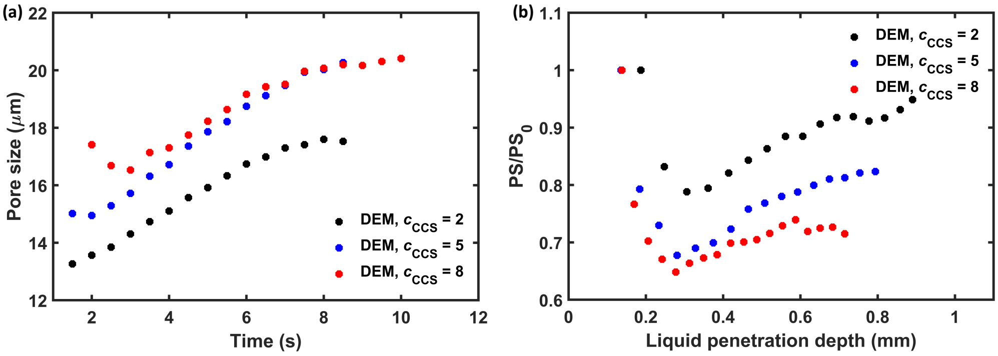

Figure 5.12: Pore size analysis of the wetted volume for PH101/CCS tablets. (**a**) The average pore size of PH101/CCS tablets at different time points during swelling. (**b**) The pore size ratio (PS/PS$_0$) of the pores placed up to 0.2 mm behind the liquid front as a function of the liquid penetration depth. PS is the pore size at time t, and PS$_0$ is the pore size at $t = 0$ s.

Pore space ahead of liquid front

As the particle swelling of the material studied was omnidirectional, it can affect the dry volume of the tablet. A change in the pore space of the dry volume impacts the liquid penetration rate, which is mostly driven by the capillary action. The capillary pressure depends on the pore size at the liquid front, i.e., at the interface of the wetted and the dry volume.

The pore space of the wetted and dry volume can be analysed through the pore size ratio (PS/PS_0) across the tablet height at different liquid front positions (Figure 5.13). The focus was on the smaller pores (<30 μm), as smaller pores have a greater impact on liquid flow compared to large pores.

The number of pores decreasing in size at the surface of the tablet was largest for PH101/CCS, c_{CCS} = 8%. At three seconds, the small pores of the c_{CCS} = 5% and c_{CCS} = 2% tablets were opening up more significantly compared to c_{CCS} = 8%. It can also be observed that the dry pores changed in size substantially during the swelling of the wetted volume with a decrease in the size of many small pores. Again, this phenomenon was most significant for the PH101/CCS tablet with c_{CCS} = 8%. The reduction in the pore size of the dry pore and wetted pores slowed down the water uptake of these tablets, which resulted in a slower swelling and ultimately delayed disintegration of the entire tablet.

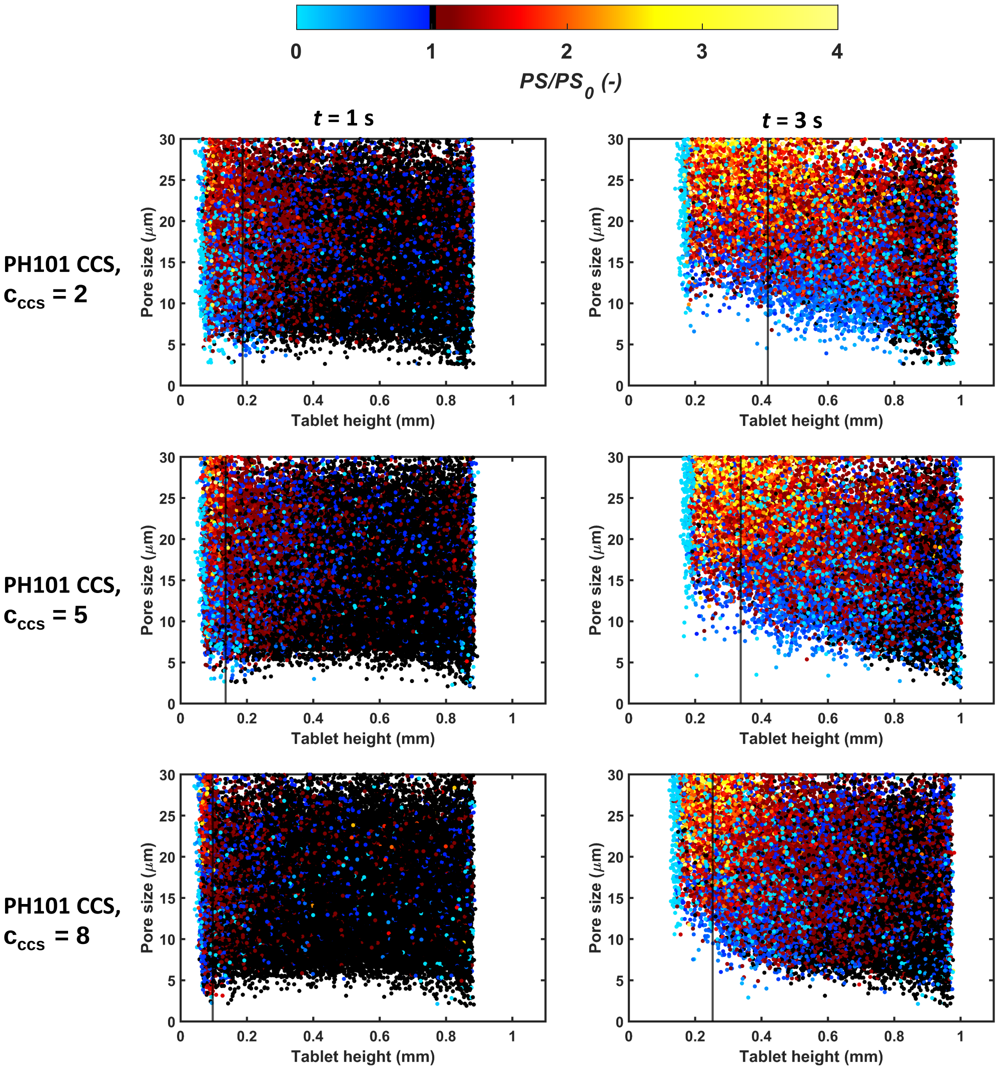

Figure 5.13: The pore size ratio (PS/PS$_0$) as a function of tablet height focusing on pores <30 μm during swelling at 1 s and 3 s. The black vertical line in each plot indicates the liquid front at that particular time point. PS is the pore size at time t, and PS$_0$ is the pore size at $t = 0$ s.

5.4 Conclusion

This study demonstrated the simulation of tablet swelling by combining DEM with a single-particle swelling model and experimental liquid penetration data. The model captured the difference in the swelling behaviour of the tablets with different porosities and formulations well. For all tablets, the pore size increased over time, and the pores opened up shortly before the break-up of the tablet. Both in the experiments and DEM, the swelling was slower for tablets with the highest disintegrant concentration (PH101/CCS with c_{CCS} = 8%) due to the closure of the pores in both the wetted volume and dry volume. The closure of pores hinders the liquid from accessing other particles and slows down the overall swelling process.

This study provides new insights into the changes in pore space during the disintegration, which is crucial to better understand the impact of porosity and formulations on the performance of tablets. This is particularly important for formulations where the liquid uptake is performance-controlling. The interplay between the formulation, manufacturing conditions, and the dynamic change of the pore space is crucial to make informed decisions during the development of a new drug product. Having a deep understanding of the fundamental changes during the disintegration and dissolution process and its link to the formulation and process conditions can accelerate the development process and increase the robustness of the design process.

Future work will focus on the incorporation of a liquid penetration model, replacing the current need for experimental data, and a dissolution model to predict drug release as a function of time. The proposed modelling approach should also be tested and validated across a larger number of relevant materials and more complex formulations.

Compared to previous studies, the model developed in this study captures all the essential mechanisms, such as liquid penetration, swelling and disruption of particle-particle bonds of the disintegration process and the interaction between them. The model predicted the swelling time for each formulation and the difference in the swelling behaviour of the tablets with different porosities and formulations well. However, as seen from Figure 5.7 the simulated and experimental swelling profiles have different trends.

This is due to factors such as (1) limited consideration of the bonding types and compaction mechanisms in DEM, (2) the assumption of a spherical particle shape in the DEM, and (3) differences between the experimental flow cell and simulation setup. The model needs to be improved to be able to capture the trend in the swelling profile, by implementing models for different bonding types such as hydrogen bonds, solid bridges, and mechanical interlocking. This can potentially be accomplished by using a different contact model for describing the swelling and tablet break-up process.

Chapter 6

Modelling the disintegration of pharmaceutical tablets by combining mathematical modelling for liquid transport and single particle swelling model

Chapter Summary

This chapter focuses on modelling the disintegration process by including a liquid penetration model and single particle model in DEM. A virtual Design of Experiment was developed to asses the disintegration time for various formulations. The contents of this chapter have not been published.

6.1 Introduction

The tablet disintegration process consists of multiple connected and interdependent mechanisms: liquid penetration, swelling, dissolution of excipients and drug particles, and break-up. One of the most critical processes is the liquid penetration through the porous tablet structure, which initiates the swelling of the particles in the tablet. This swelling builds up an internal stress, which causes the break up of the tablet into smaller agglomerates and primary particles [Markl and Zeitler, 2017, York, 2022]. In many cases, liquid penetration is the controlling mechanism for tablet disintegration, i.e., the time it takes for the tablet to disintegrate highly depends on the liquid uptake rate. It is important to note that there is a strong interdependence between these different disintegration mechanisms, e.g., particle swelling will cause a change of the pore structure, which will directly affect the liquid penetration process [Markl and Zeitler, 2017]. The transport process of liquid in a pharmaceutical table during the disintegration process is rapid, which takes place on the order of milliseconds/seconds, occurs first and is dependent on the fluid properties and solid properties. During disintegration/dissolution testing it is difficult to distinguish between liquid uptake and swelling, because of the overlap in their time scales [Jange et al., 2023, Lee et al., 2016].

Traditionally liquid penetration depth in pores media is described by the Washburn equation [Washburn, 1921]. The model presented in Cai and Yu [2011], Markl et al. [2017b], Masoodi and Pillai [2010], Masoodi et al. [2007], Schuchard and Berg [1991], Shi and Gardner [2000] modified the Washburn equation by including factors such as swelling of particle (change in pore radius), energy loss during liquid penetration and tortuosity. Shi and Gardner [2000] developed a model describing the liquid penetration depth in porous media, by considering the particle swelling in the table and the energy loss during the liquid rise process. They modified the Poiseuille's law to account for pore radius change during swelling and assumed that a small particle reaches its maximum swelling instantly after it interacts with the liquid. Schuchard and Berg [1991] developed a model to describe the liquid penetration depth in swelling porous media, they assumed a linear decrease with time of the pore radius in the wetted area of the porous medium. Cai and Yu [2011] developed a model describing the liquid flow in porous media by considering tortuosity by modifying the Hagen-Poiseuille law. Markl et al. [2017b] modified the Masoodi and Pillai [2010] model based on an empirical equation from Schott [1992a] for microcrystalline cellulose (MCC) particles to describe the liquid penetration kinetics. The authors simplified the swelling to a tablet enlargement only in axial direction to match their experimental setup. They showed that the capillary radius, r_c, decreases with increasing swelling. They assumed that fractional increase in volume of the wetted powder compact is equal to the fractional increase in the volume of a single wetted particle.

Several studies demonstrated the use of discrete element modelling (DEM) to simulate the tablet compaction process and the tablet performance [Gao et al., 2021, Hu et al., 2023, Kalný et al., 2021, Soundaranathan et al., 2023]. Kalný et al. [2021] simulated the disintegration and dissolution of a two component tablet with ibuprofen as the API and croscarmellose sodium (CCS) as a disintegrant. They assumed that only the CCS particles contribute to the total swelling and the swelling was only occurring in two spatial directions. They simplified the swelling by assuming that all particle swell simultaneously and at a constant rate, i.e. the liquid penetration behaviour was not considered. Kimber et al. [2012] developed a model for simulating the swelling and dissolution process of a polymer tablet by combining DEM particles with Fickian mass transfer. The particle was assumed to be cylindrical with swelling only occurring in the radial direction. In studies from other fields, such as hydrogeology [Sweijen et al., 2017a, 2020], have used DEM to simulate similar processes. Sweijen et al. [2017a] and Sweijen et al. [2020] applied DEM to simulate the swelling of superabsorbent particles with an integrated liquid penetration model. Sweijen et al. [2017a] simulated the swelling of a bed of SAP particles using a single particle swelling model combined with the pore finite volume (PFV) method to model the liquid flow in a powder bed. The group developed this model further [Sweijen et al., 2020] using the pore unit assembly (PUA) method, where the liquid flow was computed using a scheme of implicit pressure solver and explicit saturation update. In both of these studies initially porosities was in range of 0.35-0.40, whereas in pharmaceutical industry the porosity of the tablets are commonly in rage of 0.10-0.25. Both

PFV and PUA methods are more suitable for porous media with high porosity and pore sizes. Santagata et al. [2020] developed a liquid flow model in a swelling and absorbing SAP porous media based on Diersch et al. [2010] model which are based on Richards equation. The model is based on mass and momentum balance equations defined for the liquid and the solid phases, by modifying Darcy's law. Other method utilised to model liquid flow in porous media includes microscale Stokes flow model, Lattice-Boltzmann and Continuum-discrete Darcy flow modelling [Chareyre et al., 2012].

In existing DEM models of the disintegration process Kalný et al. [2021], Kimber et al. [2012], Soundaranathan et al. [2023], the liquid flow in the tablet has not been considered or described based on experiment data. This study will focus on modelling the disintegration process by including a liquid penetration model, from combining the tablet swelling model from [Soundaranathan et al., 2023] and liquid penetration model from [Markl et al., 2017b]. The liquid penetration model from Markl et al. [2017b] requires dynamic pore size and porosity as an input, these parameter were calculated in DEM using PFV and triangulation. A virtual Design of Experiments (vDoE) was performed to predict the disintegration time of different formulations.

6.2 Materials and Methods

6.2.1 Materials

The materials analysed in this study included MCC PH101 (Avicel PH101, Roquette, Lestrem, France) and the disintegrant croscarmellose sodium (Ac-Di-Sol, CCS, SDW-802, FMC International, Philadelphia, USA). MCC, in particular grade PH101, was selected as a model compound as it is one of the most commonly used excipients in the pharmaceutical industry. See Section 5.2.1 for more details on the materials.

6.2.2 Modelling

Figure 6.1 depicts a diagram summarising the integration of the models to simulate liquid penetration, tablet swelling and break-up. The tablet disintegration model consist of two main parts: DEM swelling model with a single particle swelling model

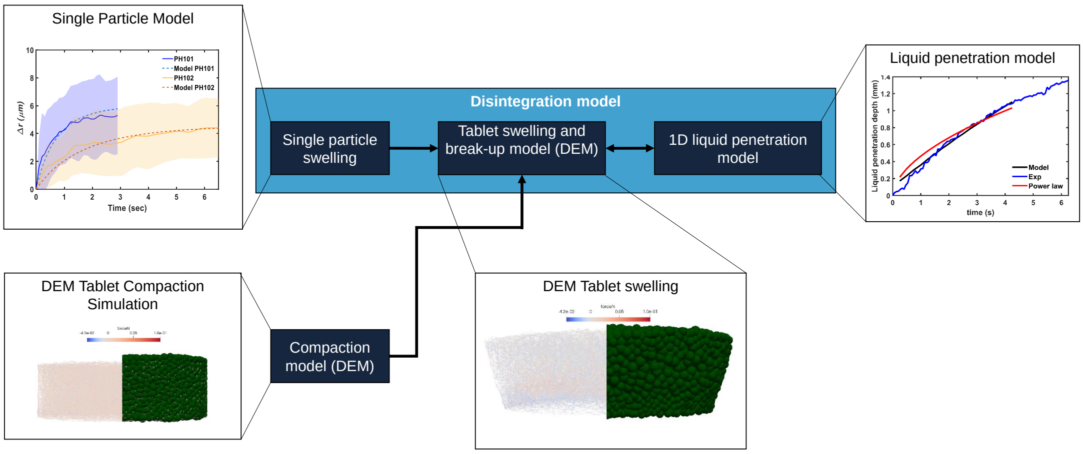

Figure 6.1: Work flow of the tablet swelling and break-up model. A single-particle model, DEM tablet compaction model, and liquid penetration model are combined to model the swelling and break-up process.

[Soundaranathan et al., 2023] and 2) 1D liquid penetration model (this chapter). A prerequisite is a tablet compaction model in DEM as presented in Chapter 5.2.3. Both the compaction and disintegration model were implemented in the open source DEM software Yade-DEM [V. Smilauer et al., 2021].

1D liquid model

The liquid penetration is based on the model developed by Markl et al. [2017b]. They describe the liquid penetration as function of the capillary pressure, P_c and the intrinsic permeability, $\mathscr{K}$ (calculated based on a modified Carman-Kozeny equation, are given in Equation 6.3.), as given in Equation 6.1

$$L = \sqrt{\frac{2P_c}{\epsilon_0 \eta} \int_0^t \mathscr{K}(t')dt'}, \tag{6.1}$$

$$P_c = \frac{\gamma cos\theta}{r_c(t)}. \tag{6.2}$$

$$\mathscr{K}(t) = (2r_{p,0})^2 \frac{z}{180} \frac{\epsilon(t)^3}{(1-\epsilon(t))^2}, \tag{6.3}$$

Where ϵ_0 is the initial porosity of the tablet, η is the viscosity, θ is the contract angle, γ is the surface tension. The values of these parameters used in this study are given in Table 6.1. $r_c(t)$ is the pore radius of the pores placed up to 0.1 mm ahead the liquid front at time point t, as seen from Figure 6.2. $r_{p,0}$ is the initial particle size, $\epsilon(t)$ is the porosity of wetted volume at time point t and z is correction factor as it is well-known that the Carman-Kozeny equation overestimates the permeability of porous beds [Rough et al., 2002].

In Markl et al. [2017b], $r_c(t)$ was calculated based on mathematical equation and $\epsilon(t)$ was described as a function of the pore radius change during swelling, by simplifying the swelling to a tablet enlargement only in axial direction to match their experimental setup. However, by using Yade-DEM the pore size and porosity at time point t can be determined directly using the pore finite volume method based on triangulation. The pore sizes were measured using the triangulation and pore finite volume method described in [Chareyre et al., 2012, Sweijen et al., 2017a]. Firstly, it applies a triangulation to the tablet using the solid particle centres as vertices for the tetrahedra. The tetrahedron spans across four neighbouring particles which defines the pore space and is referred to as a pore unit. The size and porosity of each pore unit in the tablet is then calculated. The pore size was defined as an average value of the size of each pore unit. The wetted porosity, $\epsilon(t)$, was defined as an average value of the porosity of each wetted pore unit. Therefore $\int_0^t K(t')dt'$ in Equation 6.1 can be defined as:

$$\int_0^t \mathcal{K}(t')dt' = \sum_0^t \mathcal{K}(t_i)\Delta t. \tag{6.4}$$

The unknown parameter z in the liquid penetration model (Equation 6.3) was identified through an optimisation procedure that minimises the error between the experimental liquid penetration data (Section 5.2.2) and the simulated liquid penetration. The $\epsilon(t)$ was defined as the initial porosity (ϵ_0) of the tablet in the initial stages (L < 0.2 mm) as seen from Figure 6.2, since the wetted volume was too small to be accurately measured and representative. Figure 6.2 shows how $r_c(t)$ and $\epsilon(t)$ defined during different time point of disintegration process.

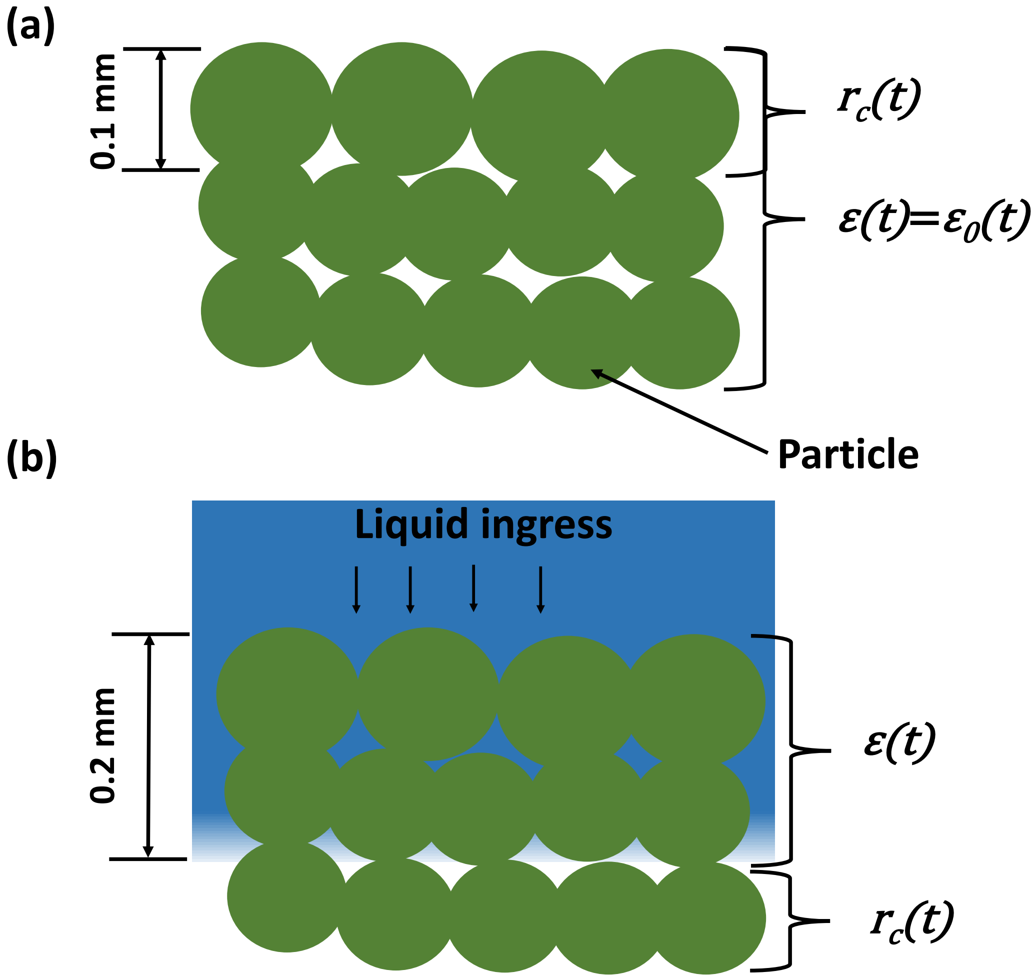

Figure 6.2: The definition of $r_c(t)$ and $\epsilon(t)$ at the time points where is L= (a) 0 mm and (b) 0.2 mm.

Properties	Value
γ	0.0723 N/m
η	1.002 mPas
θ	64.3^o

Table 6.1: Summary of the parameters used for all simulations of the liquid penetration depth [Markl et al., 2017b].

Formulation	Number of particles PH101	Number of particles CCS
PH101, ϵ_0 = 10 %	11,117	-
PH101, ϵ_0 = 15 %	10,426	-
PH101, ϵ_0 = 22 %	9,720	-
PH101/CCS, c_{CCS} = 2	10,134	720
PH101/CCS, c_{CCS} = 5	9,699	1778
PH101/CCS, c_{CCS} = 8	9,335	2828

Table 6.2: The number of particles simulated for each formulation.

Tablet disintegration

The simulations of the swelling of the tablet DEM compact was set up to closely mimic the experimental work described. The time step (Δt) was set at 10^{-6} s/step to ensure simulation stability. The number of particles simulated for each formulation are given in Table 6.2. The radius, mass and inertia of individual particles was updated according to a single particle swelling model described in Chapter 5.2.3. This model was based on the single particle swelling model developed in Sweijen et al. [2017a] and that model assumes that the entire particle is exposed to the liquid, which is not valid when the particle is part of a compact. In a compact, particles form bonds with neighbouring particles across a contact area. This reduces the effective (available) surface area of the particle that is exposed to the absorbing liquid. In Chapter 5.2.3 this is accounted for by introducing f_{w} that describes the fraction of the available surface (A_{actual}) to the total particle surface area ($A_p = 4\pi r_p$).

The entire workflow to simulate the tablet swelling and break-up is presented in Figure 6.3. The python code used to simulate tablet swelling are given in Appendix A.2.

6.2.3 Design of experiments for simulations

The formulations analysed in this study to develop the virtual Design of Experiments to predict the disintegration time are given Table 6.3.

6.2.4 Experimental

The model was validated by measured liquid penetration and tablet swelling using a commercial terahertz pulsed imaging system (TPI, TeraPulse 4000, Teraview Ltd., Cam-

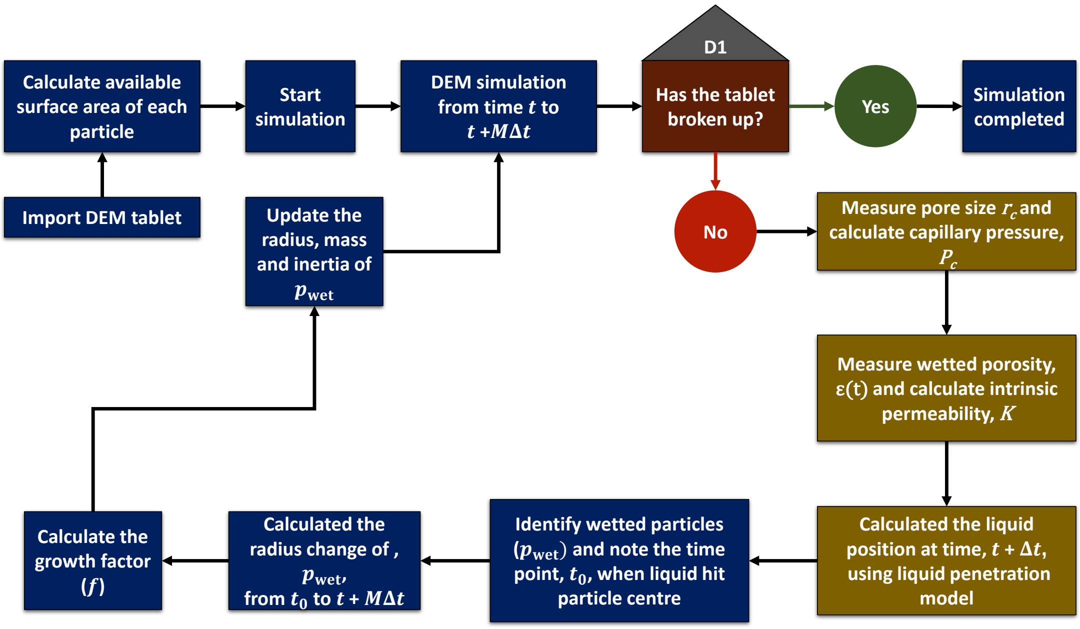

Figure 6.3: Flow chart for simulating tablet swelling using DEM using a single particle swelling model and liquid penetration model. The boxes in gold presents work for this chapter on the liquid model, while the blue boxes is the work conducted in Chapter 5 and also been used in this chapter.

Material	c_{PH101} $(\%w/w)$	Material	c_{CCS} $(\%w/w)$	ϵ_0 (%)
PH101	100	-	-	10
PH101	100	-	-	15
PH101	100	-	-	22
PH101	98	CCS	2	10
PH101	98	CCS	2	15
PH101	98	CCS	2	22
PH101	95	CCS	5	10
PH101	95	CCS	5	15
PH101	95	CCS	5	22
PH101	92	CCS	8	10
PH101	92	CCS	8	15
PH101	92	CCS	8	22

Table 6.3: Tablet formulations (PH101 concentration, c_{PH101}; CCS concentration, c_{CCS}) and porosities (ϵ_0) investigated.

Formulation	z	RMSE (mm)
PH101, ϵ_0 = 10 %	0.00193	0.04
PH101, ϵ_0 = 15 %	0.00993	0.10
PH101, ϵ_0 = 22 %	0.02420	0.13
PH101/CCS, c_{CCS} = 2	0.00801	0.12
PH101/CCS, c_{CCS} = 5	0.00522	0.18
PH101/CCS, c_{CCS} = 8	0.00376	0.19

Table 6.4: Calibrated values of correction factor z and RMSE between simulated and experimental liquid penetration data.

bridge, UK) in combination with a bespoke flow cell [Al-Sharabi et al., 2021]. The experimental data and set-up is taken from Chapter 5.2.2. The experimental procedure and THz in general are described in Section 3.3.

6.3 Results and Discussion

6.3.1 Liquid penetration model calibration

The correction factor, z, was calibrated for each formulation using the described optimisation procedure in Section 6.2.2. The results of the calibration are given in Table 6.4. The correction factor increases with increasing porosity, since the permeability of the porous tablet is positively correlated with the liquid penetration rate. The z factor is lower for tablets with higher c_{CCS}, as the permeability will get lower due to the closure of pores behind and ahead of the liquid front as discussed in Chapter 5. As seen from Figure 6.4, a power law ($z = 1.2293\epsilon^{2.5896}$) between the predicted z values and the porosity (ϵ) for pure PH101 tablets and a linear model ($z = 0.0097 - 0.0781c_{\mathrm{CCS}}$) can describe the relationship between z and c_{CCS} for PH101 CCS tablets. Based on the this linear regression and power law, can the correction factor z be estimated for other formulations enabling the simulation of the swelling process of new formulations.

From Figure 6.4(a) can it be assumed that the changes in z with porosity follows a power law, for formulations with the same material concentration. Figure 6.5 shows how changing the power law constant a and exponent b affect the z value, results indicates that changing the a would not have great impact on the liquid penetration rate compared the exponent b as small changes would have a significant effect. Therefore it

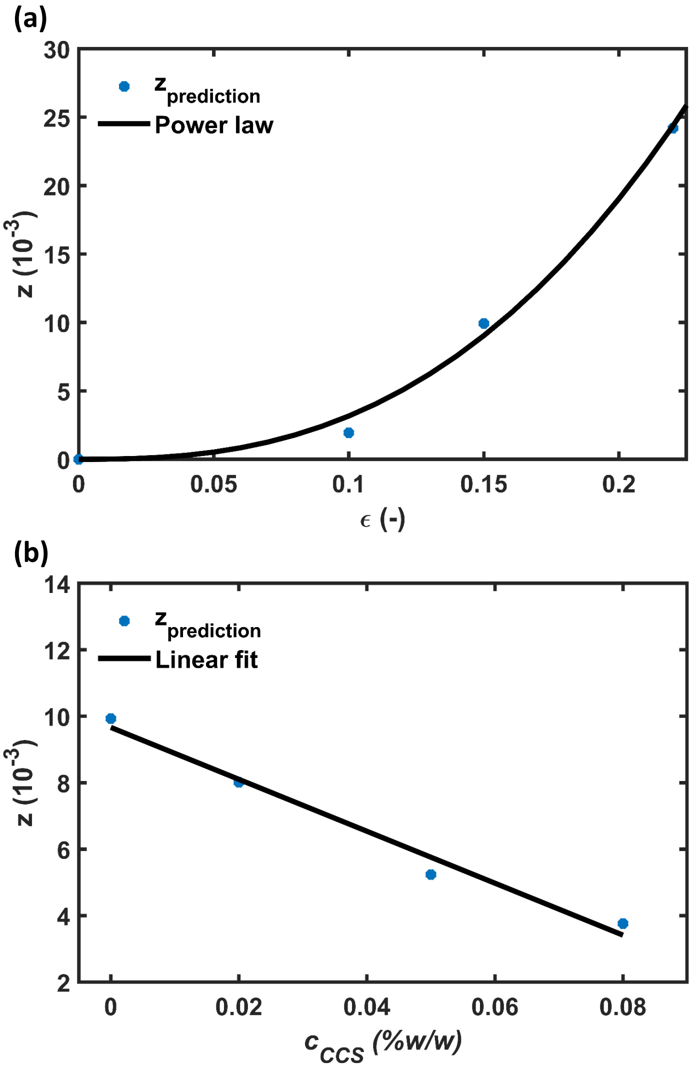

Figure 6.4: Regression between the z and (a) The tablet porosity of PH101 tablets and (b) The c_{CCS} for PH101 CCS tablets.

Formulation	ϵ_0 (%)	b	z
PH101/CCS, c_{CCS} = 2	10	2.6530	0.00273
PH101/CCS, c_{CCS} = 2	22	2.6530	0.02213
PH101/CCS, c_{CCS} = 5	10	2.8773	0.00163
PH101/CCS, c_{CCS} = 5	22	2.8773	0.01576
PH101/CCS, c_{CCS} = 8	10	3.0515	0.00109
PH101/CCS, c_{CCS} = 8	22	3.0515	0.01211

Table 6.5: Calculated values of correction factor z for PH101 CCS tablet at different porosities.

can be assumed that the constant a is the same for all formulations. The b value can be calculate for all the PH101 CCS tablets to simulate the liquid flow in various porosity for PH101/CCS, based on the z value at $\epsilon_0 = 15\%$ and the power law ($z = 1.2293 * 0.15^b$). For example for PH101 CCS $c_{\text{CCS}} = 8\%$ the equation would be $1.2293 * 0.15^b = 0.00376$, where only b is unknown. The results from calculated b and factor z for various formulation are given in Table 6.5.

6.3.2 Liquid flow simulation

Figure 6.6 shows the liquid penetration depth profile as a function of time for the various tablets analysed. The simulated liquid penetration profile is in relatively good arrangement with the experimental data, as seen from the RMSE values given in Table 6.4 which varying between 0.04 and 0.18 mm. However, the simulation slightly overestimates the liquid penetration in the initial stages for PH101, $\epsilon_0 = 10\%$ tablets, after 10 s the simulated and experimental profile match. The simulated liquid penetration in the initial stages (t > 8 s) for c_{CCS} = 5 and 8 % is slower than the experimental, after that both follows the same trend. The liquid penetration profiles for $\epsilon_0 = 22\%$ are approximately the same across all the formulations. For tablets with $\epsilon_0 = 10\%$, tablets with pure PH101 are slowest requiring 22 s, followed by PH101, $c_{\text{CCS}} = 8\%$ with 15 s and both PH101, c_{CCS} = 2 and 5 % are fastest with 12 s to reach a penetration depth of 0.5 mm. The liquid penetration profiles for $\epsilon_0 = 15\%$ are approximately the same for the formulations PH101 with c_{CCS} = 2 and 5 %. All of them take around 12 - 13 s to reach 1 mm. While PH101, $c_{\text{CCS}} = 8\%$ takes around 18 s to reach 1 mm.

Figure 6.7 shows the capillary pressure-liquid penetration depth curve for the vari-

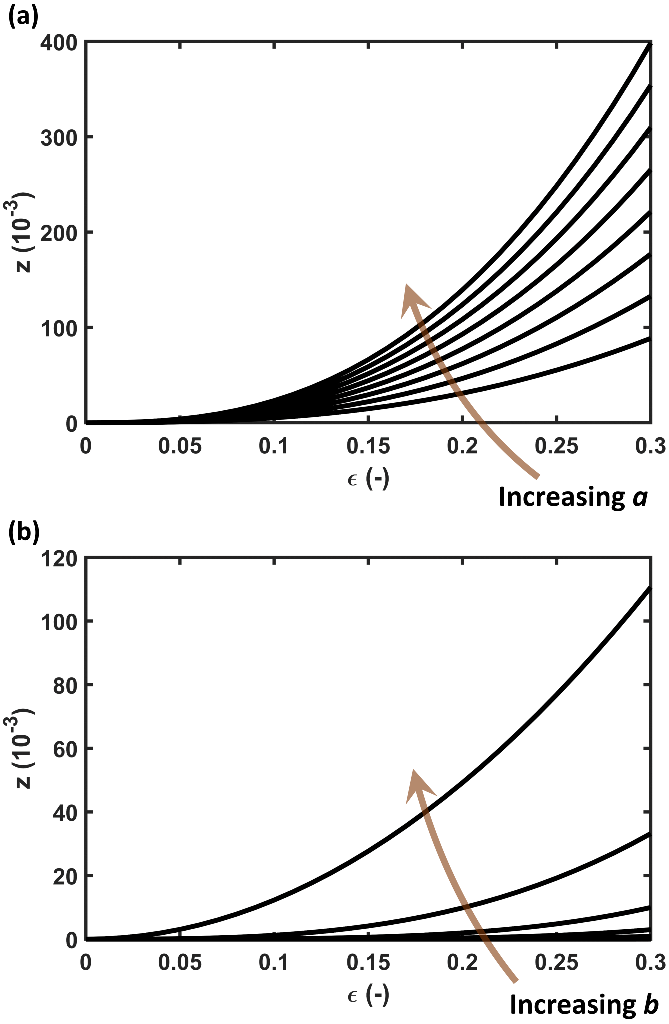

Figure 6.5: Varying the power constant for calculating z ($z = a\epsilon^a$) between values 2 till 10 for (a) a (b) b.

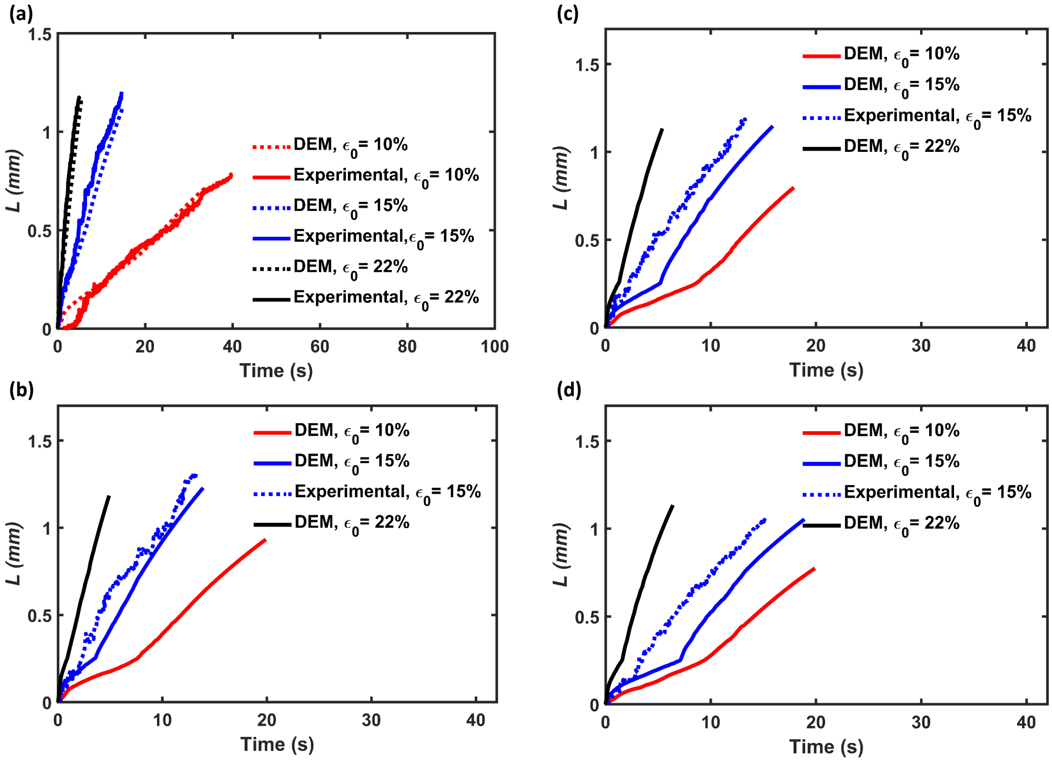

Figure 6.6: Simulate and experimental measured liquid penetration depth as a function of time for the tablets (a) PH101. (b) PH101/CCS, c_{CCS} = 2%. (c) PH101/CCS, c_{CCS} = 5%. (d) PH101/CCS, c_{CCS} = 8%.

ous tablets. Capillary pressure is a measurement of the force necessary to squeeze the liquid through a pore throat. Therefore, the capillary force is a controlling factor of the liquid penetration process [Schoenmaker et al., 2011]. The capillary pressure increases with a decrease in pore throat size. As seen from the figure, the capillary pressure increases rapidly in the initial stages of the liquid penetration, >0.2 mm, across all formulations. The increase indicates the closure of pores in the initial stages of swelling, which was also observed in Figure 5.12 and 5.13 in Chapter 5. After the initial increase, the capillary pressure decreases especially for the tablets with ϵ_0 = 10%. The decrease is due to the pores beginning to open up as tablets start to break up. This is also reflected in the liquid penetration profile (Figure 6.6) as the liquid flow rate increases for almost all the ϵ_0 = 10% tablets after around 10 s. As expected the capillary pressure is higher for formulation with lower porosity, since the pore size is smaller. The capillary pressure seems to be in a similar range for the formulation with the same porosity.

Figure 6.8 shows the permeability-time curve for the various tablets. The permeability is a measure of the capability of a porous medium to transmit fluid [Markl and Zeitler, 2017]. Ganderton and Fraser [1970] reported that factors such as tablet compaction pressure, particle size, and granulation, influenced the porosity and permeability. As seen from Figure 6.8, the permeability is higher for tablets with higher porosity as they is more space for liquid to flow. The difference between the permeability of ϵ_0 = 10% and ϵ_0 = 22% tablets is over 1000 times higher. The permeability is highest for PH101/CCS c_{CCS} = 2% tablets, especially considering ϵ_0 = 22%. Followed by c_{CCS} = 5% and pure PH101 tablet, and lowest for c_{CCS} = 8%. An increase in the CCS content has a negative influence on the liquid flow. However, adding low amount of CCS to a formulation improves the tablet's capability to transmit liquid flow.

6.3.3 Tablet swelling simulations

The swelling profiles for different conditions were simulated using the DEM with a single-particle swelling model and a mathematical model of liquid penetration are given in Figure 6.9. To account for the effect of differences in thickness, H_0, between the DEM and the experimental tablet, the swelling profiles and the time were normalised (T^*).

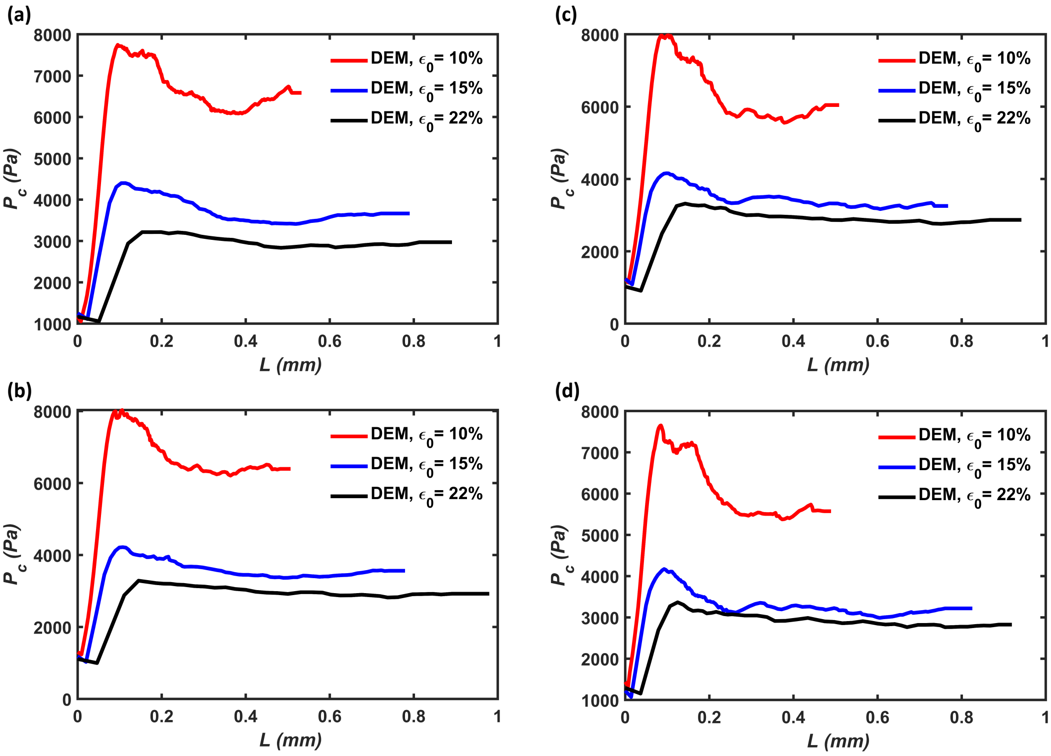

Figure 6.7: Capillary pressure-liquid penetration depth curve for the tablets (a) PH101. (b) PH101/CCS, c_{CCS} = 2%. (c) PH101/CCS, c_{CCS} = 5%. (d) PH101/CCS, c_{CCS} = 8%.

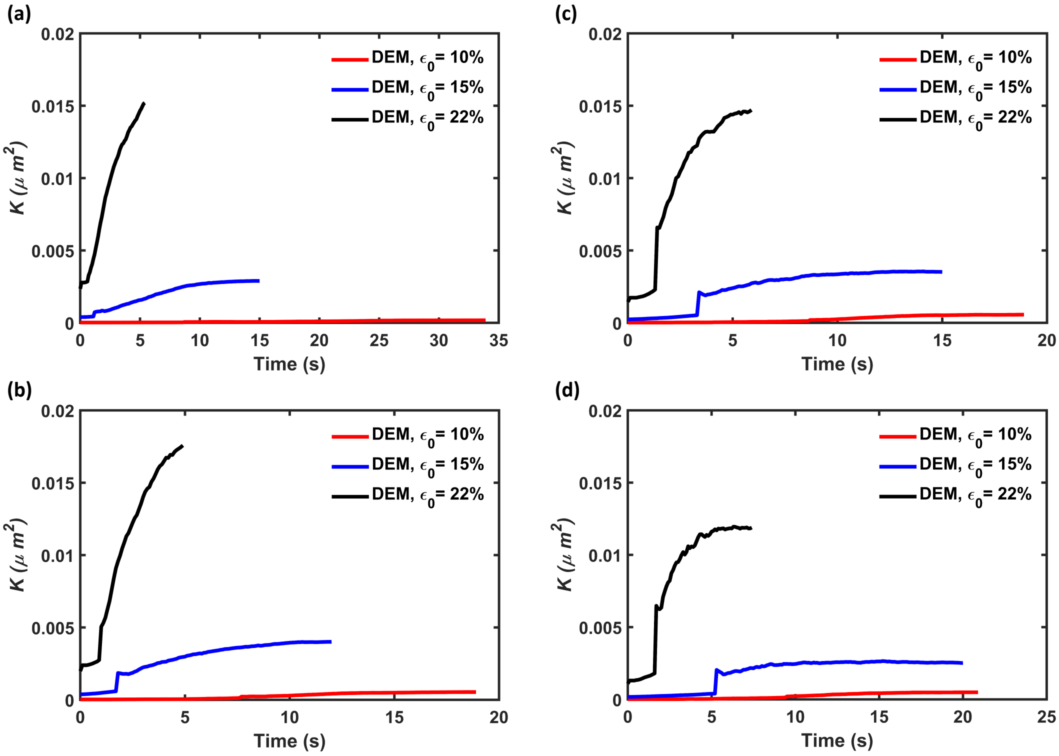

Figure 6.8: Permeability-time curve for the tablets (a) PH101. (b) PH101/CCS, c_{CCS} = 2%. (c) PH101/CCS, c_{CCS} = 5%. (d) PH101/CCS, c_{CCS} = 8%.

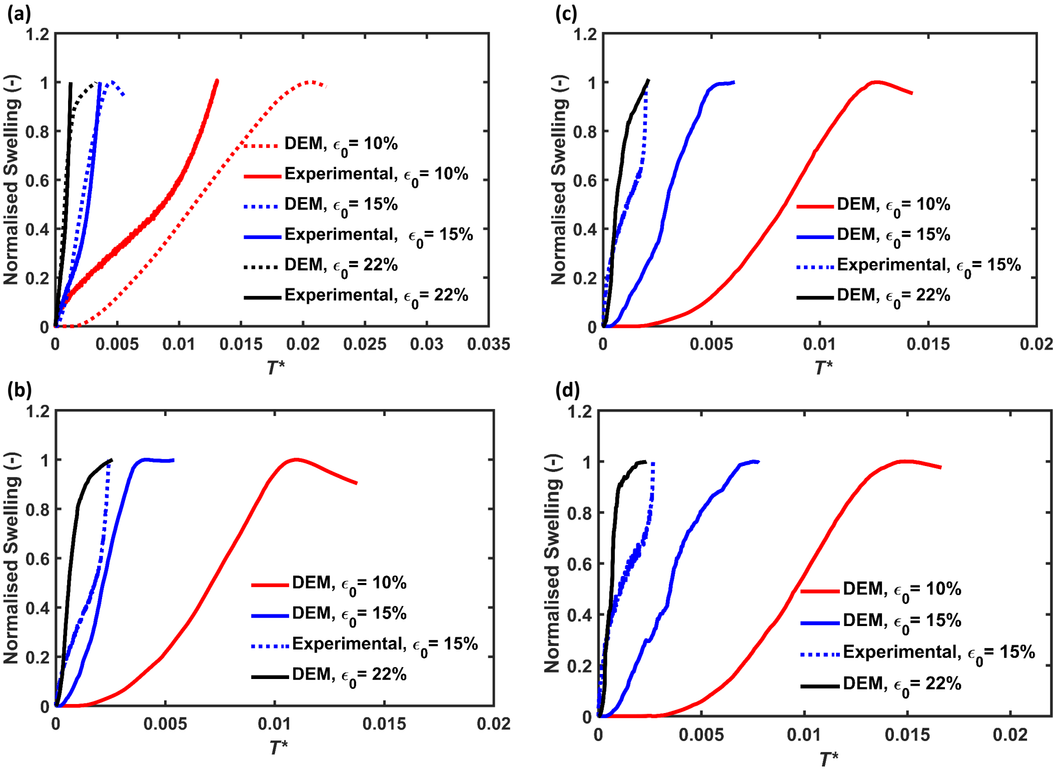

Figure 6.9: Analysis of the DEM simulation of PH101 tablets and comparison to experimental results, normalised swelling by height, as a function of normalised time, T^*. (a) PH101. (b) PH101/CCS, c_{CCS} = 2%. (c) PH101/CCS, c_{CCS} = 5%. (d) PH101/CCS, c_{CCS} = 8%.

The swelling profiles of the experiments and DEM followed different trends though. This was mainly attributed to: (1) limited consideration of the bonding types and compaction mechanisms in DEM, (2) the assumption of a spherical particle shape in the DEM, and (3) differences between the experimental flow cell and simulation setup.

All the formulation follows similar trends, as in the ϵ_0 = 10% has the slowest swelling time, followed by ϵ_0 = 15% and ϵ_0 = 22% being the fastest. The swelling time for PH101/CCS for c_{CCS} = 2% and c_{CCS} = 5% is in the same range. However, PH101/CCS c_{CCS} = 8% is slower than the other, especially for ϵ_0 = 10%. High concentration of CCS in the formulation has a negative effect on the disintegration time. For ϵ_0 = 10% tablets, the initial rate is lower for tablets containing CCS, compared to pure PH101 tablets.

6.3.4 Virtual Design of Experiments: Exploring impact of porosity and disintegrant concentration on swelling and pore structure

Figure 6.10 shows the results of the (normalised) time needed to reach the tablet's maximum swelling capacity (T^*_{max}) and the minimum pore size ratio (PS/PS_0) of the pores placed ahead the liquid front. PS_0 is the initial pore size. The map was developed based on data points for PH101/CCS at ϵ_0 = 10%, ϵ_0 = 15% and ϵ_0 = 22% for concentration c_{CCS} = 2%, c_{CCS} = 5% and c_{CCS} = 8%. The other points on the map were predicted from the simulated data.

There is a significant difference in swelling time between various CCS concentrations at lower porosity values, <ϵ_0 = 15%. c_{CCS} = 8% tablets need almost twice the time to reach their maximum swelling capacity compared to c_{CCS} = 2% tablets. This can be attributed to the closure of the pores, as seen from Figure 6.10(b) the closure is more significant for c_{CCS} > 5%. For tablets with ϵ_0 = 22%, they have almost similar disintegration times. Across all the c_{CCS} the maximum swelling time increases with decreasing the porosity.

Figure 1 in the study by Desai et al. [2014] showed similar trends for CCS as well for other disintegrants. The study showed that an increase in CCS concentration (c_{CCS} > 6%) had a negative effect on the disintegration time and also low c_{CCS} < 3% resulted in slower disintegration time. The disintegration time was lowest for $c_{\text{CCS}} \approx$ 6%. They also reported an increase in hardness for tablets with a higher CCS concentration. Also the study by Kayesh et al. [2021] observed similar correlations between disintegration time and CCS concentrations. They found an increase (c_{CCS} > 5%) in CCS concentration had a negative effect on the disintegration time and also c_{CCS} < 3% resulted in slower disintegration time. A similar trend was observed by Berardi et al. [2018], Maclean et al. [2021], who showed that the disintegration time is prolonged with higher CCS content.

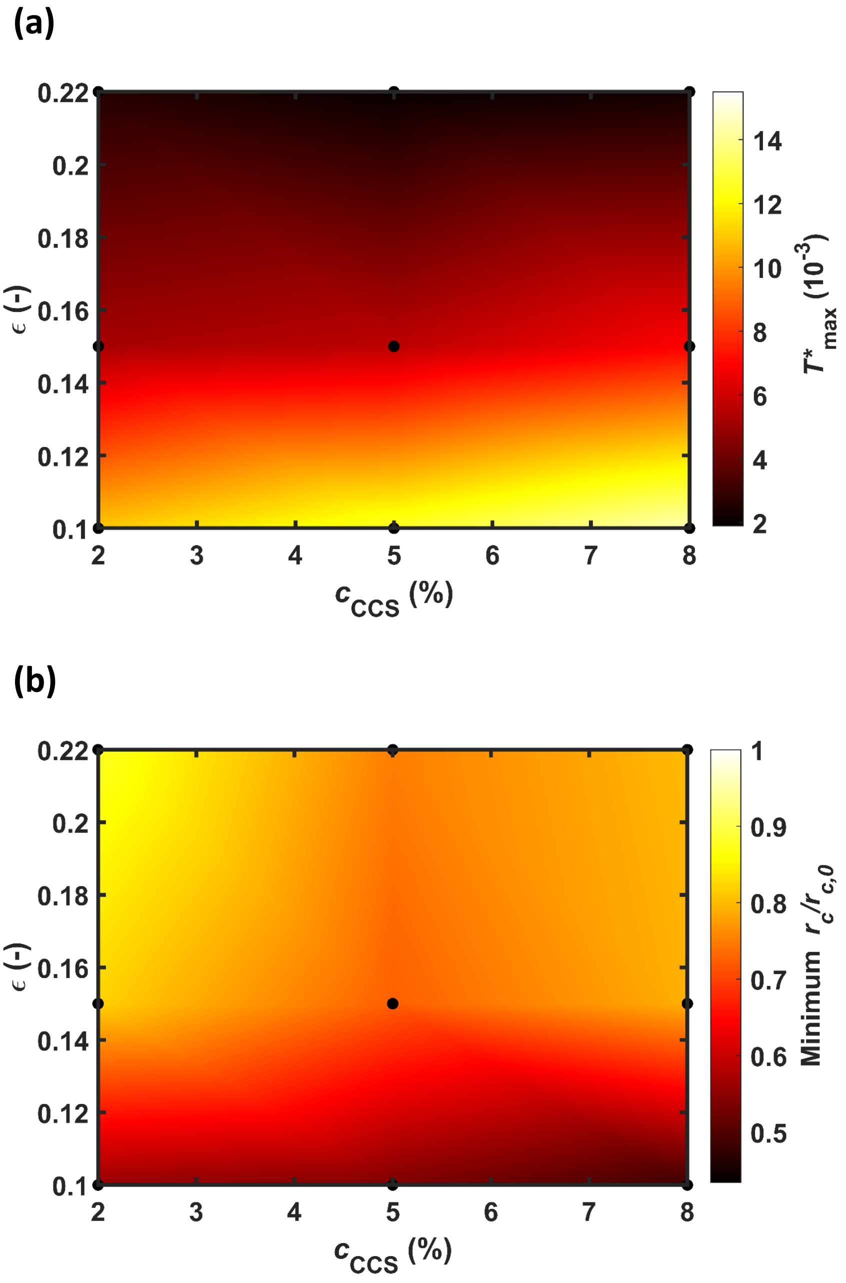

Figure 6.10: Colour map depicting (a) time (normalised) tablet needed to reach the tablet's maximum swelling capacity (T^*_{max}); (b) The minimum pore size ratio (PS/PS$_0$) of the pores placed behind the liquid front with PS$_0$ as the initial pore size.

6.4 Conclusion

This study demonstrated the simulation of tablet swelling by combining DEM with a single-particle swelling model and a mathematical model of liquid penetration. The model was able to simulate the disintegration of different formulations, i.e. varying the porosity and CCS concentration. The liquid penetration model showed that, adding lower amount of CCS to the formulation increases the permeability thereby increases the capability of the tablet to transmit fluid. The swelling profiles showed that all the formulations follow similar trends, as in the ϵ_0 = 10% has the shortest swelling time, followed by ϵ_0 = 15% and ϵ_0 = 22% being the fastest. The virtual DoE showed that across all the c_{CCS} the maximum swelling time increases with decreasing the porosity. It also showed that increasing the CCS concentration above 5% has a negative effect on the disintegration time.

Chapter 7

Conclusions and future work

7.1 Conclusion and summary

This study presents a particle-scale modelling technique for the study of the disintegration process of pharmaceutical tablets. The existing modelling technique discrete element method (DEM) was used, combined with a single particle swelling model and liquid penetration model. The tablet disintegration model developed in this study consist of three main parts: 1) tablet compaction model in DEM, 2) tablet swelling model in DEM with a single particle swelling model and 3) liquid penetration, which was determined either experimentally or through a model. Both the compaction and disintegration model were implemented in the open source DEM software Yade-DEM.

The expansion of single particles paired with a model facilitated the quantification of the swelling of eight pharmaceutical materials as monitored in-situ by a custom-built flow cell. The results clearly highlighted the different swelling behaviour for the various materials, where the swelling capacity (maximum swelling of particle) of the disintegrants follows SSG > CCS > L-HPC and MCC1000 > MCC700 > MCC500 > PH101 > PH102 for the MCC grades. In summary for the disintegrants, the swelling performance of SSG is liquid uptake ability limited, whereas it is absorption capacity limited for CCS and L-HPC. Considering the large concentration of MCC in a typical formulation, MCC contributes significantly to tablet swelling and the disintegration process. It is therefore crucial to understand the swelling characteristics of all excipients to predict the swelling of a tablet and hence be able to rank different formulations in terms of disintegration performance.

Based on single particle model, the swelling of pharmaceutical tablets was modelled on a tablet compaction model in DEM and the liquid penetration was determined using experimental data. The model captured the difference in the swelling behaviour of the tablets with different porosities and formulations well. However, as seen from Figure 5.7 the simulated and experimental swelling profiles have different trends. This is due to factors such as (1) limited consideration of the bonding types and compaction mechanisms in DEM, (2) the assumption of a spherical particle shape in the DEM, and (3) differences between the experimental flow cell and simulation setup. For all tablets, the pore size increased over time, and the pores opened up shortly before the break-up of the tablet. Both in the experiments and DEM, the swelling was slower for tablets with the highest disintegrant concentration (PH101/CCS with c_{CCS} = 8%) due to the closure of the pores in both the wetted volume and dry volume. The closure of pores hinders the liquid from accessing other particles and slows down the overall swelling process.

The tablet swelling model was further developed by include one dimensional liquid penetration model instead experimental data. By using the liquid penetration model and calibration of modelling parameter for the liquid model, the liquid penetration in various different formulation could be determined and the disintegration process of these tablets were modelled. The model was able to simulate the disintegration of different formulation, be varying the porosity and CCS concentration. The liquid penetration model showed that, adding lower amount of CCS to the formulation increase the permeability thereby increases the capability of the tablet to transmit fluid. The results showed that maximum swelling time various formulation showed that across all the c_{CCS} the maximum swelling time increases with decreasing the porosity. Increasing the CCS concentration above, c_{CCS} = 5%, would have a negative effect on the disintegration time.

This study provides new insights into the changes in pore space during the disintegration and how changes in the formulation (material concentration and porosity) affects tablet performance, which is crucial to better understand the impact of porosity and formulations on the performance of tablets. This is particularly important for formulations where the liquid uptake is performance-controlling. The interplay between the formulation, manufacturing conditions, and the dynamic change of the pore space is crucial to make informed decisions during the development of a new drug product. Having a deep understanding of the fundamental changes during the disintegration and dissolution process and its link to the formulation and process conditions can accelerate the development process and increase the robustness of the design process.

7.2 Future work

This project is a fundament for further developing digital formulation design tools for future oral medicines, and move towards simulating the disintegration process without the need of experimental data. Specifically, the following proposals would be interesting to explore and develop on the existing model:

- The studies presented in both Chapter 5 and 6 focused on simulating the disintegration process of tablet consisting of either PH101 or mixture of PH101/CCS. However, in Chapter 4 the swelling of other disintegrant and MCC grades was also quantified. The model from Chapter 6 can be explored with other formulation consisting of, such as SSG, L-HPC, and other grades of MCC. I.e formulation with PH101/SSG, PH102/SSG, PH101/L-HPC along with API to track drug release profile. Also tablet consisting of disintegrants with non-swelling materials such as dibasic calcium phosphate anhydrous (DCP) to quantify the swelling of disintegrants.

- The liquid model presented in Chapter 6 considers the liquid flow only in one dimension. The liquid model needs to be upgraded for a better representation of the disintegration process. The upgraded model will capture the mechanisms involved and pore structure change better. The liquid model presented in Sweijen et al. [2020], pore unit assembly (PUA) method could be used. PUA is already implemented in Yade-DEM, however it only works for high porosity (<0.35). The source for the PUA needs to be modified for accommodating low porosity compacts. The advantage of PUA is that the method focus on the liquid flow in each individually pore. By implementing PUA, the force between liquid and particle can be tracked. Particle-liquid force would strengthen the internal stress during swelling, which cause the bonds that are formed during compaction to break. The pore structure would also be different compared to results presented in this thesis as the liquid flow will cause particle movements, additionally to the movements caused be swelling.

- The study presented in this thesis focused mostly on tablet disintegration process, this causes the tablet to break-up eventually into smaller agglomerates and particles. The size of the disintegrated particles/agglomerates then drives the dissolution rate of the drug. The studies presented in both Chapter 5 and 6, did not consider the modelling of the dissolution process after tablet break-up. The dissolution can be modelled by the Equations presented in Section 1.4.4, also using the Noyes-Whitney equation (see Equation 1.3) and Fick's first law of diffusion (see Equation 1.2).

Appendix A

Code

A.1 Image processing

A.1.1 Large particles

```
clear all;
close all;
utPath = ['..',filesep,'..',filesep,'..',filesep,...
    'Utilities',filesep];
addpath(genpath(utPath));

% Initialisation
exp_mat = 'MCC';
exp_size = 'PH101';
exp_num = 'Exp_06_12';
%type = '*.tif';
video_name='Swelling_MCC_PH101_06_12_MP4.mp4';

light_source = 1;
plotting = 1;
video=1;
image=0;
```

```
laptop=1;
crop=1;
magnification=10;
% folderPath1 = actualFile folder
if laptop
folderPathParent ='C:\Users\njb18198\Dropbox\PhD_Mithu\Swelling';
else
    folderPathParent = 'D:\Mithu\Swelling\';
end

folderPath = fullfile(folderPathParent,exp_mat,exp_size,exp_num);
idxTmp = strfind(folderPath,'/');
folderPath(idxTmp) = filesep;

%imagefiles = dir([folderPath,filesep,type]);

%nfiles = length(imagefiles);    % Number of files found

if video
   % type='*.mp4';
   % videos = dir([folderPath,filesep,type]);
   % video_name=videos(1).name;
    swelling_video = VideoReader(fullfile(folderPath,video_name));
    video_duration = swelling_video.Duration;
    numFrames = swelling_video.NumberOfFrames;
    nfiles=numFrames;
    fps=numFrames/video_duration;
else
    type='*.tif';
    imagefiles = dir([folderPath,filesep,type]);
```

```
    nfiles = length(imagefiles);  % Number of files found
end


% Results = zeros(nfiles,2);

Hblob = vision.BlobAnalysis('MaximumCount',1000,'MinimumBlobArea',10,'PerimeterOutputPort',true,...
    'MajorAxisLengthOutputPort',true,'MinorAxisLengthOutputPort',true);

%Calculating parameter
if magnification==5;
   image_size_real = 3206.29*2404.72;
elseif magnification==10;
    image_size_real = 1603.14*1202.36;
end

if video
    test_image=read(swelling_video,1);
else
   filename = imagefiles(1).name;
   test_image=imread(fullfile(folderPath,filename));
end
[h,w,z] = size(test_image); %resolution
no_pixel = w*h;
% Calculate resolution / pixel size
area_per_pixel = image_size_real/no_pixel;
steps =5;
v = VideoWriter(fullfile(folderPath,[exp_mat,'_',exp_size,'_',
```

```
    exp_num]));
v.FrameRate =25;
open(v);
if video
    start_frame = 354;
    end_frame =1000;
else
    start_frame =22;
    end_frame =nfiles;
end
t=0;
objectProp = cell(round((end_frame-start_frame)/steps),2);
objectResults = zeros(round((end_frame-start_frame)/steps),15);
Radius_distibution=cell(round((end_frame-start_frame)/steps),2);
j=1;
area_store=[];
time_store=[];
area_ellips_store=[];
r_centroid_mean_store=[];

if crop
    if video
        crop_image=read(swelling_video,end_frame);
        [J,rect2]=imcrop(crop_image);
    elseif image
        currentfilename = imagefiles(end_frame).name;
        crop_image=imread(fullfile(folderPath,currentfilename));
        [J,rect2]=imcrop(crop_image);
    end
else
```

```
    rect2=[0 0 w h];
end

for i = start_frame:steps:(start_frame+200)
    %%
    if video
        currentimage=read(swelling_video,i);
        currentimage=imcrop(currentimage,rect2);
        currentimage = rgb2gray(currentimage);
    else
        currentfilename = imagefiles(i).name;
        [currentimage,map] = imread(fullfile(folderPath,currentfilename));
    end

    %% Image processing
    currentimage_sharpen= imsharpen(currentimage,'threshold',0.5,'Amount',2); %sharpen the image
    I_filt = imnlmfilt(currentimage_sharpen,'SearchWindowSize',11);
    mask = zeros(size(currentimage_sharpen));
    mask(25:end-25,25:end-25) = 1;
    BW=activecontour(I_filt , mask, 10000, 'Chan-Vese');
    Threshold=[(1:1:254)/255];
    BW = imbinarize(I_filt,130/255);
    Binarise='manually'
    if manually
        BW = ~imfill(~BW,'holes');
        BW=~imclearborder(~BW);
        %BW = ~bwpropfilt(~BW,'Area',1);
        se = strel('square',1);
```

```
        afterOpening = imopen(BW,se);
        BW = imclose(afterOpening,se);
        BW = ~imfill(~BW,'holes');
        BW=~imclearborder(~BW);
    else
        BW = imfill(BW,'holes');
        BW=imclearborder(BW);
        %BW = ~bwpropfilt(~BW,'Area',1);
        se = strel('square',1);
        afterOpening = imopen(BW,se);
        BW = imclose(afterOpening,se);
        BW = ~imfill(~BW,'holes');
        BW=~imclearborder(~BW);
    end

%     imfilter
    %bw2 = filledgegaps(diff_img, 100);
    %%
    BW2=bwmorph(BW,'bridge');
    BW2=bwmorph(BW2,'endpoints');
    se_value=[1:1:5];
    se = strel('disk',2);
    BW2=imclose(BW2,se);
    BW2=imclearborder(BW2);
    BW2=bwareaopen(BW2,15);
    BW2 = imfill(BW2,'holes');
    [BW2,rect3]=imcrop(BW2);
    BW2=bwmorph(BW2,'bridge');
    BW2 = imfill(BW2,'holes');

```

```
    [x2,y2,BW3,rect4]=imcrop(BW2);
    se = strel('disk',8);
    BW3=imclose(BW3,se);
%     se = strel('disk', 3); % Structuring element for dilation
%     BW3 = imdilate(BW3, se); % Dilating the image
    BW3=bwmorph(BW3,'bridge');
    BW3 = imfill(BW3,'holes');
    BW2((rect4(2)):(rect4(2)+rect4(4)),(rect4(1)):((rect4(1)+rect4(3))))=BW3;


    ed = edge(BW2);
    currentimage_disp=imcrop(currentimage,rect3);
    img_disp = currentimage_disp;
    tmp = img_disp(:,:,1);
    tmp(ed) = 255;
    img_disp(:,:,1) = tmp;

    figure(11)
    imshowpair(img_disp,BW2,'montage');

    if light_source
        BW = ~BW;
    end

    BW=imclearborder(BW);
    BW=imfill(BW,'holes');
    [area,centroid,boundingbox,perimeter,majoraxis,minoraxis] = step(Hblob,BW);
    [~,idxMax]=max(area);
```

```

    objectProp{j,1} = centroid(idxMax,:);
    objectProp{j,2} = boundingbox(idxMax,:);

    objectResults(j,1)= t;
    objectResults(j,2) = area(idxMax);
    objectResults(j,3) = perimeter(idxMax);
    objectResults(j,4) = majoraxis(idxMax);
    objectResults(j,5) = minoraxis(idxMax);

    area_sort=sort(double(area));
    len=length(area_sort);
    if length(area_sort) > 1
        len=length(area_sort);
        BW2=bwareaopen(BW,area_sort(len));
    else
        BW2=BW;
    end
    ed = edge(BW2);
    img_disp = currentimage;

    tmp = img_disp(:,:,1);

    tmp(ed) = 255;
    img_disp(:,:,1) = tmp;

    r_centroid_store=[];
    [row,col]=find(ed==1);
    ed_poistion=[row,col];
    l=1;
```

```
    for k = 1:1:length(row)
        a_2=(((ed_poistion(k,2)-centroid(idxMax,1))*(3206.29/1280))^2);
        b_2=(((ed_poistion(k,1)-centroid(idxMax,2))*(2404.72/960))^2);
        r_centroid=sqrt(a_2+b_2);
        r_centroid_store (l)=r_centroid;
        l=l+1;
    end
    r_centroid_mean_store(j,1)=mean(r_centroid_store);
    r_centroid_mean_store(j,2)=std(r_centroid_store);
    r_current=mean(r_centroid_store);
    sigma_r_current= std(r_centroid_store);
    objectResults(j,6) = r_centroid_mean_store(j,1);
    objectResults(j,7) = r_centroid_mean_store(j,2);
    objectResults(j,8) = r_current-r_centroid_mean_store(1);
    objectResults(j,9) = sqrt((sigma_r_current^2)+(r_centroid_mean_store(1,2)^2));
    objectResults(j,10) = ((r_current/r_centroid_mean_store(1))-1)*100;
    sigma_d_r_0=((r_current/r_centroid_mean_store(1,1))^2)*(r_centroid_mean_store(1,2)^2);
    objectResults(j,11)=(100/r_centroid_mean_store(1,1))*sqrt((sigma_r_current^2)...
     +sigma_d_r_0);
    area_0=4*pi*(r_centroid_mean_store(1,1)^2);
    area_current=4*pi*(r_current^2);
    objectResults(j,12) = ((area_current/area_0)-1)*100;
    sigma_A_t=(100/area_0)*((8*pi*r_current)^2)*(sigma_r_current^2);
```

```
    sigma_A_0=(100*area_current/area_0^2)*((8*pi*r_centroid_mean_store(1,1))^2)*(r_centroid_mean_store(1,2)^2);
    objectResults(j,13)=sqrt(sigma_A_t+sigma_A_0);
    volume_0=(4/3)*pi*(r_centroid_mean_store(1,1)^3);
    volume_current=(4/3)*pi*(r_current^3);
    objectResults(j,14) = ((volume_current/ volume_0)-1)*100;
    sigma_V_t=(100/volume_0)*((4*pi*(r_current^2))^2)*(sigma_r_current^2);
    sigma_V_0=(100*volume_current/volume_0^2)*((4*pi*(r_centroid_mean_store(1,1)^2))^2)*(r_centroid_mean_store(1,2)^2);
    objectResults(j,15)=sqrt(sigma_V_t+sigma_V_0);
    Radius_distibution{j,1}=t/60;
    Radius_distibution{j,2}=r_centroid_store;

    r_relative_change=r_centroid_mean_store-r_centroid_mean_store(1);
    t_store(j)= t./60;
    t_disp=t_store(j);
    J = insertText(img_disp, [50 500], sprintf('t=%2.2f min',t_disp),'FontSize',50,'BoxColor','white','BoxOpacity',1,...
        'AnchorPoint' ,'leftbottom');
    BW2(:, 1:12) = 1; % Make left column white.
    img_disp(:,(end-12):end) = 0; % Make right column white.
    % imshowpair(J,BW2,'montage');
    if plotting
        fontSize = 18;
        fig = figure(2);
        fig.Position = [200 200 600 600];
```

```
            subplot(2,1,1);
            plot(t_store,r_relative_change,'k','LineWidth',2)
            xlabel('Time (min)','FontWeight','bold','fontsize',fontSize)
            ylabel('\it \Deltar (\mum)','FontWeight','bold','fontsize',fontSize)
            xlim([0 1.5])
            ylim([0 10])
            ax.Box = 'on';
            set(gca,'FontSize',fontSize,'FontWeight','bold','linewidth',2)
            set(gcf,'color','w');
            %legend('Radius from area','Radius by ellipsoid','Location','southeast')
            subplot(2,1,2);
            imshowpair(J,BW2,'montage');
            %viscircles(centroid(idxMax,:),radius);
            %title (sprintf('time %d min',(t/60)))
            frame = getframe(gcf);
            writeVideo(v,frame);
        end
        j=j+1;
        if video
            t=t+steps/fps;
        else
            t=t+2.25;
        end
end
close(v);
```

A.1.2 Small particles

```
clear all;
close all;
utPath = ['..',filesep,'..',filesep,'..',filesep,...
    'Utilities',filesep];
addpath(genpath(utPath));

% Initialisation
exp_mat = 'Superdisintegrant';
exp_size = 'SSG';
exp_num = 'Exp_32';
%type = '*.tif';
video_name='SSG_exp_32_MP4.mp4';

light_source = 1;
plotting = 1;
video=1;
image=0;
laptop=1;
crop=1;
magnification=input('Magnification:\n');
% folderPath1 = actualFile folder
if laptop
folderPathParent ='C:\Users\njb18198\Dropbox\PhD_Mithu\Swelling';
else
    folderPathParent = 'D:\Mithu\Swelling\';
end

folderPath = fullfile(folderPathParent,exp_mat,exp_size,exp_num);
idxTmp = strfind(folderPath,'/');
```

```
folderPath(idxTmp) = filesep;

if video
  % type='*.mp4';
  % videos = dir([folderPath,filesep,type]);
  % video_name=videos(1).name;
    swelling_video = VideoReader(fullfile(folderPath,video_name));
    video_duration = swelling_video.Duration;
    numFrames = swelling_video.NumberOfFrames;
    nfiles=numFrames;
    fps=numFrames/video_duration;
else
    type='*.png';
    imagefiles = dir([folderPath,filesep,type]);
    nfiles = length(imagefiles);  % Number of files found
end

Hblob = vision.BlobAnalysis('MaximumCount',1000,'MinimumBlobArea',10,'PerimeterOutputPort',true,...
    'MajorAxisLengthOutputPort',true,'MinorAxisLengthOutputPort',true);

%Calculating parameter
if magnification==5;
    image_size_real = 3206.29*2404.72;
elseif magnification==10;
    image_size_real = 1603.14*1202.36;
elseif magnification==20;
    image_size_real = 1603.14*1202.36;
end
```

```

if video
     test_image=read(swelling_video,1);
else
    filename = imagefiles(1).name;
    test_image=imread(fullfile(folderPath,filename));
end
[h,w,z] = size(test_image); %resolution
no_pixel = w*h;
% Calculate resolution / pixel size
area_per_pixel = image_size_real/no_pixel;
steps =3;
v = VideoWriter(fullfile(folderPath,[exp_mat,'_',exp_size,'_',
    exp_num]));
v.FrameRate =25;
%open(v);
if video
     start_frame =97;
     end_frame=103;
else
     start_frame =1;
     end_frame =nfiles;
end
t=0;
objectProp = cell(round((end_frame-start_frame)/steps),2);
objectResults = zeros(round((end_frame-start_frame)/steps),16);
Radius_distibution=cell(round((end_frame-start_frame)/steps),2);
j=1;
area_store=[];
time_store=[];
```

```
area_ellips_store=[];
r_centroid_mean_store=[];

if crop
    if video
        crop_image=read(swelling_video,end_frame);
        [J,rect2]=imcrop(crop_image);
    elseif image
        currentfilename = imagefiles(1).name;
        crop_image=imread(fullfile(folderPath,currentfilename));
        [J,rect2]=imcrop(crop_image);
    end
else
    rect2=[0 0 w h];
end

start_frame=97;
t=3.6181+steps/fps;

for i = start_frame:steps:end_frame
    %%
    if video
        currentimage=read(swelling_video,i);
        currentimage=imcrop(currentimage,rect2);
        currentimage = rgb2gray(currentimage);
    else
        currentfilename = imagefiles(i).name;
        [currentimage,map] = imread(fullfile(folderPath,
            currentfilename));
        currentimage=imcrop(currentimage,rect2);
```

```
        currentimage = rgb2gray(currentimage);
    end

    %% Image processing
    currentimage_sharpen= imsharpen(currentimage,'threshold',0.5,'Amount',2); %sharpen the image
    I_filt = imnlmfilt(currentimage_sharpen,'SearchWindowSize',11);
    %I_filt = adapthisteq(I_filt);
    size_img=size(I_filt);
    if j<15;
        img=imshow(currentimage_sharpen);
    else
        ed = edge(BW);
        img_disp = currentimage_sharpen;
        tmp = img_disp(:,:,1);
        tmp(ed) = 255;
        img_disp(:,:,1) = tmp;
        img=imshow(img_disp);
      % img=imshow(currentimage_sharpen);
    end
    roi =drawassisted(img,'LineWidth',1);
    draw(roi);
    Position=round(roi.Position);
    BW=zeros(size_img(1),size_img(2));
    for k=1:length(Position);
        BW(Position(k,2),Position(k,1))=1;
    end
    BW=bwmorph(BW,'bridge');
    BW = imfill(BW,'holes');
    ed = edge(BW);
```

```
    img_disp = currentimage;
    tmp = img_disp(:,:,1);
    tmp(ed) = 255;
    img_disp(:,:,1) = tmp;
    figure(1)
    imshowpair(img_disp,BW, 'montage');

    [area,centroid,boundingbox,perimeter,majoraxis,minoraxis] =
        step(Hblob,BW);
    [~,idxMax]=max(area);

    objectProp{j,1} = centroid(idxMax,:);
    objectProp{j,2} = boundingbox(idxMax,:);

    objectResults(j,1)= t;
    objectResults(j,2) = area(idxMax);
    objectResults(j,3) = perimeter(idxMax);
    objectResults(j,4) = majoraxis(idxMax);
    objectResults(j,5) = minoraxis(idxMax);



    r_centroid_store=[];
    [row,col]=find(ed==1);
    ed_poistion=[row,col];
    l=1;
    if magnification==10;
        real_a=1603.14/1280;
        real_b=1202.36/960;
    elseif  magnification==5;
```

```
        real_a=3206.29/1280;
        real_b=2404.72/960;
    elseif  magnification==20;
        real_a=801.57/1280;
        real_b=601.18/960;
    end
    for k = 1:1:length(row)
        a_2=(((ed_poistion(k,2)-centroid(idxMax,1))*(real_a))^2);
        b_2=(((ed_poistion(k,1)-centroid(idxMax,2))*(real_b))^2);
        r_centroid=sqrt(a_2+b_2);
        r_centroid_store (l)=r_centroid;
        l=l+1;
    end
    r_centroid_mean_store(j,1)=mean(r_centroid_store);
    r_centroid_mean_store(j,2)=std(r_centroid_store);
    r_current=mean(r_centroid_store);
    sigma_r_current= std(r_centroid_store);
    objectResults(j,6) = r_centroid_mean_store(j,1);
    objectResults(j,7) = r_centroid_mean_store(j,2);
    objectResults(j,8) = r_current-r_centroid_mean_store(1);
    objectResults(j,9) = sqrt((sigma_r_current^2)+(
        r_centroid_mean_store(1,2)^2));
    objectResults(j,10) = ((r_current/r_centroid_mean_store(1))-1)
        *100;
    sigma_d_r_0=((r_current/r_centroid_mean_store(1,1))^2)*(
        r_centroid_mean_store(1,2)^2);
    objectResults(j,11)=(100/r_centroid_mean_store(1,1))*sqrt((
        sigma_r_current^2)...
        +sigma_d_r_0);
    area_0=4*pi*(r_centroid_mean_store(1,1)^2);
```

```
    area_current=4*pi*(r_current^2);
    objectResults(j,12) = ((area_current/area_0)-1)*100;
    sigma_A_t=(100/area_0)*((8*pi*r_current)^2)*(sigma_r_current^2);
    sigma_A_0=(100*area_current/area_0^2)*((8*pi*r_centroid_mean_store(1,1))^2)*(r_centroid_mean_store(1,2)^2);
    objectResults(j,13)=sqrt(sigma_A_t+sigma_A_0);
    volume_0=(4/3)*pi*(r_centroid_mean_store(1,1)^3);
    volume_current=(4/3)*pi*(r_current^3);
    objectResults(j,14) = ((volume_current/ volume_0)-1)*100;
    sigma_V_t=(100/volume_0)*((4*pi*(r_current^2))^2)*(sigma_r_current^2);
    sigma_V_0=(100*volume_current/volume_0^2)*((4*pi*(r_centroid_mean_store(1,1)^2))^2)*(r_centroid_mean_store(1,2)^2);
    objectResults(j,15)=sqrt(sigma_V_t+sigma_V_0);
    Radius_distibution{j,1}=t;
    Radius_distibution{j,2}=r_centroid_store;
    objectResults(j,16)= i;

    j=j+1;
    if video
        t=t+steps/fps;
    else
        t=t+2.25;
    end
    disp (r_centroid_mean_store)
    disp(max(area))
    colNames = {'t_sec','area','perimeter','majoraxis','minoaxis','
```

```
R_p','sigma_r','delta_r','sigma_delta_r'...
        ,'r_relative','sigma_rel_r','a_relative','sigma_rel_A','V_relative','sigma_rel_V','Image_number'};
    Results=array2table(objectResults,'VariableNames',colNames);
    Resultsfolderpath=fullfile(folderPath,['Results_1_',exp_mat,'_',exp_size,'_',exp_num,'.csv']);
    idxTmp = strfind(Resultsfolderpath,'/');
    Resultsfolderpath(idxTmp) = filesep;
    writetable(Results,Resultsfolderpath);
    folderPathParentSave = folderPathParent;
    Radius_dis = fullfile(folderPath,'Radius_distribution_1.csv'); %must end in csv
    writetable(cell2table(Radius_distibution), Radius_dis, 'writevariablenames', false, 'quotestrings', true);
end
```

A.2 DEM simulation

A.2.1 Tablet swelling model with experimental liquid penetration data

```
# -*- coding: utf-8 -*-
"""
Created on Thu Jul 15 16:29:55 2021

@author: njb18198
"""

#!/usr/bin/env python
#encoding: ascii

# Testing of the Deformation Enginge with Luding Contact Law
# Modified Oedometric Test
# The reference paper [Haustein2017]
from __future__ import print_function
from yade import utils, plot, timing
from yade import pack
import pandas as pd
import numpy as np
from PIL import Image
from yade import pack, export
from scipy.interpolate import interp1d
from csv import writer
import os
from scipy.integrate import odeint
import matplotlib.pyplot as plt
import csv
from matplotlib.pyplot import figure
```

```
from pylab import *
from scipy.optimize import curve_fit
readParamsFromTable(comp_press=0.792e8,h_tab=2.02,m_tab=0.2117,r_tab=5.015,wCCS=0.02,tab_porosity=15,tab_height=1,save=0)
from yade.params.table import *
import scipy.spatial


O = Omega()
save=save
# Physical parameters
fr_PH101 = 0.41
fr_CCS=0.69
rho_PH101 = 1561
rho_CCS =1403
D_PH101 = 7.9e-5
r1_PH101 = D_PH101/2
D_CCS = 5.4e-5
r1_CCS = D_CCS/2
#r2 = Diameter/2
k1 = 10000
kp = 140000
kc = k1 * 0.1
ks = k1 * 0.1
Chi1 = 0.34
PhiF1=0.999

O.dt = 1.0e-8
particleMass_PH101 = (4.0/3.0)*math.pi*r1_PH101*r1_PH101*r1_PH101*rho_PH101
```

```
particleMass_CCS = (4.0/3.0)*math.pi*r1_CCS*r1_CCS*r1_CCS*rho_CCS
m_tab_PH101=m_tab*1e-3*(1-wCCS)
m_tab_CCS=m_tab*1e-3*wCCS
tab_no_p_PH101=m_tab_PH101/particleMass_PH101
tab_no_p_CCS =m_tab_CCS /particleMass_CCS
Tab_rad=0.001
r_tab=r_tab*1e-3 #real size
h_tab=h_tab*1e-3
v_tab=math.pi*(r_tab**2)*h_tab
v_1mm=math.pi*(Tab_rad**2)*(1e-3)
no_p_PH101=(v_1mm/v_tab)*tab_no_p_PH101
no_p_CCS=(v_1mm/v_tab)*tab_no_p_CCS

Cyl_height=0.006
cross_area=math.pi*(Tab_rad**2)
Comp_press_up= comp_press
Comp_force_up=Comp_press_up*cross_area
Comp_press_lp= comp_press
Comp_force_lp=Comp_press_lp*cross_area

#************************************
compression_data_save=[]
sc_por_15=2
#sc_por_2=2
#sc_por_1=1
rho_mix=((wCCS/rho_CCS)+((1-wCCS)/rho_PH101))**-1
data_to_save=[comp_press/1e6,round(no_p_PH101)+round(no_p_CCS),
    rho_mix]
compression_data_save.append(data_to_save)

```

```
# Add material
matPH101 = O.materials.append(LudingMat(frictionAngle=fr_PH101, density=rho_PH101, k1=k1, kp=kp, ks=ks, kc=kc, PhiF=PhiF1, G0 = 0.0))
matCCS = O.materials.append(LudingMat(frictionAngle=fr_CCS, density=rho_CCS, k1=k1, kp=kp, ks=ks, kc=kc, PhiF=PhiF1, G0 = 0.0))

# Spheres for compression and walls
sp=pack.SpherePack()
sp.makeCloud((-8*D_PH101,-8*D_PH101,-35*D_PH101),(8*D_PH101,8*D_PH101,35.0*D_PH101), rMean=r1_PH101,rRelFuzz=0.18,num=round(no_p_PH101))
n1 = len(sp)
sp.makeCloud((-8*D_PH101,-8*D_PH101,-35*D_PH101),(8*D_PH101,8*D_PH101,35.0*D_PH101), rMean=r1_CCS,rRelFuzz=0.15,num=round(no_p_CCS))
for i,(c,r) in enumerate(sp):
    mat = matPH101 if i < n1 else matCCS
    color = (0,1,1) if i < n1 else (1,0,1)
    O.bodies.append(sphere(c,r,material=mat,color=color))

walls=O.bodies.append(yade.geom.facetCylinder((0,0,0),radius=Tab_rad,height=Cyl_height,segmentsNumber=20,wallMask=6,material=matPH101))


vtkRecorder = VTKRecorder(fileName='vtkRecorder_'+str(wCCS), recorders=['all'])
tab_porosity=tab_porosity
tab_height=tab_height
```

```

##Single particle swelling model
def model(r,t,Q_max,rho_t,rho_w,r_0,Diff):
    Q=((rho_w*(r**3))/(rho_t*(r_0**3)))-(rho_w/rho_t)+1;
    drdt  =((Diff*rho_t)/(r*rho_w))*((Q_max-Q)/Q);
    return drdt
P_PH101=[1.45,rho_PH101,1000,396.39e-12]
P_CCS=[3.16, rho_CCS, 1000, 739.75e-12]


# Add engines
o.engines = [
  ForceResetter(),
  InsertionSortCollider([Bo1_Sphere_Aabb(aabbEnlargeFactor=1.05),
                         Bo1_Wall_Aabb(),
                         Bo1_Facet_Aabb()
                         ]),
  InteractionLoop(
    [Ig2_Sphere_Sphere_ScGeom(interactionDetectionFactor=1.05),
     Ig2_Facet_Sphere_ScGeom(),
     Ig2_Wall_Sphere_ScGeom()],
    [Ip2_LudingMat_LudingMat_LudingPhys()],
    [Law2_ScGeom_LudingPhys_Basic()]
  ),
  NewtonIntegrator(damping=0.1, gravity=[0, 0,-9.81]),
  PyRunner(command='checkForce()', realPeriod=1, label="fCheck"),
  #DeformControl(label="DefControl")
]

###Compaction model###
```

```
def checkForce():
    if O.iter < 4000000:
        return
    if unbalancedForce() > 1:
        return
    global upper_punch
    upper_punch=O.bodies.append(geom.facetCylinder((0,0,((-
        Cyl_height/2)+0.0001)+utils.aabbDim()[2]),Tab_rad-.00001,0,
        segmentsNumber=50,wallMask=1))
    for i in upper_punch:
        body= O.bodies[i]
        body.state.vel = (0,0,-0.02)
    global lower_punch
    lower_punch= O.bodies.append(geom.facetCylinder((0,0,(-
        Cyl_height/2)-0.0001),Tab_rad-.00001,0,segmentsNumber=50,
        wallMask=1))
    for n in lower_punch:
        body= O.bodies[n]
        body.state.vel = (0,0,0.02)
    O.engines = O.engines + [PyRunner(command='storeData()',
        iterPeriod=1000)]+ [PyRunner(command='saveData()',
        iterPeriod=100000)]
    fCheck.command = 'unloadPlate()'

def unloadPlate():
    force_up=0
    for i in upper_punch:
        body= O.bodies[i]
        force_up=force_up+abs(O.forces.f(body.id)[2])
    force_lp=0
```

```
    for n in lower_punch:
        body = O.bodies[n]
        force_lp = force_lp + abs(O.forces.f(body.id)[2])
    if ((force_up > Comp_force_up) and (force_lp > Comp_force_lp)):
        for i in upper_punch:
            body= O.bodies[i]
            body.state.vel = (0,0,0.04)
        for n in lower_punch:
            body= O.bodies[n]
            body.state.vel = (0,0,-0.04)
        fCheck.command = 'stopUnloading()'

def stopUnloading():
    #force_up=0
    #for i in upper_punch:
        #body= O.bodies[i]
        #force_up=force_up+(O.forces.f(body.id)[2])
    force_lp=0
    for n in lower_punch:
        body = O.bodies[n]
        force_lp = force_lp + abs(O.forces.f(body.id)[2])
    if force_lp==0:
        for i in lower_punch:
            body= O.bodies[i]
            body.state.vel = (0,0,0)
    #if ((force_up==0) and (force_lp==0)):
    for i in upper_punch:
        body=O.bodies[i]
        pos_up=body.state.pos
    for i in lower_punch:
```

```
        body=O.bodies[i]
        pos_lp=body.state.pos
    if pos_up[2]> pos_lp[2]+utils.aabbDim()[2]+0.0002:
        for j in upper_punch: O.bodies.erase(j)
        fCheck.command = 'Savecheck()'

def storeData():
    if save==1:
        #for i in lower_punch:
            #body= O.bodies[i]
            #vel=body.state.vel
        #if vel==0:
            #porosity=voxelPorosity(resolution=200,start=(utils.aabbExtrema()[0]+(sc_por*D,sc_por*D,sc_por*D)),end=(utils.aabbExtrema()[1]-(sc_por*D,sc_por*D,sc_por*D)))
            #data_to_save=[porosity,0]Tablet_swelling
            #compression_data_save.append(data_to_save)
        force_up=0
        for i in upper_punch:
            body= O.bodies[i]
            force_up=force_up+abs(O.forces.f(body.id)[2])
        force_lp=0
        for n in lower_punch:
            body = O.bodies[n]
            force_lp = force_lp + abs(O.forces.f(body.id)[2])
        compression_pressure=((force_up+force_lp)/(cross_area))*1e-6
        if compression_pressure < 0.02:
            return
```

```
        #porosity_1=voxelPorosity(resolution=200,start=(utils.aabbExtrema()[0]+(sc_por_1*D,sc_por_1*D,sc_por_1*D)),end=(utils.aabbExtrema()[1]-(sc_por_1*D,sc_por_1*D,sc_por_1*D)))
        voxel_porosity=voxelPorosity(resolution=200,start=(utils.aabbExtrema()[0]+(sc_por_15*D_PH101,sc_por_15*D_PH101,sc_por_15*D_PH101)),end=(utils.aabbExtrema()[1]-(sc_por_15*D_PH101,sc_por_15*D_PH101,sc_por_15*D_PH101)))
        #utils_porosity=utils.porosity()
        #porosity_2=voxelPorosity(resolution=200,start=(utils.aabbExtrema()[0]+(sc_por_2*D,sc_por_2*D,sc_por_2*D)),end=(utils.aabbExtrema()[1]-(sc_por_2*D,sc_por_2*D,sc_por_2*D)))
        data_to_save=[voxel_porosity ,compression_pressure]
        compression_data_save.append(data_to_save)
        if voxel_porosity>0.9:
            o.pause()

def saveData():
    if save==1:
        compression_data=pd.DataFrame(compression_data_save,columns=['Porosity','Compression_pressure','density'])
        path_save='/home/mithushan/Compaction_data/Sim'
        base_filename='PH101_CCS_'+str(wCCS)+'_compression_data.csv'
        compression_data.to_csv(os.path.join(path_save,base_filename))

def Savecheck():
    if save==1:
```

```
        utils.saveVars('lower_punch',lower_punch=lower_punch)
        save_filename='PH101_CCS_'+str(wCCS)+'.xml'
        o.save(save_filename)
        o.pause()
        voxel_porosity=voxelPorosity(resolution=200,start=(utils.aabbExtrema()[0]+(sc_por_15*D_PH101,sc_por_15*D_PH101,sc_por_15*D_PH101)),end=(utils.aabbExtrema()[1]-(sc_por_15*D_PH101,sc_por_15*D_PH101,sc_por_15*D_PH101)))
        data_to_save=[voxel_porosity,0]
        compression_data_save.append(data_to_save)
        compression_data=pd.DataFrame(compression_data_save,columns=['Porosity','Compression_pressure','density'])
        path_save='/home/mithushan/Compaction_data/Sim'
        base_filename='PH101_CCS_'+str(wCCS)+'_compression_data.csv'

        compression_data.to_csv(os.path.join(path_save,base_filename))
    if save==0:
        o.engines = o.engines+[PyRunner(command='ParticleSwelling()', iterPeriod=100000)]+[PyRunner(command='ForceStore()', iterPeriod=500000)]+[PyRunner(command='PoreSize()', iterPeriod=500000)]+[PyRunner(command='VTKSave()', iterPeriod=250000)]
        fCheck.dead = True # (!!!)
        storeData.dead=True
        saveData.dead=True

##Tablet swelling model###
def ParticleSwelling():
    time_current=(o.iter-initial_save[0])*o.dt
```

```
    if wCCS==0.02:
        Liq_pos=0.1871*(time_current**0.7339) #mm
    elif wCCS==0.05:
        Liq_pos=0.1359*(time_current**0.8279) #mm
    elif wCCS==0.08:
        Liq_pos=0.0968*(time_current**0.8739)
    Liq_pos=Liq_pos*1e-3 #convert to m
    print(Liq_pos)
    print(time_current)
    radius=[]
    fw=[]
    z_min=utils.aabbExtrema()[1][2]
    radius.append(time_current)
    for b in O.bodies:
        if isinstance(b.shape, Sphere):
            par_pos=initial_save[1]-b.state.pos[2]
            k=b.id
            r_now=b.shape.radius
            if Liq_pos>=par_pos:
                r_0=r_save[0][k+1]
                if swell_t[0][k]==0:
                    swell_t[0][k]=time_current
                    radius.append(b.shape.radius-r_save[0][k+1])
                    continue
                time=time_current-swell_t[0][k]
                t = np.linspace(0,time)
                if b.mat.id==0:
                    P=P_PH101
                elif b.mat.id==1:
                    P=P_CCS
```

```
                r = odeint(model,r_0,t,args=(P[0],P[1],P[2],r_0,
                    fw_D[0][k],))
                r_new=float(r[-1])
                b.shape.radius = float(r[-1])
                radius.append(b.shape.radius-r_save[0][k+1])
                f=float(r[-1])/r_now
                mcurrent=b.state.mass
                mnew=mcurrent*(f*f*f)
                b.state.mass=mnew
                Icurrent=b.state.inertia
                Inew=Icurrent*(f*f*f*f*f)
                b.state.inertia[0]=Inew[0]
                b.state.inertia[1]=Inew[1]
                b.state.inertia[2]=Icurrent[2]
                z_current=b.state.pos[2]
                if z_min>z_current:
                    z_min=z_current
                else:
                    z_min=z_min
            elif Liq_pos<par_pos:
                radius.append(b.shape.radius-r_save[0][k+1])
    r_save.append(radius)
    start_voxel=(extrema[0][0]+1*D_PH101,extrema[0][1]+1*D_PH101,
        z_min)
    #end_voxel=(extrema[1][0]-1*D_PH101,extrema[1][1]-1*D_PH101,
        utils.aabbExtrema()[1][2])
    porosity_wetted=voxelPorosity(resolution=200,start=start_voxel,
        end=end_voxel)
    start_voxel=(extrema[0][0]+sc_por_15*D_PH101,extrema[0][1]+
        sc_por_15*D_PH101,utils.aabbExtrema()[0][2]+sc_por_15*
```

```
D_PH101)
    #end_voxel=(extrema[1][0]-sc_por_15*D_PH101,extrema[1][1]-sc_por_15*D_PH101,utils.aabbExtrema()[1][2]-sc_por_15*D_PH101)
    porosity_overall=voxelPorosity(resolution=200,start=start_voxel,end=end_voxel)
    time_current=(o.iter-initial_save[0])*o.dt
    porosity_current=[time_current,porosity_overall,porosity_wetted]
    porosity_save.append(porosity_current)
    porosity_data=pd.DataFrame(porosity_save, columns=['time','Porosity','Porosity_wetted'])
    path_save='/home/mithushan/Swelling'
    base_filename='PH101_CCS_porosity_'+str(wCCS)+'.csv'
    porosity_data.to_csv(os.path.join(path_save,base_filename))
    time_current=(o.iter-initial_save[0])*o.dt
    size_current=[time_current,utils.aabbDim()[2]]
    size_save.append(size_current)
    size_data=pd.DataFrame(size_save, columns=['time','Tablet_height'])
    base_filename='PH101_CCS_height_'+str(wCCS)+'.csv'
    size_data.to_csv(os.path.join(path_save,base_filename))
    radius_data=pd.DataFrame(r_save)
    base_filename='PH101_CCS_radius_data_'+str(wCCS)+'.csv'
    radius_data.to_csv(os.path.join(path_save,base_filename))
    id_pos_current=[]
    id_pos_current.append(time_current)
    for i in range (len(id_THz_val)):
        p_id=id_THz_val[i]
        id_pos_current.append(O.bodies[p_id].state.pos[2])
```

```
    id_pos_save.append(id_pos_current)
    THz_validation_data=pd.DataFrame(id_pos_save)
    base_filename='PH101_CCS_THz_validation_data_front_'+str(wCCS)+'.csv'
    THz_validation_data.to_csv(os.path.join(path_save,base_filename))
    id_pos_current_back=[]
    id_pos_current_back.append(time_current)
    for i in range (len(id_THz_val_back)):
        p_id_back=id_THz_val_back[i]
        id_pos_current_back.append(O.bodies[p_id_back].state.pos[2])
    id_pos_save_back.append(id_pos_current_back)
    THz_validation_data_back=pd.DataFrame(id_pos_save_back)
    base_filename='PH101_CCS_THz_validation_data_back_'+str(wCCS)+'.csv'
    THz_validation_data_back.to_csv(os.path.join(path_save,base_filename))


def PoreSize():
    time_current=(o.iter-initial_save[0])*o.dt
    file_name='PH101_CCS_particle_pos_'+str(wCCS)+'_'+str(time_current)+'.txt'
    export.text(file_name)

def VTKSave():
    vtkRecorder()

def ForceStore():
```

```
    time_current=(o.iter-initial_save[0])*o.dt
    forces=[]
    for b in O.bodies:
        if isinstance(b.shape, Sphere):
            k=b.id
            forces.append(o.forces.f(k))
    force_data=pd.DataFrame(forces)
    path_save='/home/mithushan/Swelling'
    base_filename='PH101_CCS_force_'+str(wCCS)+'_'+str(time_current)+'.csv'
    force_data.to_csv(os.path.join(path_save,base_filename))


if save==1:
    O.run()
    waitIfBatch()
    g=-9.81

if save==0:
    read_filename='PH101_CCS_'+str(wCCS)+'.xml'
    o.load(read_filename)
    utils.loadVars('lower_punch')
    from yade.params.lower_punch import *
    for b in O.bodies:
        if isinstance(b.shape, Sphere):
            #b.state.blockedDOFs = 'xyXY'

            r=b.shape.radius
            oldm=b.state.mass
            oldI=b.state.inertia
```

```

            m=oldm*3./4./r
            b.state.mass=m

            b.state.inertia[0] = 15./16./r*oldI[0]      #inertia with respect to x and y axes are not used and the computation here is wrong
            b.state.inertia[1] = 15./16./r*oldI[1]  #inertia with respect to x and y axes are not used and the computation here is wrong
            b.state.inertia[2] = 15./16./r*oldI[2]  #only inertia with respect to z axis is usefull
    o.dt=1e-6
    r_save=[]
    radius=[]
    initial_save=[]
    size_save=[]
    pos_save_z=[]
    id_pos_save=[]
    id_pos_save_back=[]
    id_pos_current=[]
    id_pos_current_back=[]
    porosity_save=[]
    initial_save.append(O.iter)
    for b in O.bodies:
        if isinstance(b.shape, Sphere):
            pos_save_z.append(b.state.pos[2])
    initial_save.append(max(pos_save_z)+r1_PH101)
    max_z=max(pos_save_z)
    id_THz_val=[]
```

```
    for b in O.bodies:
        if isinstance(b.shape, Sphere):
            if(-3.0*D_PH101<=b.state.pos[0]<=3.0*D_PH101 and -3.0*D_PH101<=b.state.pos[1]<=3.0*D_PH101  and max_z-1*D_PH101<=b.state.pos[2]<=max_z):
                id_THz_val.append(b.id)
    for i in range (len(id_THz_val)):
        if i==0:
            id_pos_current.append(0)
        p_id=id_THz_val[i]
        id_pos_current.append(O.bodies[p_id].state.pos[2])
    id_pos_save.append(id_pos_current)
    THz_validation_data=pd.DataFrame(id_pos_save)
    path_save='/home/mithushan/Swelling'
    base_filename='PH101_CCS_THz_validation_data_front_'+str(wCCS)+'.csv'
    THz_validation_data.to_csv(os.path.join(path_save,base_filename))

    min_z=min(pos_save_z)
    id_THz_val_back=[]
    for b in O.bodies:
        if isinstance(b.shape, Sphere):
            if(-5.0*D_PH101<=b.state.pos[0]<=5.0*D_PH101 and -5.0*D_PH101<=b.state.pos[1]<=5.0*D_PH101  and min_z<=b.state.pos[2]<=min_z+1*D_PH101):
                id_THz_val_back.append(b.id)
    for i in range (len(id_THz_val_back)):
        if i==0:
            id_pos_current.append(0)
```

```
        p_id_back=id_THz_val_back[i]
        id_pos_current_back.append(O.bodies[p_id_back].state.pos[2])
    id_pos_save_back.append(id_pos_current_back)
    THz_validation_data_back=pd.DataFrame(id_pos_save_back)
    path_save='/home/mithushan/Swelling'
    base_filename='PH101_CCS_THz_validation_data_back_'+str(wCCS)+'.csv'
    THz_validation_data_back.to_csv(os.path.join(path_save, base_filename))

    #start_voxel=(utils.aabbExtrema()[0]+(sc_por_15*D,sc_por_15*D,sc_por_15*D))
    end_voxel=(utils.aabbExtrema()[1]-(sc_por_15*D_PH101,sc_por_15*D_PH101,sc_por_15*D_PH101))
    radius.append(0)
    i=0
    for b in O.bodies:
        if isinstance(b.shape, Sphere):
            radius.append(b.shape.radius)
    r_save.append(radius)
    no_p = 0
    for b in O.bodies:
        if isinstance(b.shape, Sphere):
            no_p +=1
    swell_t=np.zeros((1,round(no_p)))
    fw_D=np.zeros((1,round(no_p)))
    count=0
    fw_number=0
    count_pos=0
```

```
    count_PH101=0
    count_CCS=0
    for b in O.bodies:
        if isinstance(b.shape, Sphere):
            if b.mat.id==0:
                count_PH101+=1
            elif b.mat.id==1:
                count_CCS+=1
    for b in O.bodies:
        if isinstance(b.shape, Sphere):
            k=b.id
            r_now=b.shape.radius
            surface = 4*pi*pow(r_now,2)
            center = b.state.pos
            interactions = b.intrs()
            contactPoints = [i.geom.contactPoint for i in
                interactions]
            area_save=[]
            range_p=len(interactions)-1
            for j in range (range_p):
                Lx=(center[0]-contactPoints[j][0])**2
                Ly=(center[1]-contactPoints[j][1])**2
                Lz=(center[2]-contactPoints[j][2])**2
                dis=math.sqrt(Lx+Ly+Lz)
                h=r_now-dis
                contact_area=2*math.pi*r_now*h
                if contact_area<0:
                    continue
                area_save.append(contact_area)
            surfaceActual = surface - sum(area_save)
```

```
            fw_i=surfaceActual/surface
            extrema=utils.aabbExtrema()
            if center[0]-4*r1_PH101<extrema[0][0]:
                fw_i=fw_i/2
            elif center[0]+4*r1_PH101>extrema[1][0]:
                fw_i=fw_i/2
            elif center[1]-4*r1_PH101<extrema[0][1]:
                fw_i=fw_i/2
            elif center[1]+4*r1_PH101>extrema[1][1]:
                fw_i=fw_i/2
            elif center[2]-4*r1_PH101<extrema[0][2]:
                fw_i=fw_i/2
            elif center[2]+4*r1_PH101>extrema[1][2]:
                fw_i=fw_i/2
            if fw_i<0:
                count+=1
            if fw_i>0:
                fw_number+=fw_i
                count_pos+=1
            if b.mat.id==0:
                P=P_PH101
            elif b.mat.id==1:
                P=P_CCS
            fw_D[0][k]=fw_i*P[3]

    for b in O.bodies:
        if isinstance(b.shape, Sphere):
            k=b.id
            if b.mat.id==0:
                P=P_PH101
```

```
            elif b.mat.id==1:
                P=P_CCS
            if fw_D[0][k]>P[3]:
                print(k)
            if fw_D[0][k]<0:
                print(k)
    fraction_data=pd.DataFrame(fw_D)
    base_filename='PH101_CCS_fraction_'+str(wCCS)+'.csv'
    fraction_data.to_csv(os.path.join(path_save,base_filename))
    for j in lower_punch: O.bodies.erase(j)
    for b in O.bodies:
        if isinstance(b.shape, Sphere):
            continue
        else:
            O.bodies.erase(b.id)
    O.engines=O.engines[0:3]+O.engines[4:]
    O.engines=O.engines+[NewtonIntegrator(damping=0.1, gravity=[0,
       0, 0]),]
    mn,mx=Vector3(-0.002,-0.002,-0.003),Vector3
       (0.0015,0.002,-0.001)
    young=1.e6
    O.materials.append(FrictMat(young=young,poisson=0.5,
       frictionAngle=0,density=0,label='walls'))
    walls=aabbWalls([mn,mx],thickness=0,material='walls')
    wallIds=O.bodies.append(walls)
```

A.2.2 Tablet swelling model with liquid penetration model

```
# -*- coding: utf-8 -*-
"""
Created on Wed Apr 12 17:30:55 2023

@author: Mithushan Soundaranathan
"""
from __future__ import print_function
from yade import utils, plot, timing
from yade import pack
import pandas as pd
import numpy as np
from PIL import Image
from yade import pack, export
from scipy.interpolate import interp1d
from csv import writer
import os
from scipy.integrate import odeint
import matplotlib.pyplot as plt
import csv
from matplotlib.pyplot import figure
from pylab import *
from scipy.optimize import curve_fit
readParamsFromTable(comp_press=1.9e8,h_tab=2.04,m_tab=0.2102, r_tab
    =5.015,wCCS=0.08,tab_porosity=10,tab_height=1,save=1,c_L
    =0.001092)
from yade.params.table import *
import scipy.spatial
import statistics
import math
```

```

O = Omega()
save=save
# Physical parameters
fr_PH101 = 0.41
fr_CCS=0.69
rho_PH101 = 1561
rho_CCS =1403
D_PH101 = 7.9e-5
r1_PH101 = D_PH101/2
D_CCS = 5.4e-5
r1_CCS = D_CCS/2
#r2 = Diameter/2
k1 = 10000
kp = 140000
kc = k1 * 0.1
ks = k1 * 0.1
Chi1 = 0.34

O.dt = 1.0e-8
wCCS=wCCS
particleMass_PH101 = (4.0/3.0)*math.pi*r1_PH101*r1_PH101*r1_PH101*
    rho_PH101
particleMass_CCS = (4.0/3.0)*math.pi*r1_CCS*r1_CCS*r1_CCS*rho_CCS
m_tab_PH101=m_tab*1e-3*(1-wCCS)
m_tab_CCS=m_tab*1e-3*wCCS
tab_no_p_PH101=m_tab_PH101/particleMass_PH101
tab_no_p_CCS =m_tab_CCS /particleMass_CCS
Tab_rad=0.001
r_tab=r_tab*1e-3 #real size
```

```
h_tab=h_tab*1e-3
v_tab=math.pi*(r_tab**2)*h_tab
v_1mm=math.pi*(Tab_rad**2)*(1e-3)
no_p_PH101=(v_1mm/v_tab)*tab_no_p_PH101
no_p_CCS=(v_1mm/v_tab)*tab_no_p_CCS


PhiF1=0.999
#PhiF1 = DeltaPMax*(kp-k1)*(r1+r2)/(kp*2*r1*r2)


Cyl_height=0.006
cross_area=math.pi*(Tab_rad**2)


Comp_press_up= comp_press
Comp_force_up=Comp_press_up*cross_area

Comp_press_lp= comp_press
Comp_force_lp=Comp_press_lp*cross_area

if save==1:
        path_save='/home/ubuntu/Simulations/Compaction'
elif save==0:
        path_save='/home/ubuntu/Simulations/Swelling'

compression_data_save=[]
sc_por_15=2
rho_mix=((wCCS/rho_CCS)+((1-wCCS)/rho_PH101))**-1
data_to_save=[comp_press/1e6,round(no_p_PH101)+round(no_p_CCS),
```

```
rho_mix]
compression_data_save.append(data_to_save)

# Add material
matPH101 = O.materials.append(LudingMat(frictionAngle=fr_PH101, density=rho_PH101, k1=k1, kp=kp, ks=ks, kc=kc, PhiF=PhiF1, G0 = 0.0))
matCCS = O.materials.append(LudingMat(frictionAngle=fr_CCS, density=rho_CCS, k1=k1, kp=kp, ks=ks, kc=kc, PhiF=PhiF1, G0 = 0.0))
walls1_mat=O.materials.append(FrictMat(young=1.e6,poisson=0.5,frictionAngle=0,density=0,label='walls1_mat1'))

##walls for flow engines#
mn,mx,ml=Vector3(-3*Tab_rad,-3*Tab_rad,-Cyl_height),Vector3(3*Tab_rad,3*Tab_rad,Cyl_height),Vector3(3*Tab_rad,3*Tab_rad,Cyl_height)
walls=aabbWalls([mn,mx],thickness=0,oversizeFactor=40, material=walls1_mat)
wallIds=O.bodies.append(walls)

# Spheres for compression and walls
sp=pack.SpherePack()
sp.makeCloud((-8*D_PH101,-8*D_PH101,-35*D_PH101),(8*D_PH101,8*D_PH101,35.0*D_PH101), rMean=r1_PH101,rRelFuzz=0.18,num=round(no_p_PH101))
n1 = len(sp)
sp.makeCloud((-8*D_PH101,-8*D_PH101,-35*D_PH101),(8*D_PH101,8*D_PH101,35.0*D_PH101), rMean=r1_CCS,rRelFuzz=0.15,num=round(no_p_CCS))
for i,(c,r) in enumerate(sp):
```

```
    mat = matPH101 if i < n1 else matCCS
    color = (0,1,1) if i < n1 else (1,0,1)
    O.bodies.append(sphere(c,r,material=mat,color=color))
die=O.bodies.append(yade.geom.facetCylinder((0,0,0),radius=Tab_rad,
    height=Cyl_height,segmentsNumber=20,wallMask=6,material=matPH101
    ))

base_filename='vtkRecorder_'+str(wCCS)
vtkRecorder = VTKRecorder(fileName=os.path.join(path_save,
    base_filename),recorders=['all'])



##Single particle swelling model
def model(r,t,Q_max,rho_t,rho_w,r_0,Diff):
    Q=((rho_w*(r**3))/(rho_t*(r_0**3)))-(rho_w/rho_t)+1;
    drdt =((Diff*rho_t)/(r*rho_w))*((Q_max-Q)/Q);
    return drdt
P_PH101=[1.45,rho_PH101,1000,396.39e-12]
P_CCS=[3.16, rho_CCS, 1000, 739.75e-12]

def permeability(R_p0,c_L,eps):
    perm1=(2*R_p0)**2
    perm2=(c_L/180)
    perm3=((eps**3)/((1-eps)**2))
    k_t=perm1*perm2*perm3
    return k_t
# Add engines
O.engines = [
  ForceResetter(),
```

```
  InsertionSortCollider([Bo1_Sphere_Aabb(aabbEnlargeFactor=1.05),
                         Bo1_Wall_Aabb(),
                         Bo1_Facet_Aabb()
                         ]),
  InteractionLoop(
    [Ig2_Sphere_Sphere_ScGeom(interactionDetectionFactor=1.05),
     Ig2_Facet_Sphere_ScGeom(),
     Ig2_Wall_Sphere_ScGeom()],
    [Ip2_LudingMat_LudingMat_LudingPhys()],
    [Law2_ScGeom_LudingPhys_Basic()]
  ),
  NewtonIntegrator(damping=0.1, gravity=[0, 0, -9.81]),
  PyRunner(command='checkForce()', realPeriod=1, label="fCheck"),
  TwoPhaseFlowEngine(dead=1,label="flow"),
]



def checkForce():
    if O.iter < 4000000:
        return
    if unbalancedForce() > 1:
        return
    global upper_punch
    upper_punch=O.bodies.append(geom.facetCylinder((0,0,((-Cyl_height/2)+0.0001)+utils.aabbDim()[2]),Tab_rad-.00001,0,segmentsNumber=50,wallMask=1,material=matPH101))
    for i in upper_punch:
        body= O.bodies[i]
        body.state.vel = (0,0,-0.02)
```

```
    global lower_punch
    lower_punch=O.bodies.append(geom.facetCylinder((0,0,(-Cyl_height/2)-0.0001),Tab_rad-.00001,0,segmentsNumber=50,wallMask=1,material=matPH101))
    for n in lower_punch:
        body= O.bodies[n]
        body.state.vel = (0,0,0.02)
    O.engines = O.engines + [PyRunner(command='storeData_Compaction()', iterPeriod=1000)]+ [PyRunner(command='saveData_Compaction()', iterPeriod=100000)]
    fCheck.command = 'unloadPlate()'

def unloadPlate():
    force_up=0
    for i in upper_punch:
        body= O.bodies[i]
        force_up=force_up+abs(O.forces.f(body.id)[2])
    force_lp=0
    for n in lower_punch:
        body = O.bodies[n]
        force_lp = force_lp + abs(O.forces.f(body.id)[2])
    if ((force_up > Comp_force_up) and (force_lp > Comp_force_lp)):
        for i in upper_punch:
            body= O.bodies[i]
            body.state.vel = (0,0,0.04)
        for n in lower_punch:
            body= O.bodies[n]
            body.state.vel = (0,0,-0.04)
        fCheck.command = 'stopUnloading()'

```

```
def stopUnloading():
    force_lp=0
    for n in lower_punch:
        body = O.bodies[n]
        force_lp = force_lp + abs(O.forces.f(body.id)[2])
    if force_lp==0:
        for i in lower_punch:
            body= O.bodies[i]
            body.state.vel = (0,0,0)
    #if ((force_up==0) and (force_lp==0)):
    for i in upper_punch:
        body=O.bodies[i]
        pos_up=body.state.pos
    for i in lower_punch:
        body=O.bodies[i]
        pos_lp=body.state.pos
    if pos_up[2]> pos_lp[2]+utils.aabbDim()[2]+0.0002:
        for j in upper_punch: O.bodies.erase(j)
        for j in lower_punch: O.bodies.erase(j)
        for b in O.bodies:
            if isinstance(b.shape, Sphere):
                continue
            elif b.id<max(wallIds)+1:
                continue
            else:
                O.bodies.erase(b.id)
        for b in O.bodies:
            if isinstance(b.shape, Sphere):
                r=b.shape.radius
                oldm=b.state.mass
```

```
                oldI=b.state.inertia

                m=oldm*3./4./r
                b.state.mass=m

                b.state.inertia[0] = 15./16./r*oldI[0]
                b.state.inertia[1] = 15./16./r*oldI[1]
                b.state.inertia[2] = 15./16./r*oldI[2]
            elif b.id<max(wallIds)+1:
                continue
        fCheck.command = 'Savecheck()'

def storeData_Compaction():
    if save==1:
        force_up=0
        for i in upper_punch:
            body= O.bodies[i]
            force_up=force_up+abs(O.forces.f(body.id)[2])
        force_lp=0
        for n in lower_punch:
            body = O.bodies[n]
            force_lp = force_lp + abs(O.forces.f(body.id)[2])
        compression_pressure=((force_up+force_lp)/(cross_area))*1e-6
        if compression_pressure < 0.02:
            return
        voxel_porosity=voxelPorosity(resolution=200,start=(utils.aabbExtrema()[0]+(sc_por_15*D_PH101,sc_por_15*D_PH101,sc_por_15*D_PH101)),end=(utils.aabbExtrema()[1]-(sc_por_15*D_PH101,sc_por_15*D_PH101,sc_por_15*D_PH101)))
```

```
        data_to_save=[voxel_porosity,compression_pressure]
        compression_data_save.append(data_to_save)
        if voxel_porosity>0.9:
            O.pause()

def saveData_Compaction():
    if save==1:
        compression_data=pd.DataFrame(compression_data_save, columns=['Porosity','Compression_pressure','density'])
        base_filename='PH101_CCS_'+str(wCCS)+'_'+str(tab_porosity)+'_compression_data.csv'
        compression_data.to_csv(os.path.join(path_save, base_filename))

def Savecheck():
    if save==1:
        save_filename='PH101_CCS_'+str(wCCS)+'_'+str(tab_porosity)+'.xml'
        O.save(save_filename)
        print('Compactiondone')
        O.pause()
    if save==0:
        O.engines=O.engines[0:3]+O.engines[4:]
        O.engines=O.engines+[NewtonIntegrator(damping=0.2, gravity=[0, 0, 0]),]
        O.engines =O.engines+[PyRunner(command='ParticleSwelling()', iterPeriod=swell_steps)]+[PyRunner(command='ForceStore()', iterPeriod=500000)]+[PyRunner(command='PoreSize()', iterPeriod=1000000)]+[PyRunner(command='VTKSave()', iterPeriod=250000)]+[PyRunner(command='saveData()',
```

```
            iterPeriod=500000)]
        fCheck.dead = True # (!!!)


def ParticleSwelling():
    time_current=(O.iter-initial_save[0])*O.dt
    #flow.dead=True
    flow.dead=0
    PcMax = 50000.0
    nrSteps = 80
    dPc = PcMax / float(nrSteps)
    flow.isPhaseTrapped=True #the W-phase can be disconnected from its reservoir
    flow.drainageFirst=False#Unsaturated initially, first imbition
    flow.isDrainageActivated=False
    flow.initialWetting = False
    flow.isImbibitionActivated=True #Start imbition
    flow.isCellLabelActivated=True
    flow.isInvadeBoundary=True
    flow.isActivated=True
    flow.initialPC = 0 #PCPRESSURE #3100.0 * scale]
    flow.bndCondIsPressure=[0,0,0,0,1,1]
    flow.bndCondIsWaterReservoir = [0,0,0,0,0,0]
    flow.boundaryUseMaxMin=[0,0,0,0,0,0]
    flow.bndCondValue=[0,0,0,0,0,0]
    flow.entryPressureMethod = 2 #1,2,3
    flow.entryMethodCorrection = 2#2
    flow.maximumRatioPoreThroatoverPoreBody = 0.9#0.30 #0.9
    flow.surfaceTension = 0.072 #/ 0.72 #0.042 * cos(51.0 * 3.14 / 180.0) *
```

```
    flow.truncationValue = 1e-6
    flow.truncationPrecision = 1e-6
    flow.useSolver = 3
    flow.permeabilityFactor=1
    flow.viscosity = 0.001 #* (permeability / (1.7e-11)) * scale
    flow.deltaTimeTruncation = 1e-7
    flow.defTolerance=0.3
    flow.meshUpdateInterval=1
    flow.initialization()
    porosity_cell=[]
    n_pore=flow.nCells()
    extrema=utils.aabbExtrema()
    if time_current<dt_int:
        L_current=0
    elif time_current>=dt_int:
        L_current=L_save[-1]
    store_x=[]
    store_y=[]
    store_z=[]
    for b in O.bodies:
        if isinstance(b.shape, Sphere):
            force_tot=sqrt(O.forces.f(b.id)[0]**2+O.forces.f(b.id)[1]**2+O.forces.f(b.id)[2]**2)
            if force_tot==0:
                continue
            else:
                store_x.append(b.state.pos[0])
                store_y.append(b.state.pos[1])
                store_z.append(b.state.pos[2])
    min_x=min(store_x)
```

```
    max_x=max(store_x)
    min_y=min(store_y)
    max_y=max(store_y)
    min_z=min(store_z)
    max_z=max(store_z)
    for i in range(n_pore):
        if L_current<=0.25e-3:
            pore_pos=flow.getCellCenter(i)
            if pore_pos[0]<min_x:
                continue
            elif pore_pos[0]>max_x:
                continue
            elif pore_pos[1]<min_y:
                continue
            elif pore_pos[1]>max_y:
                continue
            elif pore_pos[2]<min_z:
                continue
            elif pore_pos[2]>max_z:
                continue
            elif flow.getCellPorosity(i)<0:
                continue
            elif flow.getCellPorosity(i)>0.5:
                continue
            elif flow.getCellInSphereRadius(i)>100e-6:
                continue
            porosity_cell.append(flow.getCellPorosity(i))
        if L_current>0.25e-3:
            pore_pos=flow.getCellCenter(i)
            if pore_pos[0]<min_x:
```

```
                continue
            elif pore_pos[0]>max_x:
                continue
            elif pore_pos[1]<min_y:
                continue
            elif pore_pos[1]>max_y:
                continue
            elif pore_pos[2]<min_z:
                continue
            elif pore_pos[2]>max_z:
                continue
            elif pore_pos[2]<initial_save[1]-L_current:
                continue
            elif flow.getCellPorosity(i)<0:
                continue
            elif flow.getCellPorosity(i)>0.5:
                continue
            elif flow.getCellInSphereRadius(i)>100e-6:
                continue
            porosity_cell.append(flow.getCellPorosity(i))
    eps=statistics.mean(porosity_cell)
    r_cell=[]
    for i in range(n_pore):
        if L_current<=h_0-0.2e-3:
            pore_pos=flow.getCellCenter(i)
            if pore_pos[0]<extrema_int[0][0]:
                continue
            elif pore_pos[0]>extrema_int[1][0]:
                continue
            elif pore_pos[1]<extrema_int[0][1]:
```

```
                continue
            elif pore_pos[1]>extrema_int[1][1]:
                continue
            elif pore_pos[2]>initial_save[1]-L_current:
                continue
            elif pore_pos[2]<initial_save[1]-L_current-0.0001:
                continue
            if flow.getCellInSphereRadius(i)<100e-6:
                r_cell.append(flow.getCellInSphereRadius(i))
    if L_current<=h_0-0.2e-3:
        R_c=statistics.mean(r_cell) #m
        Rc_save.append(R_c)
    elif L_current>h_0-0.2e-3:
        R_c=Rc_save[-1]
    if time_current<dt_int:
        dt=0
    elif time_current>=dt_int:
        dt=dt_int
    Pc=((gamma*math.cos(thetha))/(R_c)) #Pa
    Pc=Pc*1e3 #mPa
    L_con=((2*Pc)/(eps_0*eta)) #(mPa/mPa s)=1/s
    ki=permeability(R_p0,c_L,eps)
    ki_dt=ki*dt
    k_save.append(ki_dt)
    Liq_pos=sqrt(L_con*(sum(k_save)))
    #Liq_pos=Liq_pos/2
    L_save.append(Liq_pos)
    print(Liq_pos)
    print(time_current)
    radius=[]
```

```
    radius.append(time_current)
    k=0
    for b in O.bodies:
        if isinstance(b.shape, Sphere):
            par_pos=initial_save[1]-b.state.pos[2]
            #k=b.id
            r_now=b.shape.radius
            if Liq_pos>=par_pos:
                r_0=r_save[0][k+1]
                if swell_t[0][k]==0:
                    swell_t[0][k]=time_current
                    radius.append(b.shape.radius-r_save[0][k+1])
                    k=k+1
                    continue
                time=time_current-swell_t[0][k]
                t = np.linspace(0,time)
                if b.mat.id==0:
                    P=P_PH101
                elif b.mat.id==1:
                    P=P_CCS
                r = odeint(model,r_0,t,args=(P[0],P[1],P[2],r_0,fw_D[0][k],))
                r_new=float(r[-1])
                b.shape.radius = float(r[-1])
                radius.append(b.shape.radius-r_save[0][k+1])
                f=float(r[-1])/r_now
                mcurrent=b.state.mass
                mnew=mcurrent*(f*f*f)
                b.state.mass=mnew
                Icurrent=b.state.inertia
```

```
                Inew=Icurrent*(f*f*f*f*f)
                b.state.inertia[0]=Inew[0]
                b.state.inertia[1]=Inew[1]
                b.state.inertia[2]=Inew[2]
            elif Liq_pos<par_pos:
                radius.append(b.shape.radius-r_save[0][k+1])
            k=k+1
        r_save.append(radius)
    #flow.dead=True
    porosity_cell=[]
    for i in range(n_pore):
        pore_pos=flow.getCellCenter(i)
        if pore_pos[0]<extrema[0][0]:
            continue
        elif pore_pos[0]>extrema[1][0]:
            continue
        elif pore_pos[1]<extrema[0][1]:
            continue
        elif pore_pos[1]>extrema[1][1]:
            continue
        elif pore_pos[2]<extrema[0][2]:
            continue
        elif pore_pos[2]>extrema[1][2]:
            continue
        elif flow.getCellPorosity(i)<0:
            continue
        elif flow.getCellPorosity(i)>0.7:
            continue
        porosity_cell.append(flow.getCellPorosity(i))
    cell_porosity=statistics.mean(porosity_cell)
```

```
    r_cell_tablet=[]
    for i in range(n_pore_int):
        pore_pos=flow.getCellCenter(i)
        if pore_pos[0]<extrema[0][0]:
            continue
        elif pore_pos[0]>extrema[1][0]:
            continue
        elif pore_pos[1]<extrema[0][1]:
            continue
        elif pore_pos[1]>extrema[1][1]:
            continue
        elif pore_pos[2]<extrema[0][2]:
            continue
        elif pore_pos[2]>extrema[1][2]:
            continue
        elif flow.getCellPorosity(i)<0:
            continue
        elif flow.getCellPorosity(i)>0.7:
            continue
        r_cell_tablet.append(flow.getCellInSphereRadius(i))
    R_c_tablet=statistics.mean(r_cell_tablet) #m
    if L_current<6*D_PH101:
        end_voxel=(extrema_int[1][0]-sc_por_15*D_PH101,extrema_int[1][1]-sc_por_15*D_PH101,extrema_int[1][2]-sc_por_15*D_PH101)
    elif L_current>=6*D_PH101:
        swe_adx=1.5
        swe_ady=1.5
        swe_adz=1.5
        end_voxel=(extrema_int[1][0]+swe_adx*D_PH101,extrema_int
```

```
        [1][1]+swe_ady*D_PH101,extrema_int[1][2]+swe_adz*D_PH101)
    start_voxel=(extrema[0][0]+sc_por_15*D_PH101,extrema[0][1]+sc_por_15*D_PH101,extrema[0][2]+sc_por_15*D_PH101)
    voxel_porosity=voxelPorosity(resolution=200,start=start_voxel,end=end_voxel)
    #flow.dead=False
    count_rel_PH101=0
    count_rel_CCS=0
    for b in O.bodies:
        if isinstance(b.shape, Sphere):
            force_tot=sqrt(O.forces.f(b.id)[0]**2+O.forces.f(b.id)[1]**2+O.forces.f(b.id)[2]**2)
            if force_tot==0:
                if b.mat.id==0:
                    count_rel_PH101+=1
                elif b.mat.id==1:
                    count_rel_CCS+=1
            else:
                continue
    par_rel_PH101=count_rel_PH101/count_PH101
    par_rel_CCS=count_rel_CCS/count_CCS
    data_current=[time_current,Liq_pos,eps,cell_porosity,ki,utils.aabbDim()[0],utils.aabbDim()[2],n_pore,voxel_porosity,R_c_tablet,par_rel_PH101,par_rel_CCS,Pc,R_c]
    Data_save.append(data_current)
    id_pos_current=[]
    id_pos_current.append(time_current)
    for i in range (len(id_THz_val)):
        p_id=id_THz_val[i]
```

```
        id_pos_current.append(O.bodies[p_id].state.pos[2])
    id_pos_save.append(id_pos_current)

def PoreSize():
    time_current=(O.iter-initial_save[0])*O.dt
    file_name='PH101_CCS_particle_pos_'+str(wCCS)+'_'+str(time_current)+'.txt'
    export.text(os.path.join(path_save,file_name))
    flow.dead=0
    PcMax = 50000.0
    nrSteps = 80
    dPc = PcMax / float(nrSteps)
    flow.isPhaseTrapped=True #the W-phase can be disconnected from its reservoir
    flow.drainageFirst=False#Unsaturated initially, first imbition
    flow.isDrainageActivated=False
    flow.initialWetting = False
    flow.isImbibitionActivated=True #Start imbition
    flow.isCellLabelActivated=True
    flow.isInvadeBoundary=True
    flow.isActivated=True
    flow.initialPC = 0 #PCPRESSURE #3100.0 * scale]
    flow.bndCondIsPressure=[0,0,0,0,1,1]
    flow.bndCondIsWaterReservoir = [0,0,0,0,0,0]
    flow.boundaryUseMaxMin=[0,0,0,0,0,0]
    flow.bndCondValue=[0,0,0,0,0,0]
    flow.entryPressureMethod = 2 #1,2,3
    flow.entryMethodCorrection = 2#2
    flow.maximumRatioPoreThroatoverPoreBody = 0.9#0.30 #0.9
    flow.surfaceTension = 0.072 #/ 0.72 #0.042 * cos(51.0 * 3.14 /
```

```
        180.0) *
    flow.truncationValue = 1e-6
    flow.truncationPrecision = 1e-6
    flow.useSolver = 3
    flow.permeabilityFactor=1
    flow.viscosity = 0.001 #* (permeability / (1.7e-11)) * scale
    flow.deltaTimeTruncation = 1e-7
    flow.defTolerance=0.3
    flow.meshUpdateInterval=1
    flow.initialization()
    filename='PH101_CCS_Porenetwork_'+str(wCCS)+'_'+str(
        time_current)
    flow.savePoreNetwork(os.path.join(path_save,filename))
    #flow.dead=False

def VTKSave():
    vtkRecorder()

def ForceStore():
    time_current=(O.iter-initial_save[0])*O.dt
    forces=[]
    for b in O.bodies:
        if isinstance(b.shape, Sphere):
            k=b.id
            forces.append(O.forces.f(k))
    force_data=pd.DataFrame(forces)
    base_filename='PH101_CCS_force_'+str(wCCS)+'_'+str(time_current
        )+'.csv'
    force_data.to_csv(os.path.join(path_save,base_filename))

```

```
def saveData():
    Sim_data=pd.DataFrame(Data_save, columns=['Time','L','Porosity_wetted','Porosity','Permeability','Tab_radius','Height','Number_pores','Voxel_porosity','Pore_radius','Released_PH101','Released_CCS','Capillary pressure','Rc'])
    base_filename='PH101_CCS_'+str(wCCS)+'_sim_data.csv'
    Sim_data.to_csv(os.path.join(path_save,base_filename))
    radius_data=pd.DataFrame(r_save)
    base_filename='PH101_CCS_radius_data_'+str(wCCS)+'.csv'
    radius_data.to_csv(os.path.join(path_save,base_filename))
    THz_validation_data=pd.DataFrame(id_pos_save)
    base_filename='PH101_CCS_THz_validation_data_'+str(wCCS)+'.csv'
    THz_validation_data.to_csv(os.path.join(path_save,base_filename))

if save==1:
    O.run()
    waitIfBatch()
    g=-9.81

##initiate swelling simulation##
if save==0:
    read_filename='PH101_CCS_'+str(wCCS)+'_'+str(tab_porosity)+'.xml'
    O.load(read_filename)
    O.dt=1e-6
    r_save=[]
    radius=[]
    initial_save=[]
    size_save=[]
```

```
    pos_save_z=[]
    id_pos_save=[]
    id_pos_current=[]
    Data_save=[]
    k_save=[]
    L_save=[]
    Rc_save=[]
    initial_save.append(O.iter)
    max_z=utils.aabbExtrema()[1][2]
    initial_save.append(max_z+r1_PH101)
    id_THz_val=[]
    for b in O.bodies:
        if isinstance(b.shape, Sphere):
            if(-4.0*D_PH101<=b.state.pos[0]<=4.0*D_PH101 and -4.0*D_PH101<=b.state.pos[1]<=4.0*D_PH101  and max_z-1*D_PH101<=b.state.pos[2]<=max_z):
                id_THz_val.append(b.id)
    for i in range (len(id_THz_val)):
        if i==0:
            id_pos_current.append(0)
        p_id=id_THz_val[i]
        id_pos_current.append(O.bodies[p_id].state.pos[2])
    id_pos_save.append(id_pos_current)
    THz_validation_data=pd.DataFrame(id_pos_save)
    base_filename='PH101_CCS_THz_validation_data_'+str(wCCS)+'.csv'
    THz_validation_data.to_csv(os.path.join(path_save,base_filename))
    radius.append(0)
    i=0
    for b in O.bodies:
```

```
        if isinstance(b.shape, Sphere):
            radius.append(b.shape.radius)
    r_save.append(radius)
    no_p = 0
    for b in O.bodies:
        if isinstance(b.shape, Sphere):
            no_p +=1
    swell_t=np.zeros((1,round(no_p)))
    fw_D=np.zeros((1,round(no_p)))
    count=0
    fw_number=0
    count_pos=0
    k=0
    for b in O.bodies:
        if isinstance(b.shape, Sphere):
            r_now=b.shape.radius
            surface = 4*pi*pow(r_now,2)
            center = b.state.pos
            interactions = b.intrs()
            contactPoints = [i.geom.contactPoint for i in interactions]
            area_save=[]
            range_p=len(interactions)-1
            for j in range (range_p):
                Lx=(center[0]-contactPoints[j][0])**2
                Ly=(center[1]-contactPoints[j][1])**2
                Lz=(center[2]-contactPoints[j][2])**2
                dis=math.sqrt(Lx+Ly+Lz)
                h=r_now-dis
                contact_area=2*math.pi*r_now*h
```

```
                if contact_area<0:
                    continue
                area_save.append(contact_area)
            surfaceActual = surface - sum(area_save)
            fw_i=surfaceActual/surface
            extrema=utils.aabbExtrema()
            if center[0]-4*r1_PH101<extrema[0][0]:
                fw_i=fw_i/2
            elif center[0]+4*r1_PH101>extrema[1][0]:
                fw_i=fw_i/2
            elif center[1]-4*r1_PH101<extrema[0][1]:
                fw_i=fw_i/2
            elif center[1]+4*r1_PH101>extrema[1][1]:
                fw_i=fw_i/2
            elif center[2]-4*r1_PH101<extrema[0][2]:
                fw_i=fw_i/2
            elif center[2]+4*r1_PH101>extrema[1][2]:
                fw_i=fw_i/2
            if fw_i<0:
                count+=1
            if fw_i>0:
                fw_number+=fw_i
                count_pos+=1
            if b.mat.id==0:
                P=P_PH101
            elif b.mat.id==1:
                P=P_CCS
            fw_D[0][k]=fw_i*P[3]
            k=k+1
    k=0
```

```
    for b in O.bodies:
        if isinstance(b.shape, Sphere):
            if b.mat.id==0:
                P=P_PH101
            elif b.mat.id==1:
                P=P_CCS
            if fw_D[0][k]<0:
                fw_D[0][k]=(fw_number/count_pos)*P[3]
            k=k+1
    k=0
    for b in O.bodies:
        if isinstance(b.shape, Sphere):
            #k=b.id
            if b.mat.id==0:
                P=P_PH101
            elif b.mat.id==1:
                P=P_CCS
            if fw_D[0][k]>P[3]:
                print(k)
            if fw_D[0][k]<0:
                print(k)
            k=k+1
    count_PH101=0
    count_CCS=0
    for b in O.bodies:
        if isinstance(b.shape, Sphere):
            if b.mat.id==0:
                count_PH101+=1
            elif b.mat.id==1:
                count_CCS+=1
```

```
    fraction_data=pd.DataFrame(fw_D)
    base_filename='PH101_CCS_fraction_'+str(wCCS)+'.csv'
    fraction_data.to_csv(os.path.join(path_save,base_filename))
    flow.dead=0
    PcMax = 50000.0
    nrSteps = 80
    dPc = PcMax / float(nrSteps)
    flow.isPhaseTrapped=True #the W-phase can be disconnected from its reservoir
    flow.drainageFirst=False#Unsaturated initially , first imbition
    flow.isDrainageActivated=False
    flow.initialWetting = False
    flow.isImbibitionActivated=True #Start imbition
    flow.isCellLabelActivated=True
    flow.isInvadeBoundary=True
    flow.isActivated=True
    flow.initialPC = 0 #PCPRESSURE #3100.0 * scale]
    flow.bndCondIsPressure=[0,0,0,0,1,1]
    flow.bndCondIsWaterReservoir = [0,0,0,0,0,0]
    flow.boundaryUseMaxMin=[0,0,0,0,0,0]
    flow.bndCondValue=[0,0,0,0,0,0]
    flow.entryPressureMethod = 2 #1,2,3
    flow.entryMethodCorrection = 2#2
    flow.maximumRatioPoreThroatoverPoreBody = 0.9#0.30 #0.9
    flow.surfaceTension = 0.072 #/ 0.72 #0.042 * cos(51.0 * 3.14 / 180.0) *
    flow.truncationValue = 1e-6
    flow.truncationPrecision = 1e-6
    flow.useSolver = 3
    flow.permeabilityFactor=1
```

```
    flow.viscosity = 0.001 #* (permeability / (1.7e-11)) * scale
    flow.deltaTimeTruncation = 1e-7
    flow.defTolerance=0.3
    flow.meshUpdateInterval=1
    flow.initialization()
    R_p0=statistics.mean(radius)#m
    n_pore_int=flow.nCells()
    porosity_cell=[]
    extrema_int=utils.aabbExtrema()
    r_cell=[]
    for i in range(n_pore_int):
        pore_pos=flow.getCellCenter(i)
        if pore_pos[0]<extrema_int[0][0]:
            continue
        elif pore_pos[0]>extrema_int[1][0]:
            continue
        elif pore_pos[1]<extrema_int[0][1]:
            continue
        elif pore_pos[1]>extrema_int[1][1]:
            continue
        elif pore_pos[2]<extrema_int[0][2]:
            continue
        elif pore_pos[2]>extrema_int[1][2]:
            continue
        elif flow.getCellPorosity(i)<0:
            continue
        r_cell.append(flow.getCellInSphereRadius(i))
    R_c0=statistics.mean(r_cell) #m
    eps_0=voxelPorosity(resolution=200,start=(utils.aabbExtrema()
       [0]+(sc_por_15*D_PH101,sc_por_15*D_PH101,sc_por_15*D_PH101))
```

```
        ,end=(utils.aabbExtrema()[1]-(sc_por_15*D_PH101,sc_por_15*
        D_PH101,sc_por_15*D_PH101)))
    #flow.dead=False
    eta=1.002  #mPas
    gamma=72.3e-3  #N/m
    thetha=64.3  #^o
    thetha=thetha*(math.pi/180)
    swell_steps=100000
    dt_int=O.dt*swell_steps
    c_L=c_L
    h_0=utils.aabbDim()[2]
```

Appendix B

Experimental data

B.1 Additional data for Chapter 5

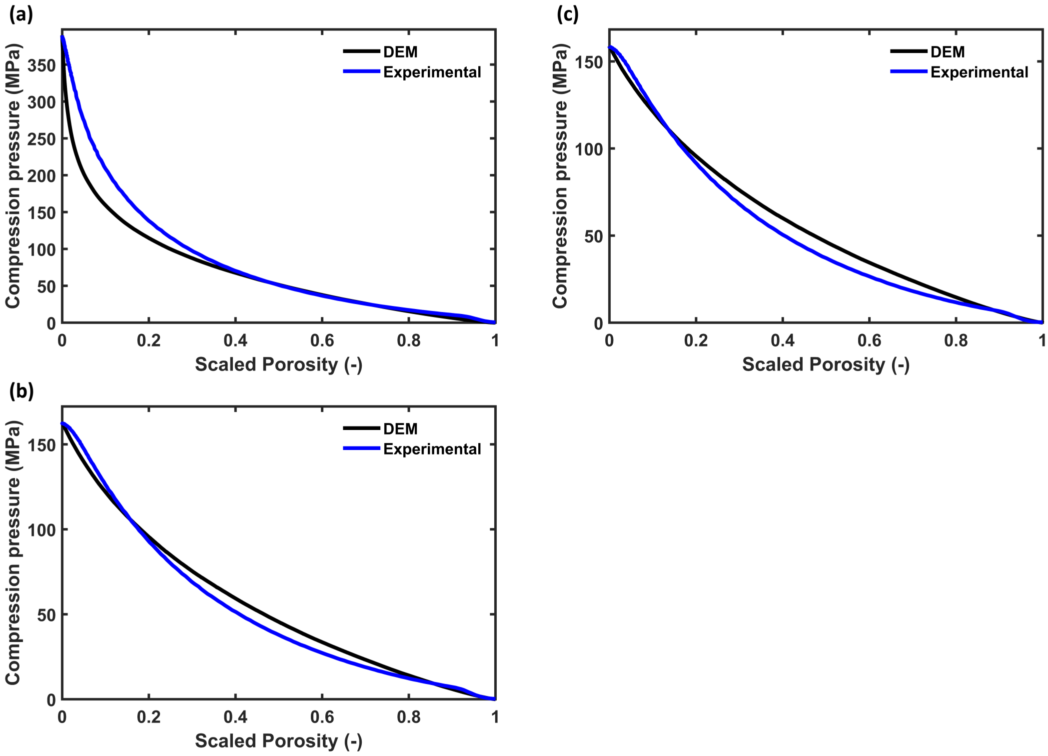

Figure B.1: Comparison of experimental and DEM compression profile to validate the calibrated $k1$ is show for (a) for MCC PH101 $\epsilon_0 = 10\%$. (b) for PH101/CCS with $c_{\mathrm{CCS}} = 5\%$ and (c) for PH101/CCS with $c_{\mathrm{CCS}} = 8\%$.

Bibliography

Abbott, D.D., Packman, E.W., Rees, E.W., Harrisson, J.W.E., 1959. A preliminary report of the effect of gastric mucous upon tablet disintegration. J. Am. Pharm. Assoc. banner 49, 19–21.

Abou-Chakra, H., Baxter, J., Tüzün, U., 2004. Three-dimensional particle shape descriptors for computer simulation of non-spherical particulate assemblies. Adv. Powder Technol. 15, 63 – 77.

Abreu, C.R., Tavares, F.W., Castier, M., 2003. Influence of particle shape on the packing and on the segregation of spherocylinders via monte carlo simulations. Powder Technol. 134, 167 – 180.

Al-Sharabi, M., Markl, D., Mudley, T., Bawuah, P., Karttunen, A.P., Ridgway, C., Gane, P., Ketolainen, J., Peiponen, K.E., Rades, T., Zeitler, J.A., 2020. Simultaneous investigation of the liquid transport and swelling performance during tablet disintegration. Int. J. Pharm. 584, 119380.

Al-Sharabi, M., Markl, D., Vivacqua, V., Bawuah, P., MacLean, N., Bentley, M., York, A.P., Marigo, M., Huang, K., Zeitler, J.A., 2021. Terahertz pulsed imaging as a new method for investigating the liquid transport kinetics of α-alumina powder compacts. Chem. Eng. Res. Des. 165, 386–397.

Alderborn, G., Duberg, M., Nyström, C., 1985. Studies on direct compression of tablets x. measurement of tablet surface area by permeametry. Powder Technol. 41, 49–56.

Alshafiee, M., AlAlaween, W.H., Markl, D., Soundaranathan, M., Almajaan, A., Walton, K., Blunt, L., Asare-Addo, K., 2019. A predictive integrated framework based on the radial basis function for the modelling of the flow of pharmaceutical powders. Int. J. Pharm. 568, 118542.

Anwar, S., Fella, J.T., Dickinson, P.A., 2005. An investigation of the disintegration of tabletsin biorelevant media. Int. J. Pharm. 290, 121–127.

Aulton, M.E., 2018. Dissolution and solubility, in: Aulton, M.E., Taylor, K.M.G. (Eds.), Aulton's Pharmaceutics The Design and Manufacture of Medicines, fift edition. Elsevier. chapter 2, pp. 18–36.

Basaleh, S., Bisharat, L., Cespi, M., Berardi, A., 2020. Temperature: An overlooked factor in tablet disintegration. Eur. J. Pharm. Sci. 151, 105388.

Basu, P., Joglekar, G., Rai, S., Suresh, P., Vernon, J., 2006. Analysis of manufacturing costs in pharmaceutical companies. J Pharm Innov 3, 30–40.

Baxter, G., Behringer, R., 1991. Cellular automata models for the flow of granular materials. Phys. D: Nonlinear Phenom. 51, 465 – 471.

Beard, M.C., Turner, G.M., Schmuttenmaer, C.A., 2002. Terahertz spectroscopy. The J. Phys. Chem. B 106, 7146–7159.

Bell, C.L., Peppas, N.A., 1996. An apparatus to measure polymer swelling under load. Int. J. Pharm. 134, 167–172.

Berardi, A., Bisharat, L., Blaibleh, A., Pavoni, L., Cespi, M., 2018. A simple and inexpensive image analysis technique to study the effect of disintegrants concentration and diluents type on disintegration. J. Pharm. Sci. 107, 1–10.

Berg, C.F., 2014. Permeability description by characteristic length, tortuosity, constriction and porosity. Transp. Porous Media 103, 381–400.

Bi, Y.X., Sunada, H., Yonezawa, Y., Danjo, K., 1999. Evaluation of rapidly disintegrating tablets prepared by a direct compression method. Drug Dev. Ind. Pharm. 24, 571–581.

Böhling, P., Khinast, J.G., Jajcevic, D., Davies, C., Carmody, A., Doshi, P., Ende, M.T.A., Sarkar, A., 2019. Computational fluid dynamics-discrete element method modeling of an industrial-scale wurster coater. J. Pharm. Sci. 108, 538–550.

Boncelet, C., 2009. Image noise models, in: Bovik, A. (Ed.), The Essential Guide to Image Processing second edition. Academic Press; Pap/Cdr edition, USA. chapter 7, pp. 143–167.

Botzolakisi, J.E., Augsburger, L.L., 1988. Disintegrating agents in hard gelatin capsules. part ii: Swelling efficiency. Drug Dev. Ind. Pharm. 14, 1235–1248.

Bouklas, N., Huang, R., 2012. Swelling kinetics of polymer gels: comparison of linear and nonlinear theories. Soft Matter 8, 8194–8203.

Braile, D., Hare, C., Wu, C.Y., 2022. Dem analysis of swelling behaviour in granular media. Adv. Powder Technol. 33, 103806.

Brown, C.J., McGlone, T., Yerdelen, S., Srirambhatla, V., Mabbott, F., Gurung, R., Briuglia, M.L., Ahmed, B., Polyzois, H., McGinty, J., Perciballi, F., Fysikopoulos, D., MacFhionnghaile, P., Siddique, H., Raval, V., Harrington, T.S., Vassileiou, A.D., Robertson, M., Prasad, E., Johnston, A., Johnston, B., Nordon, A., Srai, J.S., Halbert, G., ter Horst, J.H., Price, C.J., Rielly, C.D., Sefcik, J., Florence, A.J., 2018. Enabling precision manufacturing of active pharmaceutical ingredients: workflow for seeded cooling continuous crystallisations. Royal Soc. Chem. 3, 518–549.

Cai, J., Yu, B., 2011. A discussion of the effect of tortuosity on the capillary imbibition in porous media. Transp. Porous Media 89, 342–357.

Caramella, C., Ferrari, F., Bonferoni, M., Ronchi, M., 1990. Disintegrants in solid dosage forms. Drug Dev. Ind. Pharm. 16, 2561–2577.

Chareyre, B., Cortis, A., Catalano, E., Barthelemy, E., 2012. Pore-scale modeling of viscous flow and induced forces in dense sphere packings. Transp. Porous Media 94, 595–615.

Chen, C., Gladden, L.F., Mantle, M.D., 2014. Direct visualization of in vitro drug mobilization from lescol xl tablets using two-dimensional ^{19}f and ^{1}h magnetic resonance imaging. Mol. Pharm. 11, 630–637.

Chen, Y.Y., Hughes, L.P., Gladden, L.F., Mantle, M.D., 2010. Performance of tablet disintegrants: impact of storage conditions and relative tablet density. J. Pharm. Sci. 99, 3462–3472.

Choi, H., Joseph, D., 2001. Fluidization by lift of 300 circular particles in plane poiseuille flow by direct numerical simulation. J. Fluid Mech. 438, 101–128.

Cleary, P.W., Sawley, M.L., 2002. Dem modelling of industrial granular flows: 3d case studies and the effect of particle shape on hopper discharge. Appl. Math. Model. 26, 89 – 111.

Cleophas, T.J., Zwinderman, A.H., 2013. Machine Learning in Medicine. Springer Science+Business Media Dordrecht.

Cooper, B.F., Brecht, E.A., 1957. Surfactants in tablets to improve disintegration. J. Am. Pharm. Assoc. banner 46, 520–526.

Cundall, P.A., Strack, O.D.L., 1979. A discrete numerical model for granular assemblies. Geotech. 29, 47–65.

Cunningham, J., Sinka, I., Zavaliangos, A., 2004. Analysis of tablet compaction. i. characterization of mechanical behavior of powder and powder/tooling friction. J. Pharm. Sci. 93, 2022–2039.

Darcy, H., 1856. Les Fontaines Publiques de la Ville de Dijon. Paris: Victor Dalmont.

Dees, P.J., 1980. The Mechanisms of Tablet Dinstegration. Ph.D. thesis. University of Leiden.

Desai, P.M., Er, P.X.H., Liew, C.V., Heng, P.W.S., 2014. Functionality of disintegrants and their mixtures in enabling fast disintegration of tablets by a quality by design approach. An Off. J. Am. Assoc. Pharm. Sci. 15, 1093–1104.

Desai, P.M., Liew, C.V., Heng, P.W.S., 2015. Review of disintegrants and the disintegration phenomena. J. Pharm. Sci. 105, 1–11.

Desai, P.M., Valeri, C., Heng, L.W.S., 2012. Understanding disintegrant action by visualization. J. pharmaceutical sciences 101, 2155–2164.

Diersch, H.J.G., Clausnitzer, V., Myrnyy, V., Rosati, R., Schmidt, M., Beruda, H., Ehrnsperger, B.J., Virgilio, R., 2010. Modeling unsaturated flow in absorbent swelling porous media: Part 1. theory. Transp. Porous Media volume 83, 437–464.

Diorazio, L.J., Hose, D.R.J., Adlington, N.K., 2016. Toward a more holistic framework for solvent selections. Org. Process. Res. & Dev. 20, 760–773.

Dzyaloshinskii, I., Lifshitz, E., Pitaevskii, L., 1961. The general theory of van der waals forces. Adv. Phys. 10, 165–209.

Eggenreich, K., Windhab, S., Schrank, S., Treffer, D., Juster, H., Steinbichler, G., Laske, S., Koscher, G., Roblegg, E., Khinast, J., 2016. Injection molding as a one-step process for the direct production of pharmaceutical dosage forms from primary powders. Int. J. Pharm. 505, 341–351.

Esteves, L.P., 2011. Superabsorbent polymers: On their interaction with water and pore fluid. Cem. & Concr. Compos. 33, 717–724.

Faroongsarng, D., Peck, G.E., 1994. The swelling & water uptake of tablets iii: Moisture sorption behavior of tablet disintegrants. Drug Dev. Ind. Pharm. 20, 779–798.

Favier, J.F., Abbaspour-Fard, M.H., Kremmer, M., 2001. Modeling nonspherical particles using multisphere discrete elements. J. Eng. Mech. 127, 971–977.

Federsel, H.J., 2009. Chemical process research and development in the 21st century: Challenges, strategies, and solutions from a pharmaceutical industry perspective. Acc. Chem. Res 42, 671–680.

Fisher, R.A., 1926. On the capillary forces in an ideal soil, correction of formulate given by w.b. haines. The J. Agric. Sci. 3, 492–505.

Forsyth, A.J., Hutton, S., Osborne, C., Rhodes, M., 2002. Effects of interparticle force on the packing of spherical granular material. Phys. review letters 87, 244301.

Fujita, H., 1961. Diffusion in polymer-diluent systems. Fortschritte Der Hochpolymeren-Forschung. Adv. Polym. Sci. 3/1, 1–47.

Gallas, J.A.C., Sokolowski, S., 1993. Grain non-sphericity effects on the angle of repose of granular material. Int. J. Mod. Phys. B 7, 2037–2046.

Ganderton, D., Fraser, D.R., 1970. Some observations of the penetration and disruption of tablets by water. J. Pharm. Pharmacol. 22, 95–103.

Gao, Y., De Simone, G., Koorapaty, M., 2021. Calibration and verification of dem parameters for the quantitative simulation of pharmaceutical powder compression process. Powder Technol. 378, 160–171.

Garner, S., Strong, J., Zavaliangos, A., 2018. Study of the die compaction of powders to high relative densities using the discrete element method. Powder Technol. 330, 357 – 370.

Gasmi, H., F. Danede, J.S., Siepmann, F., 2015. Does plga microparticle swelling control drug release? new insight based on single particle swelling studies. J. Control. Release 213, 120–127.

Gernaey, K.V., Cervera-Padrell, A.E., Woodley, J.M., 2012. A perspective on pse in pharmaceutical process development and innovation. Comput. & Chem. Eng. 42, 15–29.

Gissinger, D., Stamm, A., 1980. A comparative evaluation of the properties of some tablet disintegrants. Drug Dev. Ind. Pharm. 6, 511–536.

Gostick, J.T., Khan, Z.A., Tranter, T.G., Kok, M.D., Agnaou, M., Sadeghi, M., Jervis, R., 2019. Porespy: A python toolkit for quantitative analysis of porous media images. J. Open Source Softw. 4, 1296.

Hamaker, H., 1937. The london—van der waals attraction between spherical particles. Phys. 4, 1058 – 1072.

Haustein, M., Gladkyy, A., Schwarze, R., 2017. Discrete element modeling of deformable particles in yade. SoftwareX 6, 118–123.

He, Y., Wang, Z., Evans, T., Yu, A., Yang, R., 2015. Dem study of the mechanical strength of iron ore compacts. Int. J. Miner. Process. 142, 73–81.

Hopkins, M.A., Louge, M.Y., 1991. Inelastic microstructure in rapid granular flows of smooth disks. Phys. Fluids A 3, 47–57.

Hu, J., Li, W., Zhang, L., Wu, C.Y., 2023. A microscopic diffusion-induced discrete element model for swellable particles. Chem. Eng. J. 464, 142677.

Huilin, L., Yurong, H., Wentie, L., Ding, J., Gidaspow, D., Bouillard, J., 2004. Computer simulations of gas–solid flow in spouted beds using kinetic–frictional stress model of granular flow. Chem. Eng. Sci. 59, 865 – 878.

Huyghe, L.M., Janssen, J.D., 1997. Quaadrif hasic mechanics of swelling incompressible porous media. Int. J. Eng. Sci. 35, 793–80.

Indurkhya, A., Patel, M., Sharma, P., Abed, S.N., Shnoudeh, A., Maheshwari, R., Deb, P.K., Tekade, R.K., 2018. Chapter 6 - influence of drug properties and routes of drug administration on the design of controlled release system, in: Tekade, R.K. (Ed.), Dosage Form Design Considerations. Academic Press. Advances in Pharmaceutical Product Development and Research, pp. 179–223.

Jange, C.G., Wassgren, C.R., Ambrose, K., 2023. The significance of tablet internal structure on disintegration and dissolution of immediate-release formulas: A review. Powders 2, 99–123.

Jenkins, L.M., Donald, A.M., 1997. Use of the environmental scanning electron microscope for the observation of the swelling behaviour of cellulosic fibres. Scanning 19, 92–97.

Jensen, R.P., Edil, T.B., Bosscher, P.J., Plesha, M.E., Khala, N., 2001. Effect of particle shape on interface behavior of dem-simulated granular materials. Int. J. Geomech. 1, 1–19.

Johnson, K., Johnson, K., 1987. Contact mechanics. Camb. university Press. .

Kadiri, M.S., Michrafy, A., Dodds, J.A., 2005. Pharmaceutical powders compaction: Experimental and numerical analysis of the density distribution. Powder Technol. 157, 176–182.

Kalaria, D.R., Parker, K., Reynolds, G.K., Laru, J., 2020. An industrial approach towards solid dosage development for first-in-human studies: Application of predictive science and lean principles. Drug Discov. Today 25, 505–518.

Kalný, M., Grof, Z., Štěpánek, F., 2021. Microstructure based simulation of the disintegration and dissolution of immediate release pharmaceutical tablets. Powder Technol. 377, 257–268.

Karehill, P.G., Nyström, C., 1990. Studies on direct compression of tablets xxi. investigation of bonding mechanisms of some directly compressed materials by strength characterization in media with different dielectric constants (relative permittivity). Int. J. Pharm. 61, 251–260.

Kayesh, R., Bhuiya, M.R.H., Islam, M.F., Chowdhury, J.A., 2021. Quality-by-design approach and optimization of risk factors by box-behnken design in formulation development of aspirin and glycine orally disintegrating tablet. J. Sci. Res. 13, 935–950.

Ketterhagen, W.R., am Ende, M.T., Hancock, B.C., 2009. Process modeling in the pharmaceutical industry using the discrete element method. J. Pharm. Sci. 98, 442–470.

Ketterhagen, W.R., Curtis, J.S., Wassgren, C.R., Hancock, B.C., 2008. Modeling granular segregation in flow from quasi-three-dimensional, wedge-shaped hoppers. Powder Technol. 179, 126 – 143.

Kimber, J., Kazarian, S.G., Stepanek, F., 2012. Modelling of pharmaceutical tablet swelling and dissolution using discrete element method. Chem. Eng. Sci. 69, 394–403.

Kleinebudde, P., Knop, K., 2007. Direct pelletization of pharmaceutical pellets in fluid-bed processes, in: Salma, A.D., Hounslow, M.J., Seville, J.P.K. (Eds.), Handbook of powder technology: Granulation. Elsevier. chapter 17, pp. 779–811.

Koponen, A., Kataja, M., Timonen, J., 1997. Permeability and effective porosity of porous media. Phys. Rev. 56, 19–25.

Kozicki, J., Tejchman, J., 2005. Application of a cellular automaton to simulations of granular flow in silos.s. Granul. Matter 7, 45–54.

Krishnamoorthy, V., Prasad, V.P.R., Sen, S., 2013. Clozapine-sodium starch glycolate dispersions: in vitro dissolution behaviour, physicochemical characterisation and release kinetic model fitting. Malays. J. Pharm. Sci. 11, 49–70.

KuShaari, K., Pandey, P., Song, Y., Turton, R., 2006. Monte carlo simulations to determine coating uniformity in a wurster fluidized bed coating process. Powder Technol. 166, 81 – 90.

Kutluay, S., Bahadir, A.R., Özdeş, A., 1997. The numerical solution of one-phase classical stefan problem. J. Comput. Appl. Math. 81, 135–144.

Lamberti, G., Galdi, I., Barba, A.A., 2011. Controlled release from hydrogel-based solid matrices. a model accounting for water up-take, swelling and erosion gaetano. Int. J. ofPharmaceutics 407, 78–86.

Lee, J., Radu, A., Vontobel, P., Derome, D., Carmeliet, J., 2016. Absorption of impinging water droplet in porous stones. J. Colloid Interface Sci. 471, 59–70.

Lin, X., Ng, T.T., 1997. A three-dimensional discrete element model using arrays of ellipsoids. Geotech. 47, 319–329.

Lowenthal, W., 1972. Disintegration of tablets. J. pharmaceutical Sci. 61, 1695–1711.

Lowenthal, W., Burruss, R.A., 1971. Mechanism of action of starch as a tablet disintegrant iv: Effect of medicaments and disintegrants on mean pore diameter and porosity. J. pharmaceutical Sci. 60, 1325–1332.

Luding, S., 2008. Introduction to discrete element methods basic of contact force models and how to perform the micro-macro transition to continuum theory. Eur. J. Environ. Civ. Eng. 12, 785–826.

Maclean, N., Walsh, E., Soundaranathan, M., Khadra, I., Mann, J., Williams, H., Markl, D., 2021. Exploring the performance-controlling tablet disintegration mechanisms for direct compression formulations. Int. J. Pharm. 599, 120221.

Manjón, J.V., Carbonell-Caballero, J., Lull, J.J., García-Martí, G., Martíı-Bonmatí, L., Robles, M., 2008. Mri denoising using non-local means. Med. image analysis 12, 514–23.

Markl, D., Strobel, A., Schlossnikl, R., Bøtker, J., Bawuah, P., Ridgway, C., Rantanen, J., Rades, T., Gane, P., Peiponen, K.E., Zeitler, J.A., 2018a. Characterisation of pore structures of pharmaceutical tablets: A review. Int. J. Pharm. 538, 188–214.

Markl, D., Wang, P., Ridgway, C., Karttunen, A.P., Bawuah, P., Ketolainen, J., Gane, P., Peiponen, K.E., Zeitler, J.A., 2018b. Resolving the rapid water absorption of porous functionalised calcium carbonate powder compacts by terahertz pulsed imaging. Chem. Eng. Res. Des. 132, 1082–1090.

Markl, D., Wang, P., Ridgway, C., Karttunen, A.P., Bawuah, P., Ketolainen, J., Gane, P., Peiponen, K.E., Zeitler, J.A., 2018c. Resolving the rapid water absorption of porous functionalised calcium carbonate powder compacts by terahertz pulsed imaging. Chem. Eng. Res. Des. 132, 1082 – 1090.

Markl, D., Wang, P., Ridgway, C., Karttunen, A.P., Chakraborty, M., Bawuah, P., Pääkkönen, P., Gane, P., Ketolainen, J., Peiponen, K.E., Zeitler, J.A., 2017a. Characterization of the Pore Structure of Functionalized Calcium Carbonate Tablets by Terahertz Time-Domain Spectroscopy and X-Ray Computed Microtomography. J. Pharm. Sci. 106, 1586–1595.

Markl, D., Yassin, S., Wilson, D.I., Goodwin, D.J., Anderson, A., Zeitler, J.A., 2017b. Mathematical modelling of liquid transport in swelling pharmaceutical immediate release tablets. Int. J. Pharm. 526, 1–10.

Markl, D., Zeitler, J.A., 2017. A review of disintegration mechanisms and measurement techniques. Pharm. Res. 34, 890–917.

Masoodi, R., Pillai, K.M., 2010. Darcy's law-based model for wicking in paper-like swelling porous media. Am. Inst. Chem. Eng. J. 59, 2257–2267.

Masoodi, R., Pillai, K.M., Varanasi, P.P., 2007. Darcy's law-based models for liquid absorption in polymer wicks. Am. Inst. Chem. Eng. J. 53, 2769–2782.

Mikulic, M., 2020. Global pharmaceutical industry - statistics and facts. URL: `https://www.statista.com/topics/1764/global-pharmaceutical-industry/`.

Mindlin, R.D., Deresiewicz, H., 1953. Elastic Spheres in Contact Under Varying Oblique Forces. J. Appl. Mech. 20, 327–344.

Mortier, S.T.F., De Beer, T., Gernaey, K.V., Vercruysse, J., Fonteyne, M., Remon, J.P., Vervaet, C., Nopens, I., 2012. Mechanistic modelling of the drying behaviour of single pharmaceutical granules. Eur. J. Pharm. Biopharm. 80, 682–689.

Muguruma, Y., Tanaka, T., Tsuji, Y., 2000. Numerical simulation of particulate flow with liquid bridge between particles (simulation of centrifugal tumbling granulator). Powder Technol. 109, 49 – 57.

Mustoe, G.G.W., Miyata, M., 2001. Material flow analyses of noncircular-shaped granular media using discrete element methods. J. Eng. Mech. 127, 1017–1026.

Nogami, H., Nagai, T., Fukuoka, E., Sonobe, T., 1969. Disintegration of the aspirin tablets containing potato starch and microcrystalline cellulose in various concentrations. Chem. Pharm. Bull. 17, 1450–1455.

Nordström, J., Alderborn, G., Frenning, G., 2018. Compressibility and tablet forming ability of bimodal granule mixtures: Experiments and dem simulations. Int. J. Pharm. 540, 120–131.

Nott, K.P., 2010. Magnetic resonance imaging of tablet dissolution. Eur. J. Pharm. Biopharm. 74, 78–83.

Nystrröm, C., Alderborn, G., Duberg, M., Karehill, P.G., 1993. Bonding surface area and bonding mechanism-two important factors fir the understanding of powder comparability. Drug Dev. Ind. Pharm. 19, 2143–2196.

Obradovic, J., Collins, J.H.P., Hirscha, O., Mantle, M.D., Johns, M.L., F.Gladden, L., 2007. The use of thz time-domain reflection measurements to investigate solvent diffusion in polymers. Polym. 48, 3494–3503.

Oda, M., Konishi, J., Nemat-Nasser, S., 1982. Experimental micromechanical evaluation of strength of granular materials: Effects of particle rolling. Mech. Mater. 1, 269 – 283.

Omidian, H., Hashemi, S.A., Sammes, P.G., Meldrum, I., 1998. A model for the swelling of superabsorbent polymers. Polym. 39, 6697–6704.

Østergaard, J., Meng-Lund, E., Larsen, S.W., Larsen, C., Petersson, K., Lenke, J., Jensen, H., 2010. Real-time uv imaging of nicotine release from transdermal patch. Pharm. Res. 27, 2614–2623.

Otsubo, M., O'Sullivan, C., Shire, T., 2017. Empirical assessment of the critical time increment in explicit particulate discrete element method simulations. Comput. Geotech. 86, 67–79.

Pajander, J., Baldursdottir, S., Rantanen, J., Østergaard, J., 2012. Behaviour of hpmc compacts investigated using uv-imaging. Int. J. Pharm. 427, 345–353.

Patel, N.R., Hopponent, R.E., 1966. Mechanism of action of starch as a disintegrating agent in aspirin tablets. J. Pharm. Sci. 55, 1065–1068.

Perona, P., Malik, J., 1990. Scale space and edge detection using anisotropic diffusion. Transactions on Pattern Analysis Mach. Intell. 12, 629–639.

Persson, A.S., Frenning, G., 2012. An experimental evaluation of the accuracy to simulate granule bed compression using the discrete element method. Powder Technol. 219, 249–256.

Persson, A.S., Frenning, G., 2015. An experimental evaluation of discrete element simulations of confined powder compression using an extended truncated-sphere model. Powder Technol. 284, 257–264.

Potyondy, D., Cundall, P., 2004. A bonded-particle model for rock. Int. J. Rock Mech. Min. Sci. 41, 1329–1364.

Preston, J.M., Nimkar, M.V., 1949. Measuring the swelling of fibres in water. J. Textile Inst. Proc. 40, 674–688.

Quodbach, J., Kleinebudde, P., 2014. Systematic classification of tablet disintegrants by water uptake and force development kinetics. J. Pharm. Pharmacol. 66, 1429–1438.

Quodbach, J., Kleinebudde, P., 2015. A critical review on tablet disintegration. Pharm. Dev. Technol. 21, 1–12.

Quodbach, J., Moussavi, A., Tammer, R., Frahm, J., Kleinebudde, P., 2014a. Assessment of disintegrant efficacy with fractal dimensions from real-time mri. Int. J. Pharm. 475, 605–612.

Quodbach, J., Moussavi, A., Tammer, R., Frahm, J., Kleinebudde, P., 2014b. Tablet disintegration studied by high-resolution real-time magnetic resonance imaging. J. Pharm. Sci. 103, 249–255.

Reier, G.E., Shangraw, R.F., 1966. Microcrystalline cellulose in tableting. J. Pharm. Sci. 55, 510–514.

Ridgway, C., Bawuah, P., Markl, D., Zeitler, J.A., Ketolainen, J., Peiponen, K.E., Gane, P., 2017. On the role of API in determining porosity, pore structure and bulk modulus of the skeletal material in pharmaceutical tablets formed with MCC as sole excipient. Int. J. Pharm. 526, 321–331.

Rojas, J., Guisao, S., Ruge, V., 2012. Functional assessment of four types of disintegrants and their effect on the spironolactone release properties. J. Am. Assoc. Pharm. Sci. 13, 1054 –1062.

Rough, S., Bridgwater, J., Wilson, D., 2002. In situ measurements of porosities and permeabilities of alumina pastes. Powder Technol. 123, 262–274.

Rudnic, E., Rhodes, C., Welch, S., Bernard, P., 1982. Evaluations of the mechanism of disintegrant action. Drug Dev. industrial pharmacy 8, 87–109.

Russ, J.C., Neal, F.B., 2016. The Image Processing Handbook, Seventh edition. CRC Press LLC.

Russell, A., Sibanc, R., Dreu, R., PeterMüller, 2018. Mechanics of pharmaceutical pellets—constitutive properties, deformation, and breakage behavior. J. Pharm. Sci. 107, 571–586.

Sanchez-Castillo, F.X., Anwar, J., 2003. Molecular dynamics simulations of granular compaction: The single granule case. The J. Chem. Phys. 118, 4636.

Santagata, T., Solimene, R., Aprea, G., Salatino, P., 2020. Modelling and experimental characterization of unsaturated flow in absorbent and swelling porous media. Chem. Eng. Sci. 224, 115765.

Schoenmaker, B.D., der Schueren, L.V., Vrieze, S.D., Westbroek, P., Clerck, K.D., 2011. Wicking properties of various polyamide nanofibrousstructures with an optimized method. J. Appl. Polym. Sci. 120, 305–310.

Schott, H., 1992a. Kinetics of swelling of polymers and their gels. J. Pharm. Sci. 81, 467–470.

Schott, H., 1992b. Swelling kinetics of polymers, part b. J. Macromol. Sci. 31, 1–9.

Schreiner, T., Schaefer, U.F., Loth, H., 2005. Immediate drug release from solid oral dosage forms. J. Pharm. Sci. 94, 120–133.

Schuchard, D.R., Berg, J.C., 1991. Liquid transport in composite cellulose-superabsorbent fiber networks. Wood Fiber Sci. 23, 342–357.

Schütt, M., Stamatopoulos, K., Batchelor, H.K., Simmons, M.J.H., Alexiadis, A., 2021. Modelling and simulation of the drug release from a solid dosage form in the human ascending colon: The influence of different motility patterns and fluid viscosities. Pharm. 13, 859.

Serra, J., 1986. Introduction to mathematical morphology. Comput. Vision, Graph. Image Process. 35, 283 – 305.

Seville, J., Willett, C., Knight, P., 2000. Interparticle forces in fluidisation: a review. Powder Technol. 113, 261 – 268.

Shah, U., Augsburger, L., 2002. Multiple sources of sodium starch glycolate, nf: Evaluation of functional equivalence and development of standard performance tests. Pharm. Dev. Technol. 7, 345–359.

Shi, S.Q., Gardner, D.J., 2000. A new model to determine contact angles on swelling polymer particles by the column wicking method. J. Adhesion Sci. Technol. 14, 301–314.

Shotton, E., Leonard, G.S., 1972. The effect of intra- and extragranular maize starch on the disintegration of compressed tablets. J. Pharm. Pharmacol. 24, 798–803.

Sibille, L., Lominé, F., Poullain, P., Sail, Y., Marot, D., 2014. Internal erosion in granular media: direct numerical simulations and energy interpretation. Hydrol. Process. 29, 2149–2163.

Solsvik, J., Jakobsen, H.A., 2015. The foundation of the population balance equation: A review. J. Dispers. Sci. Technol. 36, 510–520,.

Song, Y., Turton, R., Kayihan, F., 2006. Contact detection algorithms for dem simulations of tablet-shaped particles. Powder Technol. 161, 32 – 40.

Soundaranathan, M., Al-Sharabi, M., Sweijen, T., Bawuah, P., Zeitler, J.A., Hassanizadeh, S.M., Pitt, K., Johnston, B.F., Markl, D., 2023. Modelling the evolution of pore structure during the disintegration of pharmaceutical tablets. Pharm. 15, 489.

Soundaranathan, M., Vivattanaseth, P., Walsh, E., Pitt, K., Johnston, B., Markl, D., 2020. Quantification of swelling characteristics of pharmaceutical particles. Int. J. Pharm. 590, 119903.

Stalidzans, E., Zanin, M., Tieri, P., Castiglione, F., Polster, A., Scheiner, S., Pahle, J., Stres, B., List, M., Baumbach, J., Lautizi, M., Steen, K.V., Schmidt, H.H., 2020. Mechanistic modeling and multiscale applications for precision medicine: Theory and practice. Netw. Syst. Medicine 3, 36–56.

Storåkers, B., Biwa, S., Larsson, P.L., 1997. Similarity analysis of inelastic contact. Int. J. Solids Struct. 34, 3061–3083.

Sugimori, K., 2015. Compaction process of pharmaceutical tablets. J. Soc. Powder Technol. Jpn. 52, 345–352.

Sunada, H., Bi, Y., 2002. Preparation, evaluation and optimization of rapidly disintegrating tablets. Powder Technol. 122, 188 – 198.

Suryadi, H., Sutriyo, Angeline, M., Murti, M.W., 2018. Characterization of microcrystalline cellulose obtained from enzymatic hydrolysis of alpha-cellulose and its application. J. Young Pharm. 10, 87–92.

Sweijen, T., Chareyre, B., Hassanizadeh, S., Karadimitriou, N., 2017a. Grain-scale modelling of swelling granular materials; application to super absorbent polymers. Powder Technol. 318, 411–422.

Sweijen, T., van Duijna, C.J., Hassanizadeh, S.M., 2017b. A model for diffusion of water into a swelling particle with a free boundary: Application to a super absorbent polymer particle. Chem. Eng. Sci. 172, 407–413.

Sweijen, T., Hassanizadeh, M.S., Chareyre, B., Zhuang, L., 2018. Dynamic pore-scale model of drainage in granular porous media: The pore-unit assembly method. Water Resour. Res. 54, 4193–4213.

Sweijen, T., Hassanizadeh, S.M., Chareyre, B., 2020. Unsaturated flow in a packing of swelling particles; a grain-scale model. Adv. Water Resour. 142, 103642.

Tajarobi, F., Abrahmsén-Alami, S., Carlsson, A.S., Larsson, A., 2009. Simultaneous probing of swelling, erosion and dissolution by nmr-microimaging—effect of solubility of additives on hpmc matrix tablets. Eur. J. Pharm. Sci. 37, 89–97.

Thakur, S.C., Ahmadian, H., Sun, J., Ooi, J.Y., 2014a. An experimental and numerical study of packing, compression, and caking behaviour of detergent powders. Particuology 12, 2–12.

Thakur, S.C., Morrissey, J.P., Sun, J., Chen, J.F., Ooi, J.Y., 2014b. Micromechanical analysis of cohesive granular materials using the discrete element method with an adhesive elasto-plastic contact model. Granul. Matter 16, 383–400.

Thomas, P., Bray, J., 1999. Capturing non-spherical shape of granular media with disk clusters. J. Geotech. Geoenvironmental Eng. 125, 169–178.

Thoorens, G., Krier, F., Leclercq, B., Carlin, B., Evrard, B., 2014. Microcrystalline cellulose, a direct compression binder in a quality by design environment—a review. Int. J. Pharm. 473, 64–72.

Thornton, C., Ning, Z., 1998. A theoretical model for the stick/bounce behaviour of adhesive, elastic-plastic spheres. Powder Technol. 99, 154–162.

Ting, J., Meachum, L., Rowell, J., 1995. Effect of particle shape on the strength and deformation mechanisms of ellipse-shaped granular assemblagesl. Eng. Comput. 12, 99–108.

Toson, P., Doshi, P., Matic, M., Siegmann, E., Blackwood, D., Jain, A., Brandon, J., Lee, K., Wilsdon, D., Kimber, J., Verrier, H., Khinast, J., Jajcevic, D., 2021. Continuous mixing technology: Validation of a dem model. Int. J. Pharm. 608, 121065.

Tripath, A., Khakhar, D.V., 2010. Steady flow of smooth, inelastic particles on a bumpy inclined plane: Hard and soft particle simulations. Phys. Rev. E 81, 041307.

Tye, C.K., Sun, C., Amidon, G.E., 2005. Evaluation of the effects of tableting speed on the relationships between compaction pressure, tablet tensile strength, and tablet solid fraction. J. pharmaceutical Sci. 94, 465–472.

Uecker, M., Zhang, S., Frahm, J., 2010a. Nonlinear inverse reconstruction for real-time mri of the human heart using undersampled radial flash. Magn. Reson. Medicine 63, 1456–1462.

Uecker, M., Zhang, S., Voit, D., Karaus, A., Merboldt, K., Frahm, J., 2010b. Real-time mri at a resolution of 20 ms. NMR Biomed. 23, 986–994.

V. Smilauer et al., 2021. Yade Documentation 3rd ed. The Yade Project. doi:`10.5281/zenodo.5705394`. http://yade-dem.org/doc/.

Walton, O.R., Braun, R.L., 1986. Viscosity, granular-temperature, and stress calculations for shearing assemblies of inelastic, frictional disks. J. Rheol. 30, 949–980.

Wang, S., Li, H., Wang, R., Tian, R., Sun, Q., Ma, Y., 2018. Numerical simulation of flow behavior of particles in a porous media based on cfd-dem. J. Petroleum Sci. Eng. 171, 140 – 152.

Ward, A., Walton, K., Mawla, N., Kaialy, W., Liu, L., Timmins, P., Conway, B.R., KofiAsare-Addo, 2019. Development of a novel method utilising dissolution imaging for the measurement of swelling behaviour in hydrophilic matrices. Int. J. Pharm. X 1, 100013.

Washburn, E.W., 1921. The dynamics of capillary flow. Phys. Rev. 17, 273–283.

Williams, J., O'Connor, R., 1995. A linear complexity intersection algorithm for discrete element simulation of arbitrary geometries. Eng. Comput. 12, 185–201.

Wilson, D., Wren, S., Reynolds, G., 2011. Linking dissolution to disintegration in immediate release tablets using image analysis and a population balance modelling approach. Pharm. Res. 29, 198–208.

Wu, C.Y., Hancock, B., Mills, A., Bentham, A., Best, S., Elliott, J., 2008. Numerical and experimental investigation of capping mechanisms during pharmaceutical tablet compaction. Powder Technol. 181, 121–129.

Xia, B., Sun, D.W., 2002. Applications of computational fluid dynamics (cfd) in the food industry: a review. Comput. Electron. Agric. 34, 5–24.

Yanagita, T., 1999. Three-dimensional cellular automaton model of segregation of granular materials in a rotating cylinder. Phys. Rev. Lett. 82, 3488–3491.

Yassin, S., Goodwin, D.J., Anderson, A., Sibik, J., Wilsona, D.I., Gladden, L.F., Zeitler, J.A., 2015a. The disintegration process in microcrystalline cellulose based tablets, part 1: Influence of temperature, porosity and superdisintegrants. J. Pharm. Sci. 104, 3440–3450.

Yassin, S., Su, K., Lin, H., ladden, L.F., Zeitler, J.A., 2015b. Diffusion and swelling measurements in pharmaceutical powder compacts using terahertz pulsed imaging. J. Pharm. Sci. 104, 1658–1667.

York, P., 2022. Design of dosage forms, in: Aulton, M.E., Taylor, K.M.G. (Eds.), Aulton's Pharmaceutics The Design and Manufacture of Medicines, sixth edition. Elsevier. chapter 1, pp. 1–12.

Zarmpi, P., Flanagan, T., Meehan, E., Mann, J., Fotaki, N., 2017. Biopharmaceutical aspects and implications of excipient variability in drug product performance. Eur. J. Pharm. Biopharm. 111, 1 –17.

Zeitler, J.A., 2016. Pharmaceutical terahertz spectroscopy and imaging, in: Müllertz, A., Perrie, Y., Rades, T. (Eds.), Analytical Techniques in the Pharmaceutical Sciences. Springer, Switzerland. chapter 5, pp. 171–222.

Zeitler, J.A., Shen, Y., Baker, C., Taday, P.F., Pepper, M., Rades, T., 2006. Analysis of coating structures and interfaces in solid oral dosage forms by three dimensional terahertz pulsed imaging. J. Pharm. Sci. 96, 330–340.

Zeitler, J.A., Shen, Y.C., 2013. Industrial Applications of Terahertz Imaging. Springer Berlin Heidelberg, Berlin, Heidelberg. pp. 451–489.

Zeitler, J.A., Taday, P.F., Newnham, D.A., Pepper, M., Gordon, K.C., Rades, T., 2007. Terahertz pulsed spectroscopy and imaging in the pharmaceutical setting - a review. J. Pharm. Pharmacol. 59, 209–223.

Zhang, J., Fan, L.S., Zhu, C., Pfeffer, R., Qi, D., 1999. Dynamic behavior of collision of elastic spheres in viscous fluids. Powder Technol. 106, 98 – 109.

Zhao, N., Augsburger, L.L., 2005. The influence of swelling capacity of superdisintegrants in different ph media on the dissolution of hydrochlorothiazide from directly compressed tablets. Am. Assoc. Pharm. Sci. 6, 120–126.

Zhu, H., Zhou, Z., Yang, R., Yu, A., 2007. Discrete particle simulation of particulate systems: Theoretical developments. Chem. Eng. Sci. 62, 3378 – 3396.